DGK Veröffentlichungen der DGK

Ausschuss Geodäsie der Bayerischen Akademie der Wissenschaften

Reihe C | Dissertationen | Heft Nr. 795

Verena Lieb

Enhanced regional gravity field modeling from the combination of real data via MRR

München 2017

Verlag der Bayerischen Akademie der Wissenschaften

ISSN 0065-5325 ISBN 978-3-7696-5207 9

DGK Veröffentlichungen der DGK

Ausschuss Geodäsie der Bayerischen Akademie der Wissenschaften

Reihe C Dissertationen Heft Nr. 795

Enhanced regional gravity field modeling from the combination of real data via MRR

Vollständiger Abdruck

der von der Ingenieurfakultät Bau Geo Umwelt

der Technischen Universität München

zur Erlangung des akademischen Grades eines

Doktor-Ingenieurs (Dr.-Ing.)

genehmigten Dissertation

von

Verena Lieb

München 2017

Verlag der Bayerischen Akademie der Wissenschaften

ISSN 0065-5325 ISBN 978-3-7696-5207 9

Adresse der DGK:

Ausschuss Geodäsie der Bayerischen Akademie der Wissenschaften (DGK)

Alfons-Goppel-Straße 11 ● D – 80 539 München

Telefon +49 – 89 – 23 031 1113 ● Telefax +49 – 89 – 23 031 - 1283 / - 1100

e-mail post@dgk.badw.de ● http://www.dgk.badw.de

Prüfungskommission

Vorsitzender: Prof. Dr.-Ing. habil. Thomas Wunderlich

Prüfer der Dissertation:
1. Prof. Dr. techn. Roland Pail
2. apl. Prof. Dr.-Ing. Michael Schmidt
3. Prof. Frederik J. Simons, Ph.D., Princeton University

Die Dissertation wurde am
28.09.2016 bei der Technischen Universität München eingereicht
und durch die Ingenieurfakultät Bau Geo Umwelt am 07.12.2016 angenommen.

.

Diese Dissertation ist auf dem Server der Deutschen Geodätischen Kommission unter <http://dgk.badw.de/>
sowie auf dem Server der Technischen Universität München unter
<https://mediatum.ub.tum.de/603840?show_id=1325856> elektronisch publiziert

ISSN 0065-5325 ISBN 978-3-7696-5207 9

Abstract

Spectrally and spatially high-resolution gravity data are only available for specific regions on Earth. They mainly stem from terrestrial, air-/shipborne gravimetry or altimetry measurements over the oceans. A global gravity data coverage, vice versa, can only be achieved by satellite gravimetry missions taking lower spectral and spatial resolutions into account. In order to extract the valuable information of high-resolution local data sets in specific areas, a regional gravity modeling approach is established. The main challenge is hereby the consistent spectral combination of the heterogeneous observations. For this purpose, the beneficial properties of a multi-resolution representation (MRR) are used. The tool of MRR enables the composition of a signal under investigation from several detail signals, which are related to specific spectral bands, and thus, can be filled with information from various geodetic observation techniques referring to their spectral sensitivities.
The modeling approach is based on radial spherical basis functions (SBF). Due to their spatial localization characteristics they are well-suited for regional gravity field representations. Further, in analogy to spherical harmonics, they can be expanded in terms of Legendre series and allow to extract specific frequency bands of the Earth's gravity field by appropriate filtering. Both, their spectral and spatial localization characteristics are used with benefit in this work. Various issues are investigated, as e. g. setting up a flexible parameter estimation model, or balancing the minimum and maximum modeling resolution in order to exploit the signal content of the measurements as optimally as possible. Different observation equations have to be formulated for the diversity of gravitational functionals; a spectral classification of the measurement systems then establishes the basis for a spectral combination and a MRR of the Earth's gravity field.
Within simulation studies the stability and plausibility of the approach are rated and possible error sources are identified. A variety of case studies verifies the method of variance component estimation for the reasonable relative weighting of the observation groups. Combining real data at one single resolution level yields accurate high-resolution regional gravity models; the enhanced approach on multiple levels enables to further enrich those models with lower resolution signal from global satellite data (MRR composition). The internal accuracy is evaluated by the corresponding covariance information, while a cross-validation and comparisons with other regional and global models prove the external accuracy. Hereby, the MRR results show the potential of regionally refining existing global models. Vice versa, the signal under investigation can be spectrally decomposed as well (MRR decomposition), in order to detect data gaps or provide the ground for further analysis, as e. g. studying geophysical phenomena in the Earth's interior.

Zusammenfassung

Schwerefelddaten mit sehr hohen spektralen und räumlichen Auflösungen stehen nur für bestimmte Regionen der Erde zur Verfügung, da sie vor allem aus lokalen terrestrischen sowie Flug- und Schiffsgravimeter-Messungen oder aus Altimetriebeobachtungen über den Ozeanen gewonnen werden. Eine globale Datenabdeckung hingegen kann nur mittels Satellitengravimetrie und damit auf Kosten niedrigerer räumlicher und spektraler Auflösungen realisiert werden. Um den hohen spektralen Informationsgehalt der regionalen Messungen gezielt in den jeweiligen Beobachtungsgebieten zu nutzen, wird ein regionaler Schwerefeldansatz entwickelt, der insbesondere die Kombination der verschiedenartigen Schwerefelddaten begünstigen soll. Dabei bilden die Datenheterogenität und die konsistente spektrale Kombination die größten Herausforderungen. Die Realisierung gelingt mittels einer Multiresolutionsrepräsentation (MRR). Diese Methode ermöglicht ein zu untersuchendes Signal aus einzelnen Detailsignalen zusammenzufügen, welche jeweils verschiedenen Frequenzbändern zugeordnet sind und somit aus Daten von Beobachtungstechniken mit entsprechender spektraler Sensitivität gespeist werden können.
Für die regionale Schwerefeldmodellierung werden radiale, sphärische Basisfunktionen (SBF) verwendet, die sich durch ihre lokalisierenden Eigenschaften besonders für räumlich begrenzte Repräsentationen von Schwerefeldstrukturen eignen. Sie basieren ebenso wie Kugelfunktionen auf Legendre Reihen und können durch entsprechende Definition im Frequenzbereich als spektrale Filter fungieren. Diese Möglichkeit, sowohl in bestimmten räumlichen als auch in bestimmten spektralen Bereichen Schwerefeldinformationen zu extrahieren, wird im Folgenden genutzt. Der Ansatz beinhaltet u. a. das Aufstellen eines flexiblen Modells zur Parameterschätzung oder die Abwägung der minimalen und maximalen spektralen Auflösung um den Signalgehalt der Beobachtungen bestmöglichst auszuschöpfen. Aufgrund der Verschiedenartigkeit der Messdaten werden diese zunächst gemäß ihrer spektralen Eigenschaften klassifiziert und dann unter Berücksichtigung der unterschiedlichen Schwerefeldfunktionale mittels Beobachtungsgleichungen beschrieben. Die Filtereigenschaften der SBF ermöglichen schließlich die Datenkombination entsprechend der spektralen Klassifikation und die Modellierung des Erdschwerefeldes in den verschiedenen Frequenzbereichen.
Anhand von Simulationsstudien werden zunächst die Stabilität und Plausibilität des regionalen Modellierungsansatzes geprüft, beurteilt und mögliche Fehlerquellen aufgedeckt. Eine Vielzahl an Fallstudien mit realen Daten verifiziert die relative Gewichtung der unterschiedlichen Beobachtungsgruppen mittels Varianzkomponentenschätzung. Der MRR-Ansatz beinhaltet sodann nicht nur die Berechnung sehr hochaufgelöster regionaler Schwerefelder aus lokalen Datensätzen, sondern insbesondere auch die Ergänzung der Modelle mit niedriger aufgelöstem Signalgehalt aus den globalen Satellitenbeobachtungen (MRR-Komposition). Durch konsistente Fehlerschätzung kann die interne Genauigkeit der Ergebnisse beurteilt werden, während Kreuzvalidierungen und Vergleiche zu existierenden regionalen und globalen Modellen die externe Genauigkeit bewerten lassen. Die MRR-Ergebnisse zeigen hierbei das Potenzial, die globalen Schwerefeldmodelle in entsprechenden Regionen mit zusätzlicher hochaufgelöster Information zu ergänzen oder umgekehrt, diese spektral aufzuschlüsseln (MRR-Dekomposition), um Datenlücken zu identifizieren oder die Frequenzbereiche für weiterführende Analysen, beispielsweise von geophysikalischen Phänomenen im Erdinneren, nutzbar zu machen.

Contents

1 Introduction

In which direction does a river flow? – Where on Earth is the height "zero"? – What can we use as reference?

If we try to explain the need of gravity field determination in our daily live, such questions may provide food for thought: we use the Earth's gravity field as reference for many practical applications. Precise height systems e. g., deliver the basis for engineering or mapping a country. In order to relate all height measurements to a so-called "zero-height", a global reference is indispensable – we therefore use gravity. Besides geodetic applications, many neighboring disciplines – especially in geophysics – require gravitational information as well, e. g. to model the Earth's interior.
Due to density variations on the Earth's surface, above in the atmosphere, and beneath in the interior, the gravity varies in different regions: Mountains, glaciers, water storage on land, or underwater ridges in the oceans, for instance, have diverse density features. Consequently, their heterogeneously distributed masses cause different gravitational attractions, and turn the determination of the gravity field into a very complex and demanding task.

Motivation

In this work, the main focus is on the determination of the gravitational force on the Earth's surface, that varies from point to point. The primary aim is determining regional gravity fields as comprehensively, effectively and accurately as possible: The challenge is to develop a flexible regional approach combining any kind of real gravity data in order to deliver medium- up to high-resolution gravity field models. Hereby the overall motivation of setting up a "regional" approach – in contrast to a "global" one – directly results from the way how to measure the Earth's gravity field:

Why do we need regional in addition to global gravity field modeling? A variety of gravity measurement techniques has been developed over the last centuries, which are completely different in their spectral and spatial resolution, accuracy and geographical coverage. Each sensor type has its very specific advantages and disadvantages: Satellites detect the gravity field globally and capture long wavelengths, but the spatial resolution at the Earth's surface is actually limited down to around 100 km due to the attenuation of the gravity field with increasing altitude. In contrast, local measurement campaigns with terrestrial, air- or shipborne gravimeters are able to detect much finer gravitational structures and deliver spatial resolutions of less than a few kilometers. While satellite observations are the main data source for global gravity models, higher-resolution observations are needed for regional refinements. Spherical Harmonic (SH) functions are established as appropriate tool for global applications, but they capture the high-resolution information of regional, heterogeneous data insufficiently. They suffer the loss of accuracy due to data gaps, different data density and quality. Here, regional approaches come into play: **As the high-resolution data sets are available only in a very few parts on Earth, there is an urgent need of regional models, that approximate their invaluable information.** Spherical (radial) basis functions (SBF) have global support, but a localizing character. They shall be used to capture spatially limited information and express it with high efficiency and concentration. Being both spatially and spectrally as close as possible to the observations thus requires an appropriate adaptation and set up of the functions. Figure 1.1 presents the general idea.

What are the challenges of (regional) gravity modeling approaches? Localizing Spherical Basis Function (SBF)s seem to be an appropriate tool for regional gravity modeling, but there are a lot of open questions and several challenges which have to be studied: After Newton, the Earth's universal gravitation defines a global gravity field, so that local data sets and regional models capture by nature only a finite part of the gravitational signal, i. e. from the spatial point of view, functions with global support fit regionally limited data sets only

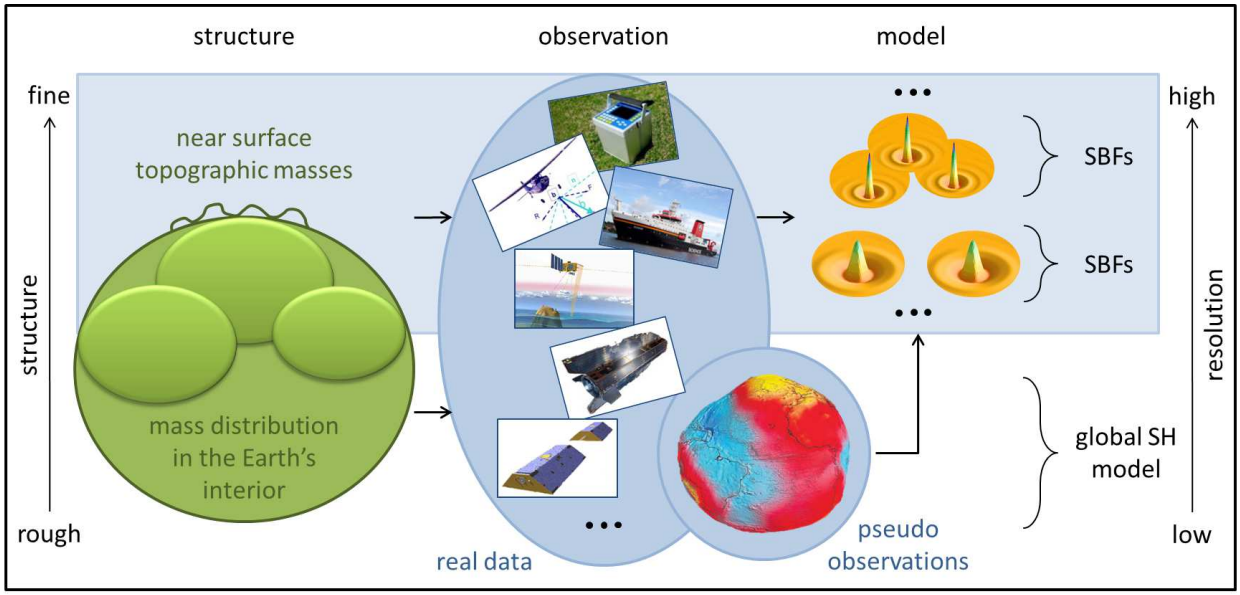

Figure 1.1: General idea: Modeling regional gravitational structure (depending on mass distribution) – from real (terrestrial, air-/shipborne, altimetry, GOCE, GRACE, ...) and pseudo (SH model) observations – in terms of SBFs (on top of a global SH model). The light-blue colored background visualizes the parts which are included in the estimation model, realized in this work.

approximately, and edge effects appear. From the spectral point of view, the Earth's gravitational potential is a continuous quantity, which theoretically could be described by series expansion up to infinity. However, on the one hand, for practical implementation series expansions have to be limited to a finite number of terms. The cut of the infinite series expansion always provokes a truncation error; it has to be studied both in regional and in global approaches. On the one hand, the spectral content, i. e. the captured gravitational information of observations is also limited. According to these spectral restrictions, unknown series coefficients have to be determined. Typically parameter estimation is used in geodetic applications (*Koch*, 1999). In mathematical applications, as for instance presented by *Michel* (2013), numerical integration is favored. It enables the direct computation of the coefficients based on a quadrature method (*Driscoll and Healy*, 1994). However, estimating the unknown parameters in the overdetermined problem of regional gravity modeling has several advantages for the task of this work: Error (co-)variances of the model parameters are estimated as well, and thus, the accuracy and precision of the resulting models can be evaluated. Using the observations at their original positions avoids additional error influences, e. g. from interpolation procedures, and enables the combination of data with different resolutions, accuracies and distribution. However, some effort is required to receive a stable solution: Especially inhomogeneously distributed observations due to data gaps and the need of downward continuation processes for measurements obtained in different heights cause a bad condition of the normal equation system. Therefore regularization schemes have to be implemented, e. g. by introducing prior information. In terms of regional modeling approaches using SBFs, the choice of an appropriate regularization strategy is much more sensitive and less investigated than in global approaches. Above all, the **variety of basis functions** (splines, wavelets, Slepians, Mascons, etc.) offers many positive features, but the selection for different applications and requirements has to be taken very carefully. Open questions append, as e. g. where to locate the functions (on a sphere, ellipsoid, on different layers inside the Earth, etc.), on which **kind of point grid** (geographical, Reuter, icosahedra grid, etc.), and how to determine and handle the related **rank deficiency** problems. The establishment of an **appropriate adjustment model** offers several possibilities how to combine the **inhomogeneous data sets**, how to implement **field transformations** of the observed gravity functionals and how to **estimate the unknown series coefficients** (e. g. by Variance Component Estimation (VCE), Least Squares Collocation (LSC), etc.). All the selections influence each other and have to be taken into account - as well as the model errors from the **truncation of the series expansion**, from **leakage** problems, and **edge effects**.

↪ The primary aim of this thesis is to investigate all those challenges and to develop a proper, stable and efficient approach, that delivers accurate, high-resolution regional gravity field models.

What are the benefits of a combination of multiple data sets via MRR? Within this approach, the spectral content of the regional models shall be enhanced by combining the different high-, medium-, and low-resolution data sets as optimally as possible. The long wavelengths of the gravity field and thus, large-scale structures of the Earth, can only be observed by global satellite observation systems, while short wavelengths are mainly detected with high accuracy by local observation systems. The idea is to combine the different data sets in specific regions in such a way that their benefits contribute as much as possible to the gravity field models. A spectral approach, introducing the resolution-depending gravity information of the different measurement systems step-by-step to the regional model, shall deliver a Multi-Resolution Representation (MRR)[1] of the resulting gravity signal.
As visualized in Fig. 1.1, the combination model is set up by a global, low-pass filtered SH model (in terms of prior information), and several regional, consecutively band-pass filtered SBF models (supplied by different gravity data sets). **Hereby, the observation techniques shall contribute information exactly in the spectral domain of their highest sensitivity, in order to exploit their content and accuracy as optimally as possible, but, as well, by means of reducing erroneous effects as efficiently as possible.** The **consistent spectral composition** of the low- and band-pass filtered gravity field representations can be guaranteed by an appropriate mathematical approach based on a level-discretization of the frequency domain. Furthermore, the connection of the so-called resolution levels could be realized by a pyramid algorithm, which is, however, not part of this thesis. Vice versa, the resulting model can be decomposed by MRR, i. e. displayed at different resolution levels. **Viewing a gravitational signal under different resolutions** enables to detect valuable features of different spectral domains of our planet, such as groundwater storage, oil reserves or density layers in the interior of the Earth.

Review of different regional gravity modeling approaches

While for global gravity field modeling, the use of SHs is well-established and physically proven, they are less appropriate for high-resolution regional gravity field modeling. SHs are optimally localizing in the spectral domain and due to their global character ideally suited for representing globally distributed data sets. However, if high-resolution data sets are only available in certain geographical regions, the spectral information might not be optimally caught: The leakage of high-resolution spectral information in unobserved areas has to be taken into account which leads to a reduced accuracy of the modeled signal. To optimally exploit the content of regional data sets, various regional modeling approaches have been proposed and further developed, especially during the last two decades. They all have different advantages, challenges and are accordingly appropriate for different applications. In the following, a short overview of the most established methods, their originating idea and their main advantages is given. Table 1.1 lists and categorizes the specific features by means of the exemplary implementation by one research group. The main differences result from the type of basis function that is used:

Spherical basis functions and multi-resolution representation Within the set of **basis functions**, which also includes SH functions, the regional gravity field community makes use of **spherical**, i. e. **radial basis functions**. *Freeden et al.* (1998) (and many other publications from his working group) provide the fundamentals of this approach, e. g. further adapted by *Schmidt et al.* (2007). Altogether the functions are based on Legendre polynomials and thus ensure the solution of the Laplace equation in a global case. In contrast to SHs, the SBFs are isotropic and characterized by their localizing feature. For this reason they are an appropriate tool for regional approaches to consider the heterogeneity of data sources (satellite, airborne, terrestrial, etc.), resulting from a different frequency content, sampling geometry, and observation stochastic. They are typically located on point grids and the related unknown coefficients which have to be estimated, feature a geophysical meaning by representing the rough structure of the signal that has to be modeled in the end. The choice of several specific parameters is justified by the findings of *Bentel et al.* (2013b) and *Naeimi* (2013). *Bentel et al.* (2013a) studied various different radial basis functions for their application in regional gravity modeling, based on the approach of *Freeden et al.* (1998) and *Schmidt et al.* (2007), using **scaling** or **wavelet functions**. Those scale-discrete functions act as low- or band-pass filters and thus allow extracting specific domains of the frequency spectrum; from the practical numerical side, they allow implementing fast computation algorithms. Wavelets on the sphere have been studied in detail e. g. by *Holschneider M.* (1996); *Freeden et al.* (1998); *Klees and Haagmans* (2000).

[1] In the literature also known as Multi-Scale Representation (MSR), e. g. *Freeden* (1999); *Freeden and Michel* (2001).

Due to the different spectral content of complementary observations techniques, *Haagmans et al.* (2002) and *Schmidt et al.* (2006) use the advantage of the scale-discretion and set up a **MRR** by combining a low-pass filtered global geopotential model with band-pass filtered satellite gradiometer and regional high-pass filtered gravity data. In view of a mathematical formulation as suggested by *Freeden et al.* (1998), the MRR decomposes the target function into several band-pass filtered detail signals, each related to a certain frequency band and resolution level (e. g. *Schmidt et al.*, 2007). Whereas *Schmidt and Fabert* (2008) applied the MRR in a top-down scenario by using a pyramidal algorithm, *Wittwer* (2009) defines a MRR as a bottom-up approach. Following the concept of adapting SBFs to the frequency content of the signal under investigation, prior variances of the expected signal can be used to construct so-called **spherical splines** (*Eicker*, 2008; *Eicker et al.*, 2013). Those kernels allow a high fine-tuning to the signal characteristics and are strictly positive definite, so that the problem is always uniquely solvable (*Michel*, 2013, p. 163). Further, the properties of the kernels are independent of the chosen point grid on which they are defined, and thus can be placed very flexibly in any region of interest.

Multipole wavelets In contrast to the previous discussed scale-discrete wavelet functions, *Panet et al.* (2006) use **Poisson multipole wavelets**. The principle idea to create different scales, i. e. resolution-depending sensitivities, is, to locate the sources at different depths (*Holschneider et al.*, 2003). Hereby, the scale corresponds to the distance of multipoles (which are based on series expansion in terms of Legendre polynomials) to the Earth's surface. Thus, multipoles can physically be interpreted as masses in the Earth's interior. The main advantages are their locality in phase which leads to quasi-diagonal matrices that are easy to invert, and their definition in the whole space which supports especially the combination of heterogeneous data at different altitudes (*Panet et al.*, 2006). The research groups using multipole wavelets further distinguish between a set of analysis coefficients defined either on a discrete sequence of scales, each containing a fix set of positions, or on different scales and positions as well. The latter method enables a higher spatial flexibility but the computation is much more time consuming.

Mascons The principle idea of simulating mass concentrations that cause differences in the gravitational potential, is applied in the approach of **Mascons** by *Rowlands et al.* (2005). The region of interest is modeled by a uniform layer of mass, e. g. a spherical cap or block, which is added to a mean field. Thus, the variations between the mass elements are scaled by differential potential coefficients (*Chao et al.*, 1987) which have to be estimated. Each set of parameters is defined for a specific epoch so that the localization both in space and time is the main advantage of this approach: On the computation side, correlations between regional solutions decrease, and on the application side, regional mass variations and related gravity field changes can be detected very well. As Mascons are optimally adapted to one observation technique, they are not appropriate for combined gravity fields from heterogeneous observation data.

Slepian functions For an optimal concentration of a gravitational signal both in space (or time) and in the spectral domain, *Simons* (2009) developed an approach using **Slepian functions** (*Slepian and Pollak*, 1961). Those functions are defined within a geographical domain and within a certain frequency bandwidth. The maximum spatial concentration of the strictly band-limited functions in a specific circular region can be found by the maximum energy ratio to respective functions on the whole sphere. The Slepians thus are based on an orthogonal set of SHs and the related unknown "concentrated" coefficients are obtained from the eigenvalue equation of the maximum energy ratio.

Least Squares Collocation The statistical method of LSC has been developed in the 1970s and 1980s (*Krarup*, 1969; *Moritz*, 1978; *Koch*, 1977). The aim is to find the most accurate approximation results on the basis of the available noisy or noise-free data (*Moritz*, 1972), e. g. approximating stochastic variables in a stochastic process or observed functionals of the Earth's gravity field (*Tscherning*, 2015). Compared with the previous mentioned approaches, the use of LSC for regional gravity modeling is the eldest and most experienced. It combines filtering of the input data by removing erroneous noise, adjustment of the unknown parameters, and prediction of a signal, i. e. computing a functional at any desired point. One of the key advantages is, that it provides together with regional gravity field and geoid models from different gravity data types, error information in the form of full covariance matrices. The covariances are assumed to be known and describe the relation between observations and output quantities. For instance *Pail et al.* (2009) and *Arabelos and Tscherning* (2010) adapted the approach for regional refinements of global gravity models and *Tscherning and Arabelos* (2011) developed a powerful software package for regional gravity field determination. *Reguzzoni and Sansò* (2012) discuss in detail a possible method for the combination of high-resolution and satellite-only gravity field models.

Table 1.1: Comparison of different regional gravity field modeling approaches and their specific features – based on the exemplary realization by research groups.

Approach	**SBFs** (*Freeden et al.*, 1998)	**Multipole wavelets** (*Holschneider et al.*, 2003)	**Mascons** (*Chao et al.*, 1987)	**Slepian functions** (*Slepian and Pollak*, 1961)	**LSC** (*Krarup*, 1969)
Realization	e. g. Scaling functions by *Schmidt et al.* (2006), Splines by *Eicker et al.* (2013)	e. g. Poisson wavelets by *Panet et al.* (2006)	e. g. block Mascons by *Rowlands et al.* (2005)	e. g. by *Simons* (2009)	e. g. by *Pail et al.* (2009); *Tscherning and Arabelos* (2011)
Basis	Legendre polynomials	Legendre polynomials	Legendre polynomials	Legendre polynomials	Legendre polynomials
Unknowns	Scaling coefficients	scales	Mascon parameters: scale factor on the set of differential coefficients	eigenvalues	coefficients of prediction
Location/ spatial reference of unknowns	Reuter grid (equidistributed grid points on a sphere, on the Earth's surface or above)	Icosahedron (hierarchical icosahedral meshes on spheres with different radii, in the Earth's interior)	geographical blocks (e. g. $4° \times 4°$) on a sphere, on the Earth's surface, beneath or above)	spherical area, defined by center and radius, on the Earth's surface	input data
Adjustment model and regularization	extended Gauß-Markov Model (GMM), using VCE; prior information from a global SH model	geometric progression of scales; forward modeling with Gaussian probability (least squares); prior information by using a generalized inverse	estimation of Mascon parameters; constraints between Mascons that are close in space and time	estimating eigenvalues from the maximum energy ratio between spatially and spectrally localizing and global functions; inverse problems linear in the data: truncated Slepian basis (at Shannon number, i. e. sum of eigenvalues)	least squares adjustment by expressing the relation between observations and output signal through covariances
consideration of model errors/ (in)completeness	error propagation including signal (truncation error) and noise	covariance matrix of data noise; covariance matrix of coefficients	correlations between the Mascons w.r.t. signal	noise covariance	direct computation of covariances between observations and output signal
Advantages and disadvantages	(+) highly localizing, (+) strict band limitation possible, (-) oscillations due to spatial truncation	(+) defined in the whole space (+) quasi-diagonal matrices easy to invert, (-) non-band limited, non-compact support	(+) high localization both in space and time (high resolution models), (+) direct gravity computation (no truncation errors from any conversion to SHs), (-) prior information: strong spatial constraints	(+) optimal spatial and spectral concentration, (+) reduced number of functions, (-) numerical instabilities due to small eigenvalues	(+) full covariance information directly provided (+) flexible for combination of any observation data (-) large equation systems to solve (depending on number of observations)
Examples of prominent (gravity field or further) applications	height systems, detection of data gaps, ...	3D analysis of the Earth's interior, lithosphere structure studies, geoid models, ...	mass variations on land (glacier), in the ocean, surface water variations, ...	localized gravitational (mass change) or geomagnetic anomalies, ...	static, combined, regional gravity field models, ...

In Fig. 1.2, the basis functions are arranged w.r.t. their spectral and spatial localization property. According to the uncertainty principle a perfect localization both in the spectral and in the spatial domain is not possible. While the SHs are optimally localizing in the spectral domain, the Dirac function (visualized as infinite small peak) is optimally localizing in the spatial domain. Consequently, SHs are appropriate for representing the signal of globally distributed data, while the Dirac function would optimally represent the signal measured at a single point. In order to represent the signal of geographically limited regions, the above presented regional approaches (except the method of LSC) use basis functions, which are all a compromise in-between an optimal spatial and spectral localization (*Freeden et al.*, 1998).

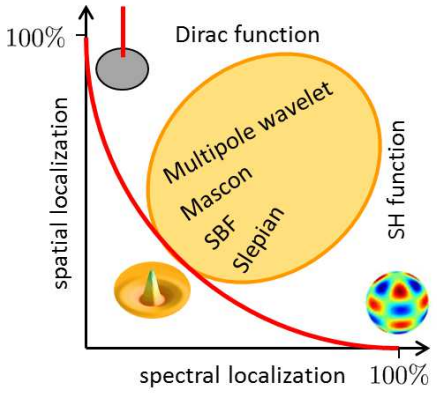

Figure 1.2: Schematic arrangement of basis functions w.r.t. their spectral and spatial localization property.

Altogether, the resulting regional models are not able to resolve the low parts of the frequency spectrum from spatially limited observation sets. In order to cover a broad range of the gravity field signal and to optimally exploit the strengths of each approach, the chosen regional model e. g. can be placed on the top of a high accurate global gravity model, usually based on global satellite observations modeled by SH basis functions. Hereby, satellite-only combination models, such as the Gravity Observation COmbination (GOCO) series (*Pail et al.*, 2010) including data from Gravity Recovery And Climate Experiment (GRACE), from Gravity field and steady-state Ocean Circulation Explorer (GOCE), and from other satellite-related data sources, are distinguished, as well as combination models, such as Earth Gravitational Model 2008 (EGM2008) (*Pavlis et al.*, 2012) including terrestrial and altimetric gravity field data. The latter enhance the spatial resolution apparently on a global scale, but in fact only in regions where a reasonable terrestrial data basis is available.

Research objectives

In this thesis a method of regional gravity field modeling is presented from the combination of various observation techniques via MRR, that enables on the one hand to extract the maximum spectral content out of each measurement system, and on the other hand to manage different observation positions, accuracies and resolutions. Hereby, the focus is on a flexible approach for the combination of real data considering all their specific features, by enhancing the approach of **Spherical basis functions**. This leads to the first research objective, handled in this thesis:

1. Developing a regional modeling approach using SBFs

   Why are SBFs appropriate functions for regional modeling? The main advantage of SBFs in contrast to SHs is their highly localizing character. Both types of globally supporting basis functions are developed in series expansion based on Legendre polynomials. As SHs are eigenfunctions of the Laplace operator (*Freeden et al.*, 1998, p. 36), they are the best choice for gravity field modeling approaches from data with full global coverage. The resulting model of the gravitational potential satisfies the Laplace condition and thus has a physical meaning. Further, the series expansion can be adapted very flexibly to any kind of observation type, e. g. to various gravitational functionals or to measurements at different heights, by applying field transformations. Thus, they are an excellent tool for the combination of different data sets. Since SBFs and SHs can be related to each other, gravity field solutions in SHs can be transformed into solutions in terms of SBFs and vice versa. Consequently, global gravity field modeling by SBFs makes use of all positive (and negative) features of the well-established SH approach. However, for regional application of SBFs, several additional challenges have to be considered, as e. g. the handling of rank deficiencies, edge effects, truncation errors, etc.
   What are the advantages of the SBF approach compared with other regional approaches? The task is, to implement a regional modeling approach which manages the difficulties of SBFs and takes their benefits, compared with and as an alternative to other regional approaches, especially in terms of combining different data sets (see 2. objective). For this case, the spectral flexibility of the functions shall be exploited: acting

as low- and band-pass filters they allow an adaptation to the spectral content of the observation data, as exactly as it is known. Spatially, they can be adapted very flexibly to the observations as well, e. g. by locating their origins anywhere within the appropriate area at the Earth's surface, or along satellite tracks. The resulting challenge is here, to balance the localization in spatial and spectral domain. As a strict band limitation, i. e. an exact frequency cut, enables the spectral combination of different data sets at appropriate resolution levels, a MRR can be applied to construct the output signal. This unique feature of the SBF approach enables to realize the second objective of this work:

2. Combining different data sets via MRR as optimally as possible

   What is the additional value of a combination? As the different measurement systems are sensitive in different frequency domains, they deliver data with different spectral resolutions. In order to model the gravitational signal as completely and as highly resolved as possible, the maximum information of the observations shall be exploited.
   Why is MRR an appropriate combination tool? A close to optimum spectral combination can be achieved by MRR: the frequency domain is split into several resolution levels and the appropriate gravitational signal is modeled from the data obtained by the measurement techniques which are sensitive in this bandwidth. Adding the so-called detail signals in the end, delivers the full gravitational signal between the lowest and the highest resolution of all contributing observations. Missing long wavelengths parts can be filled up with information from global models. Thus, not only a high-resolution regional gravity model is obtained containing as much spectral content as possible, but also information depending on the spectral resolution can be derived from the single detail signals. Different geophysical processes have different spectral sensitivities; potential relations could be derived from such a MRR of the gravitational signal.
   Vice versa to the bottom-up approach, any final gravitational signal could be set up by a top-down algorithm as well, starting with the highest-resolution data set and introducing step-by-step lower-resolution observations. *Schmidt et al.* (2015) theoretically described such a pyramid algorithm by computing the lower levels not only from new observations but also by using the information of the higher levels, considering potential correlations. In this work the bottom-up approach is presented due to its much easier implementation.

3. Enhancing the approach for the use of real data

   What can we learn from simulation studies? Besides real input data, simulated data, e. g. functionals computed from a global SH model, can be used to estimate gravitational signals. Comparing finally the resulting output model with the input model completes the so-called "closed-loop" scenario. The aim is to minimize the differences between in- and output. As the input data and comparison data relate to the same origin, the differences answer two questions: (1) **How accurately does the regional approach fit the real data?** (2) **Are the chosen modeling parameters and settings appropriate?** Simulating observations in different heights or at different noise levels, approximates the characteristic of real data more and more and enables to indicate the stability of the approach.
   What are the challenges of real data? As in most cases the stochastic of real observations is just poorly known, the objective of this work is to develop the approach at the same time as robust and flexible as possible. Especially data gaps and missing knowledge of the exact frequency content of the measurements are additional challenges that have to be considered.
   Depending on the application, the selection of data sets and/or the choice of the region have to be made: The availability, the height, the type, the accuracy, the spatial and the spectral resolution of the data are important criteria, further, the type and resolution of appropriate prior information in order to close data gaps, and finally the location and size of the area to be modeled – depending on the data coverage, edge effects and desired spectral resolution of the resulting gravity signal. As the focus of this work lies on the combination of various different measurement techniques, the regional gravity modeling approach shall not be enhanced in the sense of finding the best model fit to each *single* data set, but in the sense of finding an optimal fit in order to extract as much information as possible, i. e. to take benefit from *all* data sets.

All the challenges, mentioned in the last point, shall be studied and considered – together with the findings from simulation studies – in order to reach the first two objectives. This leads to the overall topic of this thesis: Enhanced regional gravity field modeling from the combination of real data via MRR.

Outline

The thesis is structured in seven main Chapters (including the Introduction). Each Chapter is divided and subdivided in several sections.

Chapter 2 The fundamentals are presented in Chapter 2. They contain both, the study of appropriate literature, but as well, based on appropriate literature, further development of relations which are relevant and important for this work. In the first two sections, Sec. 2.1 and Sec. 2.2, the underlying spaces, dimensions, bases, and coordinate systems are defined. They span the mathematical background. Section 2.3 introduces the physical background. Gravity and gravitational potential are described under the modeling aspect, together with their well-known representation in terms of SHs using Legendre functions. Hereby, new aspects are derived, since the here presented regional gravity modeling approach is established on Legendre Polynomials. Further, field transformations in Sec. 2.4 are studied in order to relate various gravitational functionals under the aspect of their spectral sensitivity. A selection of gravity related quantities, obtained from first and second order derivatives of the potential, is finally presented in Sec. 2.5. Relevant height definitions and reductions complete this chapter.

Chapter 3 The different functionals stem from a variety of measurement systems. They are presented in the first part, Sec. 3.1, of Chapter 3. In Sec. 3.2, a selection of existing models, computed from observables of diverse measurement systems, are presented. In this thesis, global models serve as reference for regional observation techniques, as reference for regional models according to Fig. 1.1, and for regularization purposes. From comparisons of the here computed regional and other regional or global gravitational models, the approach can either be validated, or different information can be identified. In Sec. 3.3 the specific data sets used in this work, and their pre-processing are described. Since the aim is to extract as much information as possible from the measurements, the observations shall be kept in their most original and less pre-processed state.

Chapter 4 The fundamentals of the regional modeling approach are formulated in Chapter 4. It thus comprises the core of this work. In Sec. 4.1, the SBFs are introduced and related to SH basis functions. From theoretical investigations of representing non-bandlimited functions, in Sec. 4.2, the transition to bandlimiting SBFs is discussed. Spherical convolution and referring filtering characteristics are the key elements. Further, the truncation of series expansions and corresponding errors are discussed. Finally, the SBFs are adapted to various gravitational functionals. In the third part, Sec. 4.3, the principle of MRR is introduced. The favorable filtering characteristics of SBFs are used for representing signals at different spectral resolutions. The framework for the MRR is hereby an appropriate splitting of the frequency spectrum into resolution levels.

Chapter 5 Another key role in this work plays Chapter 5. In the first part, Sec. 5.1, several tools and settings for establishing the enhanced regional gravity modeling approach are presented. Hereby, a kind of "recipe" is given for a reasonable, well-balanced parametrization. Especially restricting investigations from global gravity field representations to regional applications are discussed in detail. In the second part, in Sec. 5.2, the estimation model is set up. It is subdivided into a single-level estimation method, computing gravitational functionals from a combination of various observations in specified regions at one resolution level, and a multi-level estimation method, presenting the spectral combination at different resolution levels within the framework of a MRR.

Chapter 6 In Chapter 6, the enhanced regional modeling approach is applied to numerical studies. Besides presenting the results, classified in a variety of different study cases, different methodical parametrization is discussed. Hereby, the complexity increases with investigating a larger number of influencing factors. In principle, two categories are distinguished: Section 6.1 investigates results from the single-level estimation model, while Sec. 6.2 investigates results from the spectral combination model via MRR. First of all, within simulation studies, the stability, consistency and efficiency of the approach shall be judged and verified. Based on those findings, real data studies are discussed with the aims of computing high-resolution regional gravity fields, and regionally refining existing global models. The beneficial peculiarities and the potential of the MRR approach are compared with the single-level approach. Due to the large diversity, only a selection of results can be studied. Within the different study cases, different error influences are identified and discussed in detail.

Chapter 7 The benefits, compromises, and weaknesses of the enhanced regional gravity modeling approach are finally summarized in Chapter 7. With recommendations and ideas for further studies, this thesis closes.

2 Fundamentals

The Earth's **gravitational potential** V, resulting from attractions between masses, delivers together with the **centrifugal potential** Z, resulting from the Earth's rotation, the total **gravity potential** $W = V + Z$. From any potential equipotential surfaces can be derived, i. e. surfaces with constant potential. According to this is favorable property, the "geoid" is the most important equipotential surface in geodesy. Its according potential $W = W_0$ serves as mathematical description of the figure of the Earth (*Hofmann-Wellenhof and Moritz*, 2005, p. 47), i. e. it is ideally suited for many geodetic applications, such as providing a reference for height systems. The **gravitational potential** V is the fundamental quantity for all following considerations in this thesis due to several reasons: From the mathematical point of view, this scalar potential satisfies the Laplace equation and can be expressed as harmonic function outside the Earth's attracting masses. Consequently, essential advantages are inferred for modeling and measuring aspects: A variety of gravitational functionals, as e. g. gravity gradients, gravity anomalies or geoid heights can be derived from the (differential) potential. As mentioned, it further allows to quantify equipotential surfaces. Those unambiguous, well-observable surfaces deliver the basis for detecting density, i. e. mass variations at the Earth's surface.

The following sections give an overview of all gravity related quantities used in this work: Definitions, derivations and relations shall be explained. Special emphasis is given on the way how to describe the gravitational quantities by functional models for the global case. Hereby SHs are used as most popular basis functions. The fundamental part of all basis functions regarded in this thesis are Legendre polynomials. They and their derivatives are the key elements of the later adapted SBFs. Further, this chapter identifies common features between SHs and SBFs. It is, thus, a mixture of reviewing relevant literature, but in equal measure deriving new relations, which contribute to the basis for setting up the regional modeling approach in Chapters 4 and 5, the core of this work.
The chapter is structured as follows: First of all, the underlying spaces, dimensions, bases, and coordinate systems are introduced, spanning the mathematical background. Second, gravity and gravitational potential are introduced under the modeling aspect, together with their well-known representation in terms of SHs using Legendre functions. From the modeling perspective, normal and disturbing potential are briefly introduced, as well. The field transformations in the third part establish the relations between various gravitational functionals. The Meissl scheme hereby provides a reasonable structure and is extended to the specific requirements in this work. A selection of gravity related quantities, obtained from first and second order derivatives of the potential, is finally presented in the fourth part. Some remarks on related height definitions and reductions used in this work complete this chapter.

2.1 Spaces, dimensions and bases

In this work, all coordinate systems and functions are determined in relation to vector spaces and only real valued functions are used. Table 2.1 gives an overview of the relevant spaces, examples for their basis and elements used here. The structure of this section follows the table, starting with describing vectors in the well-known Euclidean space, transferring the investigations to the description of functions/functionals on a sphere, and finally describing elements in the exterior of a sphere, as well.

Vector space

The coordinate systems are defined in the metrical, three-dimensional **Euclidean space** $\mathbb{R}^3$ (e. g. *Heinhold and Riedmüller*, 1971, pp. 79). It needs exactly three non-collinear basis vectors $\boldsymbol{e} \in \mathbb{R}^3$ (here $\boldsymbol{e}_i, i \in \{1, 2, 3\}$) to span this vector space. Any element, e. g. the position vector $\boldsymbol{x} \in \mathbb{R}^3$, is uniquely defined within $\mathbb{R}^3$ and

Table 2.1: Overview of spaces, their basis vectors/functions, and exemplary elements.

space	dimension	basis vectors/functions	elements
$\mathbb{R}^3$	3	$\boldsymbol{e}$	$\boldsymbol{x}$ ... (position) vectors (e. g. expressed by Cartesian, spherical or ellipsoidal coordinates)
$L^2(\Omega_R)$	∞	$H^R_{l,m}$ ... surface SHs, $m = -l...l$ b ... SBFs	f ... (harmonic) functions on Ω_R $\mathcal{Y}[\tilde{V}]$ ... functionals on Ω_R (at locations $\boldsymbol{x} \in \Omega_R$)
$H_{0,1,\ldots,\infty}(\Omega_R^{\text{ext}})$, $\Omega_R^{\text{ext}} = \Omega_R \cup \Omega^{\text{ext}}$	∞	$H_{l,m}$ ... solid SHs, b ... SBFs	f ... (harmonic) functions in Ω_R^{ext} $\mathcal{Y}[\tilde{V}]$ ... functionals in Ω_R^{ext} (at locations $\boldsymbol{x} \in \Omega_R^{\text{ext}}$)
$H_{0,1,\ldots,L}(\Omega_R^{\text{ext}})$	$(L+1)^2$	$H_{l,m}$ ... solid SHs, b ... SBFs	f ... (harmonic) functions in Ω_R^{ext} $\mathcal{Y}[\tilde{V}]$ ... functionals in Ω_R^{ext} (at locations $\boldsymbol{x} \in \Omega_R^{\text{ext}}$)

can be expressed as linear combination of the three basis vectors, i. e.

$$\boldsymbol{x} = \sum_{i=1}^{3} x_i \boldsymbol{e}_i \,. \tag{2.1}$$

Each component x_i (coefficient, linear factor, respectively) can be interpreted as scaling factor of a projection of $\boldsymbol{x}$ onto $\boldsymbol{e}_i$.
If the basis vectors are unit vectors and orthogonal to each other (e. g. $\boldsymbol{e}_1 = (1,0,0)^T$, $\boldsymbol{e}_2 = (0,1,0)^T$, $\boldsymbol{e}_3 = (0,0,1)^T$), they form an orthonormal basis, i. e.

$$\left\langle \boldsymbol{e}_i, \boldsymbol{e}_j \right\rangle_{\mathbb{R}^3} = \boldsymbol{e}_i^T \, \boldsymbol{e}_j = \delta_{i,j} \,, \qquad i,j \in \{1,2,3\} \,, \qquad \delta_{i,j} = \begin{cases} 0 & \text{for } i \neq j \\ 1 & \text{for } i = j \end{cases} \tag{2.2}$$

$$\|\boldsymbol{e}\|_{\mathbb{R}^3} = \sqrt{\langle \boldsymbol{e}, \boldsymbol{e} \rangle_{\mathbb{R}^3}} = 1 \,. \tag{2.3}$$

In Eq. (2.2) the **inner** or **scalar product** is applied on two vectors $\boldsymbol{e}_i, \boldsymbol{e}_j \in \mathbb{R}^3$; Eq. (2.3) presents the **norm** of a vector $\boldsymbol{e} \in \mathbb{R}^3$. In case of orthogonal basis vectors, the elements of the Euclidean space can be described, for instance, by **Cartesian coordinates** (see Sec. 2.2.2).

Function space

A function f with a certain numerical function value $f(\boldsymbol{x})$ at a location with position vector $\boldsymbol{x}$, is defined in a function space (*Lanczos*, 1997, p. 166), cf. Tab. 2.1.

... on a sphere: In contrast to the specific finite-dimensional space $\mathbb{R}^3$, functions are in the following defined in the L^2 normed vector space. On a sphere Ω_R with radius R and surface elements $d\omega_R$ the space is introduced as $L^2(\Omega_R)$. According to Eq. (2.1), each element, e. g. a function $f \in L^2(\Omega_R)$ with $\boldsymbol{x} \in \Omega_R$

$$f = f(\boldsymbol{x}) = \sum_{i=0}^{\infty} c_i \, b_i(\boldsymbol{x}) \,, \tag{2.4}$$

can be expressed by a set of an infinite number of basis functions b_i and coefficients c_i, i. e. a linear combination of basis functions.[2]
If the scalar product of two basis functions exists, the L^2 space, also denoted space of square integrable functions, is a **Hilbert space**. The **scalar product** of two basis functions b_i, b_j (cf. *Freeden et al.* (1998), pp. 57) and the **norm** of a basis function b read

$$\left\langle b_i, b_j \right\rangle_{L^2(\Omega_R)} = \int_{\Omega_R} b_i(\boldsymbol{x}) b_j(\boldsymbol{x}) d\omega_R =: \left\langle b_i, b_j \right\rangle_{\Omega_R} \tag{2.5}$$

[2] In the following, the short form $f(\boldsymbol{x})$ is used, for instance, for describing a function $f = f(\boldsymbol{x})$ in the text, related to the literature. Basis functions b can either be one-point functions with function values $b(\boldsymbol{x})$ depending on $\boldsymbol{x}$, or two-point functions with $b = b(\boldsymbol{x}, \boldsymbol{x}_q)$, additionally depending on the location of the function's center with position vector $\boldsymbol{x}_q$.

$$\|b\|_{L^2(\Omega_R)} = \left[\int_{\Omega_R} |b(\boldsymbol{x})|^2 d\omega_R\right]^{\frac{1}{2}} =: \|b\|_{\Omega_R} < \infty \tag{2.6}$$

with $\boldsymbol{x} \in \Omega_R$. For basis functions $b_i, b_j \in L^2(\Omega_R)$ spanning an orthonormal base, the scalar product (2.5) becomes $\delta_{i,j} = \begin{cases} 0 & \text{for } i \neq j \\ 1 & \text{for } i = j \end{cases}$, $i, j \in \mathbb{N}_0$. Referring to *Freeden* (1999), p. 39, 81, the **spherical convolution** of a basis function b and an element $f \in L^2(\Omega_R)$ is defined as

$$(f * b)_{\Omega_R}(\boldsymbol{x}) = \int_{\Omega_R} f(\boldsymbol{x}) b(\boldsymbol{x}) d\omega_R = \langle f, b \rangle_{\Omega_R} . \tag{2.7}$$

It is equivalent to the inner product of f and b, cf. Eq. (2.5). In the sequel of this thesis, basis functions which are used for convolution, are denoted kernel functions or kernels.

... on and above a sphere: Functions which further shall describe properties of the exterior (ext) of a sphere Ω^{ext}, i. e. $\Omega_R^{\text{ext}} := \Omega_R \cup \Omega^{\text{ext}}$, are defined in a space $H_{0,1,\ldots,\infty}(\Omega_R^{\text{ext}})$ (*Schmidt et al.*, 2007). Compared to the L^2 space, in this expanded space the basis functions $b \in H_{0,1,\ldots,\infty}(\Omega_R^{\text{ext}})$ and their linear combinations cannot be orthogonal.

2.2 Coordinate and reference systems

From the motivation of *regional* gravity field modeling it becomes clear, that the Earth's gravity field is a position-dependent quantity. But which coordinates are appropriate in order to express the gravitational potential V (or any functional of it) at different locations? For either describing a physical phenomenon within specific models, or for measuring specific quantities, various coordinate systems are indispensable and have favorable characteristics. That is, depending on the geometrical, instrumental or practical problem, different observation techniques rely on their own specific reference systems. In order to observe and describe the dynamic system Earth from space, an inertial reference system is appropriate. Consequently, for gravity field modeling from the combination of various heterogeneously defined observables and their approximation by an appropriate model, transformation equations are needed. The most appropriate systems and their relations, i. e. transformations, to each other are presented in the following sections.
(1) A geocentric non-rotating system, (2) geocentric rotating systems, mainly used for global gravity field representations, and (3) local Earth- and satellite-bound coordinate systems, suitable for specific measurement systems, are distinguished. All systems are defined in the three-dimensional Euclidean space $\mathbb{R}^3$.

2.2.1 Geocentric, non-rotating reference system

The fundamental system in which Newton's physical laws hold, is a non-rotating, inertial reference system. Such a system is for instance appropriate for describing the movement of Earth-observing spacecrafts, independently of the Earth's rotation.

The satellite missions, from which data are used in this work, relate to a right-handed system specified by the epoch of Julian Date of 2000 (J2000): the origin O_{J2000} is defined in the center of mass (geocenter), and the axes

X_{J2000}	intersection of mean ecliptic plane with the mean equatorial plane at J2000 (counted positively towards the vernal equinox),
Z_{J2000}	orthogonal to the mean equatorial plane at J2000,
Y_{J2000}	orthogonal to the X_{J2000}- and Y_{J2000}-axes,

span a right-handed system (*Cesare*, 2008, p. 11). The example of the J2000 inertial reference system is shown in Figure 2.1. Within this system, a local oriented reference system (LOCS) is displayed as well (see Sec. 2.2.3).

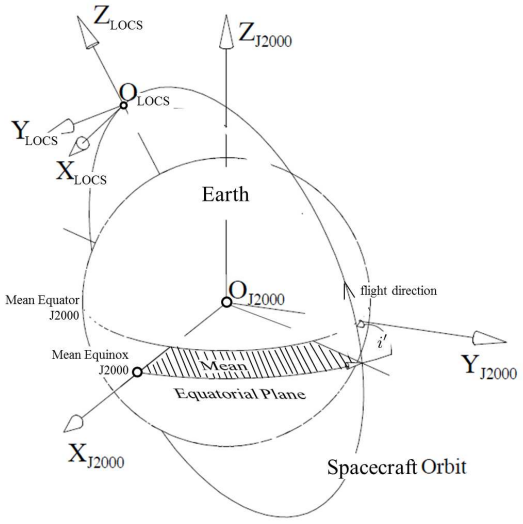

Figure 2.1: Inertial reference and local orbital coordinate system, adapted from *Cesare* (2008). i means the inclination angle of the spacecraft orbit.

2.2.2 Geocentric, rotating coordinate systems

For describing phenomena on the Earth, rotating, Earth-bound coordinate systems are appropriate. In contrast to non-rotating, inertial systems, they are non-inertial; apparent (or pseudo) forces apply, as e. g. the centrifugal or the Coriolis force. In order to model gravitational functionals related to the Earth's surface, the following four Earth-bound, geocentric coordinate systems are most convenient.

Cartesian coordinate system

The fundamental terrestrial coordinate system is defined by 3 rectangular axes X, Y, Z: They span a three-dimensional, right-hand oriented Cartesian coordinate system, see Fig. 2.2. (The local north-oriented coordinate system (LNCS), also visualized in Fig. 2.2, will be introduced in Sec. 2.2.3.) The XYZ-system rotates with the Earth and regards all masses, i. e. solid, fluid, and gaseous ones. The origin is defined in the center of mass. The coordinates of the Cartesian system are specified as

x	along the X-axis (intersection of mean equatorial plane and mean meridian plane trough Greenwich),
y	along the Y-axis (intersection of mean equatorial plane and meridian plane orthogonal to the plane through Greenwich),
z	along the Z-axis (mean rotation axis).

The coordinates x, y, z are counted in metric values. The location of any point P can be described by $P(x, y, z) = P(\boldsymbol{x})$ with $\boldsymbol{x} = [x, y, z]^T$; the distance ds between two points is defined by the square root of $ds^2 = dx^2 + dy^2 + dz^2$.

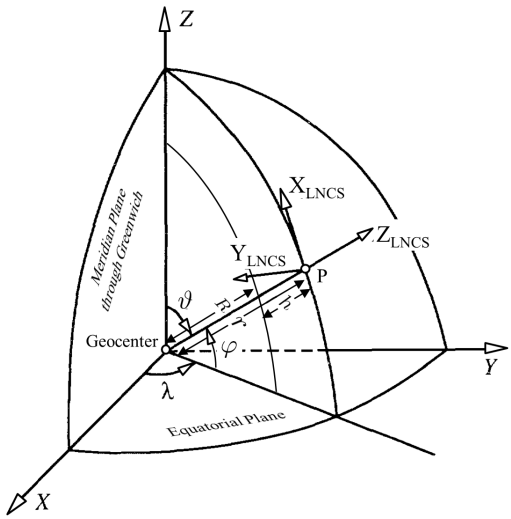

Figure 2.2: Cartesian coordinate system with spherical coordinates and local north-oriented coordinate system (LNCS), adapted from *Koop* (1993, p. 183).

Spherical coordinate system

As many geodetic problems, computations and applications are formulated and executed on a sphere, spherical coordinates are introduced with

λ	geocentric longitude (angle $[0° \cdots 360°[$, measured in equatorial plane, counted positively east-wards from meridian plane through Greenwich)
φ	geocentric latitude (angle $[-90° \cdots 90°]$, measured in meridian plane, counted positively north-wards from equatorial plane to the normal through the corresponding point on the sphere),
(ϑ	co-latitude, respectively polar distance angle $90° - \varphi$ $[0° \cdots 180°]$, measured in meridian plane, counted positively south-wards from North to South pole), and
r	radial distance from the geocenter (counted in metric units),

see Fig. 2.2. A point $P(\lambda, \varphi, r) = P(\boldsymbol{x})$ then can be identified by its geocentric position vector

$$\boldsymbol{x} = r \cdot \boldsymbol{r} = r \cdot [\, \cos\varphi \cos\lambda, \cos\varphi \sin\lambda, \sin\varphi \,]^T = r \cdot [x, y, z]^T \,. \tag{2.8}$$

Hereby $\boldsymbol{r}$ denotes the unit vector and $r = |\boldsymbol{x}| = R + h$ the radial distance of the point P with height h over the sphere Ω_R with radius R. The element of distance ds is now given as

$$ds^2 = dr^2 + r^2 d\vartheta^2 + r^2 \sin^2\vartheta d\lambda^2 \,, \tag{2.9}$$

and the surface element $d\omega_R$ on the sphere Ω_R (cf. Sec. 2.1) is defined as

$$d\omega_R = R^2 \sin\vartheta d\vartheta d\lambda \,. \tag{2.10}$$

The spherical distance angle ψ between two surface points can be computed by

$$\psi = \arccos\left(\cos\vartheta \cos\vartheta_q + \sin\vartheta \sin\vartheta_q \cos(\lambda_q - \lambda)\right) \tag{2.11}$$

(e. g. *Torge*, 2003, p. 60). The origin of the spherical coordinate system is located in the center of mass, equivalently to the origin of the Cartesian system.

Transformation: Cartesian – spherical coordinates The transformation equations from Cartesian x, y, z to spherical λ, φ, r coordinates yield

$$\begin{aligned} \lambda &= \arctan\left(\frac{y}{x}\right) , \\ \varphi &= \arctan\left(\frac{z}{\sqrt{x^2 + y^2}}\right) , \\ r &= \sqrt{x^2 + y^2 + z^2} \,. \end{aligned} \tag{2.12}$$

Ellipsoidal coordinate system

While approximating the Earth as a sphere is practical or sufficient for many geodetic applications, some require a more precise approximation: the geometrical figure of a rotating ellipsoid (ellipsoid of revolution, spheroid) is used, e. g., for national position coordinates or for the normal gravitational potential, which is described later in Sec. 2.3.4. The deviation from a sphere is expressed by the flattening f', depending on the major and minor semi-axes a and b.

f', b, and further ellipsoidal parameters, as the first and second numerical eccentricities, e and e', and the normal radius N' of curvature read

$$f' = \frac{a-b}{a} \tag{2.13}$$

$$b = a\,(1-f') \tag{2.14}$$

$$e = \frac{\sqrt{a^2-b^2}}{a} \quad , e^2 = f'(2-f') \tag{2.15}$$

$$e' = \frac{\sqrt{a^2-b^2}}{b} \tag{2.16}$$

$$N' = \frac{a^2}{\sqrt{1-e^2\sin^2\beta}} \tag{2.17}$$

(e. g. *Torge*, 2003, p. 83). According to Fig. 2.3, the center of the rotating ellipsoid coincides with the geocenter. The ellipsoidal coordinates of a point $P(\lambda, \beta, h')$ outside the ellipsoid yield

- λ ellipsoidal longitude (angle, equivalent to spherical longitude λ)
- β ellipsoidal latitude (angle, measured in meridian plane, counted between equatorial plane and ellipsoidal normal through the corresponding point on the ellipsoid),
- h' height above ellipsoid (counted in metric units along the ellipsoidal normal) .

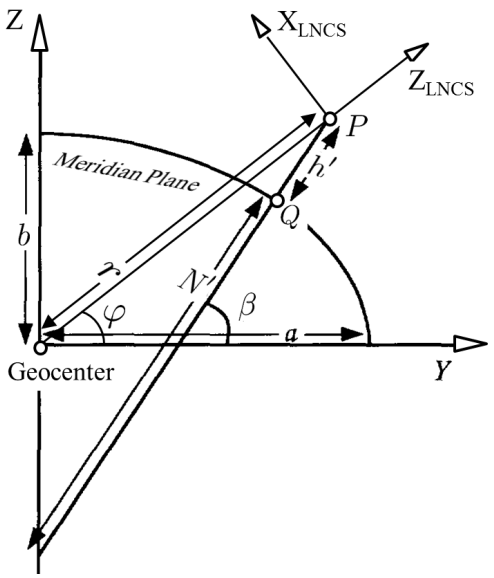

Figure 2.3: Ellipsoidal parameters in a YZ-Cartesian coordinate system, adapted from *Koop* (1993, p. 183). Spherical latitude φ, the axes X_{LNCS}, Z_{LNCS} and a reference point Q at the ellipsoid are plotted, as well.

The point $Q = Q(\lambda, \beta)$ in Fig. 2.3 is the according point on the ellipsoid with $h' = 0$. The ellipsoidal normal, denoted as unit vector $\boldsymbol{n}'$ with

$$\boldsymbol{n}' = [\cos\beta\cos\lambda, \cos\beta\sin\lambda, \sin\beta]^T\,, \tag{2.18}$$

is oriented outwards the body.

Transformation: ellipsoidal – Cartesian coordinates With the normal radius N' of the curvature from Eq. (2.17), the transformation equations from ellipsoidal λ, β, h' to Cartesian x, y, z coordinates become

$$\begin{aligned} x &= (N+h')\cos\beta\cos\lambda \\ y &= (N+h')\cos\beta\sin\lambda \\ z &= \left(\frac{b^2}{a^2}N + h'\right)\sin\beta\,. \end{aligned} \tag{2.19}$$

While the Cartesian coordinates x, y, z can be simply computed from λ, β, h', the inverse transformation requires an iterative approach, e. g. (*Hofmann-Wellenhof and Moritz*, 2005, p. 195). A direct transformation by means of an appropriate solution is presented in *Bowring* (1985).

Transformation: ellipsoidal – spherical coordinates Further, with e^2 and N' from Eqs. (2.15) and (2.17), the transformation equations from ellipsoidal λ, β, h' to spherical λ, ϑ, r coordinates yield

$$\begin{aligned} \lambda &= \lambda \\ \vartheta &= \arctan\left(\frac{(N'+h')\cos\beta}{(N'\,(1-e^2)+h')\sin\beta}\right) \\ r &= \sqrt{((N'+h')\cos\beta)^2 + ((N'(1-e^2)+h')\sin\beta)^2}\,. \end{aligned} \tag{2.20}$$

Transformation: ellipsoidal heights The height difference dh' of a Point P referenced to two slightly different ellipsoids with semi major axes a_1, a_2 and flattening parameters f_1', f_2' can be computed from

$$dh' = a_2 - a_1 + \left(a_1 f_1' - a_2 f_2'\right) \sin^2 \beta \begin{cases} > 0 & \text{for} \quad a_1 < a_2 \\ < 0 & \text{for} \quad a_1 > a_2 \end{cases} . \tag{2.21}$$

The transformation of the height h_1' of P from the first ellipsoid (a_1, f_1') into the height h_2' w.r.t. the second ellipsoid (a_2, f_2') then yields

$$h_2' = h_1' - dh' . \tag{2.22}$$

2.2.3 Local coordinate systems

The geocentric Cartesian coordinate system is very appropriate in order to describe or observe functionals of the Earth's gravity field. However, especially for in situ measurements on Earth and from space, local systems are more suitable. The most relevant local Earth-bound and orbital coordinate systems for this work are described in the following, related to (*Koop*, 1993, Appendix A). The transformation of coordinates from a geocentric, Earth-bound to a local Earth-bound system is described, as well.

Astronomical coordinate system

In order to relate all measurement-depending and Earth-bound reference systems to an universal one, an astronomical system is introduced. It connects geometric with gravitational quantities of the Earth and is, thus, of high importance: as mentioned, the gravity vector $\boldsymbol{g}$ is defined along the **plumb line** of the gravity field. Its direction intersects all equipotential surfaces of the Earth's gravity potential orthogonally and hence denotes the direction of the plumb line. The components of $\boldsymbol{g}$ can be described by two astronomical angles and the magnitude g. The system of equipotential surfaces and plumb lines spans the astronomical system.

The local astronomical coordinates, also known as natural coordinates, with center at point P, are described by

- Λ astronomical (geographic) longitude (angle $[0° \cdots 360°[$, measured in a plane through P, parallel to the equatorial plane, counted positively east-wards from a meridian plane through P, parallel to the one through Greenwich, to the meridian plane through P),
- Φ astronomical (geographic) latitude (angle $[-90° \cdots 90°]$, measured in the meridian plane through P, counted positively north-wards and negative south-wards from equatorial plane through P to the direction $\boldsymbol{n}$ of the local plumb line),
- W gravity potential,

see Fig. 2.4. Consequently, the unit vector along the plumb line is defined by $\boldsymbol{n} = [\cos\Phi\cos\Lambda, \cos\Phi\sin\Lambda, \sin\Phi]^T$, and $\boldsymbol{g}$ points in opposite direction of the unit vector $\boldsymbol{n} = -\boldsymbol{g}/g$.

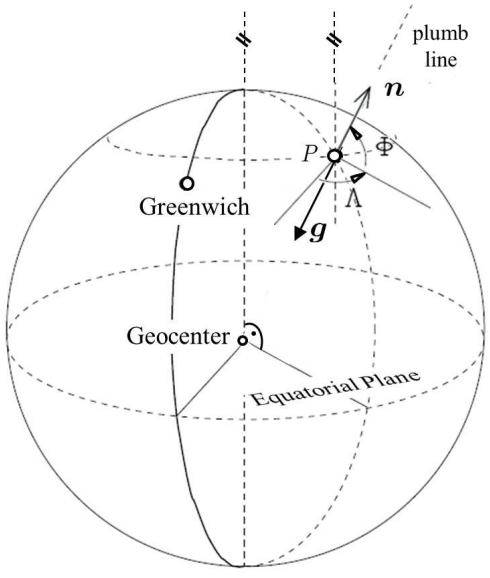

Figure 2.4: Local astronomical coordinates and gravity vector $\boldsymbol{g}$, adapted from *Vermeer M.* (2016, p. 57).

Local north-oriented coordinate system

The Local North-Oriented Coordinate System (LNCS) is an Earth-bound, right-handed Cartesian system with its origin O_{LNCS} defined in an arbitrary point P in space, see Fig. 2.2. The orientation is given by the coordinates $\boldsymbol{x}_{\text{LNCS}} = [x_{\text{LNCS}}, y_{\text{LNCS}}, z_{\text{LNCS}}]^T$ along the corresponding axes:

x_{LNCS} along the X_{LNCS}-axis, directed north,
y_{LNCS} along the Y_{LNCS}-axis, directed west,
z_{LNCS} along the Z_{LNCS}-axis, parallel to the vector from the geocenter to the origin O_{LNCS}, i. e. directed away from the Earth.

Products of the GOCE mission are typically given the LNCS, see Sec. 3.1.4.

Transformation: Cartesian system – LNCS The transformation from the coordinates of a position vector $\boldsymbol{x}$ in the Cartesian system to coordinates of the vector $\boldsymbol{x}_{\mathrm{LNCS}}$ in the LNCS yields

$$\begin{bmatrix} x \\ y \\ z \end{bmatrix} = \begin{bmatrix} -\cos\lambda\cos\vartheta & \sin\lambda & \cos\lambda\sin\vartheta \\ -\sin\lambda\cos\vartheta & -\cos\lambda & \sin\lambda\sin\vartheta \\ \sin\vartheta & 0 & \cos\vartheta \end{bmatrix} \begin{bmatrix} x_{\mathrm{LNCS}} \\ y_{\mathrm{LNCS}} \\ z_{\mathrm{LNCS}} + r \end{bmatrix} . \tag{2.23}$$

The rotation part is expressed by the angles λ,ϑ, acting also as spherical coordinates. The radial distance r from the geocenter denotes the translation of the geocenter to the origin O_{LNCS}.

Local orbital coordinate system

In contrast to the LNCS, the Local Orbital Coordinate System (LOCS) is an Earth-unbound coordinate system. Satellite measurements are performed at observation points which are typically described within a spacecraft-bound LOCS. Hereby, the origin O_{LOCS} is defined in a reference point of the spacecraft, e. g. the center of mass of a satellite, and the axes define the orientation of the coordinate system related to the movement of the spacecraft along the orbit. It thus depends on the inclination angle i' of the orbit w.r.t. an inertial coordinate system. Figure 2.1 visualizes a LOCS w.r.t. the J2000-system. The coordinates of the right-handed, orthogonal LOCS read

x_{LOCS} along the X_{LOCS}-axis, directed along track (in direction of the instantaneous orbital velocity vector of the spacecraft),
y_{LOCS} along the Y_{LOCS}-axis, directed cross track (orthogonal to X_{LOCS}-axis),
z_{LOCS} along the Z_{LOCS}-axis, directed radially outwards.

Note: the expressions "track" and "orbit" are used here equivalently to describe the direction of the actual movement of the spacecraft.

2.3 Gravity as force and potential

In this section, the Earth's gravity potential field is described. Starting from the gravitational potential V as fundamental quantity for this thesis, the first part gives a brief motivation and overview of the physical background. In order to express the potential and related quantities mathematically, a short review on typically used series expanded in terms of SHs, based on Legendre polynomials, is given in the second part. In the third and fourth parts, those series expansions are used to describe the (differential) gravitational and normal potential.

2.3.1 Physical background

The gravitational potential V depends on the attractions between mass elements of the Earth. The basis is Newton's law of gravitation, describing the force $\boldsymbol{F}$ with magnitude F between two arbitrary test bodies with masses m_1 and m_2 and distance $l = |\boldsymbol{l}|$: $\boldsymbol{F} = -G\frac{m_1 m_2}{l^2}\boldsymbol{l}/l$, in an inertial system (cf. Sec. 2.2). Hereby the gravitational force $\boldsymbol{F}$ acts mutually on both masses in opposite direction and decreases with increasing distance l. $G = 6.6742 \times 10^{-11}\ \mathrm{m^3\,kg^{-1}\,s^{-2}}$ is the gravitational constant (*Hofmann-Wellenhof and Moritz*, 2005, p. 3). Considering the Earth as attracting mass with an infinite number of differential mass elements dm, the attraction of an arbitrary point $P(\boldsymbol{x})$ with unit mass can be formulated as scalar quantity, i. e. as **gravitational potential**

$$V = V(\boldsymbol{x}) = G \int_{\text{Earth}} \frac{dm}{l} = G \int_{\text{Earth}} \frac{\rho}{l} dv\,, \qquad \text{with } \lim_{r\to\infty} V = 0 \tag{2.24}$$

(*Torge*, 2003, p. 44). Hereby, the mass elements dm are traced back to their density ρ per volume element dv, so that after Eq. (2.24), V depends on the two parameters l and $\rho = {}^{dm}/_{dv}$. For their quantification, two prominent principles apply: First, as neither the density nor the mass distribution inside the Earth are known, V cannot be computed directly. However, the fundamental fact is used, that outside the attracting masses, the gravitational potential is **harmonic**. It means that with $\rho = 0$, V is the solution of the **Laplace equation**

$$\nabla^2 V = \frac{\partial^2 V}{\partial x^2} + \frac{\partial^2 V}{\partial y^2} + \frac{\partial^2 V}{\partial z^2} = 0 \tag{2.25}$$

(*Hofmann-Wellenhof and Moritz*, 2005, p. 7). In the following, each function $f \in H_{0,1,\ldots,\infty}(\Omega_R^{\text{ext}})$ (cf. Tab. 2.1) that satisfies the Laplace equation, for instance $V \in H_{0,1,\ldots,\infty}(\Omega_R^{\text{ext}})$, is denoted as **harmonic function**.
Second, assuming the Earth's total mass M concentrated in one point, the gravitational potential V of this point mass then is proportional only to the inverse ${}^1/_l$ of the distance between the Earth's center and the attracted unit mass: $V = {}^{GM}/_l$. The product of gravitational constant G and the Earth's total mass M is typically denoted as **standard gravitational parameter** GM. It can be quantified with high numerical precision, whereas not the single terms. (In this work, GM is treated as scaling factor; its value is defined as constant parameter of each normal potential, see Sec. 2.3.4). Consequently, the **reciprocal distance** ${}^1/_l$ is the main unknown quantity of the gravitational potential of a point mass, and the simplest harmonic function (*Hofmann-Wellenhof and Moritz*, 2005, p. 8). It can be expanded in terms of Legendre polynomials, which are the basis of the regional gravity modeling approach presented in this thesis, as well, see next Sec. 2.3.2. From the physical point of view, describing V as harmonic function, i. e. as solution of the Laplace equation (2.25), delivers the fundamental background.
Note: Inside the attracting masses, V satisfies the Poisson equation $\nabla^2 V = -4\pi G\rho$. $\nabla^2 = {}^{\partial^2}/_{\partial x^2} + {}^{\partial^2}/_{\partial y^2} + {}^{\partial^2}/_{\partial z^2}$ is the Laplace operator in Cartesian coordinates, cf. 2.2.2 (*Hofmann-Wellenhof and Moritz*, 2005, p. 7).

Until now, the gravitational potential V was described in a non-rotating system. However, for specifying the total gravity potential $W = V + Z$, the dynamic process of Earth rotation has to be considered, as well. It is quantified by the **centrifugal potential** Z. In contrast to the complex gravitational potential V, Z can be determined much easier and is known with high accuracy .
For any point $P(\boldsymbol{x})$ with Cartesian coordinates x, y, z, Z only depends on the distance $\sqrt{x^2 + y^2}$ from the Earth's axis of rotation and its angular velocity ω:

$$Z = Z(\boldsymbol{x}) = \frac{1}{2}\omega^2(x^2 + y^2) \tag{2.26}$$

(*Hofmann-Wellenhof and Moritz*, 2005, p. 43).
The gradient of the total gravity potential W delivers the **gravity vector** $\text{grad}W = \boldsymbol{g}$, also denoted as **gravity acceleration**. It describes the change of the gravity potential and is defined as

$$\boldsymbol{g} = \text{grad}W = \left[\frac{\partial W}{\partial x}, \frac{\partial W}{\partial y}, \frac{\partial W}{\partial z}\right]^T \quad . \tag{2.27}$$

Its direction $\boldsymbol{n}$, defined tangentially along the **plumb line**, intersects all equipotential surfaces of the Earth's gravity field, i. e. in the following called **geopotential surfaces** with

$$W = \text{const.} \tag{2.28}$$

orthogonally. Therefore, it is often described by astronomical coordinates Λ,Φ (cf. Sec. 2.2.3).
The magnitude

$$g = |\boldsymbol{g}| \tag{2.29}$$

denotes the **gravity** $g = g_P$ in an arbitrary point P on an equipotential surface outside the Earth, i. e. on or above the geoid with potential W_0. This physical acceleration is typically given in the unit Gal ($1\,\text{Gal} = 1\,\text{cm/s}^2$) or mGal ($1\,\text{mGal} = 1 \times 10^{-5}\,\text{m/s}^2$) in honor of Galileo Galilei (*Hofmann-Wellenhof and Moritz*, 2005, p. 45). It can be measured by different techniques described in Sec. 3, and thus it is one of the most observed gravitational quantities of near Earth observations, such as of terrestrial, air- and shipborne gravimetry. The order of magnitude is around $9.8\,\text{m/s}^2$ for the spherical Earth.

2.3.2 Resources for mathematical description

In appropriate literature for global gravity field description, the potential is in general expanded in terms of SH functions, based on Legendre polynomials. The basic ideas are summarized in the following, as the regional approach in terms of SBFs, presented in this work, is also based on Legendre polynomials. However, the SBFs distinguish from the SHs, and they are adapted and enhanced to reach the specific task of regional gravity modeling.
Consequently, the following two sections do not only contain studies from the literature, but also further relations and perspectives for the explicit aim of this thesis. First of all, the mathematics are formulated for the global case of gravity modeling. They found the basis for the SBFs presented in Chapter 4. Based on these fundamentals, Chapter 5 then presents all derivations and relations for regional modeling.

Legendre polynomials and functions

In order to describe the gravitational potential from Eq. (2.24) outside attracting masses, V can be expanded in a series as a solution of the Laplace equation (2.25) in spherical coordinates λ, ϑ, r. Hereby, the reciprocal distance $1/l$ between the attracting point $Q(\lambda_q, \vartheta_q, r_q)$ and the attracted point $P(\lambda, \vartheta, r)$ with $r > r_q$, is expressed by a series in terms of **Legendre polynomials** $P_l(\cos\psi)$ (e. g. *Sigl*, 1973). The polynomial

$$P_l(t) = \frac{1}{2^l l!} \frac{\partial^l}{\partial t^l} \left(t^2 - 1\right)^l , \qquad t \in [-1, +1] \tag{2.30}$$

of degree l and argument $t = \cos\psi$, thus, only depends on the spherical distance angle ψ, according to Eq. (2.11), with

$$\cos\psi = \cos\vartheta \cos\vartheta_q + \sin\vartheta \sin\vartheta_q \cos(\lambda_q - \lambda) . \tag{2.31}$$

Derivatives of $P_l(t)$ w.r.t. the spherical co-latitude, i. e. $t = \cos\vartheta$, lead to **associated Legendre functions** $P_{l,m}(t)$, which further depend on order m. They can be composed, for instance, from the formula of Rodriguez

$$P_{l,m}(t) = (1 - t^2)^{m/2} \frac{\partial^m P_l(t)}{\partial t^m} , \tag{2.32}$$

(e. g. *Hofmann-Wellenhof and Moritz*, 2005, p. 16). To expand $1/l$ and thus the gravitational potential V in terms of SH functions on a sphere with constant radius $r = R$, typically **fully normalized Legendre functions**

$$\bar{P}_{l,m}(\cos\vartheta) = \sqrt{\frac{2(2l+1)(l-m)!}{(l+m)!(1+\delta_{0,m})}} P_{l,m}(\cos\vartheta) \quad \text{with} \quad \delta_{0,m} = \begin{cases} 1 & \text{for } m = 0 \\ 0 & \text{for } m \neq 0 \end{cases} \tag{2.33}$$

are used (e. g. *Hofmann-Wellenhof and Moritz*, 2005). All further considerations relate to this fully normalized version (2.33). The terms of $m \neq 0$ are denoted as associated Legendre functions, and the terms of $m = 0$ as Legendre polynomials.
For computing the first and second order derivatives of V and W, i. e. the terms of Eqs. (2.25) and (2.27), further the first and second order derivatives of the Legendre functions $P_{l,m}(t)$ are needed. Subsequently, those derivatives are applied for computing gravitational functionals derived from V (see Sec. 2.5). Appendix A gives a comprehensive overview of the derivatives of the Legendre polynomials and functions w.r.t. the argument t, and of the related derivatives w.r.t. λ, ϑ.

Spherical harmonics

It is well known, that series expansions in terms of SHs are an appropriate tool for describing quantities of the Earth's gravity field globally. The fundamentals are well-established in the literature (e. g. *Hofmann-Wellenhof and Moritz*, 2005; *Torge*, 2003) and used by a broad community of global gravity field modeling (e. g. *Lemoine et al.*, 1997; *Reigber et al.*, 2002; *Flechtner*, 2010; *Pail et al.*, 2010; *Pavlis et al.*, 2012; *Pail et al.*, 2013; *Mayer-Gürr et al.*, 2015). A variety of resulting global gravity models is collected by the International Centre for Global Earth Models (ICGEM) and can be found at http://icgem.gfz-potsdam.de/ICGEM/. The SHs are briefly introduced in the following for several needs: First, in order to describe the gravitational functionals (Secs. 2.3.3, 2.3.4, 2.3.5, 2.5) related to those fundamentals. Second, they are compared with

SBFs (Sec. 4.1) in the overall group of basis functions in order to emphasize the benefits of SBFs for regional applications. Third, global gravity fields modeled by SHs serve as additional information in the regional approach presented in Sec. 5. The global SH models are presented in Sec. 3.2.2.

In Sec. 2.3.1, the gravitational potential V was introduced as harmonic function $f \in H_{0,1,...,\infty}(\Omega_R^{\text{ext}})$, satisfying the Laplace equation on and above the Earth's surface. In order to describe any harmonic function $f = f(\boldsymbol{x})$ in this space, it can be represented by

$$f = f(\boldsymbol{x}) = \sum_{l=0}^{\infty} \sum_{m=-l}^{l} F_{l,m}\, H_{l,m}(\boldsymbol{x}), \qquad \boldsymbol{x} \in \Omega_R^{\text{ext}} \tag{2.34}$$

in terms of **solid SH functions** $H_{l,m} = H_{l,m}(\boldsymbol{x})$. According to Tab. 2.1, the basis functions $H_{l,m}$ span the space $H_{0,1,...,\infty}(\Omega_R^{\text{ext}})$. The dimension depends on degree l ($l \in \mathbb{N}_0$) and is computed by $(l+1)^2$. m ($m = -l, \ldots, l$) denotes the order per each degree l. $\boldsymbol{x}$ means the geocentric position vector of a point $P(\lambda, \vartheta, r) \in \Omega_R^{\text{ext}}$, given e. g. in spherical coordinates. $F_{l,m}$ are the the SH coefficients or **Stokes coefficients**.
If harmonic functions are restricted to the sphere Ω_R with $r = R$, the dependency on the radial distance vanishes. Function values of surface SHs $H_{l,m}^R$ are related to those of solid SHs $H_{l,m}$ with

$$H_{l,m}(\lambda, \vartheta, r) = \left(\frac{R}{r}\right)^{l+1} H_{l,m}^R(\lambda, \vartheta, R)\ . \tag{2.35}$$

Hereby, the term $(R/r)^{l+1}$ represents the **up-/downward continuation operator** of a harmonic function. It is discussed in detail in Sec. 2.4.1 and becomes one for $r = R$. The function values $H_{l,m}^R(\boldsymbol{x}) = H_{l,m}^R(\lambda, \vartheta, R)$ of **surface SHs** can be obtained from

$$H_{l,m}^R(\lambda, \vartheta, R) = \frac{1}{R\sqrt{4\pi}} \begin{cases} \bar{P}_{l,m}(\cos\vartheta)\cos(m\lambda) & \text{for } m = 0, 1, 2, ..., l \\ \bar{P}_{l,|m|}(\cos\vartheta)\sin(|m|\lambda) & \text{for } m = -l, ..., -2, -1 \end{cases} \qquad \boldsymbol{x} \in \Omega_R\ . \tag{2.36}$$

They are expressed in terms of fully normalized Legendre functions $\bar{P}_{l,m}$, according to Eq. (2.33), and represent the basis functions of the space $L^2(\Omega_R)$, cf. Tab. 2.1. If two surface SH functions $H_{l,m}^R$, $H_{n,k}^R$ are orthogonal to each other, the scalar product, as defined in Eq. (2.5), exists. It yields the **orthogonality relation**

$$\langle H_{l,m}^R, H_{n,k}^R \rangle_{\Omega_R} = \int_{\Omega_R} H_{l,m}^R(\boldsymbol{x})\, H_{n,k}^R(\boldsymbol{x}) d\omega_R = \delta_{l,n}\delta_{m,k}\ , \tag{2.37}$$

with $\delta_{l,n} = 0$ for $l \neq n$, and $\delta_{l,n} = 1$ for $l = n$. $d\omega_R$ is the surface element according to Eq. (2.10).
Multiplying the function values of two surface SH functions $H_{l,m}^R$ at different locations $P(\boldsymbol{x})$, $P(\boldsymbol{x}_q)$ on Ω_R, and accumulating them up to a specific degree l, leads to the **addition theorem**

$$\frac{2l+1}{4\pi R^2} P_l(\cos\psi) = \sum_{m=-l}^{l} H_{l,m}^R(\boldsymbol{x})\, H_{l,m}^R(\boldsymbol{x}_q), \tag{2.38}$$

which connects surface SH functions $H_{l,m}^R$ with Legendre polynomials P_l, Eq. (2.30), depending on the spherical distance $t = \cos\psi$ between the two locations $P(\boldsymbol{x})$, $P(\boldsymbol{x}_q)$.
If a harmonic function $f = f(\boldsymbol{x})$ is given globally on the sphere Ω_R, the **SH coefficients** $F_{l,m}$ can then be uniquely determined by

$$F_{l,m} = \langle f, H_{l,m}^R \rangle_{\Omega_R} = \int_{\Omega_R} f(\boldsymbol{x})\, H_{l,m}^R(\boldsymbol{x})\, d\omega_R \tag{2.39}$$

from the inner product, as defined in Eq. (2.37) (*Driscoll and Healy*, 1994; *Schmidt et al.*, 2007). Equation (2.39) is denoted **spherical Fourier transformation** (e. g. *Schmidt*, 2001, p. 237). The coefficients $F_{l,m}$ only depend on degree l and order m and, thus, are not localizing in space. They can be practically obtained, e. g., by solving the so-called **first boundary-value problem** (2.39) as described in *Hofmann-Wellenhof and Moritz* (2005, pp. 27), or by estimating the parameters within a Gauß-Markov model following *Schmidt* (2001, p. 241). With a set of appropriate coefficients $F_{l,m}$, linear combinations of surface and solid SHs can be

constructed. Consequently, the linear combinations are linear solutions of the Laplace equation, and thus can be used to describe any harmonic function $f = f(\lambda, \vartheta, r) \in \Omega_R^{\text{ext}}$ – i. e. as in our case gravity related quantities – on or outside the sphere Ω_R.

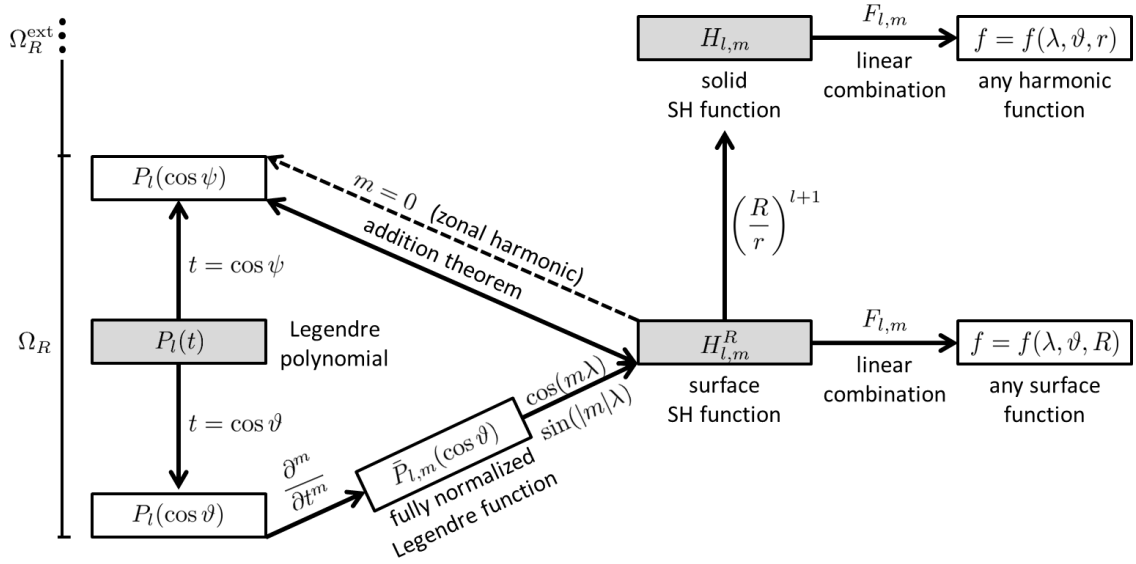

Figure 2.5: Relation between Legendre polynomials, Legendre functions, and SH functions.

Figure 2.5 schematically shows the dependency of a harmonic function $f = f(\boldsymbol{x}) = f(\lambda, \vartheta, R)$ on Legendre polynomials, cf. Eq. (2.30): as mentioned in Sec. 2.3.2, the m^{th} derivative of $P_l(t)$ w.r.t. the argument t leads to (associated) Legendre functions $P_{l,m}(t)$, cf. Eq. (2.32). Multiplying the fully normalized functions $\bar{P}_{l,m}$ with $\cos m\lambda$ or $\sin|m|\lambda$ and a scaling factor, results in **surface SH functions** $H^R_{l,m}$, cf. Eq. (2.36). Vice versa, surface SHs of order $m = 0$ represent Legendre polynomials and are typically denoted as zonal harmonics (*Hofmann-Wellenhof and Moritz*, 2005, p. 18). The dependency between P_l and $H_{l,m}$ is described by the addition theorem (2.38). Further, a linear combination of surface SHs can be used to describe any arbitrary function $f = f(\lambda, \vartheta, R)$ on the sphere Ω_R with a set of appropriate coefficients $F_{l,m}$, cf. Eq. (2.34). Applying the upward continuation operator leads to solid SHs. Finally, any harmonic function $f(\lambda, \vartheta, r)$ can be expanded in terms of solid SHs on and in the exterior of the sphere, i. e. in Ω_R^{ext}.

2.3.3 Gravitational potential

The Earth's gravitational potential V is harmonic outside attracting masses and hence can be expressed by

$$V = V(\lambda, \vartheta, r) = \frac{GM}{R} \sum_{l=0}^{\infty} \left(\frac{R}{r}\right)^{l+1} \sum_{m=0}^{l} \left[C_{l,m} \cos(m\lambda) + S_{l,m} \sin(m\lambda)\right] \bar{P}_{l,m}(\cos\vartheta) \tag{2.40}$$

at any location $P(\lambda, \vartheta, r)$ with $r \geq R$. The series expansion represents a spectral decomposition of the gravitational potential in terms of solid SHs, according to Eq. (2.34). Hereby, $H_{l,m}$, as described in Eq. (2.35), is related to the surface SHs defined in Eq. (2.36). The degree-depending up- or downward continuation term $(R/r)^{l+1}$ assigns the gravitational potential $V(\lambda, \vartheta, r), r > R$, to the potential $V(\lambda, \vartheta, R), r = R$, at the Earth's surface. Referring to Newton's theory, V decreases continuously with increasing radial distance outside the attracting masses; thus, the potential to be modeled up to a spectral degree l is smoothed for $r > R$ ($r \to \infty$). $C_{l,m}$ and $S_{l,m}$ are the (fully normalized) SH coefficients of degree l and order m, summarized and denoted as $F_{l,m}$ in Eq. (2.34). The cosine- and sine-terms yield

$$F_{l,m} = GM\sqrt{4\pi} \begin{cases} C_{l,m} \\ S_{l,m} \end{cases} \tag{2.41}$$

and describe the amplitudes of the corresponding spectral parts of the decomposition. As mentioned above, those unknowns can be unambiguously determined from gravitational boundary values at the Earth's surface. The zero-degree term ($l = 0, m = 0$) of the series (2.40) is connected with the scaling factor GM/R representing the potential of a point mass. The first-degree terms ($l = 1, m = -1, 0, 1$) are related to the shift of the geocenter from the origin of the underlying coordinate system. The coefficients $F_{1,-1}, F_{1,0}, F_{1,1}$ describe the Cartesian coordinates of the geocenter (*Hofmann-Wellenhof and Moritz*, 2005, p. 62). Setting the first-degree terms equal to zero assumes the origin of the coordinate system to coincide with the geocenter. Most of the global gravity field models are defined in such a way (see Sec. 3.2.2).

Rescaling of SH coefficients

The scaling factor GM/R depends on the product of gravitational constant G times mass M of the Earth, and the radius R of the spherical Earth. In ellipsoidal parametrization, the axes defined in the equatorial plane correspond to the radius R. If the scaling factor of the gravitational potential in the expression (2.40) changes, the coefficients $C_{l,m}$, $S_{l,m}$ change as well. The rescaling of the coefficients depends on the relative variation between the previous and the "new" parameters. The rescaled coefficients $C^{\text{new}}_{l,m}$, $S^{\text{new}}_{l,m}$ yield

$$\begin{aligned} C^{\text{new}}_{l,m} &= C_{l,m}\,(1 + (GM - GM^{\text{new}})/GM^{\text{new}}) \quad \text{for} \quad m = 0 \\ \left.\begin{aligned} C^{\text{new}}_{l,m} &= C_{l,m}\,(1 + (GM - GM^{\text{new}})/GM^{\text{new}})\,(1 + (R - R^{\text{new}})/R^{\text{new}}) \\ S^{\text{new}}_{l,m} &= S_{l,m}\,(1 + (GM - GM^{\text{new}})/GM^{\text{new}})\,(1 + (R - R^{\text{new}})/R^{\text{new}}) \end{aligned}\right\} &\quad \text{for} \quad m \neq 0\,. \end{aligned} \tag{2.42}$$

2.3.4 Normal potential and gravity

Modeling the Earth's gravitational potential is very sophisticated and there exists no method for its direct measurement. Hence, the Earth's figure is typically approximated first as sphere, or second as ellipsoid of revolution, also called spheroid. The according potential of the ellipsoid is the **normal potential** U with equipotential surfaces

$$U = \text{const.}\,, \tag{2.43}$$

in the following denoted **spheropotential surfaces** in analogy to the geopotential surfaces defined in Eq. (2.28). The key benefit is, that the mathematical description and handling of the potential becomes much easier (*Hofmann-Wellenhof and Moritz*, 2005, p. 65). The remaining differences between the ellipsoidal "normal" and the "actual" gravity field are small and, thus, allow a more precise and simpler modeling compared with the modeling of the potential V itself.
According to Eq. (2.40), the potential can be expanded in a series in terms of solid SHs up to a maximum degree $l = L$

$$U = U(\vartheta, r) = \frac{GM_0}{R} \sum_{l=0}^{L} \left(\frac{R}{r}\right)^{l+1} C_{l,0}\,\bar{P}_{l,0}(\cos\vartheta) + Z\,, \tag{2.44}$$

with some profitable simplifications: The dependencies of λ and m disappear due to the rotation symmetry of the ellipsoid. Thus, only even zonal coefficients $C_{0,0}, C_{1,0}, C_{2,0} \ldots$ with $m = 0$ remain. The series (2.44) converges very fast, so that for practical implementations, terms up to $L = 10$ are quite sufficient.
The normal potential U in Eq. (2.44) comprises, analogously to W, not only a gravitational, but also a centrifugal component Z. Thus, the velocity of revolution of the ellipsoid can be set equal to the Earth's angular velocity ω. U can be fully described by four parameters:

GM_0	product of gravitational constant G and total mass M_0 of the Earth's normal ellipsoid,
a	major semi axis of the ellipsoid of revolution,
f'	flattening of the ellipsoid of revolution, and
ω	angular velocity of the ellipsoid of revolution.

Referring to the formulas of *Moritz* (2000), the even zonal harmonic coefficients $C_{l,0}$ in Eq. (2.44) are computed from both geometric (ellipsoidal) constants b, e, and e', derived from a and f' according to Eqs. (2.14) -

(2.16), and physical constants, derived from the latter and the parameters GM_0, ω. Physical constants are, for instance, the values of normal gravity γ_a along the equator, and γ_b at the poles, i. e.

$$\gamma_a = GM_0 \frac{1 - e_m - (e_m e' q\, b)/(6q)}{ab}, \tag{2.45}$$

$$\gamma_b = GM_0 \frac{1 + (e_m e' q\, b)/(3q)}{a^2}, \quad \text{with} \tag{2.46}$$

$$e_m = (\omega a)^2 \frac{b}{GM_0},$$

$$q = \frac{1}{2}\left(1 + \frac{3}{e'^2}\right)\arctan(e') - \frac{3}{e'}.$$

By defining a parameter $c = 1/3\,(1 - 2e_m e'/(15q))$, the coefficients $C_{l,0}$ up to degree $L = 10$ result in

$$\begin{aligned} C_{2,0} &= -e^2 \frac{c}{\sqrt{5}} \\ C_{4,0} &= (10c - 1)\,\frac{e^4}{35} \\ C_{6,0} &= -(15c - 2)\,\frac{e^6}{21\sqrt{13}} \\ C_{8,0} &= (20c - 3)\,\frac{e^8}{33\sqrt{17}} \\ C_{10,0} &= -(25c - 4)\,\frac{3e^{10}}{143\sqrt{21}}; \end{aligned} \tag{2.47}$$

the coefficient $C_{0,0}$ is equal to one.

Normal gravity

Along an equipotential surface of the ellipsoid with potential U = const. the **normal gravity** γ can be computed. The horizontal (latitude and longitude) components of the gravity vector become zero due to the rotational symmetry of the ellipsoid. The vertical component, normal to the equipotential surface, mainly varies with the ellipsoidal latitude β. It can be derived, e. g. by the formula of *Somigliana* (1929), from

$$\gamma = \frac{a\gamma_a \cos^2\beta + b\gamma_b \sin^2\beta}{\sqrt{a^2\cos^2\beta + b^2\sin^2\beta}} \tag{2.48}$$

(*Hofmann-Wellenhof and Moritz*, 2005, p. 71) with γ_a, γ_b according to Eqs. (2.45), (2.46). For numerical applications, the normal gravity is typically implemented by

$$\gamma = \gamma_a \frac{1 + k\sin^2\beta}{\sqrt{1 - e^2\sin^2\beta}} \quad \text{with} \quad k = \frac{b\gamma_b}{a\gamma_a} - 1, \tag{2.49}$$

inserting e^2 from Eq. (2.15) (*Torge*, 2003, p. 95).
The normal gravity is used for the computation of several functionals of the gravitational potential. As in general, the Earth's surface does not coincide with the equipotential surface of a reference ellipsoid (potential $U = U_0$), $\gamma = \gamma_0$ has to be projected in a certain height h' above or below the ellipsoid, along the direction n' of the normal gravity vector, see Fig. 2.6. The normal gravity $\gamma_{h'}$ at ellipsoidal height h' can be obtained by expanding Eq. (2.48) in terms of a Taylor series w.r.t. h', i. e.

$$\gamma_{h'} = \gamma_0 + \left(\frac{\partial\gamma}{\partial h'}\right) h' + \frac{1}{2}\left(\frac{\partial^2\gamma}{\partial h'^2}\right) h'^2 + \cdots. \tag{2.50}$$

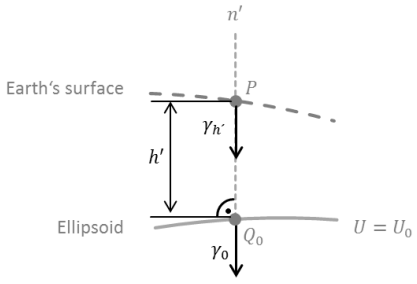

Figure 2.6: Normal gravity γ_0 at a reference ellipsoid and its projection $\gamma_{h'}$ at the Earth's surface.

The first order term is typically approximated by relating the vertical gravity gradient to a mean curvature of the ellipsoid after *Bruns* (1878) (*Torge*, 2003, p. 57). With mean values $\gamma = 9.81\,\mathrm{m/s^2}$ and $a = 6378.137\,\mathrm{km}$, the first derivative $\partial\gamma/\partial h'$ results to approximately $-3.086\,\mu\mathrm{m\,s^{-2}/m}$ (*Torge*, 2003, p. 98).
Vice versa this gradient is also applied for gravity reductions from the gravity in a certain height h' down to the normal gravity γ on the ellipsoid. Neglecting any masses, it is called **free-air reduction**, discussed in Sec. 2.7. The second order term in Eq. (2.50) can be derived from a spherical approximation of γ. As it is in the order of magnitude of $10^{-6}\,\mu\mathrm{m\,s^{-2}/m^2}$ (*Hofmann-Wellenhof and Moritz*, 2005, p. 81), it is neglected in the following.
Inserting $\partial\gamma/\partial h' = -3.086\,\mu\mathrm{m\,s^{-2}/m}$ together with $\gamma = \gamma_0$ from Eq. (2.49) in the expression (2.50), the normal gravity $\gamma_{h'}$ in a certain ellipsoidal height h' yields

$$\gamma_{h'} = \gamma_a \frac{1 + k \sin^2\beta}{\sqrt{1 - e^2 \sin^2\beta}} - 0.3086 \times 10^{-5}\,[\mathrm{mGal}]\; h' \,. \tag{2.51}$$

2.3.5 Disturbing potential

The difference between the previously introduced normal potential U, Eq. (2.44), and the total gravity potential W is called **disturbing potential** $T = W - U$. As the centrifugal component Z is contained in $W = V + Z$ and U to equal parts, and can be determined with high accuracy, the disturbing potential T describes the difference of the gravitational components of both potentials W and U. It yields

$$\begin{aligned} W &= V + Z \\ W &= T + U \end{aligned} \tag{2.52}$$

$$\begin{aligned} V &= T + U - Z \\ T &= W - U = V - U + Z \,. \end{aligned} \tag{2.53}$$

The disturbing potential thus satisfies the Laplace equation $\nabla^2 T = 0$ outside the attracting masses according to Eq. (2.25), and further can be expanded in terms of SHs. Analogously to Eq. (2.40), T can be expressed at any point $P(\lambda, \vartheta, r)$ in Ω_R^{ext} by

$$T = T(\lambda, \vartheta, r) = \frac{GM}{R} \sum_{l=0}^{\infty} \left(\frac{R}{r}\right)^{l+1} \sum_{m=0}^{l} \left[\Delta C_{l,m} \cos(m\lambda) + \Delta S_{l,m} \sin(m\lambda)\right] \bar{P}_{l,m}(\cos\vartheta) \,. \tag{2.54}$$

The difference coefficients $\Delta C_{l,m}$ and $\Delta S_{l,m}$ distinguish only in the low-degree zonal quantities C_l (typically $l \leq 10$) from the total coefficients $C_{l,m}$ and $S_{l,m}$, summarized as $F_{l,m}$ in Eq. (2.41), due to the representation of U according to Eq. (2.44) (*Torge*, 2003, p. 196). The cosine- and sine-terms yield

$$\Delta F_{l,m} = GM\sqrt{4\pi} \begin{cases} \Delta C_{l,m} \\ \Delta S_{l,m} \end{cases} \,. \tag{2.55}$$

Consequently, in order to model the Earth's gravity field, the disturbing potential T can be described w.r.t. a normal potential U, Eq. (2.44). Two benefits result from this fact for regional gravity field modeling: (1) All globally observed gravitational quantities can be reduced by a normal potential term to obtain disturbing potential quantities, as the normal potential is mathematically easy to handle. The remaining differences are small and can be considered as linear, i. e. they linearly depend on T or on derivatives of T (*Hofmann-Wellenhof and Moritz*, 2005, p. 65). Modeling small quantities allows to represent more detailed gravitational structures. (2) Spatially limited, Earth-bound measurement techniques, such as from terrestrial, ship- and airborne platforms, already deliver themselves linearized functionals, e. g. gravity anomalies or disturbances. They are introduced in Sec. 2.5 referring to the disturbing potential or its derivatives.

2.4 Field transformations

Developing and adapting a regional modeling approach for the use of real data is one of the main objectives in this work. As the gravitational potential cannot be observed directly, different techniques established for

determining a variety of gravitational functionals. In order to combine these observations, field transformations are indispensable.

In the sequel, "horizontal" and "vertical" transformations are distinguished, according to the so-called Meissl scheme in Fig. 2.7. For geodetic applications, both the horizontal transformations from one functional to another, as well as vertical transformations of a functional, observed or to be modeled in a certain altitude to another altitude, denoted "up-/ downward continuation", have to be considered. The field transformations apply two times in the modeling approach, see Fig. 2.9: (1) Different measurement systems observe various functionals of the Earth's gravity field in different heights. The input quantities, i. e. observables as well as modeled quantities, have to be homogenized for their combination. The method, realized in a software called "RegGRAV" is presented in Sec. 5. (2) The aim is to compute any gravitational quantity in any height on or above the Earth's surface. Consequently, field transformations are essential for computing the output model. The different transformations can be applied to gravitational quantities, which are, for instance, expanded in a series of SHs according to Eq. (2.34), by using several operators. Referring to *Keller* (2003), most of the functional relations are described by four operators, listed in Tab. 2.2.

Table 2.2: Field transformation operators.

operator	description	mathematical solution
$X^{l+i} = (R/r)^{l+i}$	up-/ downward continuation operator (for the i-1$^{\text{th}}$ derivative after r),	Poisson's integral (e. g. *Hofmann-Wellenhof and Moritz*, 2005, pp. 28)
$\partial/\partial r$	radial derivative operator (any parameter w.r.t. r),	Green's representation theorem, (*Keller*, 2003)
$g_l(r) = r/l+i$	gravity anomaly operator (to apply to the $(i-1)^{\text{th}}$ derivative),	Poisson's integral (e. g. *Hofmann-Wellenhof and Moritz*, 2005, pp. 99)
$1/\gamma$	normal gravity operator	Stokes (and Bruns) formula, (e. g. *Hofmann-Wellenhof and Moritz*, 2005, pp. 102).

The first three operators depend on the radial distance r. They are applied in the Meissl scheme, cf. Fig. 2.7. The scheme is adapted in the following and expanded by further operators in order to derive a variety of gravitational quantities needed in this work. As mentioned above, the observed quantities relate either to the gravitational, or to the disturbing potential. In order to apply the Meissl scheme and the field transformations as flexibly as possible, an initial parameter is defined as (differential) gravitational potential $\tilde{V}$. It summarizes

$\tilde{V} = V - U + Z = T$ disturbing potential,
$\tilde{V} = V - V_{\text{back}}$ gravitational potential reduced by the gravitational potential of a background model,
$\tilde{V} = V - 0$ full gravitational potential.

Functionals derived from the (differential) gravitational potential are in the following denoted as $\mathcal{Y}[\,\tilde{V}\,]$. The most relevant operator is hereby the (partial) derivative $\partial/\partial r$ w.r.t. a certain radial distance r.

2.4.1 Meissl scheme

Rummel and van Gelderen (1995) adapted the Meissl scheme (*Meissl*, 1971a,b) for coupling gravitational functionals depending on the radial distance r. It is appropriate for functionals related to T, stemming from near-Earth observations, as e. g. from terrestrial, air- and shipborne gravimetry. However, in this work, satellite data are used as well and they deliver information related to the gravitational potential V. Thus, a more general scheme is developed for the functionals $\mathcal{Y}[\,\tilde{V}\,]$, see Fig. 2.7, based on the principles of *Rummel and van Gelderen* (1995): The transitions (arrows) can be interpreted as eigenvalues $\bar{\lambda}_l$, i. e. integral relations in the spatial domain. The SH coefficients $F_{l,m}$ are the appropriate eigenfunctions.

... w.r.t. radial derivatives

Using the operators from Tab. 2.2, depending on radial distance r and degree l, the construction in Fig. 2.7 connects all vertical transformations of the initial (differential) gravitational potential $\tilde{V}$ by the up-/downward

continuation operator $X^{l+i} = (R/r)^{l+i}$, and all horizontal transformations by the normal derivative $(\partial/\partial r)$, and the gravity anomaly $(g_l(r) = r/l+i)$ operators. Starting exemplarily from $\tilde{V}_r$, the (differential) gravitational potential in any height (radial distance $r > R$), or from $\tilde{V}$ at the surface of a sphere Ω_R with constant radius R, e. g. approximately the Earth's surface ($r = R$), all quantities $\mathcal{Y}[\tilde{V}]$ related to the first derivatives $\partial\tilde{V}/\partial r$, $\partial\tilde{V}_r/\partial r$, can be obtained. Examples for $\tilde{V} = T$ are gravity anomalies or gravity disturbances. Pursuing in horizontal direction, all quantities related to the second derivatives $\partial^2\tilde{V}/\partial r^2$, $\partial^2\tilde{V}_r/\partial r^2$, can be received (e. g. vertical gravity gradients). The transformations based on the spherical approximation of $\tilde{V} = V$, Eq. (2.40), or $\tilde{V} = T$, Eq. (2.54), thus only depend on degree l and radial distance r.
The normal gravity operator $1/\gamma$ further connects the disturbing potential T with (quasi)geoid undulations N (ζ), according to Bruns formula, see Eq. (2.62). Naturally this transformation is only applied at the Earth's surface, computing the normal gravity $\gamma = \gamma_0$ from Eq. (2.48) referring to a rotational ellipsoid with $h = 0$. (It is neglected in Fig. 2.7.)
The black arrows in Fig. 2.7 symbolize decreasing spectral power in the high frequencies, i. e. a smoothing of the quantities as well as of their noise in case of observables – here, in total, green displayed: from gravity gradients $\partial^2\tilde{V}/\partial r^2$ at the Earth's surface to (differential) gravitational potential $\tilde{V}_r$ in height h. After *Rummel and van Gelderen* (1995), the Meissl scheme can be interpreted as follows: On the one hand, it provides a kind of "tool box" in modeling approaches for deriving gravitational functionals from $\tilde{V}$. On the other hand, it allows to propagate the signal and noise behavior of different observed gravity quantities $\mathcal{Y}[\tilde{V}]$ and their relationships. At the Earth's surface for instance, gravity anomalies (related to $\partial\tilde{V}/\partial r$) have more power in the high frequencies than the disturbing potential (or geoid undulations derived from $\tilde{V} = T$). The higher the derivatives w.r.t. r of a functional, the finer are the gravitational structures which can be determined by appropriate observation techniques, taking into account the measurement altitude.
By applying the scheme the other way round, inverse transformations amplify both signal and noise in the upper part of the frequency spectrum (red arrow). This is important for the coupling of functionals in different heights: All satellite measurements have to deal with increasing errors in downward continuation applications. However, e. g. for the gravity gradient $\partial^2\tilde{V}_r/\partial r^2$, the effect is partly compensated by the sequence of horizontal operators, making satellite gradiometry a very attractive measurement technique for globally gaining high-frequent gravitational information.

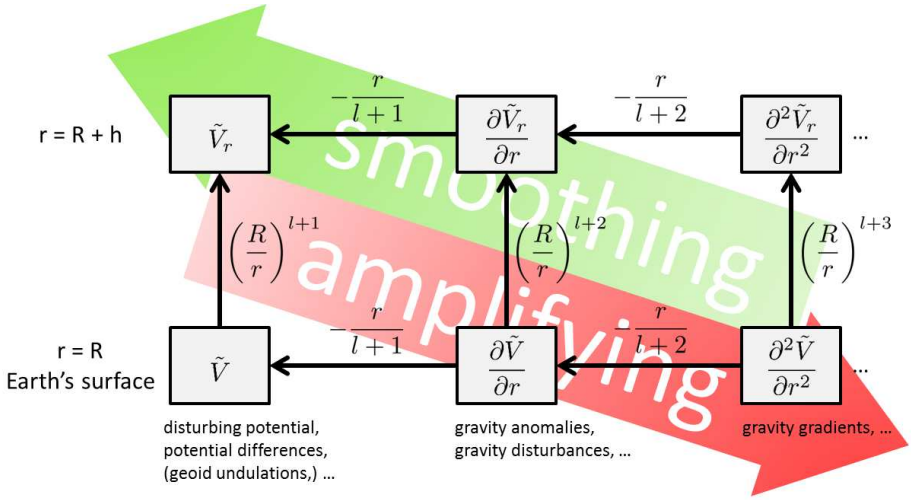

Figure 2.7: Modified Meissl scheme after *Rummel and van Gelderen* (1995), representing field transformations based on the operators $f_l(r)$ of radial-depending quantities related to the (differential) gravitational potential $\tilde{V}$, observed or to be determined in any height $h > 0$ above or at the Earth's surface ($h = 0$). The black arrows symbolize the smoothing behavior of both signal and noise (in case of observables) in high frequencies.

... w.r.t. Cartesian xyz-derivatives

The Meissl scheme originally relates gravitational functionals depending on the radial derivatives of T. It is further extended in this work by derivatives w.r.t. Cartesian xyz-coordinates, see Fig. 2.8, as the functional tensor of gravity gradients typically refers to those.[3] Hereby, the direction of the z-axis is assumed to point in radial direction. Consequently, for the first and second derivatives $\partial\tilde{V}/\partial z$, $\partial^2\tilde{V}/\partial z^2$ at the Earth's surface, respectively $\partial\tilde{V}_r/\partial z$, $\partial^2\tilde{V}_r/\partial z^2$ above the surface, the same horizontal and vertical field transformation operators yield as for radial derivatives. For derivatives w.r.t. x, y, as well as for mixed derivatives and their linear combinations, the horizontal operators consist of several terms, cf. Fig. 2.8. An analogy to Fig. 2.7, the black arrows indicate smoothing behavior in the high frequencies.

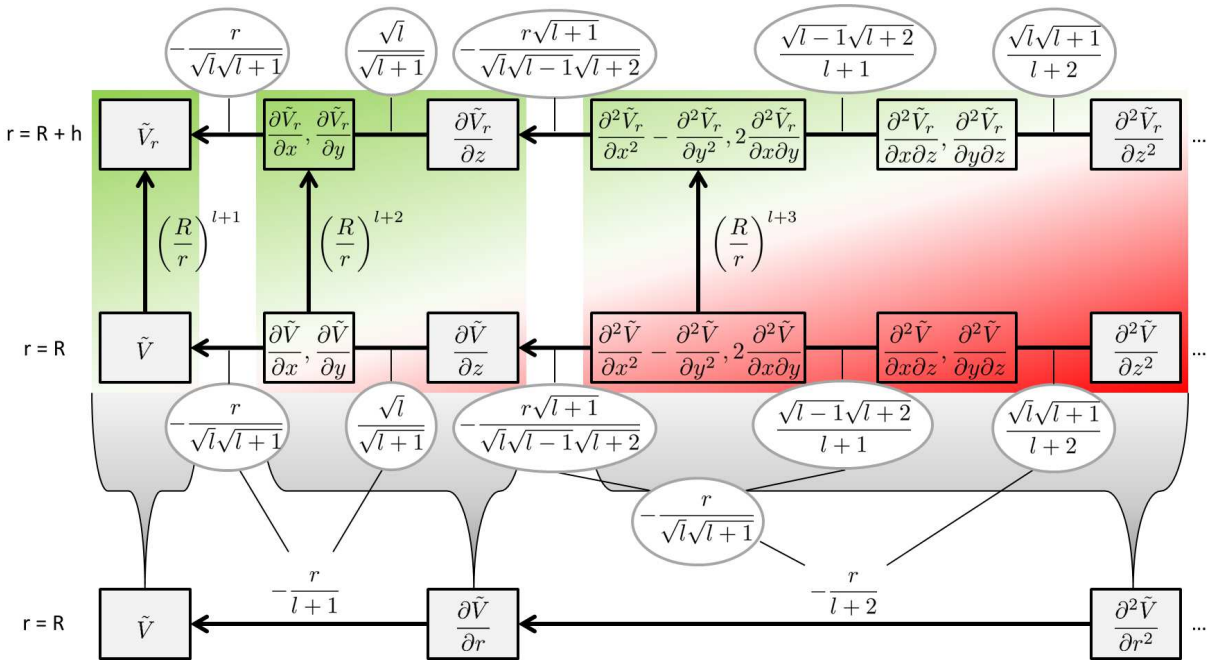

Figure 2.8: Modified Meissl scheme after *Rummel and van Gelderen* (1995), representing field transformations between (combined) xyz-elements of the gravity tensor related to the (differential) gravitational potential $\tilde{V}$, and compared with the first- and second-order derivatives w.r.t. r (bottom line) according to Fig. 2.7. Horizontal operators represent the singular values. The green color indicates smoothing behavior in high frequencies from lower right to upper left, the red color amplification vice versa.

2.4.2 Spherical derivatives of the (differential) gravitational potential in terms of SHs

The gravitational potential V is the main quantity of the Earth's gravity field; any gravitational functional $\mathcal{Y}[\tilde{V}]$ can be derived from it or from the disturbing potential T. In this section, a variety of derived quantities is expressed in terms of SHs to give a general overview. The basis functions then are replaced by SBFs in the sequel of this thesis.

The common series expansion in terms of SHs for describing $\tilde{V} = V$ was given in Eq. (2.40), $\tilde{V} = T$ in Eq. (2.54) respectively. As $\tilde{V}$ depends on the spherical coordinates λ, ϑ, r, the series expansion can be split into several parts (e. g. *Hofmann-Wellenhof and Moritz*, 2005, pp. 32): a scaling factor $f_0 = {}^{GM}/_{R}$, a first summation part $f_l(r)$ depending on the radial distance r, and a second summation part $f_{l,m}(\lambda, \vartheta)$ depending on spherical longitude λ and co-latitude ϑ. For an arbitrary functional $\mathcal{Y}[\tilde{V}]$ it yields

$$\mathcal{Y}[\tilde{V}] = f_0 \sum_{l=0}^{\infty} f_l(r) \sum_{m=0}^{l} \tilde{F}_{l,m}\, f_{l,m}(\lambda, \vartheta)\,, \tag{2.56}$$

by introducing (difference) SH coefficients $\tilde{F}_{l,m} = \{F_{l,m}, \Delta F_{l,m}\}$ according to Eqs. (2.41), (2.55). As mentioned above, the summation parts can be represented by diverse basis functions, i. e. for example by a linear

[3] The adaption to (mixed) derivatives w.r.t. λ, ϑ is neglected, because according quantities play a minor role.

combination of solid SHs $H_{l,m}(\lambda, \vartheta, r)$, cf. Eq. (2.35), or later by a linear combination of SBFs.
The first summation part $f_l(r)$ contains the eigenvalues referring to the Meissl scheme 2.7. It expresses field transformations in terms of the gravity anomaly operator $g_l(r) = g_l$, for $r = R$, and the up-/ downward continuation operator X^{l+i} from Tab. 2.2, each depending on degree l and the latter additionally on the $(i-1)^{\text{th}}$ derivative w.r.t. r, i. e.

$$f_l(r) = g_l \cdot X(r)^{l+i} \ . \tag{2.57}$$

Choosing SHs as basis functions, the second summation part $f_{l,m}(\lambda, \vartheta)$ represents the λ, ϑ-depending terms of surface SHs $H^R_{l,m}$, according to Eq. (2.36). This summation part is further split into the longitude-depending sine $f_{s,m}$ and cosine $f_{c,m}$ functions, and the co-latitude depending Legendre function, cf. Eq. (2.32), or its derivatives, cf. Eqs. (A.1), (A.2) in Appendix A, collected in $f_{P,l,m}$, by

$$f_{l,m}(\lambda, \vartheta) = \begin{cases} f_{c,m}(\lambda)\ f_{P,l,m}(\vartheta) \\ f_{s,m}(\lambda)\ f_{P,l,m}(\vartheta) \end{cases} \ . \tag{2.58}$$

Table 2.3 lists the (differential) gravitational potential $\tilde{V}$, developed in terms of SHs, and all first and second derivatives w.r.t. r, λ, ϑ according to the splitting of Eqs. (2.56) – (2.58). Such a decomposition of the series expansion of a harmonic function, cf. Eq. (2.34), in its different dependencies allows an efficient and flexible implementation in software routines and a flexible replacement of various basis functions.
Multiplying the expressions from Tab. 2.3 with appropriate gravity field operators presented in context with the Meissl scheme enables to describe a large variety of gravitational functionals. This is shown in Sec. 2.5 in terms of SHs, and in Sec. 4.2.5 in terms of SBFs.

Table 2.3: Zero, first and second order derivatives of the (differential) gravitational potential $\tilde{V}$ in terms of SHs w.r.t. spherical coordinates r, λ, ϑ, according to Eqs. (2.56) – (2.58).

$\mathcal{Y}[\tilde{V}]$	f_0	$f_l(r)$			$f_{l,m}(\lambda, \vartheta)$		
		g_l	X^{l+i}	i	$f_{s,m}(\lambda)$	$f_{c,m}(\lambda)$	$f_{P,l,m}(\vartheta)$
$\tilde{V}$	$\frac{GM}{R}$	1	$\left(\frac{R}{r}\right)^{l+i}$	1	$\cos(m\lambda)$	$\sin(m\lambda)$	$P_{l,m}(\cos\vartheta)$
$\frac{\partial \tilde{V}}{\partial r}$	$\frac{GM}{R}$	$-\frac{l+1}{R}$	$\left(\frac{R}{r}\right)^{l+i}$	2	$\cos(m\lambda)$	$\sin(m\lambda)$	$P_{l,m}(\cos\vartheta)$
$\frac{\partial \tilde{V}}{\partial \lambda}$	$\frac{GM}{R}$	1	$\left(\frac{R}{r}\right)^{l+i}$	1	$m\cos(m\lambda)$	$-m\sin(m\lambda)$	$P_{l,m}(\cos\vartheta)$
$\frac{\partial \tilde{V}}{\partial \vartheta}$	$\frac{GM}{R}$	1	$\left(\frac{R}{r}\right)^{l+i}$	1	$\cos(m\lambda)$	$\sin(m\lambda)$	$\frac{\partial P_{l,m}(\cos\vartheta)}{\partial \vartheta}$
$\frac{\partial^2 \tilde{V}}{\partial r^2}$	$\frac{GM}{R}$	$\frac{(l+1)(l+2)}{R^2}$	$\left(\frac{R}{r}\right)^{l+i}$	3	$\cos(m\lambda)$	$\sin(m\lambda)$	$P_{l,m}(\cos\vartheta)$
$\frac{\partial^2 \tilde{V}}{\partial r \partial \lambda}$	$\frac{GM}{R}$	$-\frac{l+1}{R}$	$\left(\frac{R}{r}\right)^{l+i}$	2	$m\cos(m\lambda)$	$-m\sin(m\lambda)$	$P_{l,m}(\cos\vartheta)$
$\frac{\partial^2 \tilde{V}}{\partial r \partial \vartheta}$	$\frac{GM}{R}$	$-\frac{l+1}{R}$	$\left(\frac{R}{r}\right)^{l+i}$	2	$\cos(m\lambda)$	$\sin(m\lambda)$	$\frac{\partial P_{l,m}(\cos\vartheta)}{\partial \vartheta}$
$\frac{\partial^2 \tilde{V}}{\partial \lambda^2}$	$\frac{GM}{R}$	1	$\left(\frac{R}{r}\right)^{l+i}$	1	$-m^2\cos(m\lambda)$	$-m^2\sin(m\lambda)$	$P_{l,m}(\cos\vartheta)$
$\frac{\partial^2 \tilde{V}}{\partial \vartheta \partial \lambda}$	$\frac{GM}{R}$	1	$\left(\frac{R}{r}\right)^{l+i}$	1	$m\cos(m\lambda)$	$-m\sin(m\lambda)$	$\frac{\partial P_{l,m}(\cos\vartheta)}{\partial \vartheta}$
$\frac{\partial^2 \tilde{V}}{\partial \vartheta^2}$	$\frac{GM}{R}$	1	$\left(\frac{R}{r}\right)^{l+i}$	1	$\cos(m\lambda)$	$\sin(m\lambda)$	$\frac{\partial^2 P_{l,m}(\cos\vartheta)}{\partial \vartheta^2}$

Spherical approximations

Expressing gravitational functionals in terms of basis functions, as e. g. SHs or radial SBFs, related to spherical coordinates is very convenient from the modeling point of view. Due to the flattening of the Earth, the quantities would be better approximated by ellipsoidal functions. However, the computational effort is enormous compared with **spherical approximations**. The deviation between quantities, computed on a sphere

or on a reference ellipsoid which is treated as a sphere, is maximal in the order of magnitude of only 3×10^{-3} (*Hofmann-Wellenhof and Moritz*, 2005, p. 96). This corresponds to the order of magnitude of the flattening. The deviations between ellipsoidal or spherical derivatives of the gravitational potential, which are needed for the computation of several functionals, are even smaller. Consequently, expanding series in terms of spherical functions suffices for many applications.
For the regional gravity field modeling approach presented in this thesis, the computations are related to a sphere with constant radius $r = R$, and the functionals are projected in the end to ellipsoidal (or any other) coordinates. The following spherical approximations are applied, neglecting second (or higher) order terms (e. g. *Hofmann-Wellenhof and Moritz*, 2005, pp. 96,97):

$$\frac{\partial}{\partial h} = \frac{\partial}{\partial n'} \approx \frac{\partial}{\partial r} \approx \frac{\partial}{\partial n}\,, \tag{2.59}$$

$$\frac{\partial \gamma}{\partial h} \approx -\frac{2\gamma}{R}\,. \tag{2.60}$$

Equation (2.59) approximates the normal derivative operator w.r.t. ellipsoidal height h' by the radial derivative operator from Tab. 2.2. The normal vector $\boldsymbol{n}$ on a sphere with magnitude n has the same direction r as the radius vector $\boldsymbol{r}$; and the normal n' on an ellipsoid with the according vector $\boldsymbol{n}'$ defined in Eq. (2.18) is the direction of the ellipsoidal height h'. The latter Eq. (2.60) describes the vertical gradient of the normal gravity γ w.r.t. ellipsoidal height h', approximated by a term which only varies with the normal gravity γ. Depending on the application, either the spherical approximation suffices, or it is applied for upward continuation of gravity, i. e. for **gravity reduction**, discussed in Sec. 2.7.

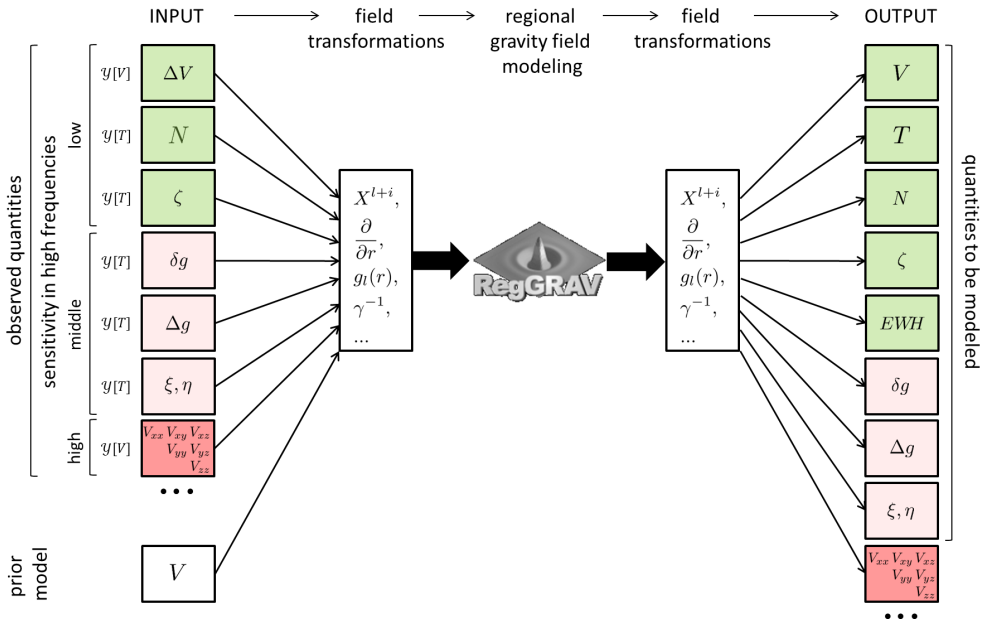

Figure 2.9: Functionals and field transformations in the regional gravity modeling approach. The sensitivity to high frequencies is color-shaded according to Fig. 2.7.

2.5 Gravitational functionals

Based on the field transformations from Sec. 2.4, various functionals $\mathcal{Y}[\,\tilde{V}\,]$ can be derived from the gravitational and the disturbing potential. Figure 2.9 presents a variety of in- and output quantities which are used in the studies of this work. The relations in terms of field transformations are described by the Meissl scheme, in Figs. 2.7 and 2.8. The "RegGRAV" (Regional GRAVity modeling) logo in the middle symbolizes the regional gravity field modeling approach, which is presented in Sec. 5. Parts of this thesis have been studied in the

frame of the "RegGRAV I and II" projects[4], where the logo was introduced.
The following sections introduce the observable input functionals, but now, on the one hand from the physical perspective, and on the other hand from the modeling perspective. As mentioned, the gravitational potential V is the fundamental quantity. Hence, the arrangement of the derived functionals follows the application of more and more field transformation operators, which corresponds to increasing spectral power in high frequencies, referring to Fig. 2.9. The selection of functionals can be supplemented by further (output) quantities, as e. g. equivalent water heights (EWH), which are not part of this study. The corresponding measurement systems are described in Sec. 3; the observation equations of the modeling approach are presented in Tab. 4.7.
According to Fig. 2.9, gravitational potential differences ΔV (Sec. 2.5.1) and gravity gradients V_{ab}, $a, b \in \{x, y, z\}$, (Sec. 2.5.7) are functionals $\mathcal{Y}[\tilde{V}] = \mathcal{Y}[V]$ of the gravitational potential; geoid heights N (Sec. 2.5.2), quasigeoid heights ζ (Sec. 2.5.3), gravity disturbances δg (Sec. 2.5.4), gravity anomalies Δg (Sec. 2.5.5), and deflections of the vertical η, ξ (Sec. 2.5.6) relate to the disturbing potential, i. e. $\mathcal{Y}[\tilde{V}] = \mathcal{Y}[T]$, after reducing V by a normal potential U.
For functionals $\mathcal{Y}[T]$ are further distinguished: The approximation of the gravitational by a normal potential allows to determine the differences between two equipotential surfaces, a spheropotential surface with potential U and a geopotential surface of the Earth's gravity field, e. g. the geoid with potential W_0. It is known as **Stokes theory**. As in most cases, the Earth's surface does not coincide with the geoid, another theory, the **Molodensky theory**, has established. It considers the gravitational functionals as differences between the Earth's surface and the telluroid. Both theories are needed in this work, as different observation data relate as well to the theories of Stokes and of Molodensky. They are briefly mentioned when describing the single functionals. For more details see e. g. *Hofmann-Wellenhof and Moritz* (2005); a comprehensive overview is given e. g. by *Sánchez* (2015).

2.5.1 Gravitational potential difference

Modeling the gravitational potential V of the Earth as accurately and highly resolving as possible, would in theory require the direct measurement of V outside all attracting masses. As mentioned before, no observation technique is able to realize this. However, the satellite mission GRACE, consisting of two spacecrafts, delivers **gravitational potential differences** $\mathcal{Y}[\tilde{V}] = \Delta V$, i. e.

$$\Delta V = \Delta V(\boldsymbol{x}^i, \boldsymbol{x}^{ii}) = V(\boldsymbol{x}^i) - V(\boldsymbol{x}^{ii}), \tag{2.61}$$

obtained from highly accurate distance measurements between the satellites (i),(ii) at positions $P(\boldsymbol{x}^i)$ and $P(\boldsymbol{x}^{ii})$. Several approaches have been established and realized in order to derive ΔV from the distance measurements, as e. g. the acceleration or the energy balance approach. Details are explained in Sec. 3.1.5.
Expressing $\mathcal{Y}[\tilde{V}] = \Delta V$ in terms of spherical relations according to (2.56), only the scaling factor f_0 is identical for $V(\boldsymbol{x}^i)$ and $V(\boldsymbol{x}^{ii})$. The summation parts $f_l(r)$ and $f_{l,m}(\lambda, \vartheta)$ distinguish due to the different positions $P(\boldsymbol{x}^i)$ and $P(\boldsymbol{x}^{ii})$ of the two satellites. Comparing the sensitivity to high frequencies with the one of other gravitational quantities, it is relatively low and can be arranged referring to $\tilde{V}_r$ within the Meissl scheme 2.7.

2.5.2 Geoid undulation

Equipotential surfaces of the Earth's gravity field are suitable for height reference systems. The geoid for instance, defined as geopotential surface $W = W_0$ according to Eq. (2.28), coincides with the undisturbed, continuously extended mean sea level of the oceans over the whole globe. The approximation of the geoid by an ellipsoid with normal potential U and spheropotential surfaces defined in Eq. (2.43), is implicitly realized by the low-degree terms of global gravity field models. A selection is presented in Sec. 3.2.

[4]Projects funded by the Centre for Geoinformation of the German Armed Forces (ZGeoBw), Euskirchen, Germany: Generation of a software application for producing high precise regional gravity models as a height reference surface.

According to Fig. 2.10, the metric difference between a reference ellipsoid (with potential U_0) and the geoid (with potential W_0) can be described by the **geoid height** or **geoid undulation** N. It is the distance between a certain point P_0 of the geoid and the – along the ellipsoidal normal n' – projected point Q_0 onto the normal potential surface with the same potential $U = U_0 = W_0$ (*Hofmann-Wellenhof and Moritz*, 2005, p. 91). The **Bruns formula**

$$N = \frac{T}{\gamma} \tag{2.62}$$

(e. g. *Hofmann-Wellenhof and Moritz*, 2005, p. 93) relates this geometric distance N to the physical quantity T via the normal gravity operator $1/\gamma$, cf. Tab. 2.2.

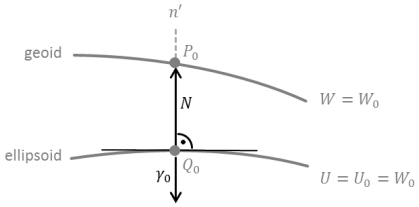

Figure 2.10: Geoid undulation N following Stokes theory.

Following the Stokes theory, assuming that there are no masses outside the geoid, the disturbing potential $T = T(P_0)$ from Eq. (2.54) is computed at the geoid point P_0, while the normal gravity $\gamma = \gamma_0(Q_0)$ according to Eq. (2.48), is computed at the ellipsoidal point Q_0. The mathematical relations between the geometrical and physical quantities are given in Appendix A. Modeling $T(P_0)$ in terms of SHs, the spherical relations $\mathcal{Y}[\tilde{V}] = V$ from Tab. 2.3, and the spherical approximations $\partial/\partial r \approx \partial/\partial n'$ from cf. Eq. (2.59) apply in Eq. (2.54). Arranging geoid undulations $\mathcal{Y}[\tilde{V}] = N$ in the order of the Meissl scheme (Fig. 2.7) at the Earth's surface, this functional would be located along with $\tilde{V}$.

2.5.3 Quasigeoid undulation

As mentioned in Sec. 2.3.5, the disturbing potential satisfies the Laplace equation $\nabla^2 T = 0$ outside attracting masses. However the geoid, as described in Sec. 2.5.2, generally does not coincide with the Earth's surface: especially on land, the topography causes masses above or below the geoid. Consequently, the determination of geoid heights from Eq. (2.62) following Stokes theory, requires the reduction of measured gravity quantities at the Earth's surface down to the geoid. One method applied in this work is presented in Sec. 2.7.

Following the **Molodensky theory**, another option is the introduction of **quasigeoid heights** or **quasigeoid undulations**

$$\zeta = \frac{T}{\gamma}\,, \tag{2.63}$$

applying Bruns formula according to Eq. (2.62), but now considering a point P at the Earth's surface. Projecting P from the Earth's surface along the ellipsoid normal n' onto a surface with potential $U = U_Q = W_P$, results in the geometric distance $\zeta = PQ$, see Fig. 2.11. Physically, this quasigeoid undulation between the geopotential surface with $W = W_P$ through a point P at the Earth's surface and the spheroidal surface with $U = U_Q = W_P$ is defined analogously to N. The quantities in Eq. (2.63) are computed at geopotential surface for $T = T(P)$, and at the spheroidal surface for $\gamma_Q = \gamma_Q(Q)$, see Appendix A.

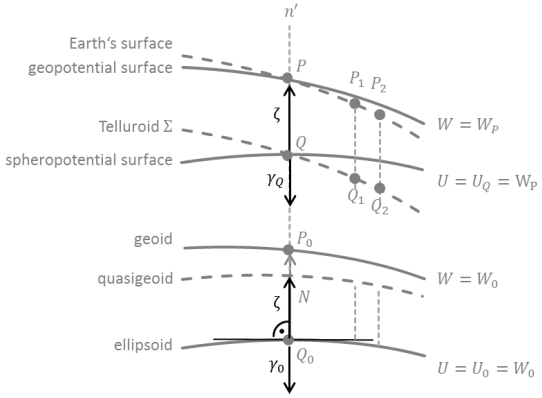

Figure 2.11: Quasigeoid undulation following Molodensky w.r.t. the ellipsoid and analog w.r.t. the telluroid. Dashed lines denote non-equipotential surfaces.

Geometrically, the projections of surface points $P_1, P_2, \ldots$ with different potential values $W_1, W_2, \ldots$ onto points $Q_1, Q_2, \ldots$ with the same normal potential values $W_1 = U_1, W_2 = U_2, \ldots$ describe a new surface, denoted as **telluroid** Σ, see Fig. 2.11. It is an artificial point-wise defined surface. Counting the metric distances ζ vice versa, w.r.t. the ellipsoid (potential $U = U_0$), results in the surface called **quasigeoid**. Over the ocean, it is practically identical with the geoid (e. g. *Hofmann-Wellenhof and Moritz*, 2005, p. 299), due to the absence of topographic masses.

For $\mathcal{Y}[\,\tilde{V}\,] = \zeta$, the same spherical approximations and field transformations account as for N, discussed in the previous section. Hence, the spectral power of quasigeoid undulations in high frequencies and the arrangement in the Meissl scheme (Fig. 2.7) corresponds to the ones of geoid undulations.

2.5.4 Gravity disturbance

Physically, the **gravity disturbance** δg describes the difference

$$\delta g = g_P - \gamma_P \tag{2.64}$$

between the magnitude g_P of the gravity vector $\boldsymbol{g}_P$ along the plumb line n and the magnitude γ_P of the normal gravity vector $\boldsymbol{\gamma}_P$ along the ellipsoidal normal n', in one and the same point P at the Earth's surface following Molodensky, see Fig. 2.12. The gravity disturbance vector $\delta\boldsymbol{g}$ is oriented along n' and expresses the gradient of T: $\delta\boldsymbol{g} = [{}^{\partial T}/_{\partial x}, {}^{\partial T}/_{\partial y}, {}^{\partial T}/_{\partial z}]^T = \operatorname{grad} T$. For modeling purposes, its magnitude (2.64) is expressed by

$$\delta g = -\frac{\partial T}{\partial h'} \,. \tag{2.65}$$

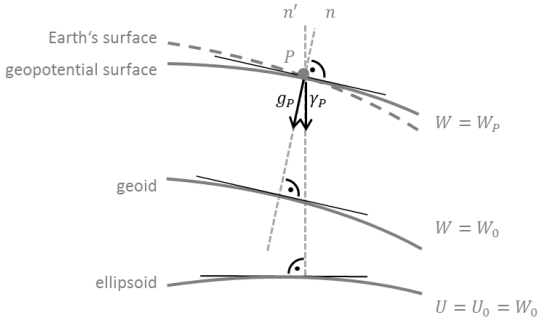

Figure 2.12: Gravity disturbance following Molodensky w.r.t. the Earth's surface.

Note, within the physical relation according to Eq. (2.64) the direction of $\boldsymbol{\gamma} = \boldsymbol{\gamma}_P$ is oriented inwards the ellipsoid, while in Eq. (2.65) the ellipsoidal height h' is counted positively outwards. According to the Molodensky theory, the disturbing potential and the normal gravity are computed at the Earth's surface with $T = T(P)$, $\gamma = \gamma_P(P)$. In the spherical approximation according to Eq. (2.59) the gravity disturbance from Eq. (2.65) becomes

$$\delta g = -\frac{\partial T}{\partial r} \,. \tag{2.66}$$

and the spherical relations $\mathcal{Y}[\,\tilde{V}\,] = {}^{\partial \tilde{V}}/_{\partial r} = {}^{\partial T}/_{\partial r}$ from Tab. 2.3 can be applied, neglecting the difference of the directions of $\boldsymbol{r}$ and $\boldsymbol{n}'$.
Following the Meissl scheme (Fig. 2.7), gravity disturbances δg contain more power in high frequencies than T or N, as they relate to the first derivative of T. For instance, computing geoid undulations N from observed gravity disturbances δg at the Earth's surface consequently smooths the high-frequent signal contents. With the advent of the Global Navigation Satellite System (GNSS) measurements, the determination of δg becomes more and more prominent: GNSS delivers directly ellipsoidal coordinates λ, β, h of a point P, which enables the computation of the normal gravity $\gamma_P = \gamma_h(P)$ according to Eq. (2.50) of this point P at ellipsoidal height h'.

2.5.5 Gravity anomaly

In contrast to gravity disturbances δg, the difference of the gravity vector $\boldsymbol{g}_P$ at a point P at the Earth's surface with potential W_P and the vector $\boldsymbol{\gamma}_Q$ at a point Q of a spheropotential surface $U = U_Q$, see Fig. 2.13, is defined as gravity anomaly vector $\Delta\boldsymbol{g} = \boldsymbol{g}_P - \boldsymbol{\gamma}_Q$. The corresponding magnitude Δg of the vector is denoted **gravity anomaly**

$$\Delta g = g_P - \gamma_Q \tag{2.67}$$

in the sense of Molodensky. It can be determined easily by measuring the magnitude $g = g(P)$ of the total gravity point-wise at the Earth's surface, and reducing it by appropriate normal gravity values $\gamma = \gamma_Q(Q)$, computed at the telluroid points Q by Eq. (2.48). Following Stokes, the gravity anomaly in a point P_0 on the geoid W_0 is defined as difference $g(P_0) - \gamma_0(Q_0)$. Vice versa to the projection of a point P_0 onto a point Q_0, the normal gravity $\gamma_0(Q_0)$ can be continued from the reference ellipsoid to the geoid with increasing height h' in order to express the according value $\gamma(P_0) = \gamma_0(Q_0) + {}^{\partial\gamma}/_{\partial h'}\, N$.

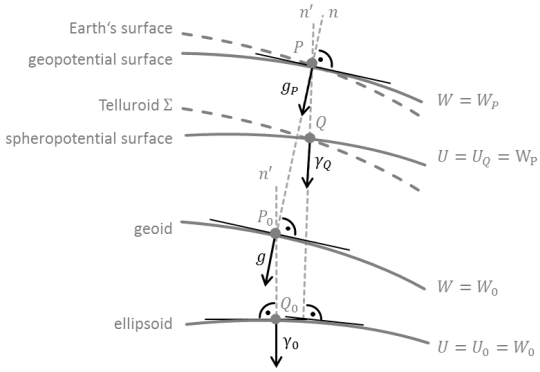

Figure 2.13: Gravity anomaly following Molodensky w.r.t. the Earth's surface, and following Stokes w.r.t. the geoid.

Extending the relation from Eq. (2.65) by an up-/ downward continuation operator (depending on the surface of the normal potential, if it is below or above the geoid), the gravity anomaly typically is expressed by

$$\Delta g = -\frac{\partial T}{\partial h'} + \frac{\partial \gamma}{\partial h'} N \ . \tag{2.68}$$

With Bruns formula according to Eq. (2.62) and the spherical approximation ${}^{\partial T}/_{\partial h} \approx {}^{\partial T}/_{\partial r}$ (cf. Sec. 2.4.2), the gravity anomaly yields

$$\Delta g = -\frac{\partial T}{\partial r} - \frac{2}{R} T \tag{2.69}$$

and the relation $\mathcal{Y}[\,\tilde{V}\,] = {}^{\partial \tilde{V}}/_{\partial r}$ from Tab. 2.3 applies. The signal content in the high frequencies of Δg is equivalent to that of δg and can be related to other gravitational quantities by the Meissl scheme (Fig. 2.7). The connection of gravity anomalies Δg and geoid undulations N is given by the Stokes operator; the connection to gravity disturbance δg by the fundamental equation of physical geodesy, which is for instance used as boundary condition for the first boundary-value problem according to Eq. (2.41). The relations are described in Appendix A. However, they are not applied in this work, as all quantities are directly derived from the (differential) gravitational potential $\tilde{V}$.

2.5.6 Deflection of the vertical

As mentioned before, the gravity anomaly vector $\Delta \boldsymbol{g}$ is defined by the difference between the gravity vector $\boldsymbol{g}_P$ pointing along the plumb line n at a point P at the Earth's surface, and the normal gravity vector $\boldsymbol{\gamma}_Q$ oriented along the ellipsoidal normal n' in the projected point Q on the telluroid, following Molodensky. The normal gravity vector $\boldsymbol{\gamma}_P$ in point P, as it is used for describing gravity disturbance vectors $\delta \boldsymbol{g}$, points in the same direction as $\boldsymbol{\gamma}_Q$.

The difference in direction of both vectors $\Delta \boldsymbol{g}$ and $\delta \boldsymbol{g}$, i. e. of the according unit vectors $\boldsymbol{n}$ and $\boldsymbol{n}'$, is displayed in Fig. 2.14 and denoted as **deflection of the vertical**. The magnitude is expressed by a north-south (ξ) and an east-west (η) component. Hence, physically they express the direction of $\boldsymbol{g}$, i. e. of the gradient grad$W$ of the potential field W, in longitude (north-south) and latitude (east-west) direction with

$$\begin{aligned} \xi &= -\frac{1}{\gamma R} \frac{\partial T}{\partial \varphi} \\ \eta &= -\frac{1}{\gamma R \cos\varphi} \frac{\partial T}{\partial \lambda} \ , \end{aligned} \tag{2.70}$$

(*Hofmann-Wellenhof and Moritz*, 2005, p. 117).

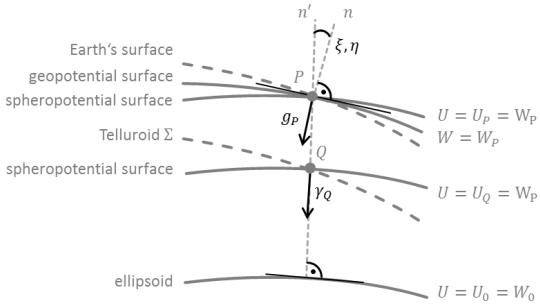

Figure 2.14: Deflection of the vertical in north-south (ξ) and east-west (η) direction, with n' through Q following Molodensky, and with n' through P following Helmert.

Geometrically, the quantities ξ, η describe the angle between the direction of the plumb line and the ellipsoidal normal n' in a point P, expressed by astronomical (Λ,Φ) and ellipsoidal (λ,β) coordinates, i. e.

$$\begin{aligned} \xi &= \Phi - \beta\,, \\ \eta &= (\Lambda - \lambda)\cos\beta\,. \end{aligned} \tag{2.71}$$

Following Molodensky, the direction of n' is defined through Q at the telluroid. Consequently, $T = T(Q)$ and $\gamma = \gamma_Q(Q)$ have to be computed in Eq. (2.70) w.r.t. the according spheropotential surface (potential $U = U_Q$, cf. Fig. 2.14). Another definition established for practical applications (*Torge*, 2003, p. 199): Helmert defined n' through P at the Earth's surface. Hence, the curvature of the plumb line between telluroid and the Earth's surface (order of magnitude of a few $0.11''$) is neglected in favor of an easy determination of the direction of n'. $T = T(P)$ and $\gamma = \gamma_P(P)$ relate to the according spheropotential surface through P (potential $U = U_P$). The quantities $\mathcal{Y}[\,\tilde{V}\,] = \{\eta, \xi\}$ are referred to the first derivatives of the disturbing potential T after φ and λ. In modeling approaches, the Eqs. (2.70) are described by the spherical approximations $\partial T/\partial\varphi$ and $\partial T/\partial\lambda$ from Tab. 2.3. η, ξ cannot be directly arranged in the Meissl scheme in Fig. 2.7: according to Fig. 2.3, the functionals do not depend on the radial derivative, but on the operators $f_{l,m}(\lambda, \vartheta)$.

2.5.7 Gravity gradients

While the three components of the gravity vector $\boldsymbol{g}$ describe the change of gravity potential W along the three axes of a Cartesian coordinate system, **gravity gradients** $\mathcal{Y}[\,\tilde{V}\,] = (V_{ab})$, $a, b \in \{x, y, z\}$ quantify the change of gravity (in the three-dimensional space $\mathbb{R}^3$), i. e.

$$\Delta\boldsymbol{V} = (V_{ab}) = \left(\frac{\partial^2 V}{\partial a \partial b}\right)\,, \tag{2.72}$$

w.r.t. a Cartesian coordinate system. Physically they describe a Marussi tensor $\Delta\boldsymbol{V}$, referring to Antonio Marussi (1908-1984), of nine elements

$$\Delta\boldsymbol{V} = (V_{ab}) = \begin{bmatrix} V_{xx} & V_{xy} & V_{xz} \\ V_{yx} & V_{yy} & V_{yz} \\ V_{zx} & V_{zy} & V_{zz} \end{bmatrix}\,, \tag{2.73}$$

containing all second-order derivatives of V. The gravity gradients are typically given in the unit Eötvös (1 E $= 1 \times 10^{-9}\,\mathrm{s}^{-2}$), named after the Hungarian physicist Loránd Eötvös (1848-1919).
Following *Rummel and van Gelderen* (1992), the two most important characteristics of the Gravity Gradient (GG) tensor are: The gravitational potential V is harmonic ($\nabla^2 V = 0$) and irrotational ($\nabla \times \nabla V = 0$) outside the attracting masses. Consequently, the Laplace equation (2.25) can be written in Cartesian coordinates as $V_{xx} + V_{yy} + V_{zz} = 0$, i. e. the trace of the gravity tensor (2.73) is zero, and each two of the diagonal elements are linear dependent. Further, the tensor is symmetric with $(V_{ab}) = (V_{ba})$ so that $V_{xy} = V_{yx}, V_{xz} = V_{zx}, V_{yz} = V_{zy}$. In total, five independent components remain.
Following *Koop* (e. g. 1993, p. 32), the elements can be expressed w.r.t. spherical coordinates λ, ϑ, r, i. e.

$$V_{xx} = \frac{1}{r}\frac{\partial V}{\partial r} + \frac{1}{r^2}\frac{\partial^2 V}{\partial \vartheta^2}\,, \tag{2.74}$$

$$V_{xy} = \frac{1}{r^2 \sin\vartheta}\frac{\partial^2 V}{\partial\vartheta\partial\lambda} - \frac{\cos\vartheta}{r^2 \sin^2\vartheta}\frac{\partial V}{\partial\lambda}\,, \tag{2.75}$$

$$V_{xz} = \frac{1}{r^2}\frac{\partial V}{\partial\vartheta} - \frac{1}{r}\frac{\partial^2 V}{\partial r\partial\vartheta}\,, \tag{2.76}$$

$$V_{yy} = \frac{1}{r}\frac{\partial V}{\partial r} + \frac{1}{r^2\tan\vartheta}\frac{\partial V}{\partial\vartheta} + \frac{1}{r^2\sin^2\vartheta}\frac{\partial^2 V}{\partial\lambda^2}\,, \tag{2.77}$$

$$V_{yz} = \frac{1}{r^2\sin\vartheta}\frac{\partial V}{\partial\lambda} - \frac{1}{r\sin\vartheta}\frac{\partial V^2}{\partial r\partial\lambda}\,, \tag{2.78}$$

$$V_{zz} = \frac{\partial^2 V}{\partial r^2}\,. \tag{2.79}$$

Modeling the components (V_{ab}) in terms of SHs, the first- and second-order derivatives of $\tilde{V} = V$ from Tab. 2.3 are inserted in the Eqs. (2.74) - (2.79). In spherical approximation it yields $V_{zz} \approx V_{rr}$. According to the Meissl scheme (Fig. 2.7), the amplification of high frequencies is exemplarily demonstrated for the component V_{rr}. Although spaceborne observations, observed in a certain height $r > R$, contain less information at small wavelengths, the effect of downward continuation (vertically arranged operator to the power of $l + 3$ in Fig. 2.7) is partly compensated for the second derivatives by the multiplication of several horizontally arranged operators, as e. g. the gravity anomaly operator $g_l(r)$. Consequently, those differentiation operators counteract the attenuation operator such that gravity gradients are especially profitable for the detection of high frequencies (*Rummel et al.*, 2002).
In analogy to the Meissl scheme in Fig. 2.7 referring to field transformations w.r.t. spherical coordinates, cf. Tab. 2.3, a second scheme has been developed in Fig. 2.8 w.r.t. Cartesian coordinates, cf. *Rummel and van Gelderen* (1995). Herein, exemplarily the relation of the zz-derivative, Eq. (2.79), is derived according to the spectral power in high frequencies.

2.6 Height definitions

Related to the physically defined gravitational and normal potential, several geometric distances can be specified. Geoid and quasigeoid heights are directly derived from the disturbing potential, and represent gravitational functionals, as introduced in Eqs. (2.62), (2.63). They deliver the basis for establishing national and international height systems and thus are the fundamental quantities for connecting gravity and geometry of the Earth.
In order to assess the full range between a reference ellipsoid with normal potential $U = U_0$, which can be easily described by Eq. (2.44), and the Earth's surface, which deviates in most cases from the geoid, the most common height definitions are presented in the following.
Ellipsoidal heights h' refer to the normal potential $U = U_0$ and are counted along the ellipsoid normal n', see Fig. 2.15. They present the vertical component of ellipsoidal coordinates and can be directly derived from GNSS measurements.

Geoid heights, as introduced in Eq. (2.62), describe an geopotential surface (with potential W_0) w.r.t. the reference ellipsoid (with normal potential U_0), and are defined along n'. The distance between the geoid and a point P at the Earth's surface, counted along the local plumb line n through P, is called **orthometric height** H_{orth}, see Fig. 2.15. The ellipsoidal height h' thus can be decomposed by

$$h' = N + H_{\text{orth}}\,, \tag{2.80}$$

neglecting the curvature of n. For the determination of H_{orth}, the gravity g along the plumb line is needed; the computation of N requires the reduction of masses above the geoid. Both quantities cannot be derived without geophysical assumptions.

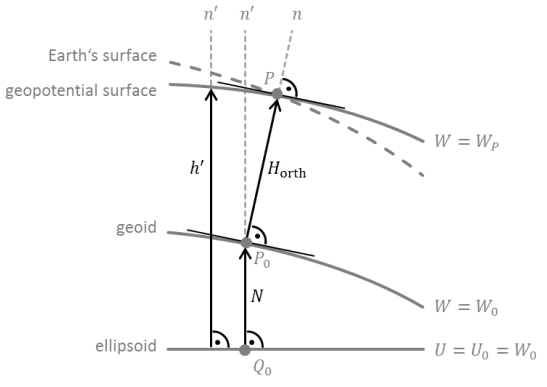

Figure 2.15: Ellipsoidal, geoid and orthometric height.

In order to avoid related uncertainties, many height reference systems are related to **quasigeoid** and **normal heights** H_{norm}, i. e.

$$h' = \zeta + H_{\text{norm}}\,, \tag{2.81}$$

cf. Fig. 2.16. Quasigeoid heights ζ as described in Eq. (2.63), refer to the ellipsoid or telluroid. Accordingly, the distance from the quasigeoid up to the geopotential surface through P, or from the ellipsoid up to the geopotential surface through the telluroid point Q, along the ellipsoid normal n', indicates the normal height H_{norm}.

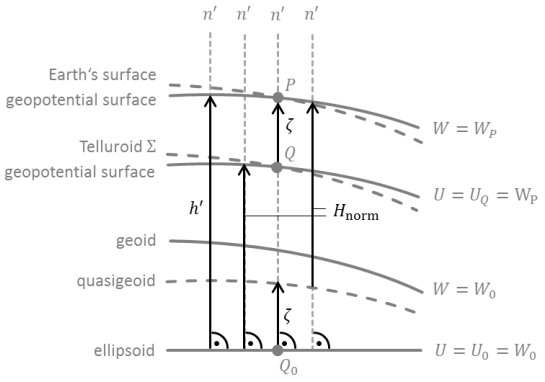

Figure 2.16: Ellipsoidal, quasigeoid and normal height.

2.7 Free-air reduction

Following Stokes theory, all gravitational computations are related to the geoid, assuming no masses above, if T is harmonic on this geopotential surface with potential $W = W_0$, and the Laplace equation (2.25) is valid. As in most cases the Earth's surface does not coincide with the geoid, topographic masses have either to be reduced or to be added, or the functionals have to be computed following Molodensky's theory w.r.t. the Earth's surface. The different reduction methods, as e. g. free-air, Bouguer, or Prey (*Hofmann-Wellenhof and Moritz*, 2005, pp. 134-148), mainly distinguish between topographic models, and most of them require an estimated density of the masses above the geoid.

The **free-air reduction** hereby continues gravity g in any height H_{orth} down to the geoid, assuming no masses above it. It can be expressed by a Taylor expansion according to Eq. (2.50) (e. g. *Hofmann-Wellenhof and Moritz*, 2005, p. 134). For most applications the linear term, and further the downward continuation along the ellipsoidal normal n' (instead of along the plumb line n) suffice. That is, the free-air gravity gradient

$$\frac{\partial g}{\partial H_{\text{orth}}} \approx \frac{\partial \gamma}{\partial h'} \approx -0.3086\,\text{mGal/m} \tag{2.82}$$

can be approximated by the normal gradient. This numerical estimate from Eq. (2.82) typically serves for pre-processing of gravity measurements. In this work, it is applied for homogenization of diverse observation data sets. The discussion of different gravity reductions is not part of the studies. The spherical approximation of the normal gradient in Eq. (2.60) is mainly used for modeling purposes of gravitational functionals, e. g. of the disturbing potential according to Eq. (2.69).

3 Measurement systems, models and data

The direct measurement of gravitational potential V is not possible. Instead, existing observation techniques detect functionals $\mathcal{Y}[\,\tilde{V}\,]$ of the (differential) gravitational potential $\tilde{V}$. The Meissl scheme (Fig. 2.7) gives an overview of the sensitivity to high frequencies of gravitational functionals derived from V or T, depending on the radial distance r, and thus, the measurement height. The more field transformation operators $f_l(r)$ are applied, the higher is the sensitivity to short wavelengths. The main aspects which have to be considered for gravity observations are:

- Higher-order derivatives of $\tilde{V}$ w.r.t. r are more sensitive than $\tilde{V}$ itself, and gravitation decreases with increasing distance, so that near Earth observables contain more information than the ones in a certain height above.
- Satellite measurements deliver lower spectral and spatial resolutions than terrestrial, air-, or shipborne measurements, but a good data coverage over the whole globe.
- However, vice versa, modeling gravitational functionals at the Earth's surface from satellite data amplifies both signal and noise. The same effect appears for the modeling of lower-order derivatives from higher-order observables.

Consequently, in order to observe the range of the gravitational frequency spectrum (1) as complete as possible, (2) up to very high spectral and spatial resolution, (3) achieving a global coverage, (4) with reasonable technical effort and expenses, and in order to obtain a selection of functionals for many applications, a variety of different measurement systems is needed. The first part of this chapter gives an overview of this variety. Special focus lies on the GOCE mission. In contrast to the traditional observation systems and in contrast to the CHAMP and GRACE satellite missions, for the first time global three-dimensional gravity information was obtained. The integration of this information in regional gravity field models is innovative; Technical benefits and advantages are discussed in Sec. 3.1.4. In the second part, a selection of global and regional models is presented, computed from observables of those measurement systems. The global models serve on the one hand as reference for regional observation techniques, on the other hand as reference for regional models, and – specific to the modeling approach presented in this thesis according to Fig. 1.1 – they deliver the long-frequent spectral information of the regional models and fill data gaps. In the last part of this chapter, the data sets and their pre-processing are described. Detailed information about the data sets is indispensable for a well-balanced combination, in the sense of extracting and retrieving all their benefits. As the aim is, to extract as much information as possible from the measurements, a very important principle is followed: keeping the observations in their most original and less pre-processed state.

3.1 Measurement systems

The following sections give an overview of diverse existing measurement techniques and their observed functionals. Advantages and difficulties figure out the challenges of gravity field determination. The systems which are used in this work are discussed in detail. These are: the satellite missions GRACE and GOCE, satellite altimetry, ship-/airborne, and terrestrial gravimetry. In Tab. 3.1 they are descriptively quantified according to the four main criteria mentioned above. Measurement precision and observed and/or derived functionals are given as well. Note, that altimetry is not explicitly developed for gravity field detection. However, the observables are very well suited for deriving gravitational information. For the sake of completeness, further gravity and gravity-related satellite missions which contribute mainly to global models, are briefly introduced in the end.

From Tab. 3.1 it is obvious that the global satellite gravity missions GRACE and GOCE are suited to detect the low frequency spectrum of the Earth's gravity field. Hereby, the spectral range is relatively small. The according spectral (and spatial) resolution is low, but, in contrast, the spatial coverage is very high, as well

Table 3.1: Descriptive comparison of observation techniques, their measurement precision and derived functionals.

observation techniques	GRACE	GOCE	Altimetry	Shipborne gravimetry	Airborne gravimetry	Terrestrial gravimetry
(1) range of frequency spectrum	small	small	wide	medium	medium	wide
(2) spectral resolution	low	low	medium	medium	high	high
(3) spatial coverage	global	global	semi-global	regional	regional	regional (point-wise)
(4) cost for campaign	high	high	high	medium	medium	low
measurement precision	10 µm (range), 1 µm/s (range rate)	10×10^{-12} $m/s^2/\sqrt{Hz}$	3 cm, i. e. $0.3\,m^2/s^2$	1 mGal to 3 mGal	2 mGal	2 µGal to 3 µGal (absolute), 0.01 mGal to 0.02 mGal (relative)
observed / pre-processed functionals	range, ΔV	V_{ab}	SSH T	g Δg, δg	g Δg, δg	g (absolute), Δg, δg (relative), ξ, η

as the cost of the satellite missions. Altimetry derived gravity data cover a wide spectral range and deliver medium (up to high) resolution information in the spectral domain. However, gravitational signal can only be derived over the ocean. Near Earth observation techniques, such as ship- and airborne gravimetry, detect medium up to high-resolution signal. The campaigns are spatially restricted to specific regions, but the costs are much lower than for satellite missions. With in situ terrestrial observations, the highest spectral and spatial resolutions can be achieved. The mixture of absolute and relative observation techniques allows a very flexible and efficient application.

3.1.1 Terrestrial gravimetry

The obvious approach to measure the Earth's gravity field is terrestrial gravimetry. During the last decades various instruments have been developed based on different principles. Hereby, absolute and relative gravimeters are distinguished, determining gravity as sum of gravitational and centrifugal accelerations and gravity differences.

Absolute gravimetry

The dynamic measurement of gravity is achieved by **absolute gravimetry**. It delivers directly the magnitude g of the gravity vector with precision of $20\,nm/s^2$ to $30\,nm/s^2$ (2 µGal to 3 µGal), i. e. in the order of magnitude of 2×10^{-9} to 3×10^{-9} (source: `http://www.bkg.bund.de`, 05/03/2016), but it requires a lot of technical effort, is expensive, and thus only installed at a few stations in a country.
In the most established principle, the free fall of a proof mass in a vacuum tube is interferometrically determined, i. e. the vertical location z of the proof mass is detected at time t during its free fall, assuming the magnitude of gravity $g = g(z)$ to be constant during the measurement period. Referring to *Vermeer M.* (2016, pp. 182), the equation of motion of the proof mass yields

$$\frac{d^2z}{dt^2} = g(z)\,, \tag{3.1}$$

and the observation equation for one location z (start position and velocity z_0, v_0) results to

$$z = z_0 + v_0 t + \frac{1}{2} g t^2\,. \tag{3.2}$$

Repeating the measurement cycle several thousand times, the magnitude of gravity can be estimated with high precision from the average, e. g. by least-squares adjustment, depending on the precision of the corresponding time measurement. Typically, a prism serves as proof mass. Erroneous influences which have to be considered and reduced stem from

- microseismic, instabilities of the ground (traffic, construction work, ...)
  → mostly compensated by damping with a superspring[5],
- air pressure and temperature
  → mostly compensated by isolated vacuum tube,
- vertical gravity gradient $^{dg}/_{dh}$ (gravity g not constant),
- magnetic field of the Earth ,
- instability of laser instrument and time measurement,

(*Dietrich*, 2003). Recently upcoming instruments, so-called atomic or quantum gravimeters, measure the fall of atoms. Gravity g can be determined with higher precision, but at a much larger technical and financial expense (*Vermeer M.*, 2016, p. 184).

Relative gravimetry

More efficient, but less accurate is **relative gravimetry**: Modern spring gravimeters have sensitivities better than 0.005 mGal, but the standard deviation of observations in exploration surveys is in the order of 0.01 mGal to 0.02 mGal (source: `https://www.britannica.com`, 05/03/2016). The instruments enable to measure gravity differences w.r.t. the absolute stations. In contrast to dynamic measurements, the motion of the proof mass due to gravity g is constrained by a controlled force (*Rummel*, 1986). Hence, the observables are static. A spring with its specific spring constant k and start length l_0 balances the gravitational effect on the proof mass m, which causes oscillation of the spring to an instantaneous length l. The equation of motion for a vertical spring then reads

$$m\left(\frac{d^2l}{dt^2} - g\right) = -k(l - l_0)\,, \tag{3.3}$$

(*Vermeer M.*, 2016, p. 176) and the equilibrium holds for

$$mg = k(l - l_0)\,. \tag{3.4}$$

Consequently, the change dg of gravity is linear with the change dl of the spring length, according to

$$\frac{dg}{dl} = \frac{k}{m} = \frac{g}{l - l_0} \tag{3.5}$$

(*Torge*, 2003, p. 162) and the sensitivity of a relative gravimeter yields

$$\frac{dl}{dg} = \frac{T^2}{4\pi^2}\,. \tag{3.6}$$

with oscillation period $T = 2\pi\sqrt{m/k}$. *Vermeer M.* (2016) gives a rough estimate: The gravity change of 1 mGal produces a lengthening of the spring by only 50 nm. Consequently highly sensitive instruments are indispensable. So-called astatized gravimeters achieve an improvement of sensitivity by around 50, mainly due to the changed geometry and a smaller parameter l_0. For details see *Vermeer M.* (2016, pp. 177) or *Torge* (2003, pp. 162).
As mentioned, relative instruments perform static gravity measurements and further are especially designed for transportation. Therefore, special emphasis has to be given on the stability of the instrument and of the measurement performance. Due to elastic and viscous material properties, the geometry of the instrument changes and the measurements are systematically influenced. This instrumental drift has to be determined and reduced from the observations (*Torge*, 2003, pp. 165). Further erroneous influences which have to be taken into account, stem from

[5] actual length of the spring electronically extended to an operative length of around 100 m

- air pressure and temperature
  → partly compensated by isolation,
- external magnetic fields
  → partly compensated by demagnetization in the interior,
- microseismic, instabilities of the ground (traffic, construction work, ...)
  → partly compensated by damping,

(*Dietrich*, 2003).

Network hierarchy

Terrestrial measurement campaigns are hierarchically organized. The "International Gravity Standardization Net 1971" (IGSN71) is the global reference system and official gravity datum worldwide (*Morelli et al.*, 1971). It consists of 10 absolute and around 25 000 relative gravity measurements. The precision of the measurement stations is better than 1 $\mu m/s^2$. National reference systems are integrated in this global network.
The "Deutsche Schweregrundnetz 1994" (DSGN94) provides the German basis network with 32 stations and a precision of 50 nm/s^2 (*Torge et al.*, 1999). Several nation-wide distributed locations serve as knot points at which absolute gravity measurements are regularly repeated, twice a year, by the German Federal Agency for Cartography and Geodesy (BKG), Frankfurt/Leipzig. It is refined by relative measurements of the federal states, yielding the "Deutsche Hauptschwerenetz 1996" (DHSN96). Least-squares adjustment delivers a standard deviation of 50 nm/s^2 (source: `http://www.bkg.bund.de`, 05/03/2016). The advantages and disadvantages of terrestrial gravimetry are listed in Tab. 3.2.

Table 3.2: Advantages vs. disadvantages in terrestrial gravimetry.

Advantages	Disadvantages
extremely high spatial resolution	not globally achievable
in situ measurements, choice of location very flexible coupling with height reference points possible	topographic restrictions (mountainous, polar, desert,... regions difficult to access)
standardization of national reference systems within the IGSN71	political restrictions (data not publicly available)
repetition measurements at exactly the same locations possible	time consuming (point-wise system not practical for large areas)
relative measurements at low expenses	absolute measurements very expensive relative measurements require corresponding heights (with adequate accuracy)
GNSS allows efficient (ellipsoidal) height measurement → delivering gravity disturbances δg, Eq. (2.64)	leveled (orthometric) heights very time consuming → delivering gravity anomalies Δg, Eq. (2.67)

3.1.2 Ship- and airborne gravimetry

Kinematic gravity measurements on board of a ship or an airplane are denoted as shipborne or airborne gravimetry. The sea or aerial gravimeters follow the measurement principle of relative gravimetry (*Forsberg and Olesen*, 2010), but distinguish from the terrestrial ones by an extremely powerful damping (*Vermeer M.*, 2016, p. 189). Typical sampling rates of 1 s to 10 s lead to quasi-continuous measurements along the profiles. The instruments are installed on stabilized platforms in the vehicles, and thus inertial accelerations due to the motion of the platform relatively to the geocentric system have to be taken into account (in analogy to the inertial accelerations additionally to the gravitational acceleration, acting on the rotating Earth in an inertial system, mentioned in Sec. 2.3.1). In general, the measurement consist of

- gravity g,
- inertial acceleration (non-gravitational acceleration).

Hereby, one gravity value $g(t)$ is obtained from the observed gravitational acceleration $\Gamma(t)$ and the geometric acceleration $\boldsymbol{a}(t)$ of the platform at a specific time t. With the vector $\boldsymbol{n}$ of the local plumb line it yields

$$g = g(t) = \Gamma(t) - \langle \boldsymbol{a}(t) \cdot \boldsymbol{n} \rangle \tag{3.7}$$

(*Vermeer M.*, 2016, p. 189). The geometric acceleration $\boldsymbol{a}(t)$ is derived from the actual position $\boldsymbol{x}(t)$ of the platform w.r.t. t by

$$\boldsymbol{a}(t) = \frac{d^2\boldsymbol{x}(t)}{dt^2}, \tag{3.8}$$

measured by GNSS with high precision.
Denoting g' the obtained gravity measurement on a moving platform, the gravity g in the geocentric system is extended by two terms, considering the horizontal component of inertial acceleration, due to (1) the Coriolis force and (2) the centrifugal force, acting on the moving platform in (1) east-west and (2) north-south direction. It yields

$$g = \frac{GM}{r^2} - \omega^2 r \cos^2\varphi, \tag{3.9}$$

$$g' = \frac{GM}{r^2} - (\omega + \underbrace{\frac{v \sin\alpha}{r\cos\varphi}}_{(1)})^2 r \cos^2\varphi - (\underbrace{\frac{v\cos\alpha}{r}}_{(2)})^2 r, \tag{3.10}$$

$$\boldsymbol{v} = \begin{cases} v\sin\alpha & \text{east-west} \\ v\cos\alpha & \text{north-south} \end{cases}.$$

If the terms (1) and (2) in Eq. (3.10) become zero, g' becomes g according to Eq. (3.9). ω is the angular velocity of the Earth's rotation (which was introduced together with the centrifugal potential Z in Eq. (2.26)), $\boldsymbol{v}$ the velocity vector (with magnitude v) of the platform relatively to the Earth, and α the azimuth of the direction of movement (*Dietrich*, 2003), according to Fig. 3.1. Reducing those horizontal non-gravitational accelerations from g is called **Eötvös reduction** δg_{Et}. It results to

$$\delta g_{Et} = g - g' = 2\omega v \cos\varphi \sin\alpha + \frac{v^2}{r}. \tag{3.11}$$

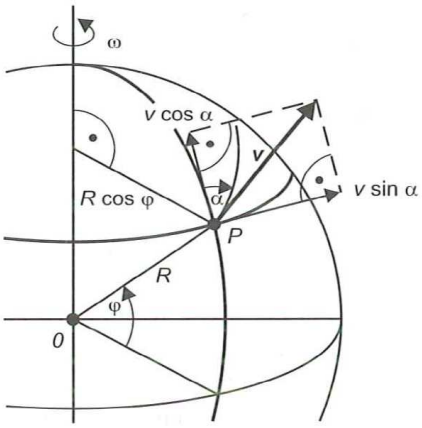

Figure 3.1: Eötvös effect on a platform in point P with radial distance $r = R$ (source: *Torge*, 2003, p. 170).

The vertical component of non-gravitational acceleration acts in the same direction as $\boldsymbol{g}$. The separation from g is very challenging. For shipborne gravimetry, damping, i. e. low-pass filtering, reduces high-frequent effects and thus most of the vertical component. The horizontal component yields, according to Eq. (3.11) with $r \approx R = 6371$ km, approximately

$$\delta g_{Et} = 40 v \cos\varphi \sin\alpha + 0.012 v^2 \mu\text{m/s}^2 \tag{3.12}$$

(*Torge*, 2003, p. 170). The achievable precision of a sea gravimeter counts 1 mGal to 3 mGal (*Dietrich*, 2003, p. 62).
A larger horizontal reduction, up to around $10\,\mu\text{m/s}^2$, is applied to airborne gravimetry measurements, especially as the velocity v of the aircraft is much higher than the one of ships or boats. The speed further restricts the damping methods of aerial instruments, so that vertical non-gravitational accelerations cause erroneous effects on the measurements. Additionally, the radial distance r varies with flight height and external effects due to wind and air pressure influence airborne more than shipborne measurements. However, the precision could be significantly improved during the last decades due to the advent of GNSS measurements. Several antennas, installed on the aircraft, allow to monitor its motion with centimeter-accuracy. Typical gravity results are at a Root-Mean-Square (RMS) level of 2 mGal (*Forsberg et al.*, 2015).

3.1.3 Satellite altimetry

Radar satellite altimetry primary serves as measurement technique for determining the Sea Surface Higth (SSH). As this target quantity is very close to the geoid and the remaining small differences are well-studied, it can be used vice versa for computing marine gravity field structures. The general measurement principle of satellite altimetry, some specific missions and the derivation of geoid undulations and the disturbing potential are explained in the following.
The observable of an altimeter instrument on board of a satellite is the travel time of a transmitted radar signal to the surface of the ocean and back. Hence, the range between the position of the satellite along the orbit and its ground track is derived along the ellipsoidal normal of the satellite's reference ellipsoid. The relevant quantities of the measurement concept are depicted in Fig. 3.2. Hereby the SSH results from the difference between the ellipsoidal height h' of the satellite and the observed range. Due to several hydrodynamic processes which lead to mass changes in the ocean, as e. g. tides, eddies, air pressure or temperature variations, the (mean) sea surface deviates from the geoid.

The difference is denoted Dynamic Ocean Topography (DOT) and the amplitude varies between ±2 m (*Bosch et al.*, 2013). Thus, in order to receive geoid undulations from the SSH, information on the instantaneous DOT is required. Along the altimeter profile the geoid height N is obtained from

$$N = SSH - DOT\,. \tag{3.13}$$

Consequently, gravity related quantities derived from satellite altimetry are restricted to the ocean and not globally available. According to the Bruns equation (2.62), N can be transformed into disturbing potential by

$$T = \gamma N = \gamma(SSH - DOT)\,. \tag{3.14}$$

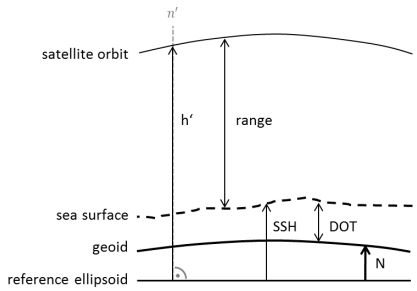

Figure 3.2: Relevant quantities of the concept of satellite altimetry.

Besides the reduction of diverse atmospheric and oceanic influences via the DOT, further erroneous effects have to be considered. They stem from

- solar pressure or atmospheric drag, for instance, leading to orbital perturbation
  → registered by GNSS measurement of the actual position of the satellite,
- the roughness of the ocean, i. e. the significant wave height
  → considered by retracking algorithms analyzing the return pulse,
- tropospheric and ionospheric characteristics leading to propagation delay
  → partly compensated by on-board measurements or atmospheric models,
- instrumental instabilities
  → mostly corrected by in-flight calibration of the altimeter.

The resulting precision of SSH altimetry observations reaches on average 3 cm (*Vermeer M.*, 2016, pp. 205). The according precision of disturbing potential values $T = \gamma(SSH - DOT)$ yields around $0.3\,\mathrm{m^2/s^2}$ by error propagation from $^{dT}/_{dSSH} \cdot 3\,\mathrm{cm} = \gamma \cdot 3\,\mathrm{cm}$, with a mean value of $\gamma = 9.81\,\mathrm{m/s^2}$ and by neglecting the uncertainty of the DOT.

Altimeter missions

Table 3.3 shows a selection of past and current satellite altimetry missions. The primary mission goals reach from detecting the marine gravity field (Geosat), over determining the sea surface topography (TOPEX/Poseidon), until studying polar sea ice (Cryosat-2). Some of them distinguish during their lifetime several orbit phases: classical (not explicitly mentioned), geodetic mission (gm), extended mission (em), e and f (specific for ERS-1). They differ mainly in their mean orbit height. A lower height increases the measurement accuracy, as the footprint, i. e. the reflecting surface of the conical beam, is smaller. Consequently, the arrival time of the back-scattered radar signal, and thus the derived SSH, can be determined with higher accuracy. The mean orbit height h' of the altimeter satellite relates to a reference ellipsoid and hence is regulated by the

magnitude a of the semi major axis. In Tab. 3.3 the missions and relating orbit phases are depicted, whose data are most relevant for gravity field modeling according to their time span, mean height h', and further orbit parameters. For instance, the repeat cycle defines the temporal resolution, the according number of revolutions increases the precision by averaging, the inclination defines the maximum latitude of the ground tracks and thus the spatial coverage. A comprehensive overview can be found at the Open Altimeter Database (OpenADB), "openadb.dgfi.tum.de". The parameters of the reference ellipsoids are presented in Sec. 3.2.

Table 3.3: Selection of altimeter missions and specific parameters, chronologically arranged w.r.t. the begin of their (first) orbit phase. The mean height h' is only given for finished missions.

Mission	Agency	Orbit phase	Time period	Semi major axis a	Reference ellipsoid	Mean height h'	Mean cross-track distance
Geosat	US Navy	gm	1985-03-12 - 1990-01-31	7166.400 km	GRS80	780 km	160 km
ERS-1	ESA[6]	e	1994-04-11 - 1994-09-29	7147.191 km	WGS84	770 km	80 km
		f	1994-09-29 - 1994-03-21	7147.191 km		770 km	
TOPEX/ Poseidon	NASA[7], CNES[8]		1992-09-25 - 2002-08-15	7714.428 km	TOPEX	1336 km	315 km
		em	2002-09-16 - 2005-10-08	7714.428 km		1336 km	
Jason-1	NASA, CNES		2002-01-15 - 2009-01-26	7714.428 km	TOPEX	1336 km	315 km
		em	2009-02-10 - 2012-09-15	7714.428 km		1336 km	
		gm	2012-05-07 - (ongoing)	7702.437 km		(ongoing)	
Envisat	ESA		2002-05-14 - 2010-10-22	7142.000 km	WGS84	784 km	80 km
		em	2010-10-26 - 2012-04-08	7142.000 km		784 km	
Jason-2	NASA, CNES, NOAA[9], EUMETSAT[10]		2008-07-12 - (ongoing)	7714.428 km	TOPEX	(ongoing)	315 km
Cryosat-2	ESA		2011-02-01 - (ongoing)	7095.349 km	WGS84	(ongoing)	8 km

Cross-calibration

The different altimeter missions, listed in Tab. 3.3 deliver heterogeneous SSH data sets as they refer, for instance, to different time periods or show geographically correlated error patterns. Further, systematic errors, as listed above, remain due to uncertainties in sensor calibration, drift terms or atmospheric reductions. As a consequence, a radial offset directly affects the SSH (*Bosch et al.*, 2014). The inconsistencies propagate onto the disturbing potential T in Eq. (3.14), when subtracting DOT from SSH, according to Eq. (3.13), which serves as input for gravity field modeling.
For consistency between the data from different altimeter systems, *Bosch et al.* (2014) set up a multi-mission cross-calibration. The data sets have to be carefully harmonized in advance, e. g. by applying the same geophysical (tidal, atmospheric, ...) reductions. In the analysis, single- and dual-satellite crossover differences are globally estimated between contemporaneous altimeter systems. The differences mainly capture range

[6]European Space Agency
[7]National Aeronautics and Space Administration
[8]Centre national d'études spatiales
[9]National Oceanic and Atmospheric Administration
[10]European Organisation for the Exploitation of Meteorological Satellites

biases. As a result, radial errors then are modeled for every single pass of each mission and applied to the data. The latest version of cross-calibrated data is "MMXO14" (Multi-Mission Crossover Analysis, version 14).

Instantaneous DOT

In order to compute an instantaneous value DOT_i at observation site P from the difference between the measured SSH_i and the according geoid undulation N_i, i. e.

$$DOT_i = SSH_i - N_i\,, \tag{3.15}$$

cf. Eq. (3.13), spectral and spatial consistency is required for the quantities. As mentioned above, the SSH_i values feature high frequent variations and are observed along altimeter ground tracks, whereas N_i is typically globally derived from a band-limited SH gravity field model and, thus, much smoother. *Bosch et al.* (2013) present a profile approach computing instantaneous DOT_i values for each observation site P along one ground track by consistently filtering both quantities SSH_i and N_i. They aim to keep as much high resolution information as possible in the SSH_i data. Hereby, cross-calibrated data are used.

3.1.4 GOCE satellite gradiometry

Gradiometry describes the method of measuring gravity gradients V_{ab}, introduced in Eq. (2.72), with a torsion balance instrument dating back to Eötvös. The basic idea is, that two proof masses are fixed along an axis with a constant distance. If gravity changes, i. e. GGs act on the proof masses along the connecting line, a torque is produced and would lead to a rotation of the axis. A fiber counterbalances this torque and thus, the force to constrain the motion gives the measure of the GG for the restoring torque (*Koop*, 1993, p. 4).
In Satellite Gravity Gradiometry (SGG), this principle is extended to six proof masses, arranged in a three-dimensional setup, i. e. with three orthogonal axes, each comprising two proof masses, see Fig. 3.3. If the intersection point of all three axes is located in the center of mass of a spacecraft, surrounding the Earth on a circular orbit, gravitational and centrifugal acceleration would compensate in this point. Proof masses shifted from this point on an equipotential surface, are located on different plumb lines. In contrast, proof masses shifted along one plumb line are situated on different equipotential surfaces (*Rummel*, 1986). Consequently, the masses experience a gravitational force which can be detected relatively to the intersection point or relatively between two proof masses, symmetrically arranged on one axis (*Koop*, 1993, p. 9).

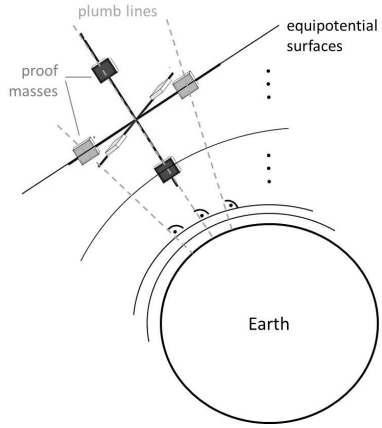

Figure 3.3: Principle of satellite gravity gradiometry in a three-dimensional setup. Proof masses on an equipotential surface are related to two different plumb lines, while proof masses on one plumb line are related to different equipotential surfaces.

Installing the proof masses in fix positions enables to measure the force needed to keep the masses in their positions, thus the **gravitational acceleration** relatively to the intersection point of the axes. Such an instrument is called **accelerometer**. This direct measurement of the second derivatives of the gravitational potential is beneficial, as discussed in the frame of the Meissl scheme in Fig. 2.7.
The difference in gravitational acceleration between two fixed masses allows, on the one hand, to separate the target quantity **gravitational gradients** from linear and angular acceleration. This is the essential aspect for SGG in a rotating system. The instrument for measuring differential gravitational acceleration, **differential accelerometry** respectively, is called **gradiometer** (e. g. *Forward*, 1974; *Balmino et al.*, 1985; *Rummel*, 1986). On the other hand, differential accelerometry partly eliminates external non-gravitational forces, as e. g. solar pressure or atmospheric drag, as they act in the same manner on each accelerometer, assuming the instruments to be exactly identically built and installed.

GOCE satellite mission

Within the GOCE mission, the principle of SGG was established (*Rummel*, 2011). The satellite, launched in March 2009 by European Space Agency (ESA), provided GG data from Nov 1, 2009 until Nov 11, 2013. The motivation was to provide gravity observations in order to compute a global geoid model with unprecedented accuracy for several applications, cf. *Koop* (1993, pp. 15-17), *Cesare* (2008, p. 10):

- Globally available geoid undulations N with adequate accuracy (at least 1 cm over a distance of 100 km in terms of a series expansion in SHs) for the computation of orthometric heights H_{orth} from ellipsoidal, GNSS-derived heights h.
- Gravity anomalies at the Earth's surface with an accuracy of at least 1 mGal over 100 km.
- Satellite orbit prediction and determination with cm-accuracy.
- Contribution to physical studies of the solid Earth for a better understanding of, e. g., density distribution, mantle convection, lithosphere extent, core-mantle boundary in the Earth's interior, from a combination with altimetry, topography, bathymetry or seismic tomography data.
- Sea surface topography determination as deviation of the mean SSH (measured by altimetry) from the equipotential geoid due to local (long-term) variations of temperature, salinity, atmospheric pressure, currents, tides, etc.

In order to realize these objectives, two complementary measurement techniques were performed on board of the satellite: [1] SGG and [2] Precise Orbit Determination (POD). While POD enables to reconstruct low frequencies by satellite-to-satellite tracking with Global Positioning System (GPS) measurements and by Satellite Laser Ranging (SLR), SGG provides resolutions in the medium spectral domain from gravity gradiometry. Up to degree $l \approx 15$, POD provides better performances, while SGG predominates the spectral domain above, approximately up to degree 300 (*Cesare*, 2008, p. 10). The contribution of low-frequency information is less important in the regional gravity modeling approach of this work. The long wavelengths are caused by global phenomena of the Earth's body and typically are represented by global SH models, cf. Fig. 1.1. Consequently, this study restricts in the following to the SGG measurements. Before the latter will be explained, GOCE specific coordinate systems and reference frames are introduced. Then, the relevant instruments and observables of the sensor system are presented. Table 3.4 summarizes them and their purposes. The measured and derived quantities are collected with letters (a) - (j) in order to give an overview of their relations. In the last part, the measurement precision is discussed.

GOCE specific coordinate systems and gradiometer reference frame

In order to describe the three-dimensional measurement principle of GOCE, which was installed in the spacecraft surrounding the rotating Earth, and finally to use the data for modeling the gravity field in selected geographic regions, several coordinate systems and transformations are needed. Figure 3.4 depicts the most relevant systems for the modeling approach presented in this work. They are explained in the sequel by describing (1) the orbit of the spacecraft in a LOCS, (2) the measurements in a Gradiometer Reference Frame (GRF), and (3) the products in a LNCS.

Local orbital coordinate system The instantaneous movement of the GOCE satellite along the orbit was determined by the GOCE SST data (*Bouman et al.*, 2009) and described in an Earth-unbound LOCS, as introduced in Sec. 2.2.3. In Fig. 3.4, the LOCS is visualized w.r.t. the J2000 coordinate system. The origin O_{LOCS} is defined in the actual center of mass of the GOCE satellite; the direction of the Z-axis is nearly oriented along the plumb lines of the Earth's gravity field, i. e. the direction with largest signal amplitude. However, due to orbit perturbations, such as atmospheric drag and radiation pressure, the Z_{LOCS}-axis is not exactly oriented along the radial direction r from the geocenter to the center of the satellite. Depending on the inclination angle i', the angular deflection counts maximally 0.26° (*Cesare*, 2008, p. 11). It is neglected in the sequel of this work, cf. Eq. (2.79).

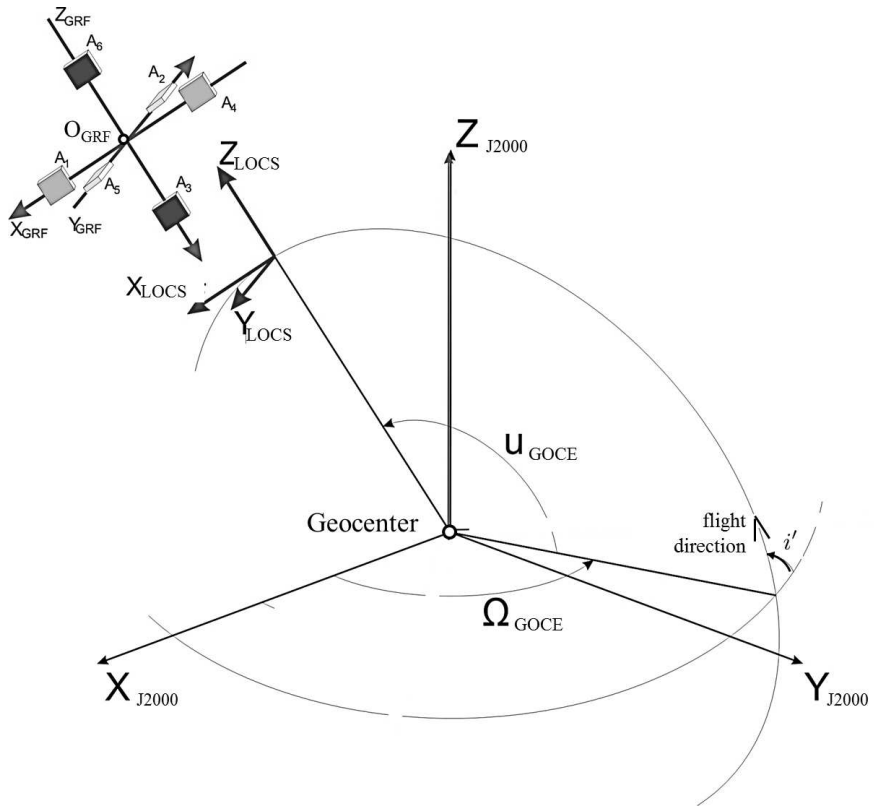

Figure 3.4: Gradiometer Reference Frame and LOCS in the J2000 coordinate system, adapted from *Gruber et al.* (2014).

Gradiometer reference frame The accelerometer measurements are obtained in the GRF[11]. The three pairs of each two accelerometers, i. e. three one-axis gradiometer, are installed on orthogonal axes spanning a three-dimensional setup following the measurement principle of SGG as depicted in Fig. 3.3. The distance between each two accelerometers, i. e. the length of each baseline, counts around 50 cm (*Cesare*, 2008, p. 13). The baselines define the axes of the coordinate system of the measurement frame, i. e. the GRF. The origin O_{GRF} of this GOCE specific instrumental reference frame is located in the intersection point of the three orthogonal axes, which coincide per definition with the physical beams of the measurement system. The axes are approximately aligned to the LOCS with $X_{\mathrm{LOCS}} \approx X_{\mathrm{GRF}}$, $Y_{\mathrm{LOCS}} \approx -Y_{\mathrm{GRF}}$, and $Z_{\mathrm{LOCS}} \approx -Z_{\mathrm{GRF}}$, cf. Fig. 3.4. The coordinates yield

x_{GRF}	along the X_{GRF}-axis (roll), directed along track (motion of the satellite),
y_{GRF}	along the Y_{GRF}-axis (pitch), directed cross track,
z_{GRF}	along the Z_{GRF}-axis (yaw), directed towards the Earth.

Technical restrictions limit the exact accordance of the axes of GRF and LOCS, resulting in small angular deviations, described by the roll, pitch and yaw angles of a few degrees. During the mission, the satellite and the gradiometer were kept as good as possible aligned with the LORF by magnetic torquers (*Bouman et al.*, 2009). However, the Z_{GRF}-axis neither coincides with the Z_{LOCS}-axis, nor with the radial direction of the plumb lines of the Earth's gravity field. The small angular deflections are neglected in the sequel of this work.

Local north-oriented coordinate system The calibrated GOCE gravity gradients are provided in an Earth-bound LNCS, in contrast to the Earth-unbound LOCS. The LNCS was introduced and displayed in Fig. 2.2 w.r.t. the Cartesian XYZ system. The origin O_{LNCS} of the North-West-Up frame is located in the nominal center of mass of the satellite; the Y_{LNCS}-axis is parallel to the normal vector of the geocentric meridian plane of the satellite; the X_{LNCS}-axis is parallel to the normal vector of the plane defined by Y_{LNCS} and Z_{LNCS} and forms a right-handed system. As mentioned above, the Earth-bound LNCS deviates from the Earth-unbound LOCS by small angles.

[11] The Gradiometer Reference Frame (GRF) is the realization of the Gradiometer Reference System. In GOCE related literature the transformations are typically described between "reference frames". As in this work, all considerations refer to systems, the GOCE specific GRF is interpreted as system as well, but the typical notification "GRF" is kept.

Transformations

In order to use GOCE satellite data for regional gravity field modeling, transformations between the components, observed in the instrumental GRF, and according values in local Earth-bound systems are indispensable.

GRF – LNCS For the transformation of the GG tensor $\Delta\boldsymbol{V}^{\mathrm{GRF}}$, as introduced in Eq. (2.73), given in the instrumental GRF, to the GG tensor $\Delta\boldsymbol{V}^{\mathrm{LNCS}}$, defined in the geographic LNCS, a three step matrix rotation is implemented in the standard GOCE data processing software (*Gruber et al.*, 2014). It contains (1) a rotation by the matrix $\boldsymbol{R}^{\mathrm{J2000}}_{\mathrm{GRF}}$ from the GRF to the inertial coordinate system J2000 according to Sec. 2.2, using inertial attitude quaternions from GOCE, (2) a rotation by the matrix $\boldsymbol{R}^{\mathrm{XYZ}}_{\mathrm{J2000}}$ to an Earth-fixed geocentric Cartesian XYZ system using the quaternions from GPS orbit determination, and (3) a rotation by the matrix $\boldsymbol{R}^{\mathrm{LNCS}}_{\mathrm{XYZ}}$ to the LNCS using the relations from Eq. (2.23). The rotation matrix $\boldsymbol{R}^{\mathrm{LNCS}}_{\mathrm{GRF}}$ with components $(r_{ij}), i, j \in \{1, 2, 3\}$, is obtained by multiplying the three matrices, i. e.

$$\boldsymbol{R}^{\mathrm{LNCS}}_{\mathrm{GRF}} = \left(\begin{bmatrix} r_{11} & r_{12} & r_{13} \\ r_{21} & r_{22} & r_{23} \\ r_{31} & r_{32} & r_{33} \end{bmatrix} \right) = \boldsymbol{R}^{\mathrm{J2000}}_{\mathrm{GRF}} \cdot \boldsymbol{R}^{\mathrm{XYZ}}_{\mathrm{J2000}} \cdot \boldsymbol{R}^{\mathrm{LOCS}}_{\mathrm{XYZ}} \, . \tag{3.16}$$

Consequently, with Eq. (3.16), the transformation of the GG tensor from GRF to LNCS yields

$$\Delta\boldsymbol{V}^{\mathrm{LNCS}} = (\boldsymbol{R}^{\mathrm{LNCS}}_{\mathrm{GRF}})^{T} \, \Delta\boldsymbol{V}^{\mathrm{GRF}} \, \boldsymbol{R}^{\mathrm{LNCS}}_{\mathrm{GRF}} \, . \tag{3.17}$$

GRF – LOCS The observations from star trackers allow to determine the difference of the orientation of GRF and LOCS. A rotation matrix $\boldsymbol{R}^{\mathrm{LOCS}}_{\mathrm{GRF}}$ is set up in order to transform the GG tensor in the GRF into the GG tensor in the LOCS. The matrix $\boldsymbol{R}^{\mathrm{LOCS}}_{\mathrm{GRF}}$ contains small rotation angles describing the orientation of the GRF in the LOCS. According to *Fuchs and Bouman* (2011), the point wise rotation of the tensor $\Delta\boldsymbol{V}^{\mathrm{GRF}}$ from GRF to the tensor $\Delta\boldsymbol{V}^{\mathrm{LOCS}}$ in the LOCS reads

$$\Delta\boldsymbol{V}^{\mathrm{LOCS}} = (\boldsymbol{R}^{\mathrm{LOCS}}_{\mathrm{GRF}})^{T} \, \Delta\boldsymbol{V}^{\mathrm{GRF}}_{ab} \, \boldsymbol{R}^{\mathrm{LOCS}}_{\mathrm{GRF}} \, . \tag{3.18}$$

GOCE sensor system and measurements

In order to obtain valuable information of the Earth's gravity field from SGG, the GOCE sensor system is composed of several instruments. Hereby, a **three axes gravity gradiometer** is the core of the system. It consists of six accelerometers, in Fig. 3.4 denoted with A_i, $i \in \{1, 2, ..., 6\}$. The accelerometer cages are rigidly connected with the satellite, and the relative accelerations of the proof masses to the cages are detected. Together with **star sensor** measurements, a variety of quantities is obtained. As described by *Cesare* (2008, pp. 32-36), these quantities contain

(a) the diagonal and off-diagonal GGs, composing the tensor $\Delta\boldsymbol{V}^{\mathrm{GRF}}$ according to Eq. (2.73),

(b) the positions of the centers of each accelerometer (i. e. of the proof masses) relatively to the center of mass of the satellite,

(c) the angular rates (i. e. velocities) ω_{ab} and

(d) the angular accelerations $\dot{\omega}_{ab}$, both describing centrifugal, linear and Coriolis accelerations of the proof masses,

(e) internal accelerations of the accelerometer cage relatively to the satellite due to material and structure characteristics (e. g. thermo-elastic deformations),

(f) linear accelerations $\boldsymbol{\delta}$ of the center of mass of the satellite due to external non-gravitational forces (e. g. atmospheric drag, solar radiation pressure),

(g) linear accelerations of the proof masses due to internal self-gravity effects inside the GOCE satellite,

(h) linear accelerations of the proof masses due to influences from the external magnetic field.

On the one hand, by building the mean value of the two oppositely measured accelerations of one axis (**common-mode accelerations**), information about the linear non-gravitational acceleration can be derived, i. e. about the components of $\boldsymbol{\delta} = [\delta_X, \delta_Y, \delta_Z]^T$. Vice versa, the measurement of $\boldsymbol{\delta}$ provides error estimates of the GGs. On the other hand, by building the **differential-mode accelerations** according to *Cesare* (2008, p. 35), the non-gravitational effects are partly eliminated, and the GGs (V_{ab}) can be computed, coupled with the centrifugal and angular accelerations of the center of mass of the satellite. The angular rates ω_{ab} are derived from star sensor measurements and hence, disturbing self-gravity and magnetic field effects can be estimated. Following the processing steps of *Cesare* (2008), the calibrated GGs (a) are separated from the angular rates ω_{ab} (c) and accelerations $\dot{\omega}_{ab}$ (d) and the tensor $\Delta\boldsymbol{V}$ can be set up. An improvement of the processing steps is presented by *Stummer et al.* (2012).

Besides the technical restrictions which would constrain the coincidence of the axes of GRF and LOCS as mentioned above, the actual orientation and shift of the gradiometer instrument differ in most cases from the movement of the satellite due to the external forces. In order to partly compensate the linear accelerations $\boldsymbol{\delta}$, a so-called "drag-free" system is installed. The angular differences between the orientation of GRF and LOCS are controlled by **magneto-torquers**. Due to the dependency on the magnetic field, the z-axis is less controlled close to the magnetic poles and the x-axis is less controlled close to the magnetic equator, as the axes are aligned along the magnetic field lines (*Fuchs and Bouman*, 2011). Over the equator, maximum angular deflection of 3.5° of the satellite w.r.t. the Z_{LOCS}-axis is reached due to forces caused by the Earth's rotation. The effect is compensated by steering the satellite w.r.t. the LOCS (*Gruber et al.*, 2014, p. 22).
Additional erroneous effects due to technical restrictions, as e. g. caused by (time-variable) misplacement of the proof masses, misalignment of the axes, or shift of the origins, require an on-board calibration of the gradiometer (*Cesare*, 2008, pp. 37-47). Different intermediate in-flight calibrations have been performed during the satellite mission and are applied in terms of a calibration matrix to the common- and differential-mode accelerations. Hence, further instruments are necessary in the GOCE satellite. Related to *Gruber et al.* (2014), the most relevant components of the sensor system and their purposes are summarized in Tab. 3.4.

Table 3.4: GOCE sensor system.

sensor	purpose	quantity	
gravity gradiometer	[1] SGG		
	measuring GG tensor components	(a)	(V_{ab})
	measuring angular accelerations	(d)	$\dot{\omega}_{ab}$
	determining common-mode accelerations	(i)	
	determining linear non-gravitational accelerations	(f)	$\boldsymbol{\delta}$
star sensor	measuring angular rates	(c)	ω_{ab}
	measuring inertial angular orientation of the spacecraft	(j)	
magneto-torquers	attaining angular control of the spacecraft from (d) and (j)		
ion thrusters	attaining drag control from (i)		
cold gas thrusters	calibrating the gradiometer on board during flight		
GPS receiver	[2] POD		
	measuring orbit trajectory reconstructing long wavelengths of the gravity field		
Laser retro reflector	validating orbit by SLR		

Measurement precision and bandwidth

The separation of GGs from angular rates and accelerations is the key benefit for achieving a high precision GG tensor. *Rummel* (1986) gives an estimate for the SGG precision independent of a specific mission. Following those requirements the GOCE gradiometer has been designed. Together with the accelerometer precision, it delivers the most accurate measurements in the spectral range from 5 mHz to 100 mHz, specified as **Measurement BandWidth (MBW)** (*Cesare*, 2008, p. 10). In the spectral domain below and above, the

errors of the gradients increase reciprocal to the frequency (*Rummel*, 2011).[12]
Within the MBW, the technically restricted precision of an accelerometer counts $10 \times 10^{-12}\,\mathrm{m/s^2/\sqrt{Hz}}$ (*Gruber et al.*, 2014, p. 15). Each accelerometer consists of two accurate and one less accurate axes. In the three-dimensional setup they are arranged such that highest precision is achieved for the diagonal components of the GG tensor V_{ab}. Detailed information can be found in *Cesare* (2008). The four gradients $V_{xx}, V_{yy}, V_{zz}, V_{xz}$ in the GRF have high accuracy whereas the two gradients V_{xy}, V_{yz} are less accurate due to the arrangement of the accelerometers (*Rummel*, 2011).
Fuchs and Bouman (2011) further study the effective MBW, where the signal-to-noise ratio of the GGs defines the boundaries. Both, the upper and lower boundaries slightly vary for the four accurate gradients and for geographic regions. Especially the V_{yy} component shows anomalous signal close to the magnetic poles, possibly due to cross-track thermosphere winds which cannot be compensated by the drag-free system (*Bouman et al.*, 2014). On average, the lower boundary of the effective MBW, i. e. the maximum of the integrated signal-to-noise ratio, is with 4 mHz slightly beneath the boundary of the specified MBW. For a signal-to-noise ratio of one, the upper boundary yields around 30 mHz and thus is clearly beneath the upper boundary of the specified MBW.

Products

As it is typical for satellite-derived data, the GOCE products are categorized in levels according to their degree of pre-processing, cf. Tab. 3.5. Level 0 data are the raw observations without any pre-processing; level 1a data comprise time series of payload data with calibration data attached including satellite ancillary data (*Cesare*, 2008, p. 31). After transformation in an appropriate reference system, calibration and conversion into physical units, level 1b products are generated. In the case of GOCE, the level 2 products are the resulting GGs (from [1] SGG, cf. Tab. 3.4) and the precise orbits (from [2] POD). A large variety is presented in *Gruber et al.* (2014). The products, which are relevant for this work, are summarized and briefly described following Tab. 3.5.

Table 3.5: GOCE products.

level	measurement technique	name	input	description
0	SGG, SST			time-ordered raw data down-linked from the satellite
1a	SGG, SST			time series of payload data, calibration data, satellite ancillary data
1b	SGG	EGG_NOM_1b		internally calibrated GOCE GGs
1b	SGG	EGG_IAQ_1b		GRF to J2000 inertial attitude quaternions
2	SST	SST_PSO_2		reduced dynamic precise science orbit
2	SGG	EGG_NOM_2	EGG_NOM_1b, EGG_IAQ_1b, SST_PSO_2,	externally calibrated GGs in GRF, daily, corrected for temporal gravity field variations, validated against external gravity data, outliers flagged
2	SGG	EGG_TRF_2	EGG_NOM_2, EGG_IAQ_1b, SST_PSO_2, a priori SH model	externally calibrated GGs in LNCS, monthly, obtained by direct point-wise rotation, less accurate gradients replaced by model information, high-pass filtered and filled up with model information, correction, validation and flagging according to EGG_NOM_2

From level 1b to level 2 The product EGG_NOM_1b[13] contains internally calibrated GOCE GGs. In order to derive level 2 products, external calibration, temporal corrections, data screening and validation have to be

[12] The single error contributors have been listed and numbered by *Cesare* (2008, pp. 76,77).
[13] EGG-C European GOCE Gravity Consortium, NOMinal data, level 1b

applied (*Bouman et al.*, 2009). Therefore, inertial attitude quaternions (IAQ) from the product EGG_IAQ_1b are needed, as well as precise orbit data (PSO) from SST_PSO_2. The resulting product EGG_NOM_2 contains a time series of GGs composing the tensor $\Delta \boldsymbol{V}^{\mathrm{GRF}}$ in GRF. The temporal resolution yields 1 s and corresponds to 8 km along-track spatial resolution (*Gruber et al.*, 2014).

Level 2 As the instrumental GRF continuously rotates around its three axes w.r.t. an Earth-fixed system, it seems reasonable to transform the observables from the GRF into such a geographical system. The transformation of the gravity tensor $\Delta \boldsymbol{V}^{\mathrm{GRF}}$ in the GRF, to a tensor $\Delta \boldsymbol{V}^{\mathrm{LNCS}}$ in the LNCS, can be performed by direct point-wise rotation according to Eq. (3.17) using the matrix $\boldsymbol{R}^{\mathrm{LOCS}}_{\mathrm{GRF}}$, cf. Eq. (3.16). The components (r_{ij}) are derived from the star tracker measurements and the common-mode accelerations, and vary maximally by 2.2°, 2.0°, 7.6° for roll, pitch and yaw (*Fuchs and Bouman*, 2011). The components of the tensor $\Delta \boldsymbol{V}^{\mathrm{LNCS}}$, thus, are linear combinations of the components of $\Delta \boldsymbol{V}^{\mathrm{GRF}}$; the small shift of the origin can be neglected. However, the tensor transformation would significantly reduce the quality of the GGs. As mentioned in Sec. 3.1.4, the two components V_{xy} and V_{yz} are less accurately determined. A rotation of the GG tensor from the GRF to a geographical coordinate system would project the corresponding larger errors onto the four accurate components. In analogy, the long wavelengths with increasing errors would leak into the MBW. Therefore, *Fuchs and Bouman* (2011) suggested a substitution of the less accurate gradients and the low frequency part by model gradients, e. g. from a GRACE-based SH model, expecting the GRACE data to contain more information in this spectral domain than the GOCE measurements. The tensor with substituted components V_{xy}, V_{yz}, and long wavelengths, finally is rotated into the LOCS, provided in terms of the product EGG_TRF_2[14], see Tab. 3.5.

Using level 2 GGs, *Pail et al.* (2011a) present three approaches of gravity field analysis and carve out the impact of the GOCE mission in order to reach the mission goals listed at the beginning of this section. The approaches distinguish in their processing philosophies: While in the direct (DIR) approach the SH coefficients are estimated as parameters from a large normal equation system starting with an a priori gravity field model and adding subsequently GOCE information, in the time-wise (TIM) approach a rigorous estimation only based on GOCE data is applied, and in the space-wise (SPW) approach LSC is performed benefiting from spatial correlations of the gravity field (*Pail et al.*, 2011a). The resulting models may be denoted as level 3 products.

Resolution of gravity field recovery

In summary, from the aspects of SGG and instrumental manufacturing, GOCE enables a global gravity field recovery down to a spatial resolution of around 70 km. Together with the orbit performances of the satellite mission, GOCE SGG allows to detect the Earth's gravity field with

- medium spectral and spatial resolution, related to the limits of the MBW, the sampling rate of 1 Hz, and one orbit revolution of about 5400 s,
- nearly global coverage (inclination angle $i' = 96.5°$, i. e. ground track coverage of ±83° latitude).

In terms of globally deriving geoid heights at a spatial resolution of 100 km from two month GOCE gravity field models, the precision is given with 10 cm, and for gravity anomalies with 3 mGal (*Pail et al.*, 2011a). The first GOCE-only model, containing the full observation period is published by *Brockmann et al.* (2014). It is based on the TIM-approach and provided up to SH degree $l = 280$, i. e. resolving spatial structures down to around 70 km. At a spatial resolution of 100 km, the precision of geoid heights and gravity anomalies globally averages 2.4 cm and 0.7 mGal. Thus, up to now, the previously mentioned mission goals are not yet reached for geoid heights (1.0 cm), but even exceeded for gravity anomalies (1 mGal).

3.1.5 GRACE satellite mission

The GRACE mission is a project of National Aeronautics and Space Administration (NASA) and Deutsches Zentrum für Luft- und Raumfahrt (DLR), planned by University of Texas Center for Space Research (UTCSR),

[14] EGG-C, Terrestrial Reference Frame, level 2

GeoForschungsZentrum (GFZ) and Jet Propulsion Laboratory (JPL), and launched in March 2002 (*Tapley et al.*, 2004). The main objective is to detect temporal variations of the Earth's gravity field especially in its atmosphere and hydrosphere at monthly intervals or smaller. With an increasing temporal resolution, a lower spatial resolution has to be taken into account.
The GRACE space segment consists of two identical satellites, surrounding the Earth in the same nominal orbit, at an altitude of around 450 km, with a distance of around 220 km. The initial altitude of 500 km decreases due to a natural decline.[15] The low orbit enables high gravitational sensitivity, the inclination of about 89° nearly global coverage, and the non sun-synchronous orbit separating periodic phenomena, as e. g. atmospheric variations during day and night.

The measurement principle of low-low Satellite-to-Satellite Tracking (SST) is displayed in Fig. 3.5. Main observable is the distance between both satellites. It changes, because their positions along the orbits are influenced by the Earth's gravity field. If satellite 1 passes e. g. a region with higher density, i. e. more mass and thus larger gravitational acceleration than in the surrounding area, it is stronger attracted than satellite 2 (and vice versa). The exact separation distance between the satellites and its rate of change are detected by a microwave link in the K-band with a wavelength of about 1.5 cm, at a precision of about 10 µm and 1 µm/s, respectively (*Reigber et al.*, 2005).

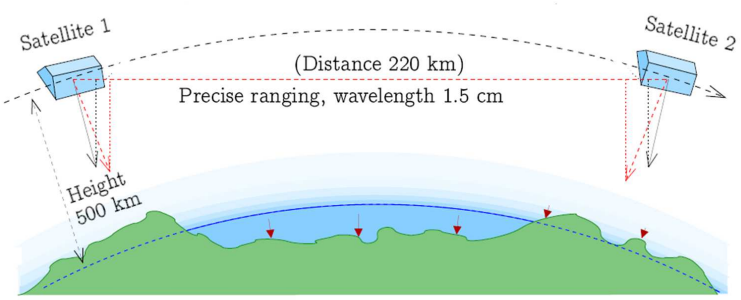

Figure 3.5: GRACE measurement principle taken from *Vermeer M.* (2016), p. 218. The larger gravitational acceleration of a satellite is displayed by a red dashed vector, in contrast to the scenario without additional masses indicated by a black acceleration vector. The mass distribution might be static in the Earth's interior or varying with time in the ocean and atmosphere. Solid red arrows indicate the vertical components of time-dependent mass shifts, which are detectable by GRACE.

Non-gravitational forces acting on the spacecraft, e. g. due to atmospheric drag, are detected by accelerometers on board of the satellites, and subtracted at the data pre-processing stage. The actual positions of the satellites are measured by GPS. This high-low SST allows to perform a POD. From the analysis of the kinematic orbits, long-wavelength structures of the gravity field can be determined (*Mayer-Gürr*, 2006, p. 12).

Processing strategies

Different methods of gravity field recovery exist; among them, the

(a) dynamic method (*Reigber et al.*, 2003a, 2005), applied by the three official processing centers GFZ (*Dahle et al.*, 2012), Center for Space Research (CSR) (*Bettadpur*, 2012), JPL (*Watkins and Yuan*, 2012), and by many others, as e. g. *Luthcke et al.* (2006); *Bruinsma* (2010),

(b) integral equation approach (*Mayer-Gürr*, 2006), applied at the IGG Bonn (Institut für Geodäsie und Geoinformation der Universität Bonn), e. g. by *Mayer-Gürr et al.* (2007); *Kurtenbach* (2009),

(c) acceleration approach (*Ditmar and van Eck van der Sluijs*, 2004), applied e. g. by *Chen et al.* (2008); *Liu et al.* (2010),

(d) energy balance approach (*Jekeli*, 1999), applied e. g. by *Han et al.* (2006); *Shang et al.* (2015),

(e) celestial mechanics approach (*Beutler*, 2010), applied e. g. by *Meyer et al.* (2012).

(a) Dynamic method In the dynamic method, the orbits of the two GRACE satellites 1 and 2 are numerically integrated (*Reigber et al.*, 2005). The linearized observation equations of both, the low-low SST between the GRACE spacecraft, as well as the high-low SST to GPS satellites, are set up and may be solved, e. g. by least

[15] The actual altitude can be found on `www.csr.utexas.edu/grace`, 23/08/2016.

squares adjustment. Besides estimating the gravity field unknowns, i. e. the fully normalized SH coefficients $S_{l,m}$, $C_{l,m}$ complete to degree and order 150, orbit and instrument specific parameters are estimated as well. The approach is applied by the three official GRACE processing centers GFZ in Potsdam, Germany, CSR in Texas, USA, and JPL in California, USA. Release 05 is the latest version.

(b) Integral equation approach The integral equation approach is based on Newton's equation of motion, which is formulated as a boundary value problem for short arcs of the GRACE orbits and, thus, also denoted short-arc method. The lengths of the arcs are chosen with approximately 30 min in order to avoid the accumulation of modeling errors (*Mayer-Gürr et al.*, 2010). *Mayer-Gürr* (2006) presents the fundamentals of the integral equation approach using range observations between the GRACE satellites, depending on their positions. The functional model can be set up for range rates or range accelerations, as well.

(c) Acceleration approach The acceleration approach as presented by *Ditmar and van Eck van der Sluijs* (2004) uses the above mentioned range accelerations of the GRACE satellites. They are obtained from the precise orbit data. The functional model is set up based on Newton's second law, according to approach (b). Weighted average accelerations are derived by numerical differentiation. Hereby a frequency-dependent weighting allows to take into account the high-frequent noise in the orbit-derived accelerations stemming from the double differentiation. From the in situ accelerations, finally gravity field parameters are derived in a straightforward way (*Liu et al.*, 2010).

(d) Energy balance approach The energy balance or energy integration approach follows the principle of energy conservation of the kinematic and the potential energy between the GRACE satellites. Hereby the energy equation expresses the relation between geopotential and satellite data in an inertial frame (*Jekeli*, 1999). In situ geopotential observables or differences are directly estimated at the satellite altitude, for each satellite 1 and 2, or between both satellites, and then applied for gravity field modeling. The estimation procedure benefits from the linear relationship between the observables and the gravity coefficients, analog to approach (c). The observables have an explicit geophysical interpretation and can serve as intermediate product between the satellite measurements and the derived gravity field models (*Shang et al.*, 2015).

(e) Celestial mechanics approach The celestial mechanics approach is a comprehensive and flexible approach comprising different processing strategies; among them the solution types (a) and (b). A POD is performed based on piecewise deterministic equations of motion of one or several satellites. The solution types are chosen immediately prior to the combination of the satellite-, arc- and technique-specific normal equation systems (*Beutler*, 2010). *Meyer et al.* (2012) set up an approach by numerically integrating the equations of motion of the GRACE satellites, comparing the resulting arcs with the kinematic positions obtained from GPS, and to the K-band range data. The nonlinear least-squares estimation model delivers estimates of orbit parameters and corrections. Among them are the coefficients of the gravity field.

Level 2 products

Depending on the degree of pre-processing, several GRACE products exist. Typically, calibrated and geolocated level 1b products are the input data for the different processing strategies. From the obtained sets of estimated SH coefficients, i. e. the level 2 products, the Earth's gravitational potential V can be modeled, e. g., by a series expansion in terms of SHs according to Eq. (2.40). The resulting global models are available in different spectral and spatial resolutions. Following the mission objectives, time series of monthly solutions are the main products. Static gravity models are also generated from a long-term mean.
Within the ITG-Grace series, which is based on approach (b), version 03 is developed up to degree 180, containing monthly solutions up to degree 40. Version 2010 contains even daily solutions up to degree 40, corresponding to a spatial resolution of around 500 km. In contrast, the static version 2010s up to degree 180 allows to recover spatial structures with a resolution better than 200 km.[16] The latest release is ITSG-Grace2014 (static gravity field recovery up to degree 200, secular and annual variations up degree 100) (*Mayer-Gürr et al.*, 2014).

[16] Source: `http://www.igg.uni-bonn.de/apmg/index.php?id=gravitationsfeldmodelle`

The European Improved Gravity field of the Earth by New techniques (EIGEN) GRACE-only models 01S and 02S are based on approach (a) and published by GFZ.[17] They are available up to degree 120 and 150, respectively. The combination of GRACE with further satellite missions is, for instance, realized by EIGEN-6S4 (*Foerste et al.*, 2015). It is the latest combined, satellite-only model, available up to degree 300, and including GRACE information up to degree 120. Various other models exist. A comprehensive overview can be found at `http://icgem.gfz-potsdam.de/ICGEM/`. Selected global models which are important for this work are presented in Sec. 3.2.

The predominant disadvantage of all GRACE products is, that they contain meridional stripes and artifacts due to the anisotropic observation geometry of the satellite mission (*Dahle et al.*, 2015) and due to aliasing errors, i. e. high-frequent gravity field variations, cannot be resolved in monthly products and result in the well-known error stripe pattern. An appropriate smoothing of the solutions has to be applied, e. g. by a spatial Gaussian filter, a stochastic Wiener-type filter, a filter designed by *Swenson and Wahr* (2006), or the computation of temporal high resolution models, as e. g. daily solutions by Kalman filtering (*Kurtenbach*, 2009). Within this work, a similar smoothing of GRACE products is achieved by SBFs acting as low-pass filters in the framework of a MRR, presented in Chapter 4.

3.1.6 CHAMP satellite mission

The GFZ satellite CHAllenging Minisatellite Payload (CHAMP) was launched in July 2000 and reentered the atmosphere in September 2010. It was the first mission with the aim of active gravity field detection (*Reigber et al.*, 1996). The initial orbit height was around 450 km. Due to atmospheric drag it decreased to only around 350 km in the end. With an inclination of about 87°, almost global coverage was achieved.

The measurement principle of high-low SST displayed in Fig. 3.6 is based on two instruments on board of the satellite – a GPS antenna and an accelerometer. From GPS measurements to at least four satellites (GPS-1, -2, -3, -4), a POD is derived, i. e. the position $\boldsymbol{x}(t)$ of the satellite in space as a function of time t, is determined with high precision. The second differentiation w.r.t. t delivers the geometric acceleration according to Eq. (3.8).
From the measurements of the accelerometer, non-gravitational influences from solar pressure and atmospheric drag are quantified and reduced.

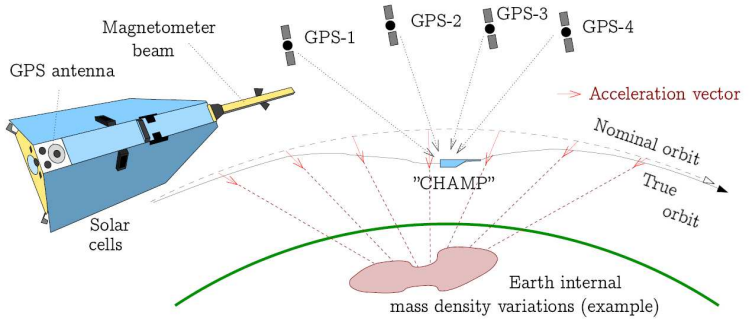

Figure 3.6: CHAMP measurement principle taken from *Vermeer M.* (2016), p. 218: The satellite contains an accelerometer (inside, not visible), a GPS antenna, solar cells for electric power and a magnetometer beam for measuring the Earth's magnetic field.

The combination of both measurement principles was unique at this time and allowed to compute the differences between the true and the nominal orbit with a precision of approximately 1 cm each second.
The remaining gravitational accelerations (indicated by red vectors in Fig. 3.6) enable for instance detecting Earth internal mass variations, and thus deriving global static geopotential models with unprecedented resolution (*Vermeer M.*, 2016, p. 217). The EIGEN series established e. g., with EIGEN-1 up to degree 119 (*Reigber et al.*, 2002), or EIGEN-2 up to degree 140 (*Reigber et al.*, 2003b). *Gerlach et al.* (2003) study the fundamentals of the energy balance approach (cf. GRACE processing strategy (d)) by means of real CHAMP data for gravity field recovery. *Schmidt et al.* (2005a) use CHAMP disturbing potential data at satellite altitude in order to study MRR applications in regional gravity field modeling. However, CHAMP data are not used within this work.

[17] Source: `http://op.gfz-potsdam.de/grace/results/`

3.1.7 Swarm satellite mission

The satellite mission Swarm (*Friis-Christensen et al.*, 2008) belongs to ESA's Earth Explorer Programme and was launched in November 2013. Main objective is the measurement of the Earth's geomagnetic field and its temporal evolution with high precision. Instruments are a vector field magnetometer, an absolute scalar magnetometer, an electric field instrument, an accelerometer, GPS receivers, startrackers and a laser retroreflector. The latter four further allow to the recover the static and time-variable gravity field.
The Swarm mission consists of three identical satellites A, B, C. They are "copies" of the CHAMP satellite. The pair A+B surrounds the Earth side-by-side, in near-polar, circular orbits with an inclination of 87.4°, an initial altitude of 450 km, and an east-west separation of 1° to 1.5° longitude. Satellite C is in a polar orbit of 530 km with an inclination of 86.8°. Due to the orbital drift, satellite C is crossing the path of A+B at an angle of 90° after three years, as displayed in Fig. 3.7. Hence, the constellation allows a quasi-global coverage.

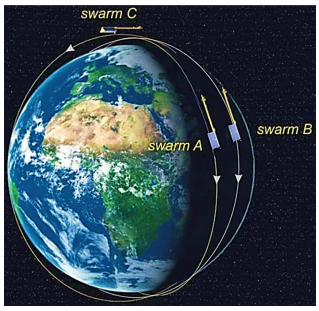

Figure 3.7: Swarm constellation; source: `http://www.swarm-projektbuero.de`.

For instance, *Jäggi et al.* (2016) use 1.5 years of Swarm GPS data for gravity field determination applying the celestial mechanics approach (e), mentioned above under the GRACE processing strategies.

3.1.8 Satellite Laser Ranging

Precise and unambiguous range observations from stations on Earth to various passive geodetic satellites are obtained by SLR. These accurate distance measurements enable to derive information about gravitational forces acting on the satellite. Especially the long wavelengths parts of the Earth's gravity field are detectable (*Klosko*, 1998).
Restrictions on the spatial resolution result from the geographic distribution of the observing stations on Earth and the high altitude of the satellites. *Bloßfeld* (2015) gives an overview of SLR satellites that are suited for gravity field recovery. Their spherical shape simplifies the modeling of the non-gravitational forces and their observation at optical wavelengths allows an accurate reduction of erroneous atmospheric influences, as e. g. the refractive delay.
Since the launch of Starlette and LAGEOS-1 (Laser Geodynamics Satellite) and satellites in the mid 1970s (at altitudes of 800 km and 5600 km), SLR data deliver valuable information and provide the foundation for a significant advancement of gravity field models up to present. An example of a combined model is EIGEN-6s (*Shako et al.*, 2014), obtaining GRACE, GOCE and SLR data. The latter support the determination of Stokes coefficients up to degree and order 30. *Bloßfeld et al.* (2015) present the SLR-only determination of low-degree SH coefficients from a combination of various SLR satellites by VCE.
SLR data are indirectly included in this work in terms of their long-wavelength contribution to global models. Typically, the SH coefficients of degree two are derived from SLR observations.

3.2 Models

In the context of regional gravity field modeling, it is reasonable to relate the approach and the output models to a global reference.

- The earlier introduced normal potential can be well determined and easily modeled. Consequently, long wavelengths parts are described by normal potential models, which serve as reference for all regional measurements.
- Further, global satellite observations can be captured very well by global SH gravitational potential models. The according low- and medium-frequency parts cannot be resolved by spatially limited observations. Hence, referring to Fig. 1.1, the regional gravity modeling approach of this thesis incorporates global SH gravitational potential models (briefly denoted as SH models in the following) as so-called "background models". They also relate to a specific normal potential.

The underlying geometric reference ellipsoids, the global geophysical normal and gravitational potential models used in this work, as well as an available regional model, are introduced now.

3.2.1 Reference ellipsoids and normal potential models

As mentioned in Sec. 2.3.4, the normal potential U of a spheroid can be described by four parameters. Various reference ellipsoids have been developed approximating either globally (e. g. GRS80, WGS84) or regionally (e. g. Bessel in Europe, Hayford in USA, Krassowsky in Russia) the Earth's body. For gravity field modeling in terms of SBFs with global support, a global reference ellipsoid is reasonable. Table 3.6 lists the most established reference ellipsoids and their parameters describing the related normal gravity field. The referring normal potential models GRS80 and WGS84 can be developed as series expansions in terms of SHs according to Eq. (2.44). Herein, the SH coefficients $C_{l,0}$ are computed from the four parameters as described by Eqs. (2.47). Note, the TOPEX/Poseidon (TOPEX) ellipsoid is a pure geometric ellipsoid, specified by the parameters a and f'. It is derived from altimetry measurements of the TOPEX/Poseidon mission and mainly serves as reference for the different altimetry missions.

Table 3.6: Reference ellipsoids and according parameters.

Reference ellipsoid	GM	semi major axis a	inverse flattening $1/f$	angular velocity ω
GRS80	$3\,986\,005 \times 10^8\ \mathrm{km^3/s^2}$	6 378 137.0 m	298.257 222 101	$7.292\,115 \times 10^{-5}$ rad/s
WGS84	$3\,986\,004.418 \times 10^8\ \mathrm{km^3/s^2}$	6 378 137.0 m	298.257 223 563	$7.292\,115 \times 10^{-5}$ rad/s
TOPEX		6 378 136.3 m	298.257	

The Geodetic Reference System 1980 (GRS80) (*Moritz*, 2000) is the official reference system of the International Union of Geodesy and Geophysics (IUGG). It replaced the previous Geodetic Reference System 1967 by more accurate values in 1979, and served as foundation for the more recent World Geodetic System 1984 (WGS84) (*Hofmann-Wellenhof and Moritz*, 2005, pp. 84). The latter is a conventional terrestrial reference system and delivers the basis, e. g., for GPS. The referring ellipsoids of revolution have an about 70 cm larger semi major axis than the TOPEX ellipsoid.
As different geometric or gravitational data sets relate to different reference ellipsoids or normal potential models, transformations are indispensable. Height transformations relate to Eq. (2.22), while the rescaling of the series expansion of a potential is performed by an according rescaling of the SH coefficients, cf. Eq. (2.42). The formulas are applied in the pre-processing of the data in next sections.
In this work, GRS80 is chosen as reference for all regional gravity fields to be modeled. Consequently, all measurements have to be transformed in this system and all numerical implementations are restricted to the according values.

3.2.2 Global SH gravity field models

The global gravity field models addressed in this work relate on series expansions in terms of SHs. In literature, they are usually described by expanding the gravitational potential V in the series according to Eq. (2.40) starting from $l = 0$. The zero-degree term is set to one; setting the first-degree terms equal to zero, i. e. assuming the origin of the global SH models coinciding with the geocenter, can be justified by deriving the low-degree terms ($l = 2, 3, 4, \ldots$ up to around $l = 20$) from analysis of satellite orbit perturbations (*Vermeer M.*, 2016, p. 46). A comprehensive set of models can be accessed from the International Centre for Global Earth Models (ICGEM), GFZ Potsdam, through `http://icgem.gfz-potsdam.de/ICGEM/`.

EGM96 and EGM2008

With the Earth Gravitational Model 1996 (EGM96) researchers from The Ohio State University developed one of the first well-approved global gravity field models. This combination model was published by *Lemoine et al.* (1998) and is mainly based on gravimetric data collected by the American NIMA (National Imagery and Mapping Agency) (*Vermeer M.*, 2016, p. 46). The intensive investigations in global data collection enabled to expand a series in terms of SHs, cf. Eq. (2.34), up to degree $L = 360$. It served for many decades as reference in various applications, such as referencing height systems on land, or determining the DOT over the sea.

At the beginning of this millennium, the CHAMP and especially the GRACE satellite missions revolutionized global gravity field determination by the ability of global gravity data collection. An enormous progress was achieved in precise long wavelength gravitational modeling. The National Geospatial-Intelligence Agency (NGA) developed a new release of EGM: EGM2008. This global SH model combines

- low- and medium-resolution GRACE data in terms of
- the global ITG-GRACE03s (static solution of ITG-GRACE2010, developed up to degree and order 180, *Mayer-Gürr et al.* (2010)), with
- high-resolution terrestrial, airborne and altimetry data in terms of a global 5 arc-minute grid of gravity anomalies, filled up with topography information in case of data gaps, as described by *Pavlis et al.* (2012).

The SH series of EGM2008 is expanded up to degree 2190; complete gravitational information is contained up to degree and order 2159, corresponding to a spatial resolution down to less than 10 km – in case of data coverage. Up to present, this global gravity field model is unique in its high spectral and spatial resolution.

EIGEN-6C3stat

Based on the 4th Release of the GOCE direct approach (*Pail et al.*, 2011a), the EIGEN-6C3stat was published by *Foerste et al.* (2014) in 2014 as a new release of EIGEN-6C (*Foerste et al.*, 2012). It is a static high resolution global combined gravity field model, developed in SH expansion up to degree and order 1949. The data which are used for the SH series expansion stem from

- SLR (LAGEOS-1/2, 25 years),
- GRACE (GRGS RL02 from degree 2 to 100, including 8 years, and GFZ RL05 from degree 55 to 180, including 9 years from GPS-SST and K-band range-rate observations),
- GOCE (contributing up to degree 235 from 19 months SGG data)
- ground data (gridded global gravity anomalies from the DTU12 ocean geoid and the EGM2008 geoid).

Consequently, beyond degree 235, EIGEN-6C3stat is a reconstruction of the EGM2008 model.

GOCO03s and GOCO05s

The GOCO series presents global SH gravity models mainly from a combination of GRACE and GOCE data. The satellite-only GOCO03s model (*Mayer-Gürr et al.*, 2012) incorporates

- 7.5 years of GRACE and
- 18 months of GOCE data. Further data stem from
- CHAMP (8 years) and
- SLR (5 years).

The series expansion is developed up to degree and order 250. GRACE information is contained in the long wavelengths from the SH model ITG-Grace2010s. The content in the medium wavelengths stems from GOCE gradiometry applying the processing strategy of *Pail et al.* (2011b). Due to regularization, full signal content is only ensured up to approximately degree 200.

The latest release GOGO05s (*Mayer-Gürr et al.*, 2015) is given with a spectral resolution up to degree and order 280 and contains significant information at least up to degree 200, i. e. it delivers a spatial resolution of around 100 km. The combined model consists of

- GOCE gradiometry data from the complete mission (48 months),
- the ITSG-Grace2014s model from 10.5 months GRACE observations (*Mayer-Gürr et al.*, 2014),
- SLR measurements, as well as data from

- CHAMP, Swarm A+B+C, and the Earth observation satellites TerraSAR-X[18] and TanDEM-X[19].

GRACE contributes to low- and medium-resolution spectral content approximately up to degree 150, whereas the significant GOCE information predominates from degree 120 on.

3.2.3 Regional model: GCG2011

The German Combined QuasiGeoid 2011 (GCG2011) is the official German height reference of the "Arbeitsgemeinschaft der Vermessungsverwaltungen der Länder der Bundesrepublik Deutschland (AdV)" describing quasigeoid heights, according to Eq. (2.63) w.r.t. the reference ellipsoid GRS80.

It is provided in terms of a $1'$ longitude times $1.5'$ latitude geographic grid by *BKG* (2011). The corresponding spatial resolution yields about 1.8 km × 1.7 km; the position coordinates refer to European Terrestrial Reference System 1989 (ETRS89) (*Boucher and Altamimi*, 1992). The quasigeoid heights in Fig. 3.8 are given in the "Deutsches Haupthöhennetz (DHHN) 1992" (*Weber*, 1994). The DHHN is the primary leveling network of Germany. The resolution counts 1 mm, the accuracy reaches 1 cm to 2 cm and varies depending on (1) geographical structures and (2) data availability. Over the Alps, the values are less accurate with 3 cm to 4 cm, and over the North and Baltic Sea even worse with 4 cm to 10 cm. The GCG2011 is obtained by averaging two independent solutions from BKG and IfE (Institut für Erdmessung der Leibnitz Universität Hannover). Whereas BKG uses an adjustment approach based on point masses, IfE applies integration and collocation. Based on a new release DHHN2016, a new release GCG2016 is planned, as well (*AdV*, 2014).

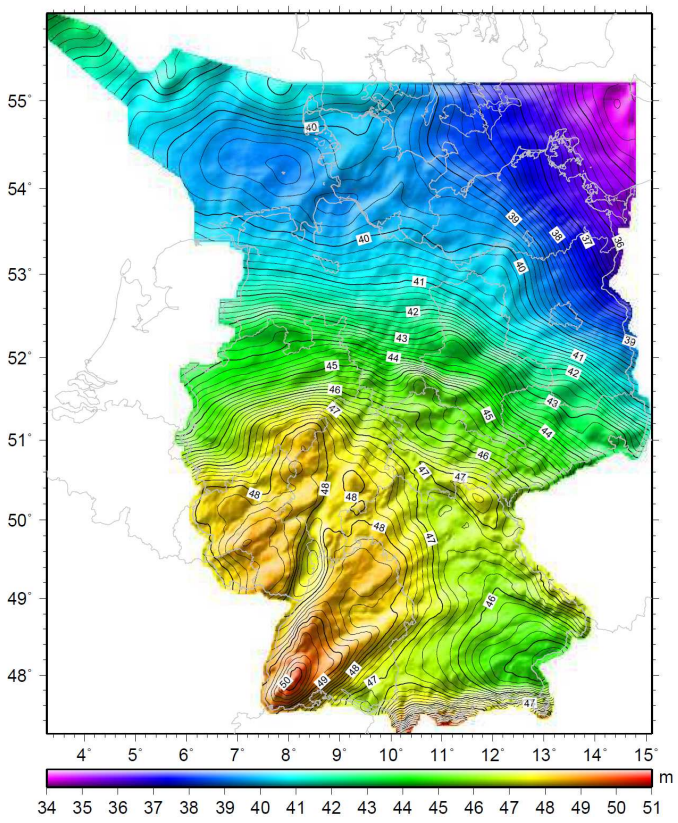

Figure 3.8: German combined quasigeoid 2011; source: *BKG* (2011).

3.3 Data

In order to study the combination of real data in this work, appropriate terrestrial, ship-, airborne and altimetry data sets are introduced. The values of the spatial resolutions serve as rough estimate for setting up the approach in Sec. 5 at an appropriate resolution level.

3.3.1 Terrestrial data set

Different terrestrial gravity data sets are provided by the surveying offices of the according federal states *Schleswig-Holstein*, *Mecklenburg-West Pomerania*, and *Lower Saxony*, in Northern Germany. They are obtained from measurement campaigns during the past decade, amongst others in the frame of the project "DHHN-Erneuerung 2006-2011" by the German AdV. The DHHN contains gravity information at 250 points, most of them recently installed and their positions determined by GNSS. Hereby, around 80 % of the leveling lines of the previous network DHHN92 were re-measured by high-precision relative gravimetry and absolute gravity values were observed at 100 points (source: www.bkg.bund.de). The data sets, displayed in yellow

[18] Latin "Terra" means Earth; the satellite carries on board an interferometric SAR (Synthetic Aperture Radar) instrument, operating in the X-band
[19] TerraSAR-X add-on for Digital Elevation Measurement

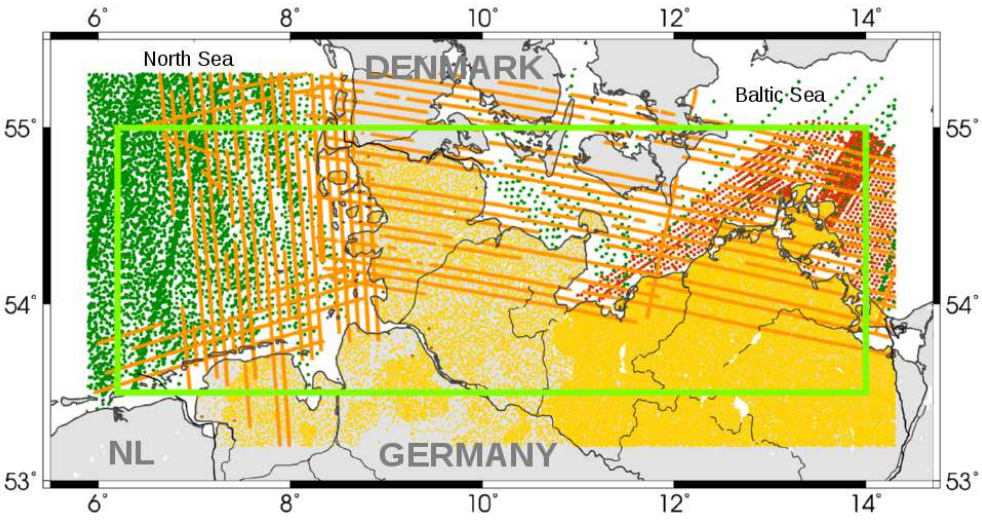

Figure 3.9: Distribution of the observations in the test area *Northern Germany* (green bordered): satellite altimetry (dark green), shipborne (red), airborne (orange), and terrestrial data (yellow). Thin black lines mark rivers and canals.

in Fig. 3.9, further encompass gravity measurements from the German gravity archive and from Deutsches Geodätisches ForschungsInstitut (DGFI), department 1+2 (nowadays DGFI-TUM and Institut für angewandte Geodäsie (IfAG), Frankfurt), taken in the 1950s.
The BKG homogenized the terrestrial data for the computation of the GCG2011 and provided a consistent data set, in the following denoted as "BKGterr". It contains in total 31 703 gravity values g referenced to IGSN71, at observation sites with ellipsoidal coordinates λ, β in the ETRS89 w.r.t. GRS80, and normal heights H_{norm}, as defined in Eq. (2.81), w.r.t. DHHN92.
The spatial resolution of the observation sites yields <1 km in *Mecklenburg-West Pomerania* and *Schleswig-Holstein*. In *Lower Saxony* data gaps of several kilometers occur and lead to a worse spatial resolution. An average point distance of 5 km is reached for the three federal states (*Lieb et al.*, 2016).

Pre-processing

In order to make the data set usable for the regional gravity modeling approach, the absolute gravity values g given at observation sites P (ellipsoidal coordinates λ, β) with potential W_P, are transformed into gravity anomalies Δg (cf. Fig. 2.13) at the referring locations described by spherical coordinates λ, φ. The following steps are performed for each observation point P:

(1)	computing normal gravity $\gamma_Q(Q)$ with $U_Q = W_P$ at height H_{norm},	cf. Eq. (2.51),
(2)	subtracting γ_Q from g_P in order to obtain gravity anomalies Δg,	cf. Eq. (2.67),
(3)	transforming ellipsoidal to spherical coordinates $(\lambda, \beta, H_{\text{norm}}) \rightarrow (\lambda, \varphi, r)$,	cf. Eq. (2.20).

Note: the normal height H_{norm} of an observation sites P (geopotential value W_P) refers to the quasigeoid. The distance along the ellipsoidal normal n' can be counted from the reference ellipsoid up to the according telluroid point Q with $U_Q = W_P$, as visualized in Fig. 2.16. Consequently, after coordinate transformation, the spherical coordinates relate to telluroid points $Q(\lambda, \varphi, r)$ and the values Δg refer to reference ellipsoid GRS80.

3.3.2 Shipborne data set

The terrestrial data set provided by BKG originally also contained off-shore data in the *Baltic Sea*. They stem from a prototype of gravimetric shipborne measurements after A. Graf and were collected in the 1950s (*Neunhöfer et al.*, 1997). The federal state *Mecklenburg-West Pomerania* reprocessed the data at sea level. BKG integrated the data within the GCG2011 model and provided the values g at observation sites $P(\lambda, \beta, 0.0)$. As the measurement technique of those off-shore data, their pre-processing, their corresponding spectral and

spatial resolution, and the time epoch entirely differ from those of the terrestrial observations, they are separated from the latter according to their height H_{norm}, which was set to zero by BKG. Consequently, the values are given on the quasigeoid, cf. Fig. 2.16. The spatial resolution of the generated data set "BKGship" averages 4 km. The measurement accuracy is assumed to be low due to the early period of shipborne gravimetry (*Lieb et al.*, 2016). Detailed information is not available.

Pre-processing

The pre-processing of the shipborne data at locations $P(\lambda, \beta, H_{\text{norm}})$ with potential W_P comprises:

(1)	computing normal gravity $\gamma_Q(Q)$ (with $U_Q = W_P$) at a height of 0.0 m, i. e. at the reference ellipsoid,	cf. Eq. (2.51),
(2)	subtracting γ_Q from g_P resulting in gravity anomalies Δg,	cf. Eq. (2.67),
(3)	transforming ellipsoidal to spherical coordinates $(\lambda, \beta, 0.0) \rightarrow (\lambda, \varphi, r)$,	cf. Eq. (2.20).

The gravity anomalies Δg at positions (λ, φ, r) refer to the reference ellipsoid GRS80.

3.3.3 Airborne data sets

The airborne gravity data stem from two flight campaigns, operated by Danish National Space Center (DNSC): "BALGRACE06" (BG06) over the *Baltic Sea* in 2006 and "NORTHGRACE07_08" (NG0708) over the *North Sea* in 2007/2008. The gravity data, provided in terms of gravity disturbances δg, refer to the ISGN71. Reference system of the according ellipsoidal coordinates λ, β of the observation sites along the flight tracks is ETRS89 (reference ellipsoid GRS80); reference system of the according normal heights H_{norm} at flight altitude (around 30 m) is DHHN92.
Both data sets BG06 (6834 observations) and NG0708 (6063 observations) are pre-processed by DNSC and compared with terrestrial and shipborne gravity data by BKG. Due to flight turbulence during the first campaign in 2006, some observations show larger differences. Removing those outliers results in a reduced data set BG06red (6677 observations).
Within the framework of homogenizing the measurements for their contribution to GCG2011, BKG did further embracing evaluations. As a result, both data sets were reduced by a constant offset of −2.0 mGal (BG06), and −0.6 mGal (NG0708), respectively.
The east-west oriented flight tracks in Fig. 3.9 are related to BG06, the north-south oriented flight tracks to NG0708. The along- and cross-track spatial resolution averages 10 km (*Lieb et al.*, 2016).

Pre-processing

Due to the comprehensive pre-processing of the airborne data by BKG and DNSC, only transforming the ellipsoidal to spherical coordinates $(\lambda, \beta, H_{\text{norm}}) \rightarrow (\lambda, \varphi, r)$, cf. Eq. (2.20), is necessary. The gravity disturbance values δg given at normal heights H_{norm} refer to telluroid points $Q(\lambda, \varphi, r)$ w.r.t. GRS80.

3.3.4 Altimetry data

The altimetry data originate from satellite missions of different agencies as listed in Tab. 3.3. DGFI-TUM provides a broad variety of data products at OpenADB "openadb.dgfi.tum.de", derived from the official level 2 GDRs (Geophysical Data Record). The instantaneous *DOT* values DOT_i, according to Eq. (3.15) are obtained from cross-calibrated range measurements, referring to 1 Hz SSH data from MMXO14. The geoid undulations N are obtained from the SH model GOCO03s. All data are referenced to the ellipsoid "TOPEX/Poseidon", cf. Tab. 3.6.
The sampling rate defines the along-track resolution of each satellite mission. 1 Hz data ensure a balanced signal to noise ratio. It corresponds to about 7 km along-track spatial resolution at the Earth's surface. The cross-track resolution depends on the orbit configuration of each mission. Table 3.3 lists the corresponding mean values. Due to the meridian convergence with increasing latitude, the spatial along- and cross-track resolution of the altimeter missions further depends on the geographic region.

Pre-processing

For each point $P(\lambda, \beta, SSH_i)$ of the different altimetry data sets, the following pre-processing procedure is applied:

(1)	subtracting instantaneous DOT_i values from SSH_i data (resulting in geoid undulations N_i),	cf. Eq. (3.13),
(2)	transforming h' from the TOPEX to the GRS80 reference ellipsoid: $h'(\text{GRS80}) = \text{h}'(\text{TOPEX}) - \text{dh}'$,	cf. Eq. (2.22),
(3)	computing normal gravity γ on the ellipsoid at $h' = 0$ (γ_a and k w.r.t. GRS80),	cf. Eq. (2.51),
(4)	transforming ellipsoidal to spherical coordinates $(\lambda, \beta, h') \rightarrow (\lambda, \varphi, r)$,	cf. Eq. (2.20),
(5)	computing disturbing potential T with N_i from (1) and γ from (3),	cf. Eq. (3.14).

Consequently, a consistent data set of values T is obtained for each point $P(\lambda, \varphi, r)$ w.r.t GRS80.

3.3.5 GOCE SGG data

The GOCE SGG data refer to the final release of Level 2 products "EGG_NOM_2", cf. Tab. 3.5, from March 06, 2014. They can be accessed from ESA through the GOCE Virtual Online Archive (VOA) `http://eo-virtual-archive1.esa.int` and are provided in a time series (one day temporal coverage) from Nov 1, 2009 until Nov 11, 2013 along the GOCE orbit. The spatial resolution averages 8 km along track, derived from 1 Hz spectral resolution.

The nominal data given in GRF are chosen, as a general aim of this work is, to keep all data in their most original, untouched, non-preprocessed mode. Within the product "EGG_TRF_2", the tensor rotation would transfer model information to the originally observed tensor elements (*Fuchs and Bouman*, 2011). Consequently, the tensor rotation has to be applied vice versa in this study: the GOCE observation equations (see next chapter, Tab. 4.7) of the estimation model, which is set up in Sec. 5.2, comprise a rotation of the GGs from the Earth-bound LNCS into the GRF in order to keep most valid GOCE information.

Pre-processing

Due to errors in the long wavelengths and increasing errors in the high frequencies, GOCE measured gravity gradients are band-pass filtered from 7.5 mHz to 100 mHz, following *Fuchs and Bouman* (2011). In order to reduce the anomalous signal in the V_{yy} component close to the magnetic poles, the according values are band-pass filtered from 15 mHz to 120 mHz. The signal below the MBW is replaced by model GGs derived from the global SH model GOCO03s. The model is low-pass filtered with the complement of the band-pass filter.
Outliers in the four accurate GGs are eliminated using a 3.5-sigma threshold of the along track standard deviation w.r.t. GOCO03s. The less accurate components remain with the approximately 200 times higher noise level.
The total observation period is split into three parts due to different accuracies and resolutions of the data:

11/2009 - 02/2010	less accurate data due to the erroneous on-board Central Processing Unit (CPU)-A side (a switch to CPU-B side caused impacts on the error characteristics; the residuals of V_{zz}, for instance, become around 1.5 times smaller (*Bouman et al.*, 2014)),
03/2010 - 07/2012	nominal phase at a mean altitude of 255 km,
08/2012 - 11/2013	lower orbit phase (higher sensitivity of the gradiometer due to a step-wise orbit lowering, down to around 225 km).

Consequently, each of the three data sets contains observation sites $P(\lambda, \varphi, r)$ in the GRF with the following information:

$V_{xx}, V_{yy}, V_{zz}, V_{xy}, V_{xz}, V_{yz}$	GGs in the GRF,
λ, φ, r	spherical coordinates,
$r_{11}, r_{12}, r_{13}, r_{21}, r_{22}, r_{23}, r_{31}, r_{32}, r_{33}$	components of the rotation matrix $\boldsymbol{R}_{\text{GRF}}^{\text{LNCS}}$.

3.3.6 GRACE level 2 data

GRACE measurements are not directly integrated in the regional gravity field modeling approach presented in this work. Observation equations would have to be set up for GRACE measurements processed by one of the strategies (a) - (e), presented in Sec. 3.1.5. However, those processed data are not publicly available. Thus, instead, gravitational potential differences according to Eq. (2.61) are computed from level 2 SH products. The GRACE release 05 data are available from April 2002 up to present in terms of monthly solutions from GFZ (*Dahle et al.*, 2012). The SH coefficients $C_{l,m}$, $S_{l,m}$ are provided up to degree and order 90 at `http://icgem.gfz-potsdam.de/ICGEM/shms/monthly/gfz-rl05/` and refer to the normal potential parameters $a = 6\,378\,136.460\,\mathrm{m}$, $GM = 3\,986\,004.415 \times 10^8\,\mathrm{km}^3/\mathrm{s}^2$.

Pre-processing

From those coefficients, gravitational potential values $V(\boldsymbol{x}^i)$ and $V(\boldsymbol{x}^{ii})$ are computed at positions $\boldsymbol{x}^i = (\lambda^i, \varphi^i, r^i)^T$ and $\boldsymbol{x}_{ii} = (\lambda^{ii}, \varphi^{ii}, r^{ii})^T$ of the two GRACE satellites (i),(ii) along their orbits with a sampling rate of 5 s. Gravitational potential differences ΔV then are obtained between each two neighboring positions:

(1) computing gravitational potential values $V(\boldsymbol{x}^i)$ and $V(\boldsymbol{x}^{ii})$ from SH coefficients with corresponding normal potential values a, GM, cf. Eq. (2.40),
(2) computing gravitational potential differences $\Delta V(\boldsymbol{x}^i, \boldsymbol{x}^{ii})$, cf. Eq. (2.61).

The time span from Nov 2009 until Nov 2012 is pre-processed, related to the availability of GOCE data, in order to generate an overlapping time period. The GRACE data set contains the values $\Delta V(\lambda^i, \varphi^i, r^i, \lambda^{ii}, \varphi^{ii}, r^{ii})$.

Overview of pre-processed data sets

The pre-processed and homogenized data sets, witch will be used in the sequel of this work, are summarized in Tab. 3.7.

Table 3.7: Overview of pre-processed data sets.

number	type	name	functional $\mathcal{Y}[\tilde{V}]$	coordinates	height	normal potential
[1]	terr	BKGterr	Δg	λ, φ, r	H_{norm}	GRS80
[2]	ship	BKGship	Δg	λ, φ, r	H_{norm}	GRS80
[3]	air	BG06	δg	λ, φ, r	H_{norm}	GRS80
[4]	air	NG0708	δg	λ, φ, r	H_{norm}	GRS80
[5]	alti	ERS-1e	T	λ, φ, r	h'	GRS80
[6]	alti	ERS-1f	T	λ, φ, r	h'	GRS80
[7]	alti	TOPEX	T	λ, φ, r	h'	GRS80
[8]	alti	Jason-1	T	λ, φ, r	h'	GRS80
[9]	alti	Envisat	T	λ, φ, r	h'	GRS80
[10]	alti	Jason-2	T	λ, φ, r	h'	GRS80
[11]	alti	Cryosat	T	λ, φ, r	h'	GRS80
[12]	goce	GOCE0911-1002	(V_{ab})	λ, φ, r		
[13]	goce	GOCE1003-1207	(V_{ab})	λ, φ, r		
[14]	goce	GOCE1208-1309	(V_{ab})	λ, φ, r		
[15]	grace	GRACE0911-1211	ΔV	$\lambda^i, \varphi^i, r^i, \lambda^{ii}, \varphi^{ii}, r^{ii})$		

4 Spherical basis functions and multi-resolution representation

In general, a **basis function** is an element of a basis for a function space. As introduced in Sec. 2.3.2, the surface SH functions, Eq. (2.36), span for example the $L^2(\Omega_R)$ space defined on a sphere Ω_R and form a complete orthonormal basis. The solid SHs, Eq. (2.35), span the space $H_{0,1,\ldots,\infty}(\Omega_R^{\text{ext}})$ and are well suited for globally describing the Earth's gravity field, since $\nabla^2 H_{l,m} = 0$.
The overall aim of setting up a modeling approach is to represent input data as optimally as possible: From the spectral point of view, SH functions can be easily adapted to any frequency domain. However, in the spatial domain they require data sets with nearly worldwide coverage due to their global nature. The era of satellite gravimetry hereby provides suitable observations, but their spatial resolution reaches nowadays 70 km to 80 km at the Earth's surface. Much higher spatial resolutions are achieved by air-, shipborne or terrestrial gravimetry, but the observations are typically only available in regionally limited areas.
Here radial SBFs come into play: although they are also global functions, they have a highly localizing character in space (e. g. *Freeden et al.*, 1998; *Schmidt et al.*, 2007), and are a compromise between spatially and spectrally localizing functions, as depicted in Fig. 1.2. SBFs are suited to reproduce the signal content of (high-resolution) regional data sets. This makes them very attractive for regional gravity field modeling up to very high spectral degrees. They may capture information from spatially limited measurements and fit the regional data sets with high accuracy, while SHs are perfect spectrally localizing functions and appropriate to reproduce information from global satellite observations.
Since SBFs belong to the same group of basis functions as SHs, based on series expansion in the spectral domain in terms of Legendre polynomials, they share many positive features, as e. g. satisfying the Laplace differential equation (2.25) outside the Earth. In the Introduction, Tab. 1.1 highlights the main properties of other possible functions which are appropriate for regional gravity modeling as well. The beneficial choice of SBFs amongst them is carved out in this section for the specific tasks of this thesis, discussing the main characteristics of SBFs and further comparing them with the well-known and -established SHs.
Based on those findings, the single data sets from Chapter 3 could be fitted with high accuracy, if their measurement resolution is exactly known. However, this is not the aim of this work. In contrast, for the ambition of combining heterogeneous data sets, i. e.

- enhanced regional gravity modeling
- from real, heterogeneous data sets
- of different spatial distributions, spatial and spectral resolutions, and accuracies,
- which are often just approximately known,

a discretization of the frequency spectrum seems reasonable: several degrees l are collected in one resolution level j, i. e. the frequency domain is split into several spectral bands. The levels enable to set up an approach reacting flexibly on all the challenges. It is called **multi-resolution** method and is introduced and adapted to the needs of this work in the third part of this chapter.

The chapter is structured as follows: first, in Sec. 4.1, the SBFs are introduced referring to SH basis functions, and how to use them for theoretically representing non-bandlimited functions. Second, in Sec. 4.2, the transition to bandlimiting SBFs is discussed including truncation of series expansion and corresponding errors. Further, various gravitational functionals are formulated in terms of SBFs. In the third part, Sec. 4.3, the idea of a MRR (de)composition is introduced. Therefore, the filtering characteristics of SBFs are applied for representing signals within different spectral resolutions. Requirement is an appropriate splitting of the frequency spectrum into resolution levels, defining the framework for MRR.

4.1 Series expansion in terms of SBFs

Theoretically, any harmonic function $f = f(\boldsymbol{x}), \boldsymbol{x} \in \Omega_R^{\text{ext}}$, can be expressed by a linear combination, i. e. a series expansion in terms of an infinite number of suitably weighted basis functions $b'_q = b'_q(\boldsymbol{x}) = b'(\boldsymbol{x}, \boldsymbol{x}_q)$, with the weighting coefficients c_q.[20]

4.1.1 SBF: definition and properties

In the spatial domain, a SBF $b'(\boldsymbol{x}, \boldsymbol{x}_q)$ is expressed by the infinite series expansion over degree l

$$b'_q = b'(\boldsymbol{x}, \boldsymbol{x}_q) = \sum_{l=0}^{\infty} \frac{2l+1}{4\pi R^2} \left(\frac{R}{r}\right)^{l+1} B_l \; P_l(\boldsymbol{r}^T \boldsymbol{r}_q) \; . \tag{4.1}$$

Hereby, the basis functions b'_q shall span the space $H_{0,1,\ldots,\infty}(\Omega_R^{\text{ext}})$ with $\boldsymbol{x} = r \cdot \boldsymbol{r} \in \Omega_R^{\text{ext}}$, according to Eq. (2.8), denoting the geocentric position vector of any point $P(\lambda, \phi, r) = P(\boldsymbol{x}) = P$, and with $\boldsymbol{x}_q \in \Omega_R$ denoting the geocentric position vector of the point $P(\lambda_q, \varphi_q, r_q) = P(\boldsymbol{x}_q) = P_q, r_q = R$, and representing the center of the basis function on the sphere Ω_R (*Schmidt et al.*, 2007). Analogously to SHs, the SBF b'_q is based on Legendre polynomials P_l, Eq. (2.30), of degree l, and the definitions and features from Sec. 2.3.2 apply. This ensures the validity of the Laplace differential equation. In contrast to the associated SHs $H^R_{l,m}(\boldsymbol{x})$, Eq. (2.36), or $H_{l,m}(\boldsymbol{x})$, Eq. (2.35), which have global support and further depend on order m (cf. Fig. A.1 in Appendix A), the SBFs are global two-point kernel functions, centered in $P_q \in \Omega_R$, radially symmetric and have spatially localizing character, cf. Fig. 1.2. If both locations P, $P_q \in \Omega_R$, the SBF $b(\boldsymbol{x}, \boldsymbol{x}_q)$ does not longer depend on the radial distance r and becomes rotationally symmetric, i. e. isotropic (*Narcowich and Ward*, 1996). The computation of function values $b'(\boldsymbol{x}, \boldsymbol{x}_q)$ at locations $P(\boldsymbol{x})$ depends on the spherical distance angle between $P(\boldsymbol{x})$ and $P(\boldsymbol{x}_q)$, respectively vector product of the referring unit vectors of $\boldsymbol{x} = r \cdot \boldsymbol{r}$ and $\boldsymbol{x}_q = r_q \cdot \boldsymbol{r}_q$, cf. Eq. (2.8), i. e.

$$t = \cos\psi_q = \boldsymbol{r}^T \boldsymbol{r}_q \; . \tag{4.2}$$

t is the argument of the Legendre polynomials according to Eq. (2.31). B_l are the Legendre coefficients. They specify the spectral behavior of the SBF in the frequency domain and define the shape of the SBF in the spatial domain. The derivation of expression (4.1), its embedding in the overall group of basis functions, and its relation to SHs will be discussed in the following.

Legendre coefficients

Any SBF, cf. Eq. (4.1), can be used as low-, band- or high-pass filter. According to *Freeden* (1999), pp. 70, two cases are distinguished: functions with (a) non-bandlimiting or (b) bandlimiting properties. In case (a), an infinite number of coefficients B_l is different from zero, whereas in case (b) only a finite number of coefficients B_l is different from zero, e. g. by setting the coefficients $B_l = 0$ for $l > l'$ (*Schmidt et al.*, 2005a). The corresponding Hilbert spaces (a) $H_{0,1,\ldots,\infty}(\Omega_R^{\text{ext}})$, (b) $H_{0,1,\ldots,l'}(\Omega_R^{\text{ext}})$, cf. Tab. 2.1, then are of infinite or finite dimension. However, in addition, a truncation of the series expansion at a certain degree L is always necessary in practical implementations. In the sequel, four cases are distinguished: Figure 4.1 schematically depicts the Legendre coefficients B_l; according to this classification, Tab. 4.1 assigns the application of the corresponding series expansions in this thesis.

- As SBFs are naturally infinite, i. e. the number of coefficients B_l is infinite as well, they are denoted non-bandlimit*ing* in case (a), and bandlimit*ing* in case (b), if only a sequence of coefficients is different from zero. The term (non-)bandlimiting is associated with an active property of the SBFs.
- In contrast, (non-)bandlimiting, but additionally truncated functions are denoted bandlimit*ed*, cases (c) and (d), denoting a passive feature.

The upper row of Fig. 4.1 visualizes the two artificial cases: infinite series expansions for (a) a non-bandlimiting SBF and (b) a bandlimiting SBF at degree l'. The Legendre coefficients in the lower row belong to applicable

[20] Note, in the sequel, all basis functions expressed by an infinite series, i. e. $l \to \infty$, are marked with an apostrophe, e. g. b'_q, while those, expanded by a finite series, are marked without apostrophe, i. e. b_q.

SBFs, truncated at degree L, i. e. finite series expansions (dashed lines in Fig. 4.1 c, d). The referring SBF of case (c) is truncated at degree L, while the one of (d) is truncated and bandlimiting at degree $L = l'$.

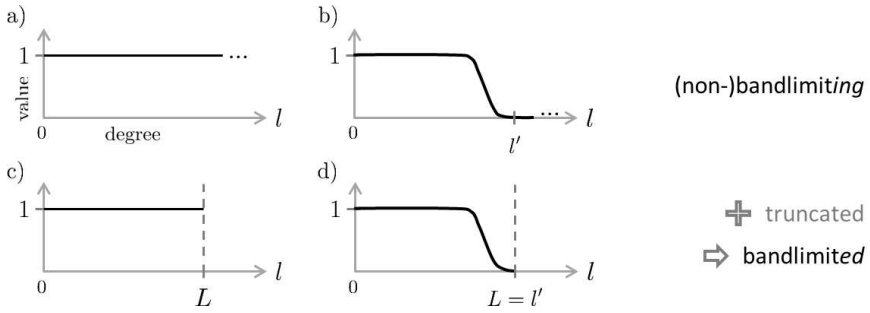

Figure 4.1: Legendre coefficients B_l of SBFs: (a) non-bandlimiting, (b) bandlimiting at degree l', (c) non-bandlimiting and truncated (i. e. bandlimited) at degree L, (d) bandlimiting and truncated at degree $L = l'$.

Table 4.1: Band limitation and truncation of series expansions and their application in this thesis.

case	band limitation	truncation	application, e. g.	Eq.
(a)	no	no	SBF definition b'_q Abel-Poisson kernel k'_q	(4.1) (4.3)
(b)	yes: l'	no	bandlimiting SBF b_q spherical convolution	(4.5)
(c)	no	yes: L	practical issues	
(d)	yes: l'	yes: $L = l'$	transformation of SHs into SBFs by bandlimited SBFs, MRR	(4.14), (4.15) (4.33)

Case (a) is, e. g., used for defining the Abel-Poisson kernel in the next section, case (b) for presenting the general concept of spectral filtering by spherical convolution, and case (c) visualizes the truncation of a series expansion in general. Case (d) is finally implemented and applied in the core of this work, i. e., the MRR in Sec. 4.3 is set up by means of bandlimiting, truncated SBFs.

Spherical convolution with an Abel-Poisson kernel

In case of setting $B_l = 1$ for $l \in \mathbb{N}_0$, Eq. (4.1) defines the **Abel-Poisson kernel** $b'(\boldsymbol{x}, \boldsymbol{x}_q) = k'(\boldsymbol{x}, \boldsymbol{x}_q)$, i. e.

$$k'_q = k'(\boldsymbol{x}, \boldsymbol{x}_q) = \sum_{l=0}^{\infty} \frac{2l+1}{4\pi R^2} \left(\frac{R}{r}\right)^{l+1} P_l(\boldsymbol{r}^T \boldsymbol{r}_q) \tag{4.3}$$

with $\boldsymbol{x} \in \Omega_R^{\text{ext}}$, $\boldsymbol{x}_q \in \Omega_R$. The **convolution** of a harmonic function $f(\boldsymbol{x}), \boldsymbol{x} \in \Omega_R^{\text{ext}}$ on the sphere Ω_R, as introduced in Eq. (2.7), with the non-bandlimiting kernel k'_q from Eq. (4.3), yields

$$f(\boldsymbol{x}) = \left(k'_q * f\right)_{\Omega_R}(\boldsymbol{x}) = \langle f, k' \rangle_{\Omega_R} \ . \tag{4.4}$$

It results exactly in the function $f(\boldsymbol{x})$ and is equivalent to the inner product, cf. Eq. (2.7). The ability of the unique reproduction of a harmonic function $f(\boldsymbol{x})$ is one of the essential characteristics of the Abel-Poisson kernel. According to *Freeden* (1999), pp. 72, it belongs to the group of (reproducing) rational non-bandlimiting kernels.

Table 4.2: Relation of SHs and SBFs (right column) in the group of basis functions. Based on several fundamentals (left column), the dependency is derived within five steps. The spherical convolution is the essential key.

basis function	
... linear combination in terms of:	SHs
1	$f = f(\boldsymbol{x}) = \sum_{l=0}^{\infty}\sum_{m=-l}^{l} F_{l,m} H_{l,m}(\boldsymbol{x}) = \sum_{l=0}^{\infty}\sum_{m=-l}^{l} \left(\frac{R}{r}\right)^{l+1} F_{l,m} H^R_{l,m}(\boldsymbol{x})$
2 ... inserting coefficients (obtained as inner product) $F_{l,m} = \int_{\Omega_R} f(\boldsymbol{x}_q) H^R_{l,m}(\boldsymbol{x}_q) d\omega_R = \langle f, H^R_{l,m}\rangle_{\Omega_R}$	$f = f(\boldsymbol{x}) = \sum_{l=0}^{\infty}\sum_{m=-l}^{l} \left(\frac{R}{r}\right)^{l+1} \int_{\Omega_R} f(\boldsymbol{x}_q)\, H^R_{l,m}(\boldsymbol{x}_q) d\omega_R \, H^R_{l,m}(\boldsymbol{x})$
3 ... applying the addition theorem $\frac{2l+1}{4\pi R^2} P_l(\cos\psi) = \sum_{m=-l}^{l} H^R_{l,m}(\boldsymbol{x})\, H^R_{l,m}(\boldsymbol{x}_q)$	$f = f(\boldsymbol{x}) = \int_{\Omega_R} f(\boldsymbol{x}_q) \sum_{l=0}^{\infty} \left(\frac{R}{r}\right)^{l+1} \frac{2l+1}{4\pi R^2} P_l(\cos\psi)\, d\omega_R$
4 ... inserting the Abel-Poisson kernel $k'(\boldsymbol{x}, \boldsymbol{x}_q) = \sum_{l=0}^{\infty} \frac{2l+1}{4\pi R^2} \left(\frac{R}{r}\right)^{l+1} P_l(\boldsymbol{r}^T \boldsymbol{r}_q)$	$f = f(\boldsymbol{x}) = \int_{\Omega_R} f(\boldsymbol{x}_q)\, k'(\boldsymbol{x}, \boldsymbol{x}_q)\, d\omega_R$
5 ... applying the definition of convolution $(k'_q * f)_{\Omega_R}(\boldsymbol{x}) = \int_{\Omega_R} k'_q(\boldsymbol{x}) f(\boldsymbol{x}) d\omega_R$	$f = f(\boldsymbol{x}) = (k'_q * f)_{\Omega_R}(\boldsymbol{x})$
... relates SBFs and SHs	$f = f(\boldsymbol{x}) = \sum_{l=0}^{\infty}\sum_{m=-l}^{l} F_{l,m} H_{l,m}(\boldsymbol{x})$

4.1.2 Relation to SHs

As introduced in Sec. 2.3.2, SHs are well suited for global gravity field modeling. They belong to the overall group of basis functions, as well as SBFs. The relation of both is derived in Tab. 4.2:

1. The harmonic function $f(\boldsymbol{x})$, with $\boldsymbol{x} \in \Omega_R^{\text{ext}}$, can be expressed in terms of SHs, according to the series expansion (2.34). Hereby, $F_{l,m}$ are the Stokes coefficients according to Eq. (2.39). $H_{l,m}(\boldsymbol{x})$, $\boldsymbol{x} \in \Omega_R^{\text{ext}}$, cf. Eq. (2.35), are the solid SHs (dark-green bordered terms in Tab. 4.2); $H^R_{l,m}(\boldsymbol{x})$, $\boldsymbol{x} \in \Omega_R$, cf. Eq. (2.36), are the surface SHs (light-green bordered terms).
2. For the coefficients $F_{l,m}$, Eq. (2.39) is inserted as inner product of the harmonic function $f = f(\boldsymbol{x}_q)$ and the surface SH function $H^R_{l,m}(\boldsymbol{x}_q)$ according to Eq. (2.36), at location $P(\boldsymbol{x}_q)$ (red brackets in Tab. 4.2).
3. The addition theorem (2.38) of surface SHs is applied by depicting the appropriate terms (yellow brackets).
4. The blue-marked series expansion in Tab. 4.2, represents the Abel-Poisson kernel $k'(\boldsymbol{x}, \boldsymbol{x}_q)$, cf. Eq. (4.3).
5. By definition from Eq. (2.7) (purple marked) and application in Eq. (4.4), the spherical convolution of the function $f(\boldsymbol{x})$ on Ω_R shows the relation of SBFs to SHs (dark green).

The relation of SBFs and SHs is exemplarily derived for the Abel-Poisson kernel as one specific basis function. The admission of equivalently replacing the latter by any other appropriate SBF is approved by the tool of spherical convolution in Sec. 4.2.2. Consequently, the scheme in Fig. 2.5, which shows the foundation of SHs on Legendre polynomials, can be extended to basis functions in general, see Fig. A.1 in Appendix A.

4.2 Band limitation

In order to practically implement the representation of a function by series expansion in terms of basis functions, the series has to be limited to a finite number of terms, and consequently to a finite number of coefficients and basis functions. According to Eq. (4.1), the basis function b'_q itself is also expanded as a series and has to be limited for numerical realization. This bandlimiting feature is of beneficial relevance: a bandlimiting basis function may act as spectral filter. The spherical convolution with a bandlimiting kernel in the spatial domain corresponds to filtering in the spectral domain. It is the essential tool for setting up the MRR (*Schmidt et al.*, 2007), presented in Sec. 4.3. Both, the band limitation of basis functions, and the band limitation of the series for representing filtered functions, will be studied in the following.

4.2.1 Bandlimiting SBF

As mentioned before, a SBF, defined in Eq. (4.1), may act as a low-pass filter by setting a sequence of Legendre coefficients B_l to zero, e. g. for an arbitrary high frequency domain of $l > l'$, $l' \in \mathbb{N}$. Case (b) in Fig. 4.3 applies. The corresponding **bandlimiting SBF** is denoted as $b_q = b(\boldsymbol{x}, \boldsymbol{x}_q)$ and the series expansion (4.1) reduces to

$$b_q = b(\boldsymbol{x}, \boldsymbol{x}_q) = \sum_{l=0}^{\infty} \frac{2l+1}{4\pi R^2} \left(\frac{R}{r}\right)^{l+1} B_l \; P_l(\boldsymbol{r}^T \boldsymbol{r}_q) \qquad \text{with} \qquad B_l = 0 \qquad \text{for} \qquad l > l' \tag{4.5}$$

$$= \sum_{l=0}^{l'} \frac{2l+1}{4\pi R^2} \left(\frac{R}{r}\right)^{l+1} B_l \; P_l(\boldsymbol{r}^T \boldsymbol{r}_q) \; . \tag{4.6}$$

According to Tab. 2.1, these bandlimiting basis functions span the space $H_{0,1,\ldots,l'}(\Omega_R^{\text{ext}})$ of dimension $(l'+1)^2$. In case of setting the Legendre coefficients $B_l = 1$ for $l = 0, \ldots, l'$, Eq. (4.6) defines the **Shannon kernel**, in analogy to the non-bandlimiting Abel-Poisson kernel k'_q, cf. Eq. (4.3). A selection of different kernels is presented in Sec. 4.3.4.

4.2.2 Filtering by convolution

In the spatial domain, the spherical convolution with any bandlimiting kernel b_q, cf. Eq. (4.5), against a function $f(\boldsymbol{x}), \boldsymbol{x} \in \Omega_R$, can be described by a linear combination of Q terms. The filtered function g then is represented by

$$g = g(\boldsymbol{x}) = \left(b_q * f\right)_{\Omega_R}(\boldsymbol{x}) = \sum_{q=1}^{Q} d_q \, b(\boldsymbol{x}, \boldsymbol{x}_q) \, . \tag{4.7}$$

Following Tab. 4.3, this convolution (4.7) in the spatial domain, which results in the filtered function g, can equivalently be expressed by the multiplication of coefficients of a series expansion in terms of SH functions in the spectral domain. The SH coefficients $F_{l,m}$ are multiplied with the bandlimiting Legendre coefficients B_l and $G_{l,m}$ are the resulting filtered SH coefficients, i. e.

$$G_{l,m} = B_l F_{l,m} \, . \tag{4.8}$$

Hereby, Parseval's identity corresponds to the Funk-Hecke formula (*Schreiner*, 1996). The four fundamental steps in the left column of Tab. 4.3 are derived reversely to Tab. 4.2. Figure 4.2 visualizes the equivalence of spatial and spectral filtering: (a) spherical convolution in the spatial domain and (b) multiplication in the spectral domain. In case (b), the coefficients are schematically displayed according to Fig. 4.1. Since the bandlimited function g from Eq. (4.7) further can be expressed by

$$g(\boldsymbol{x}) = \sum_{l=0}^{l'} \sum_{m=-l}^{l} G_{l,m} \, H_{l,m}(\boldsymbol{x}) \tag{4.9}$$

in terms of SH functions, cf. Tab. 4.3, the bandlimiting basis functions b_q span the space $H_{0,\ldots,l'}(\Omega_R^{\text{ext}})$ with dimension $N_{l'} = (l'+1)^2$, cf. Tab. 2.1. Consequently, the number Q of terms of the series (4.7) follows the

requirement that an admissible point system

$$S_Q = \left\{ \boldsymbol{x}_q \in \Omega_R | q = 1, 2, ..., Q \right\} \tag{4.10}$$

is guaranteed. Following *Freeden et al.* (1998), pp. 80, and *Schmidt et al.* (2007), an admissible point system on the sphere Ω_R allows the unique determination of the coefficients $G_{l,m}$ in Eq. (4.9). Hence, the point system S_Q, Eq. (4.10), is **admissible** for $Q \geq N_{l'}$; it is called **fundamental**, for $Q = N_{l'}$. The latter case practically never applies when dealing with real data. In the sequel, all point systems are required to be at least admissible.

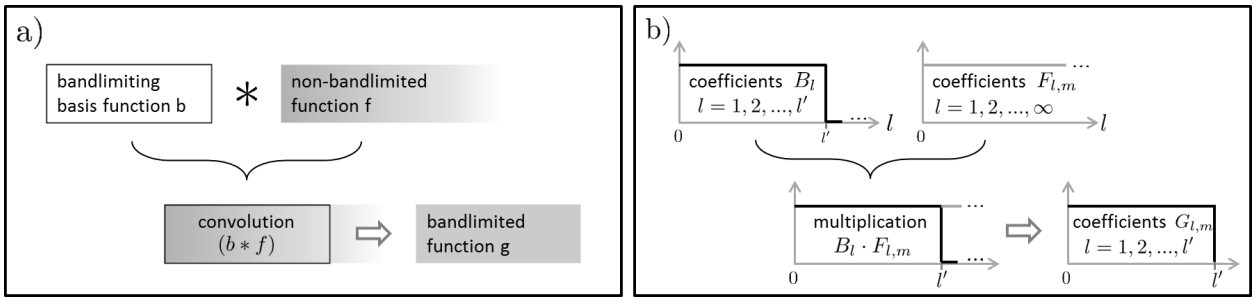

Figure 4.2: Filtering by (a) convolution of basis functions in the spatial domain, (b) multiplication of SH coefficients in the spectral domain.

Table 4.3: Filtering of SH coefficients by multiplication with bandlimiting Legendre coefficients. The spherical convolution is the essential key. The relation of bandlimiting SBFs and SHs, based on four fundamental steps (left column), is derived in analogy to Tab. 4.2.

basis function		
	the definition of convolution yields	SBFs
1	$(b_q * f)_{\Omega_R}(\boldsymbol{x}) = \int_{\Omega_R} b_q(\boldsymbol{x}) f(\boldsymbol{x}) d\omega_R$	$g = g(\boldsymbol{x}) = (b_q * f)_{\Omega_R}(\boldsymbol{x})$
2	... inserting bandlimiting basis function $b(\boldsymbol{x}, \boldsymbol{x}_q) = \sum_{l=0}^{l'} \frac{2l+1}{4\pi R^2} \left(\frac{R}{r}\right)^{l+1} B_l P_l(\boldsymbol{r}^T \boldsymbol{r}_q)$	$g = g(\boldsymbol{x}) = \sum_{l=0}^{l'} \frac{2l+1}{4\pi R^2} \left(\frac{R}{r}\right)^{l+1} B_l \int_{\Omega_R} P_l(\boldsymbol{r}^T \boldsymbol{r}_q) f(\boldsymbol{x}_q) d\omega_R$
3	... applying the addition theorem $\frac{2l+1}{4\pi R^2} P_l(\cos\psi) = \sum_{m=-l}^{l} H_{l,m}^R(\boldsymbol{x}) H_{l,m}^R(\boldsymbol{x}_q)$	$g = g(\boldsymbol{x}) = \sum_{l=0}^{l'} \left(\frac{R}{r}\right)^{l+1} B_l \sum_{m=-l}^{l} H_{l,m}^R(\boldsymbol{x}) \int_{\Omega_R} H_{l,m}^R(\boldsymbol{x}_q) f(\boldsymbol{x}_q) d\omega_R$
4	... inserting coefficients $F_{l,m} = \int_{\Omega_R} f(\boldsymbol{x}_q) H_{l,m}^R(\boldsymbol{x}_q) d\omega_R = \langle f, H_{l,m}^R \rangle_{\Omega_R}$ ... relates SHs and SBFs	$g = g(\boldsymbol{x}) = \left(\frac{R}{r}\right)^{l+1} \sum_{l=0}^{l'} \sum_{m=-l}^{l} B_l F_{l,m} H_{l,m}^R(\boldsymbol{x})$ $= \sum_{l=0}^{l'} \sum_{m=-l}^{l} B_l F_{l,m} H_{l,m}(\boldsymbol{x})$
	... yields bandlimited SH coefficients $G_{l,m} = B_l F_{l,m}$	$g(\boldsymbol{x}) = \sum_{l=0}^{l'} \sum_{m=-l}^{l} G_{l,m} H_{l,m}(\boldsymbol{x})$

Freeden et al. (1998) further show, that for different basis functions $b_{q,1}(\boldsymbol{x}, \boldsymbol{x}_q)$, $b_{q,2}(\boldsymbol{x}, \boldsymbol{x}_q)$, but both band-limiting at degree l', i. e. spanning the same space $H_{0,\dots,l'}(\Omega_R^{\text{ext}})$ or subspaces of $H_{0,\dots,l'}(\Omega_R^{\text{ext}})$, the filtered functions $g_1(\boldsymbol{x})$, $g_2(\boldsymbol{x})$, $\boldsymbol{x} \in \Omega_R^{\text{ext}}$, can be expressed by the same set of coefficients d_q, i. e.

$$g_1(\boldsymbol{x}) = \left(b_{q,1} * f\right)_{\Omega_R}(\boldsymbol{x}) = \sum_{q=1}^{Q} d_q b_1(\boldsymbol{x}, \boldsymbol{x}_q)$$
$$g_2(\boldsymbol{x}) = \left(b_{q,2} * f\right)_{\Omega_R}(\boldsymbol{x}) = \sum_{q=1}^{Q} d_q b_2(\boldsymbol{x}, \boldsymbol{x}_q) \tag{4.11}$$

The set of coefficients d_q does not depend on the choice of the bandlimiting SBF. Several beneficial conclusions follow from this fact:

- With a known set of coefficients d_q, convolutions of the function f with different kernels $b_{q,1}, b_{q,2}$, strictly bandlimiting at the same degree l', can be performed according to Eq. (4.11) (p. 225 *Freeden*, 1999).
- The function f can be filtered with different bandlimiting kernels $b_{q,1}, b_{q,2}, \dots$ and the resulting bandlimited functions can be calculated by the according weighted sum of function values $b_1(\boldsymbol{x}, \boldsymbol{x}_q), b_2(\boldsymbol{x}, \boldsymbol{x}_q), \dots$.
- This advantageous property is used for defining and applying different low- and band-pass filters in order to set up a MRR in Sec. 4.3.

4.2.3 Truncation of series expansions

Besides the truncation of the series expansion (4.7) at Q terms, the degree-l'-depending basis function b_q, Eq. (4.5) has to be limited, as well, i. e. truncated at a specific degree L. In the following, the truncation of the previously introduced SHs (2.34) and SBFs (4.5) at a maximum degree L is considered by exposing differences, dependencies, and the direct relation to the limitation of appropriate $Q =: Q_L$ terms of the overall series expansion (4.7). Figure 4.3 schematically connects the truncation at a maximum spectral degree L for both types of basis functions with the limitation of Q_L components of the series expansions. Both restrictions, truncation and band limitation, deliver the impact on the dimension of the spaces, spanned by the set of basis functions. The adequate dimension is requirement for relating SHs and SBFs, according to Tab. 4.2. The details are discussed in the following w.r.t. Fig. 4.3.

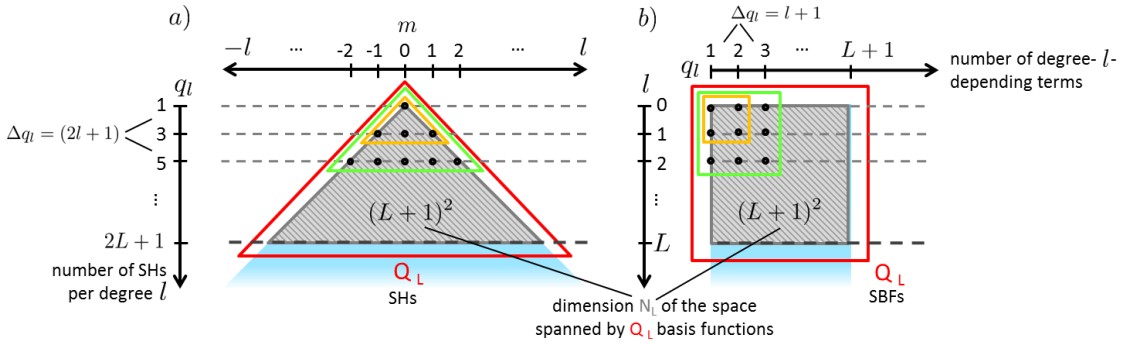

Figure 4.3: Dimension $N_L = (L+1)^2$ (gray dashed) of the space $H_{0,1,\dots,L}(\Omega_R^{\text{ext}})$ spanned by Q_L basis functions (red bordered) up to maximum degree L, in terms of (a) SHs (step width $\Delta q_l = 2l + 1$ per degree l), (b) SBFs (step width $\Delta q_l = l + 1$ per degree l). Exemplarily, a number of 4 and 9 basis functions is indicated by black bullets spanning spaces of dimension $(1+1)^2$ (yellow bordered) and $(2+1)^2$ (green bordered). The spectral domain $l > L$ is blue shaded.

... in terms of SHs

Truncating the series expansion (2.34) in terms of SHs at a certain maximum degree L, represents a function g in the **bandlimited** spectral domain $l = 0, 1, 2, ..., L$, i. e.

$$g = g(\boldsymbol{x}) = \sum_{l=0}^{L} \sum_{m=-l}^{l} G_{l,m}\, H_{l,m}(\boldsymbol{x}) = \sum_{l=0}^{L} \sum_{m=-l}^{l} \left(\frac{R}{r}\right)^{l+1} G_{l,m}\, H^R_{l,m}(\boldsymbol{x}), \tag{4.12}$$

here with $G_{l,m} = F_{l,m}$. According to Tab. 2.1, the dimension N_L of the space $H_{0,...,L}(\Omega_R^{\text{ext}})$ or $H_{0,...,L}(\Omega_R)$, spanned by solid or surface SHs $H_{l,m}$, $H^R_{l,m}$, yields

$$N_L = \sum_{l=0}^{L} (2l + 1) = (L + 1)^2 \tag{4.13}$$

(p. 101 *Michel*, 2013). With increasing degree l ($m = -l, \ldots, 0, \ldots, l$), the number of SHs (respectively coefficients $G_{l,m}$) augments with a step width of $\Delta q_l = 2l + 1$, $\Delta q_l \in \mathbb{N}$. The dimension is illustrated as dashed gray triangle in Fig. 4.3 a). For a number of $Q_L = N_L$ SH functions (red bordered) up to maximum degree L, the point system S_Q, Eq. (4.10), becomes fundamental. Exemplarily, the number of basis functions spanning the corresponding spaces, are indicated as black bullets. It yields four basis functions spanning a space of dimension $N_1 = (1 + 1)^2$ (yellow bordered), respectively nine for spanning a space of dimension $N_2 = (2 + 1)^2$ (green bordered). Due to the truncation at degree L, the blue shaded part of the overall infinite space in Fig. 4.3 is neglected and cannot be represented by Eq. (4.12). This omission error is handled in Sec. 4.2.4.

... in terms of SBFs

In order to equivalently represent the function g, Eq. (4.12), by a series expansion in terms of SBFs, the fundamental requirement is, that the sets of basis functions b_q and $H^R_{l,m}$ span the same space with dimension $N_L = (L + 1)^2$. Truncating the series expansion (4.5) at maximum degree L yields

$$b(\boldsymbol{x}, \boldsymbol{x}_q) = \sum_{l=0}^{L} \frac{2l + 1}{4\pi R^2} \left(\frac{R}{r}\right)^{l+1} B_l\, P_l(\boldsymbol{r}^T \boldsymbol{r}_q), \tag{4.14}$$

and the function g is represented by a bandlimited series expansion in terms of $Q_L = (L + 1)^2$ basis functions through

$$g = g(\boldsymbol{x}) = \sum_{q=1}^{Q_L} d_q\, b_q(\boldsymbol{x}) = \sum_{q=1}^{Q_L} d_q \sum_{l=0}^{L} \frac{2l + 1}{4\pi R^2} \left(\frac{R}{r}\right)^{l+1} B_l\, P_l(\boldsymbol{r}^T \boldsymbol{r}_q)\,. \tag{4.15}$$

Hereby, the total global number Q_L of SBFs $b_q(\boldsymbol{x})$, respectively coefficients d_q, depends on maximum degree L (the number of degree-l-depending terms augments with a step width of $\Delta q_l = l + 1$). According to Eq. (4.10), the point system S_Q is admissible for $Q \geq Q_L$ and fundamental for $Q = Q_L = N_L$. In Fig. 4.3 b), the gray dashed rectangle specifies the dimension $N_L = \dim H_{0,...,L}(\Omega_R)$ and covers the same space as in Fig. 4.3 a). For instance, by a number of 4 or 9 SBFs (black bullets), the space of the same dimension $N_1 = (1 + 1)^2$ or $N_2 = (2 + 1)^2$ is spanned, as by SHs, cf. Fig. 4.3 a). The number Q_L of basis functions spanning the space of dimension N_L is red bordered. Consequently, the limitation of the series expansion (4.15) to Q_L terms ensures the transformation from SHs into SBFs, which is presented in Tab. 4.2 for the theoretical non-bandlimiting case. Respectively, the number of Legendre coefficients B_l in Eq. (4.14) is limited as well, which is shown in Fig. 4.1, case (c). The effect of truncating a series expansion at degree $L = l'$ according to Eq. (4.14) can be compared with restricting the Legendre coefficients to $B_l = 0$ for $l > l'$, visualized in Fig. 4.1, case (d).

The basis functions b_q are in the following denoted as **scaling functions** and the coefficients d_q as **scaling coefficients**, since their values are interpreted as scaling factors, defining the amplitude of a basis function in the spatial domain.

Summary: Band limitation and truncation

A summary of the different types of (non-)bandlimiting SBFs and the represented (non-)bandlimited, i. e. (in-) finite functions is given in Tab. 4.4. Hereby, the spherical convolution is the essential tool in order to describe the filtering. Band limitation is realized by truncation of the according series expansion at the same degree $l' = L$.

- Infinite series expansion (green) of a non-bandlimited function f (green) in terms of a non-bandlimiting SBF b'_q (green), Eq. (4.1); convolution of k'_q, Eq. (4.3), as one specific SBF, against f yields the same non-bandlimited function f (green), Eq. (4.4).
- Finite series expansion (blue) of a bandlimited function g (blue) in terms of a bandlimiting SBF b_q (blue), Eq. (4.6) – realized by an appropriate set of Legendre coefficients B_l; convolution of b_q against f yields the filtered, i. e. bandlimited, function g (blue), Eq. (4.7). Different bandlimited functions can be computed by different SBFs, but with one and the same set of coefficients d_q (gray shaded), Eq. (4.11).
- Finite series expansion (orange) of a truncated (and thus, bandlimited) function g (orange), Eq. (4.15) in terms of a bandlimiting SBF b_q (orange), Eq. (4.14) – realized by truncation.

Table 4.4: Representation of functions g (f) by series expansions in terms of (non-)bandlimiting SBFs b_q (b'_q, k'_q).

THEORY		
no band limitation ($l \to \infty$)	$b'(\boldsymbol{x}, \boldsymbol{x}_q) = \sum_{l=0}^{\infty} \frac{2l+1}{4\pi R^2} \left(\frac{R}{r}\right)^{l+1} B_l P_l(\boldsymbol{r}^T \boldsymbol{r}_q)$	infinite series expansion in terms of... any SBF
	$k'(\boldsymbol{x}, \boldsymbol{x}_q) = \sum_{l=0}^{\infty} \frac{2l+1}{4\pi R^2} \left(\frac{R}{r}\right)^{l+1} P_l(\boldsymbol{r}^T \boldsymbol{r}_q)$	specific SBF
	$f(\boldsymbol{x}) = (k'_q * f)_{\Omega_R}(\boldsymbol{x})$	reproducing property

BAND LIMITATION by CONVOLUTION		
band limitation ($l > l' : B_l = 0$)	$b(\boldsymbol{x}, \boldsymbol{x}_q) = \sum_{l=0}^{l'} \frac{2l+1}{4\pi R^2} \left(\frac{R}{r}\right)^{l+1} B_l P_l(\boldsymbol{r}^T \boldsymbol{r}_q)$	any bandlimiting SBF
	$g(\boldsymbol{x}) = (b_q * f)_{\Omega_R}(\boldsymbol{x})$	convolution yields bandlimited function(s) and allows to...
	$\begin{Bmatrix} g_1(\boldsymbol{x}) \\ g_2(\boldsymbol{x}) \end{Bmatrix} = \left(\begin{Bmatrix} b_{q,1} \\ b_{q,2} \end{Bmatrix} * f \right)_{\Omega_R}(\boldsymbol{x}) = \sum_{q=1}^{Q} d_q \begin{Bmatrix} b_1(\boldsymbol{x}, \boldsymbol{x}_q) \\ b_2(\boldsymbol{x}, \boldsymbol{x}_q) \end{Bmatrix}$	(1) filter a continuous function f by different SBFs and
	$g(\boldsymbol{x}) = \sum_{q=1}^{Q} d_q b(\boldsymbol{x}, \boldsymbol{x}_q)$	(2) compute filtered functions by finite series expansions with only one set of coefficients

LINK between Q ↔ L by TRUNCATION		
truncation ($l' = L$)	$b(\boldsymbol{x}, \boldsymbol{x}_q) = \sum_{l=0}^{L} \frac{2l+1}{4\pi R^2} \left(\frac{R}{r}\right)^{l+1} B_l P_l(\boldsymbol{r}^T \boldsymbol{r}_q)$	any truncated SBF
	$g(\boldsymbol{x}) = \sum_{q=1}^{Q_L} d_q b(\boldsymbol{x}, \boldsymbol{x}_q)$	finite series expansion of a bandlimited function

4.2.4 Modeling errors and energy content

On the one hand, band limitation and/or truncation enable(s) to filter specific parts of the frequency spectrum, as explained above. On the other hand, truncation is necessary for all practical implementations, and thus, provokes a certain truncation error. In the sequel, the filtered as well as the neglected parts of the frequency spectrum shall be specified w.r.t. their energy content. The following terms are equivalently used:

physical meaning	modeling procedure
function	signal
representation	model, data fit.

Referring to *Jekeli* (2012), three different types of modeling errors are distinguished: commission, omission and aliasing errors. They are briefly introduced according to Fig. 4.4; a possibility of estimating the omission error, resulting from the truncation of the series expansion (4.15), is explained based on the energy content of a bandlimited signal g. Following Fig. 4.4 top-down, it yields:

- The naturally non-bandlimited signal f (green curve; top line) is detected by observations (black curve; mid line) up to a specific maximum frequency L_{obs}, depending on the properties of the measurement principle (e. g. resolution, data distribution). Additionally, errors (red-yellow curve; mid line) occur due to the limited measurement accuracy, both from the instruments and from diverse external conditions (e. g. climatic influences).
- Using the observations, the signal (purple curve; bottom line) is modeled in terms of bandlimiting SBFs b_q up to degree $L \leq L_{\text{obs}}$ (orange box). I. e. the maximum spectral resolution at degree L_{obs} of the observations limits the maximum achievable resolution at degree L of the model. Usually, L_{obs} is not exactly known when dealing with real data.
- The measurement error is separated into a spectral part of degree $l \leq L$ (red curve) and a spectral part of degree $l > L$ (yellow curve). The error of degree $l \leq L$ directly affects the estimated coefficients d_q of the modeled signal g (purple box), expanded by a series according to Eq. (4.15), and further into all derived quantities. It is denoted **commission error** (red shaded). The variance σ_l^2 per degree l of the error is known as error degree variance and the variance of the coefficients as degree variance (*Sansò et al.*, 2012).
- The neglected high-frequent part (above degree L) of the non-bandlimited signal f, which is not captured within the model g, is denoted **omission error** (blue shaded; bottom line). If $L_{\text{obs}} > L$, i. e. usually in case of real data, the un-modeled signal is not independent of the commission error, as the neglected observed signal of degree $l > L$ affects especially the high-frequent part of the estimated coefficients. Thus, the modeled signal g contains an additional **aliasing error** (yellow shaded). The effect is also known as frequency folding.

Energy and omission error

As mentioned, due to neglecting the terms $q > Q_L$ in Eq. (4.15), the naturally non-bandlimited signal f is not represented in the high frequencies. The truncation of the linear combination (4.15) at Q_L according to the truncation of the series expansion (4.14) at L, provokes the above discussed omission error for degrees larger than L (green in Fig. 4.4). Hence, Eqs. (4.7) and (4.11) are only approximately valid.
The neglected non-stochastic high-frequency part, i. e. the omission error, can be rated by estimating its influence on the determination of the coefficients d_q. It is derived from the inverse power spectrum, i. e. the neglected energy content of the bandlimited signal g. In Fig. 4.4, the omission error is blue shaded depending on the spectral degree $l > L$, cf. as well Fig. 4.3.

SHs Referring to *Schmidt et al.* (2007), the norm, cf. Eq. (2.6), of a signal f can be interpreted as its energy content or as global root-mean-square value. Modeling a gravitational signal, by the bandlimited signal g, the latter contains less energy than the non-bandlimited signal f. In terms of SH basis functions, this loss of energy, i. e. the omission error, can be estimated from Parseval's identity. The relations are presented in

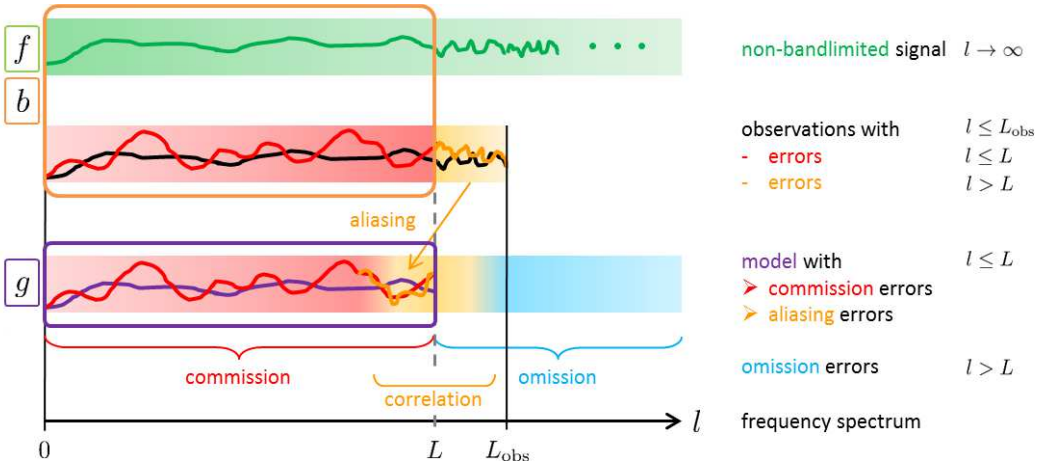

Figure 4.4: Modeling errors.

Tab. A.1 in Appendix A in analogy to Tab. 4.2. By definition of the norm (2.6), the degree variances $\sigma_l^2(g)$ describe the power spectrum, i. e. the energy E_g, of the bandlimited signal g in the frequency domain up to degree L (*Tscherning and Rapp*, 1974). It yields

$$E_g = \int_{\Omega_R} |g(\boldsymbol{x})|^2 d\omega_R = \| g \|_{\Omega_R}^2 = \sum_{l=0}^{L} \sigma_l^2(g) = \sum_{l=0}^{L} \sum_{m=-l}^{l} |G_{l,m}|^2 \,. \tag{4.16}$$

Consequently, the neglected energy contained in the higher frequencies of degree $l > L$ delivers an estimate for the variance σ_{om}^2 of the omission error. The latter results from the L^2 norm of the difference of non-bandlimited (f) and bandlimited (g) signal, i. e.

$$\sigma_{\text{om}}^2 = \| f - g \|_{\Omega_R}^2 = \sum_{l=L+1}^{\infty} \sigma_l^2(f) \,. \tag{4.17}$$

Hereby, the degree variances $\sigma_l^2(g)$ describe the errors per degree l for all order values (*Jekeli*, 2012).

SBFs – global modeling As the global modeling of a signal f can be equivalently computed in terms of SHs and SBFs according to Tab. 4.2, the total energy E_g of g in terms of SBFs is derived using the fundamental relations of SHs according to Tab. 4.5, cf. *Schmidt* (2001), p. 151, *Bußе* (2015).

Expressing the energy E_g of the signal g in terms of SBFs is comparable with computing the degree variances $\sigma_l^2(g)$ of g in terms of SHs. The variance σ_{om}^2 of the omission error then corresponds to the difference of the energy E_f of a non-bandlimited signal f and the energy E_g of the bandlimited signal g

$$\sigma_{\text{om}}^2 = \| f - g \|_{\Omega_R}^2 = E_f - E_g \,, \tag{4.18}$$

in analogy to Eq. (4.17).

SBFs – regional modeling Compared with SH functions which are optimally localizing in the frequency domain, cf. Fig. 1.2, additional edge effects appear for spatially localizing SBFs when they are used for regional modeling. All considerations up to now refer to a global modeling procedure, where SBFs and SHs can be used equivalently. However, benefiting from the localizing character of SBFs in the regional approach of this work, provokes further modeling errors due to the spatial restriction onto a certain geographical area. In order to overcome the difficulties, many parameters have to be carefully chosen and adapted when using SBFs in the modeling approach. As the total error budget of regional models consists – besides the omission error – of a variety of further influences, special emphasis is given, e. g., to the selection of the truncation degree L and number Q_L of SBFs within the region (see Sec. 5.1.5), a suitable computation grid (see Sec. 5.1.1), and appropriate SBFs (see Sec. 4.3.4), in order to reduce erroneous effects. Further influences are discussed by means of the numerical applications in Sec. 6. An overview of the remains is given in the end, in Tab. 7.1.

Table 4.5: Energy of a bandlimited signal g in terms of SBFs.

energy of bandlimited signal		
	in terms of:	SBFs
1	... expressed by norm $\|g\|^2_{\Omega_R} = \int_{\Omega_R} \|g(\boldsymbol{x})\|^2 d\omega_R$	$E_g = \int_{\Omega_R} \|g(\boldsymbol{x})\|^2 d\omega_R = \int_{\Omega_R} \|\sum_{q=1}^{Q_L} d_q\, b(\boldsymbol{x},\boldsymbol{x}_q)\|^2 d\omega_R$
2	... using the SBF $b(\boldsymbol{x},\boldsymbol{x}_q)$, $b(\boldsymbol{x},\boldsymbol{x}_p)$ at different locations	$E_g = \int_{\Omega_R} \sum_{q=1}^{Q_L} d_q\, b(\boldsymbol{x},\boldsymbol{x}_q) \sum_{p=1}^{Q_L} d_p\, b(\boldsymbol{x},\boldsymbol{x}_p)\, d\omega_R = \sum_{q=1}^{Q_L}\sum_{p=1}^{Q_L} d_q\, d_p \int_{\Omega_R} b(\boldsymbol{x},\boldsymbol{x}_q)\, b(\boldsymbol{x},\boldsymbol{x}_p)\, d\omega_R$
3	... inserting series expansion of SBFs on Ω_R $\left(\frac{R}{r}\right)^{l+1} = 1 \quad \text{for} \quad r = R$	$= \sum_{p=1}^{Q_L}\sum_{q=1}^{Q_L} d_p\, d_q \int_{\Omega_R} \sum_{l=0}^{L} \frac{2l+1}{4\pi R^2} B_l\, P_l(\boldsymbol{r}^T\boldsymbol{r}_q) \sum_{n=0}^{L} \frac{2n+1}{4\pi R^2} B_n\, P_n(\boldsymbol{r}^T\boldsymbol{r}_p)\, d\omega_R$
4	... applying addition theorem of SHs $\frac{2l+1}{4\pi R^2} P_l(\cos\psi_q) = \sum_{m=-l}^{l} H^R_{l,m}(\boldsymbol{x})\, H^R_{l,m}(\boldsymbol{x}_q)$	$= \sum_{q=1}^{Q_L}\sum_{p=1}^{Q_L} d_q\, d_p \sum_{l=0}^{L}\sum_{n=0}^{L} B_l\, B_n \int_{\Omega_R} \sum_{m=-l}^{l} H^R_{l,m}(\boldsymbol{x}) H^R_{l,m}(\boldsymbol{x}_q) \sum_{k=-n}^{n} H^R_{n,k}(\boldsymbol{x}) H^R_{n,k}(\boldsymbol{x}_p)\, d\omega_R$
5	... applying orthogonality relation $\langle H^R_{l,m}, H^R_{n,k}\rangle_{\Omega_R} = \int_{\Omega_R} H^R_{l,m}(\boldsymbol{x})\, H^R_{n,k}(\boldsymbol{x}) d\omega_R = \delta_{l,n}\delta_{m,k}$	$= \sum_{q=1}^{Q_L}\sum_{p=1}^{Q_L} d_q\, d_p \sum_{l=0}^{L} B_l^2 \sum_{m=-l}^{l} H^R_{l,m}(\boldsymbol{x}_q) H^R_{l,m}(\boldsymbol{x}_p)$
6	... applying addition theorem of SHs $\frac{2l+1}{4\pi R^2} P_l(\cos\psi_{p,q}) = \sum_{m=-l}^{l} H^R_{l,m}(\boldsymbol{x}_p)\, H^R_{l,m}(\boldsymbol{x}_q)$	$= \sum_{q=1}^{Q_L}\sum_{p=1}^{Q_L} d_q\, d_p \sum_{l=0}^{L} B_l^2 \frac{2l+1}{4\pi R^2} P_l(\boldsymbol{r}_p^T\boldsymbol{r}_q)$
	... yields energy $E_{g,q}$ per location $\boldsymbol{x}_q$ and total energy E_g of bandlimited signal	$E_g = \sum_{q=1}^{Q_L} d_q\, E_{g,q} = \sum_{q=1}^{Q_L} d_q \sum_{p=1}^{Q_L} d_p \sum_{l=0}^{L} \frac{2l+1}{4\pi R^2} B_l^2\, P_l(\boldsymbol{r}_p^T\boldsymbol{r}_q)$

4.2.5 Gravitational functionals in terms of SBFs

The splitting of $\tilde{V}$ expressed by SHs in Eqs. (2.56) – (2.58) in its r, λ, ϑ-depending terms can be equivalently applied to the series expansions in terms of SBFs. Formulating Eq. (4.15) more general, for any (differential) gravitational potential or functional of it, it yields

$$\begin{aligned} \mathcal{Y}[\,\tilde{V}\,] &= \sum_{q=1}^{Q_L} d_q\, \tilde{b}(\boldsymbol{x},\boldsymbol{x}_q) \\ &= \sum_{q=1}^{Q_L} d_q \sum_{l=0}^{L} f_0(l)\, f_l(r)\, B_l\, f_{P,l}(\lambda,\vartheta)\ . \end{aligned} \tag{4.19}$$

Hereby, the basis functions $b(\boldsymbol{x},\boldsymbol{x}_q)$ from Eq. (4.14) have to be adapted to the different quantities. The degree l-depending terms of $\tilde{V}$ and its first and second order derivatives are listed in Tab. 4.6, according to Tab. 2.3. $f_0(l)$ represents the scaling factor, $f_l(r)$ comprises the up-/downward continuation operator X^{l+i} and corresponding derivatives w.r.t. r, summarized within $g_l(r) = g_l$ for $r = R$, according to Tab. 2.2, and $f_{P,l}(\lambda,\vartheta)$ contains the Legendre polynomials $P_l(\boldsymbol{r}^T,\boldsymbol{r}_q) = P_l(\cos\psi_q)$ and its first and second order derivatives w.r.t. λ,ϑ. The argument, cf. Eq. (2.31), describes the cosine of the spherical distance angle

ψ_q between a point P of interest with position vector $\boldsymbol{x} \in \Omega_R^{\text{ext}}$ and the center P_q of the basis function with position vector $\boldsymbol{x}_q \in \Omega_R$.

Table 4.6: Zero, first and second order derivatives of the (differential) gravitational potential $\tilde{V}$ in terms of SBFs w.r.t. spherical coordinates r, λ, ϑ.

$\mathcal{Y}[\tilde{V}]$	$f_0(l)$	$f_l(r)$			$f_{P,l}(\lambda,\vartheta)$
		g_l	X^{l+i}	i	
$\tilde{V}$	$\frac{2l+1}{4\pi R^2}$	1	$\left(\frac{R}{r}\right)^{l+i}$	1	$P_l(\cos\psi_q)$
$\frac{\partial\tilde{V}}{\partial r}$	$\frac{2l+1}{4\pi R^2}$	$-\frac{l+1}{R}$	$\left(\frac{R}{r}\right)^{l+i}$	2	$P_l(\cos\psi_q)$
$\frac{\partial\tilde{V}}{\partial \lambda}$	$\frac{2l+1}{4\pi R^2}$	1	$\left(\frac{R}{r}\right)^{l+i}$	1	$\frac{\partial P_l(\cos\psi_q)}{\partial\lambda}$
$\frac{\partial\tilde{V}}{\partial \vartheta}$	$\frac{2l+1}{4\pi R^2}$	1	$\left(\frac{R}{r}\right)^{l+i}$	1	$\frac{\partial P_l(\cos\psi_q)}{\partial\vartheta}$
$\frac{\partial^2\tilde{V}}{\partial r^2}$	$\frac{2l+1}{4\pi R^2}$	$\frac{(l+1)(l+2)}{R^2}$	$\left(\frac{R}{r}\right)^{l+i}$	3	$P_l(\cos\psi_q)$
$\frac{\partial^2\tilde{V}}{\partial r\partial \lambda}$	$\frac{2l+1}{4\pi R^2}$	$-\frac{l+1}{R}$	$\left(\frac{R}{r}\right)^{l+i}$	2	$\frac{\partial P_l(\cos\psi_q)}{\partial\lambda}$
$\frac{\partial^2\tilde{V}}{\partial r\partial \vartheta}$	$\frac{2l+1}{4\pi R^2}$	$-\frac{l+1}{R}$	$\left(\frac{R}{r}\right)^{l+i}$	2	$\frac{\partial P_l(\cos\psi_q)}{\partial\vartheta}$
$\frac{\partial^2\tilde{V}}{\partial \lambda^2}$	$\frac{2l+1}{4\pi R^2}$	1	$\left(\frac{R}{r}\right)^{l+i}$	1	$\frac{\partial^2 P_l(\cos\psi_q)}{\partial\lambda^2}$
$\frac{\partial^2\tilde{V}}{\partial \vartheta\partial \lambda}$	$\frac{2l+1}{4\pi R^2}$	1	$\left(\frac{R}{r}\right)^{l+i}$	1	$\frac{\partial^2 P_l(\cos\psi_q)}{\partial\vartheta\partial\lambda}$
$\frac{\partial^2\tilde{V}}{\partial \vartheta^2}$	$\frac{2l+1}{4\pi R^2}$	1	$\left(\frac{R}{r}\right)^{l+i}$	1	$\frac{\partial^2 P_l(\cos\psi_q)}{\partial\vartheta^2}$

The gravitational functionals $\mathcal{Y}[\tilde{V}]$, which are relevant within this work, stem from different observation techniques, summarized in Tab. 3.7. In order to use them as input for regional gravity field modeling, as schematically displayed in Fig. 2.9, observation equations have to be formulated. Inserting the expressions from Tab. 4.6 in the corresponding equations of the functionals $\Delta V, \boldsymbol{V}_{a,b}, T, \Delta g, \delta g$, derived in Sec. 2.5, yields the adapted basis functions $\tilde{b}(\boldsymbol{x}, \boldsymbol{x}_q)$, listed in Tab. 4.7. The observation equations are set up within the analysis of the estimation models presented in Sec. 5.2. The relations from Tab. 4.7 further serve for computing output quantities by setting up corresponding modeling equations in the synthesis.

4.3 Multi-resolution representation

In Chapter 3, various measurement techniques and data sets have been introduced. Further, in the first and second part of this chapter, it was shown, that SBFs expanded by a series in terms of spectral degrees l, are appropriate for modeling gravitational functionals. For enhanced regional gravity modeling in terms of SBFs, the consistent combination of the heterogeneous data via MRR seems appropriate:

- The spatial coverage of the data varies from global (GRACE, GOCE), over ocean-wide (altimetry), down to regionally limited (air-/shipborne, terrestrial). Further, especially terrestrial data sets show internally heterogeneous spatial distribution and data gaps.
- The measurement techniques have different spectral resolutions, reaching from "low" and "medium" for satellite data, up to "high" for terrestrial data.
- Depending on the measurement instruments and on the operation of the measurement campaigns, the accuracy of the data sets may differ a lot. Stemming from various sources, information on the pre-processing procedures might be missing, as well.

Based on the definitions of spectral and spatial resolution, discussed in Secs. 4.3.1 and 4.3.2, a MRR approach is set up and adapted to the challenges of this thesis in Sec. 4.3.3. Hereby, the main aims are to preserve as much as possible valuable signal content in each data set and to reduce at the same time omission and aliasing errors, cf. Fig. 4.4.

Table 4.7: Selection of adapted basis functions $\tilde{b}_q = \tilde{b}(\boldsymbol{x}, \boldsymbol{x}_q)$ for formulating observation equations in the analysis of gravity functionals $\mathcal{Y}[\tilde{V}]$, observed at locations $\boldsymbol{x} = \boldsymbol{x}^p$, and for formulating modeling equations in the synthesis at different locations $\boldsymbol{x} = \boldsymbol{x}^c$. The vertical arrangement follows the spectral resolution of the observation techniques from low- up to high-resolution.

observation technique	**functional** $\mathcal{Y}[\tilde{V}]$		**adapted basis function** $\tilde{b}_q$
GRACE	ΔV	Eq. (2.61)	$\tilde{b}(\boldsymbol{x}^i, \boldsymbol{x}^{ii}, \boldsymbol{x}_q) = \sum_{l=0}^{L} \frac{2l+1}{4\pi R^2} \left[\left(\frac{R}{r^i}\right)^{l+1} B_l \; P_l(\cos\psi_q^i) - \left(\frac{R}{r^{ii}}\right)^{l+1} B_l \; P_l(\cos\psi_q^{ii}) \right]$
GOCE	V_{xx}	Eq. (2.74)	$\tilde{b}(\boldsymbol{x}, \boldsymbol{x}_q) = \sum_{l=0}^{L} \frac{2l+1}{4\pi R^2} \left(\frac{R}{r}\right)^{l+1} B_l \left(\frac{-l+1}{r^2} P_l(\cos\psi_q) + \frac{1}{r^2} \frac{\partial^2 P_l(\cos\psi_q)}{\partial \vartheta^2} \right)$
	V_{xy}	Eq. (2.75)	$\tilde{b}(\boldsymbol{x}, \boldsymbol{x}_q) = \sum_{l=0}^{L} \frac{2l+1}{4\pi R^2} \left(\frac{R}{r}\right)^{l+1} B_l \left(\frac{1}{r^2 \sin\vartheta} \frac{\partial P_l(\cos\psi_q)}{\partial \vartheta} - \frac{\cos\vartheta}{r^2 \sin^2\vartheta} \frac{\partial P_l(\cos\psi_q)}{\partial \lambda} \right)$
	V_{xz}	Eq. (2.76)	$\tilde{b}(\boldsymbol{x}, \boldsymbol{x}_q) = \sum_{l=0}^{L} \frac{2l+1}{4\pi R^2} \left(\frac{R}{r}\right)^{l+1} B_l \left(\frac{1}{r^2} \frac{\partial P_l(\cos\psi_q)}{\partial \vartheta} + \frac{l+1}{r^2} \frac{\partial P_l(\cos\psi_q)}{\partial \vartheta} \right)$
	V_{yy}	Eq. (2.77)	$\tilde{b}(\boldsymbol{x}, \boldsymbol{x}_q) = \sum_{l=0}^{L} \frac{2l+1}{4\pi R^2} \left(\frac{R}{r}\right)^{l+1} B_l \left(\frac{-l+1}{r^2} P_l(\cos\psi_q) + \frac{1}{r^2 \tan\vartheta} \frac{\partial P_l(\cos\psi_q)}{\partial \vartheta} + \frac{1}{r^2 \sin^2\vartheta} \frac{\partial P_l(\cos\psi_q)}{\partial \lambda} \right)$
	V_{yz}	Eq. (2.78)	$\tilde{b}(\boldsymbol{x}, \boldsymbol{x}_q) = \sum_{l=0}^{L} \frac{2l+1}{4\pi R^2} \left(\frac{R}{r}\right)^{l+1} B_l \left(\frac{1}{r^2 \sin\vartheta} \frac{\partial P_l(\cos\psi_q)}{\partial \lambda} + \frac{l+1}{r^2 \sin\vartheta} \frac{\partial P_l(\cos\psi_q)}{\partial \lambda} \right)$
	V_{zz}	Eq. (2.79)	$\tilde{b}(\boldsymbol{x}, \boldsymbol{x}_q) = \sum_{l=0}^{L} \frac{2l+1}{4\pi R^2} \left(\frac{R}{r}\right)^{l+1} B_l \; P_l(\cos\psi_q) \frac{(l+1)(l+2)}{r^2}$
altimetry	T	Eq. (3.14)	$\tilde{b}(\boldsymbol{x}, \boldsymbol{x}_q) = \sum_{l=0}^{L} \frac{2l+1}{4\pi R^2} \left(\frac{R}{r}\right)^{l+1} B_l \; P_l(\cos\psi_q)$
ship-/air-borne and terrestrial gravimetry	Δg	Eq. (2.69)	$\tilde{b}(\boldsymbol{x}, \boldsymbol{x}_q) = \sum_{l=0}^{L} \frac{2l+1}{4\pi R^2} \frac{l-1}{r} \left(\frac{R}{r}\right)^{l+1} B_l \; P_l(\cos\psi_q)$
	δg	Eq. (2.66)	$\tilde{b}(\boldsymbol{x}, \boldsymbol{x}_q) = \sum_{l=0}^{L} \frac{2l+1}{4\pi R^2} \frac{1-l}{r} \left(\frac{R}{r}\right)^{l+1} B_l \; P_l(\cos\psi_q)$

4.3.1 Definition of spectral and spatial resolution

The measurement techniques as introduced in Chapter 3, deliver heterogeneous gravitational functionals in space and time, defining spatial and spectral **measurement resolution**. As the SBFs $\tilde{b}(\boldsymbol{x}, \boldsymbol{x}_q)$ from Tab. 4.6, based on Legendre Polynomials $P_l(\cos\psi_q)$, cf. Eq. (2.30), are centered in $P_q \in \Omega_R$, their spatial influence depends on the spherical distance angle ψ_q between $\boldsymbol{x}_q$ and the observation site P with $\boldsymbol{x} = \boldsymbol{x}^p$. Hence, the arrangement on the sphere Ω_R is related to the spatial resolution of the observations. This aspect is be discussed in Sec. 5.1.2.

The maximum degree L of the series expansion (4.14) indicates the **modeling resolution** of a signal both in the frequency, and in the spatial domain. The corresponding **spatial resolution** ρ_L is given as

$$\rho_L = \frac{\pi r}{L} \tag{4.20}$$

(*Kern*, 2003, p. 105), with $r = R$ denoting the radius of the sphere Ω_R. The spectral modeling resolution can be analogously expressed by means of the wavelength λ_L, i. e.

$$\lambda_L = \frac{2\pi r}{L} \quad \text{or} \quad \frac{\lambda_L}{2} = \frac{\pi r}{L} = \rho_L \tag{4.21}$$

(*Gerlach*, 2003, p. 51). According to the Nyquist theorem, a bandlimited signal with highest frequency f_L thus can only be reconstructed by a function with maximum wavelength $\lambda_L/2$. The referring maximum spatial resolution $\rho_{\max,L}$ reads

$$\rho_{\max,L} \leq \frac{\pi r}{L}, \tag{4.22}$$

cf. *Lieb et al.* (2016).

4.3.2 Discretization of the frequency spectrum

In order to consistently combine data from different observation techniques the frequency domain is discretized, and the observation techniques accordingly classified w.r.t. their spectral resolution. Therefore, resolution levels $j \in \mathbb{N}_0$ defining frequency bands and collecting a specific number of degree values, are introduced. The upper boundary of each level j is classified by a level-depending maximum degree

$$l_j = \left\lceil o^j - 1 \right\rceil , \tag{4.23}$$

with base $o \in \mathbb{R}^+$, defining the bandwidth (in terms of degrees l) of each level (*Schmidt et al.*, 2007). Typically $o = 2$ is used (*Freeden*, 1999, p. 162), so that Eq. (4.23) becomes

$$l_j = 2^j - 1 . \tag{4.24}$$

The adaptation of the resolution levels by a base $o \neq 2$ increases the flexibility of the approach, see studies in *Schmidt et al.* (2007). In this work, all further derivations are related to the frequency discretization with base $o = 2$. The corresponding **resolution levels**

$$j = \left\lfloor \log_2 \left(l_j + 1 \right) \right\rfloor . \tag{4.25}$$

are appropriate for the classification and combination of the different observation techniques – both in space and in frequency domain, compromising a balanced number of resolution levels: The higher the level, the wider is the bandwidth in terms of degrees l, and the finer is the discretization of the spatial domain.
Three observation groups (high-, mid-, and low-resolution) are classified in the following, based on the underlying measurement principles, which have been presented in detail in Chapter 3. Hereby, the maximum spectral resolution of an observed signal, defines the maximum degree L of the series expansion (4.14). In analogy to L, a maximum level J can be defined with upper spectral boundary $l_J \leq L$.
Table 4.8 shows the classification of the different observation techniques w.r.t. resolution level j depending on their spatial ρ_L (4.20) resolution. Referring to Eq. (4.22), $\rho_{\max,j}$ is the corresponding maximum spatial resolution for one level j

$$\rho_{\max,j} = \frac{\pi R}{l_j} , \tag{4.26}$$

with the mean radius $R = 6\,378\,137$ m of the sphere Ω_R, representing the Earth's surface.

Table 4.8: Extraction of the frequency domain which is split into several resolution levels j. Each level is related to a maximum degree l_j of a series expansion and a maximum spatial resolution $\rho_{\max,j}$. The different observation techniques are classified by their resolution: low (satellite gravimetry data in yellow) – medium (altimetry in green) – high (air-/shipborne and terrestrial gravimetry in orange).

j	1	2	3	4	5	6	7	8	9	10	11	12	...
l_j [deg]	1	3	7	15	31	63	127	255	511	1023	2047	4095	...
$\rho_{max,j}$ [km]	20000	6667	2857	1333	645	317	157	78	39	20	10	5	...
			satellite gravimetry										
					altimetry								
								terrestrial, air-/shipborne gravimetry					
resolution →													

4.3.3 Multi-resolution (de)composition

The gravitational structure of the Earth's surface is detected by several observation types, as schematically displayed in Fig. 1.1. The "model" component will be discussed in the sequel in more detail, using the advantageous principle of MRR. Figure 4.5 gives a more detailed insight in the third part of Fig. 1.1. It comprises

(a) spectrally splitting the frequency domain into long-, medium-, short-wavelength parts by levels j,

(b) classifying data sets according to their low, medium, or high (spectral/spatial) resolution,

(c) applying SBFs as low- and band-pass filters by setting a specific, level-depending number of Legendre coefficients different from zero,

(d) summing up the detail signals.

Following Fig. 4.5, those steps are explained by introducing the mathematical relations and specific settings of the MRR (de)composition in this work, using Shannon functions. Main focus is on step (c). The methodical implementation is presented in Sec. 5.3, and the numerical application to real data in Chapter 6.

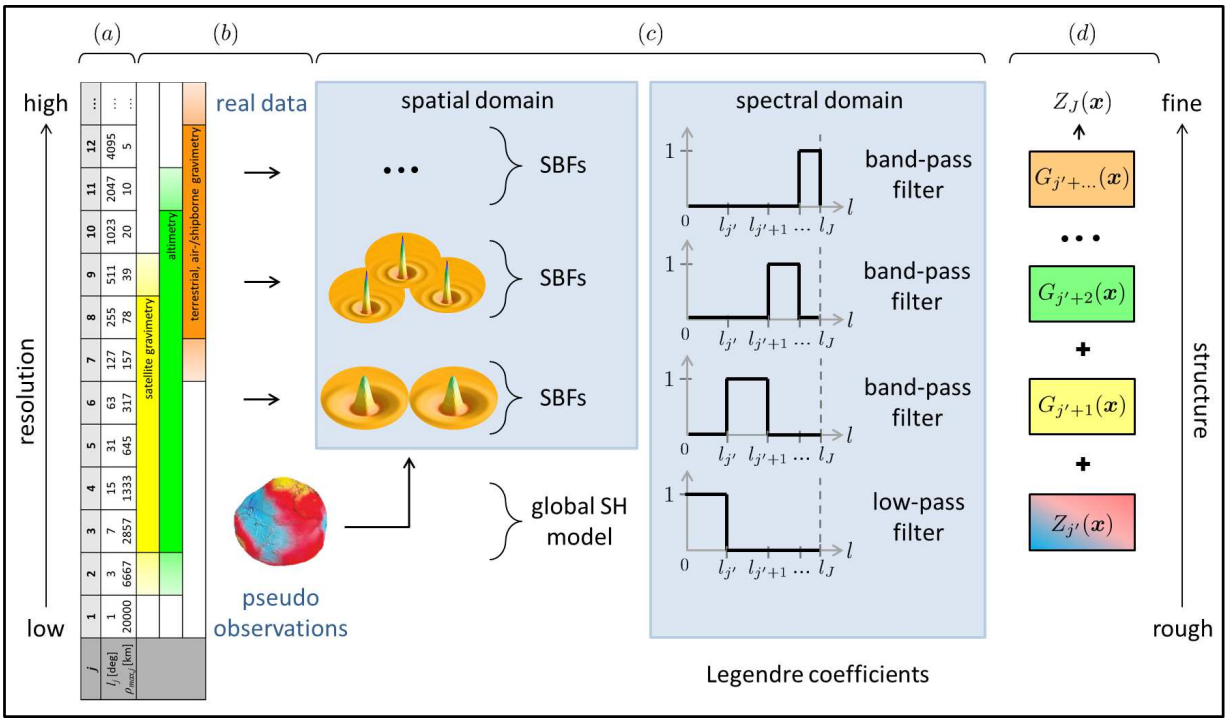

Figure 4.5: Implementation and application of multi-resolution representation within the regional gravity modeling approach using SBFs. The implementation of the spectral filtering (c) is visualized in spatial and spectral domain (light blue shaded) and is mainly discussed in this section.

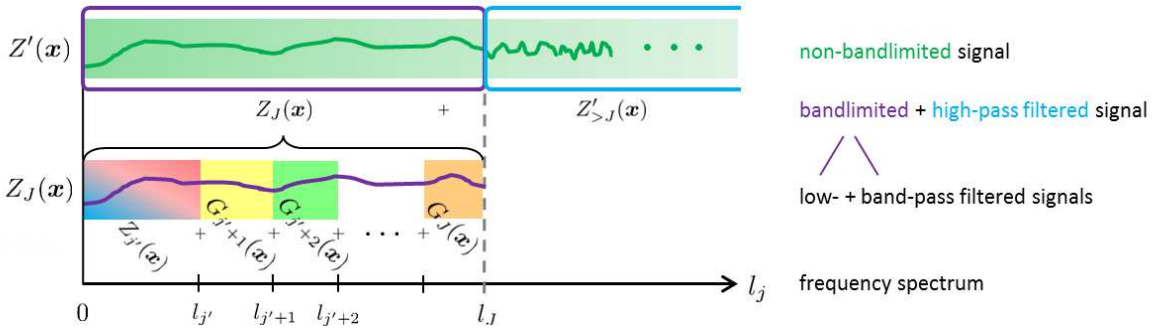

Figure 4.6: Spectral splitting of a non-bandlimited signal $Z'(\boldsymbol{x})$ (green) into a bandlimited, low-pass filtered signal $Z_J(\boldsymbol{x})$ (purple) and a high-pass filtered signal $Z'_{<J}$ (blue) in the frame of a MRR up to maximum level J. $Z_J(\boldsymbol{x})$ further is split into a low-resolution component $Z_{j'}(\boldsymbol{x})$ and several medium- and high-resolution detail signals G_j.

In order to apply a multi-resolution representation, the frequency domain is split into several spectral bands, cf. step (a) in Fig. 4.5. According to *Lieb et al.* (2016), this is done in terms of the level-depending fragmentation,

presented in Tab. 5.5. By collecting several degrees l in one **resolution level** j, Eq. (4.25), a flexible spectral modeling of any bandlimited signal $g = Z(\boldsymbol{x}) = Z_J(\boldsymbol{x})$ up to maximum resolution level J is feasible. In terms of the above introduced Shannon kernel, the signal

$$\underbrace{Z_J(\boldsymbol{x})}_{\substack{\text{bandlimited,}\\ \text{low-/ band-pass filtered}\\ \text{signal}}} = \underbrace{Z'(\boldsymbol{x})}_{\substack{\text{non-bandlimited}\\ \text{signal}}} - \underbrace{Z'_{>J}(\boldsymbol{x})}_{\substack{\text{high-pass filtered}\\ \text{signal}}}, \tag{4.27}$$

contains full information up to the level-depending degree l_J. The neglected high-resolution part $Z'_{>J}$ comprises the spectral domain of degree $l > l_J$ (respectively of level $j > J$). The spectral splitting is visualized in Fig. 4.6, referring to Fig. 4.4: The non-bandlimited signal $f = Z'(\boldsymbol{x})$ (green) is represented by the sum of the bandlimited signal $g = Z_J(\boldsymbol{x})$ (purple) up to maximum resolution level J, and the high-resolution part $Z'_{>J}(\boldsymbol{x})$ (blue). $Z_J(\boldsymbol{x})$ further can be split into a low-resolution component $Z_{j'}(\boldsymbol{x})$ (blue-red) up to a minimum level j' (degree $l_{j'}$), and several bandlimited detail signals, i. e. $G_{j'+1}(\boldsymbol{x})$ (yellow) up to level $j'+1$ (degree $l_{j'+1}$), $G_{j'+2}(\boldsymbol{x})$ (green) up to level $j'+2$ (degree $l_{j'+2}$), ..., up to $G_J(\boldsymbol{x})$ (orange) up to level J (degree l_J). The colors refer to the classification of observation types in Fig. 5.5 according to their spectral sensitivity and, thus, to their expected contribution to the detail signals $G_j(\boldsymbol{x})$ in Fig. 4.5. The here presented approach comprises regionally modeling the spectral domain of degree $l = l_{j'}+1, \ldots, l_J$; the low-resolution part stems from an existing global SH model, which further is introduced as prior information (pseudo observations, blue-red colored in Fig. 4.5).
In the sequel (see Sec. 4.3.5), the spectral splitting of a gravitational signal $g(\boldsymbol{x})$ will be realized by band-pass filtering in terms of SBFs, as indicated in Fig. 4.5 (c). Within the modeling procedure, then two strategies are distinguished, cf. Fig. 4.7: the composition and the decomposition of $Z_J(\boldsymbol{x})$ up to, or down from a maximum level J.

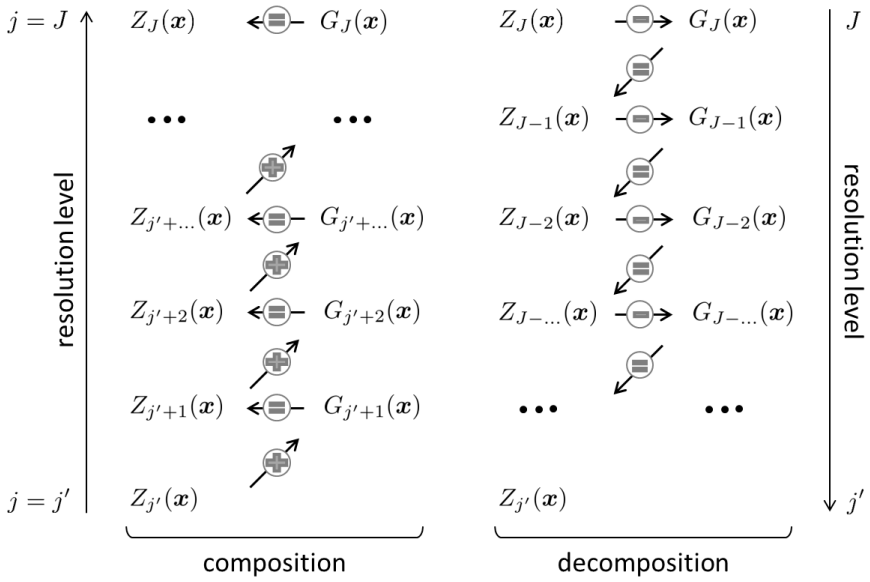

Figure 4.7: Multi-resolution (de)composition as bottom-up (left) and top-down (right) approach.

MRR composition The composition (Fig. 4.7, left side) starts from a low-resolution signal $Z_{j'}(\boldsymbol{x})$ containing information up to level j' (in the following the minimum level j' of the MRR), adding a number of $J - j'$ detail signals $G_j(\boldsymbol{x})$, each representing one after another frequency band, i. e. level j, up to the total signal $Z_J(\boldsymbol{x})$. This **bottom-up** approach enables to react flexibly on any kind of data set by combining them in an optimal sense, i. e. introducing them level by level where they contain maximum spectral information.

MRR decomposition The decomposition (Fig. 4.7, right side), vice versa, starts from the high-resolution signal $Z_J(\boldsymbol{x})$ and sequently splits it in $J - j'$ single detail signals $G_j(\boldsymbol{x})$ down to the smoothed

representation $Z_{j'}(\boldsymbol{x})$, by means of levels j. This **top-down** approach allows to study a given signal in different frequency domains.

The fundamental equation of a MRR (de)composition yields

$$Z_J(\boldsymbol{x}) = Z_{j'}(\boldsymbol{x}) + \sum_{j=j'+1}^{J} G_j(\boldsymbol{x})\,. \tag{4.28}$$

SBFs (4.5) are hereby suitable functions in order to extract specific frequency domains from both, measured signals, cf. step (c) in Fig. 4.5, setting up the bottom-up composition, as well as from modeled signals applying the top-down decomposition. The spherical convolution of a harmonic function f with a bandlimiting SBF, cf. Eq. (4.7), representing a weighting operator (*Driscoll and Healy*, 1994), allows to filter a signal $Z_J(\boldsymbol{x})$ in the spectral domain (*Schmidt et al.*, 2007). This property is of great importance for the MRR. The composition is focused in this work for the spectral combination of real data; however, the decomposition is also applied to resulting models in Sec. 6.2.

4.3.4 Types of bandlimiting SBFs

Among the basis functions in general, the SBFs themselves constitute a large range of different types. On the one hand, the variety enables a high flexibility of establishing a regional gravity modeling approach, but on the other hand, suitable types for appropriate need should be selected very carefully, as the choice has a large influence on the modeled results. A numerical example is given in Sec. 6.1.1. *Freeden* (1999) presents e. g. a large variety of SBFs; *Bentel et al.* (2013a) studied many properties for their applicability in regional gravity modeling. Based on these findings, three examples with focus on their spectral and spatial characteristics are presented in the following: Shannon, Blackman, Cubic Polynomial.

According to Fig. 1.2, a perfect localization of basis functions both in the spatial and in the spectral domain is not possible. In Fig. 4.8, the here presented SBFs, Shannon, Blackman and Cubic Polynomial, are arranged relatively to each other w.r.t. their spectral and spatial localization properties. They are all exactly bandlimiting, but whereas the CuP function is more localizing in the spatial domain at the expense of losing information in the spectral domain, the Shannon function is more localizing in the spectral domain at the expense of scattering information in the spatial domain. Blackman compromises spectral and spatial localization. For several exemplarily chosen resolution levels j, the (a) Shannon, (b) Blackman, and (c) Cubic Polynomial scaling functions and their referring scaling coefficients (e), (f), (g), are shown in Fig. 4.9.

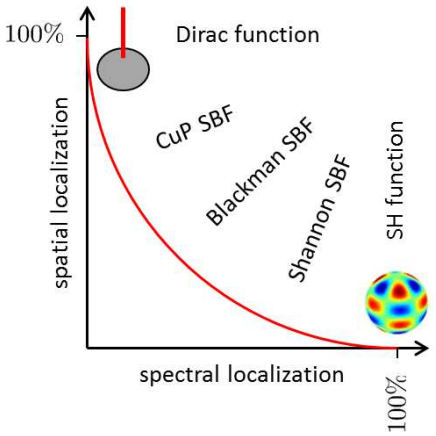

Figure 4.8: Schematic arrangement of SBFs w.r.t. their spectral and spatial localization property.

Shannon

The Shannon function represents the bandlimited version of the Abel-Poisson kernel, Eq. (4.3). The Legendre coefficients B_l of the Shannon (Sha) SBF are defined as

$$B_l = \left\{ \begin{array}{ll} 1 & \text{for} \quad l = 0, \ldots, 2^j - 1 \\ 0 & \text{for} \quad l \geq 2^j \end{array} \right\} =: \phi_{l,j}^{\text{Sha}}\,. \tag{4.29}$$

The higher the level j, the sharper is the peak in the spatial domain, cf. Fig. 4.9 a), and the wider the frequency spectrum of coefficients, cf. Fig. 4.10 d). The general features – independent of j – are:

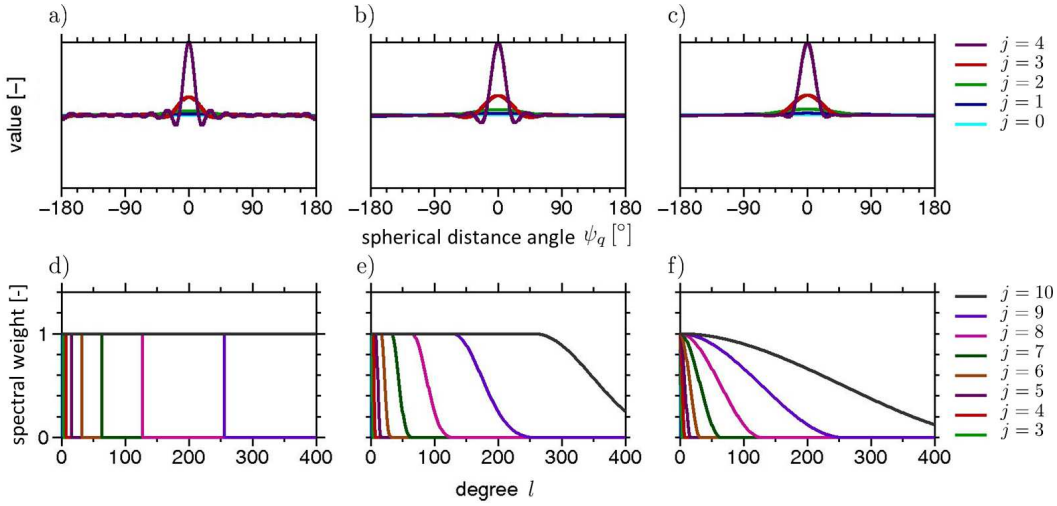

Figure 4.9: Different types of scaling functions in the spatial domain (one-dimensional w.r.t. spherical distance angle ψ_q): (a) Shannon, (b) Blackman, (c) Cubic Polynomial, and referring scaling coefficients (d), (e), (f) in the spectral domain, for several exemplarily chosen resolution levels j.

	spatial domain		spectral domain
(+)	sharp peak, but	(+)	step function, i. e.
(–)	strong sidelobes (oscillations),		exactly band limitation at highest degree $l_j = 2^j - 1$ of each level,
(–)	less localization;	(+)	relation to SHs possible.

A for this work very relevant positive (+) feature of the Shannon function is the exact band limitation without loosing any spectral information, i. e. representing an optimal low-pass filter in the frequency domain. This is of particular importance for setting up a MRR in terms of SBFs, i. e. extracting specific frequency domains. As presented in Tab. 4.2, SBFs and SHs can be related in case of setting $B_l = 1$, i. e. in case of Shannon functions. However, the sharpness in the spectral domain causes sidelobes with large amplitudes, i. e. obvious uncertainties in the spatial domain, a quite negative (–) aspect.

Blackman

In contrast to Shannon, the Blackman function acts as low-pass filter with a certain smoothing decay. The Legendre coefficients B_l of the Blackman (Bla) SBF are defined as

$$B_l = \left\{ \begin{array}{ll} 1 & \text{for} \quad l = 0, \ldots, 2^{j-1} - 1 \\ A_j(l) & \text{for} \quad l = 2^{j-1}, \ldots, 2^j - 1 \\ 0 & \text{for} \quad l \geq 2^j \end{array} \right\} =: \phi_{l,j}^{\mathrm{Bla}} , \tag{4.30}$$

The function is based on the Blackman window with

$$A_{l'}(l) = \frac{21}{50} - \frac{1}{2} \cos\left(\frac{2\pi l}{l'+1}\right) + \frac{2}{25} \cos\left(\frac{4\pi l}{l'+1}\right) ,$$

which is often used in classical signal analysis (*Schmidt et al.*, 2007). Figures 4.9 b) and e) show the characteristics in the spectral and spatial domain. Compared with the features from Figs. 4.9 a) and d), it yields:

	spatial domain		spectral domain
(+)	less oscillations than Shannon and, thus,	(+)	exactly band limitation at degree l_j, but
(+)	more localization, i. e. more quasi-compact support;	(–)	smoothing decay within spectral domain $l = 2^{j-1}, \ldots, 2^j - 1$.

The decay behavior of the Legendre coefficients in the spectral domain yields a low-pass filtering SBF, smoothing the high frequencies of the function to be represented. In spite of this unfavorable aspect, the big

advantage is the significant reduction of oscillations in the spatial domain. The Blackman function is , thus, a good compromise between a smoothing function in the spectral and an oscillating function in the spatial domain.

Cubic Polynomial

An even stronger spectral smoothing behavior shows the Cubic Polynomial (CuP) function. The Legendre coefficients B_l are defined as

$$B_l = \left\{ \begin{array}{ll} \left(1 - 2^{-j}l\right)^2 \left(1 + 2^{-j+1}l\right) & \text{for} \quad l = 0, ..., 2^j - 1 \\ 0 & \text{for} \quad l \geq 2^j \end{array} \right\} =: \phi_{l,j}^{\text{CuP}} \,, \tag{4.31}$$

The according characteristics in the spectral and spatial domain can be seen in Fig.s 4.9 c) and f). In comparison to Figs. 4.9 a), b) and d), e) the main features are:

	spatial domain		spectral domain
(+)	weak oscillations,	(+)	exactly bandlimiting at degree l_j, but
(+)	strongest localization, i. e.	(–)	strong smoothing decay
	highest quasi-compact support		at degrees $l = 2, ..., 2^j - 1$

The Legendre coefficients immediately decline for degree $l > 1$, independent of the bandlimiting degree l_J. Consequently, the spectral information is strongly low-pass filtered. Although the oscillations almost disappear in the spatial domain, the CuP function extracts much less spectral information compared with the Blackman or Shannon SBF.

4.3.5 Spectral filtering by scaling and wavelet functions

Referring to the classification of data sets, i. e. real data and pseudo observations in terms of global SH models, cf. step (b) in Fig. 4.5, the low-resolution signal $Z_{j'}(\boldsymbol{x})$ is obtained from low-resolution data, while the detail signals $G_j(\boldsymbol{x})$ are derived from medium- and high-resolution data.
Step (c), thus, has to comprise not only

- a spectral filtering component (for each single data set: discussed in this section), but also
- a transformation component (for each single data set: adapting SBFs to the different observed gravitational functionals, applying the relations from Tab. 4.7), and
- a relative weighting component (for combining several heterogeneous data sets, i. e. selecting the data at each level according to their spectral content by variance component estimation within the estimation model, which is presented in Sec. 5.2).

Low-pass filtering

As summarized in Tab. 4.4, the spherical convolution of a non-bandlimiting function f with a bandlimiting SBF $b(\boldsymbol{x}, \boldsymbol{x}_q)$ acting as low-pass filter up to degree l' results in a low-pass filtered function g. In analogy to Eq. (4.15), any bandlimited signal $Z_j(\boldsymbol{x})$ with spectral information up to level j, can be obtained from the non-bandlimited signal Z' by

$$Z_j = Z_j(\boldsymbol{x}) = (\Phi_{q,j} * Z')_{\Omega_R}(\boldsymbol{x}) = \sum_{q=1}^{Q_j} d_{q,j} \Phi_j(\boldsymbol{x}, \boldsymbol{x}_q) \,. \tag{4.32}$$

The low-pass filtering (spherical) scaling functions $\Phi_{q,j}$, centered at positions $\boldsymbol{x}_q \in \Omega_R$, and depending on level j, read

$$\Phi_{q,j} = \Phi_j(\boldsymbol{x}, \boldsymbol{x}_q) = \sum_{l=0}^{l_j} \frac{2l+1}{4\pi R^2} \left(\frac{R}{r}\right)^{l+1} \phi_{l,j} \; P_l(\boldsymbol{r}^T \boldsymbol{r}_q) \,, \tag{4.33}$$

cf. Eq. (4.14). The degree-l-depending Legendre coefficients become $B_l = \phi_{l,j} \in \left\{\phi_{l,j}^{\mathrm{Sha}}, \phi_{l,j}^{\mathrm{Bla}}, \phi_{l,j}^{\mathrm{CuP}}\right\}$ (*Schmidt et al.*, 2007) and vanish for $l > l_j$. At the upper boundary of each resolution level j, defined by the bandlimiting spectral degree $l' = l_j$ according to Eq. (4.24), the Legendre coefficients $\phi_{l,j}$ decrease down to zero. Hereby, the values characterize the spectral weights, i. e. they define a low-pass filter. As discussed in Sec. 4.3.4, the Shannon type declines abruptly from one to zero at degree l_j, while Blackman features a smoothing character within the spectral domain $l_{j-1}, ..., l_j$, and Cubic Polynomials over the whole bandwidth. The maximum degree l_j further defines the number Q_j of terms of the series expansion up to level j. In analogy to Eq. (4.10), an admissible point system $S_{Q_j} = \left\{\boldsymbol{x}_q \in \Omega_R | q = 1, 2, ..., Q_j\right\}$ has to be chosen by $Q_j \geq (l_j + 1)^2$ basis functions $\Phi_j(\boldsymbol{x}, \boldsymbol{x}_q) \in H_{0,...,l_j}$ with dimension $N_{l_j} = (l_j + 1)^2$, cf. Eq. (4.13). Corresponding to the series expansion (4.15) of the bandlimited signal g, the series of Z_j reads

$$Z_j = Z_j(\boldsymbol{x}) = \sum_{q=1}^{Q_j} d_{q,j}\, \Phi_j(\boldsymbol{x}, \boldsymbol{x}_q) = \sum_{q=1}^{Q_j} d_{q,j} \sum_{l=0}^{L_j} \frac{2l+1}{4\pi R^2} \left(\frac{R}{r}\right)^{l+1} \phi_{l,j}\, P_l(\boldsymbol{r}^T \boldsymbol{r}_q)\,, \tag{4.34}$$

with $L_j = l_j$.

Band-pass filtering

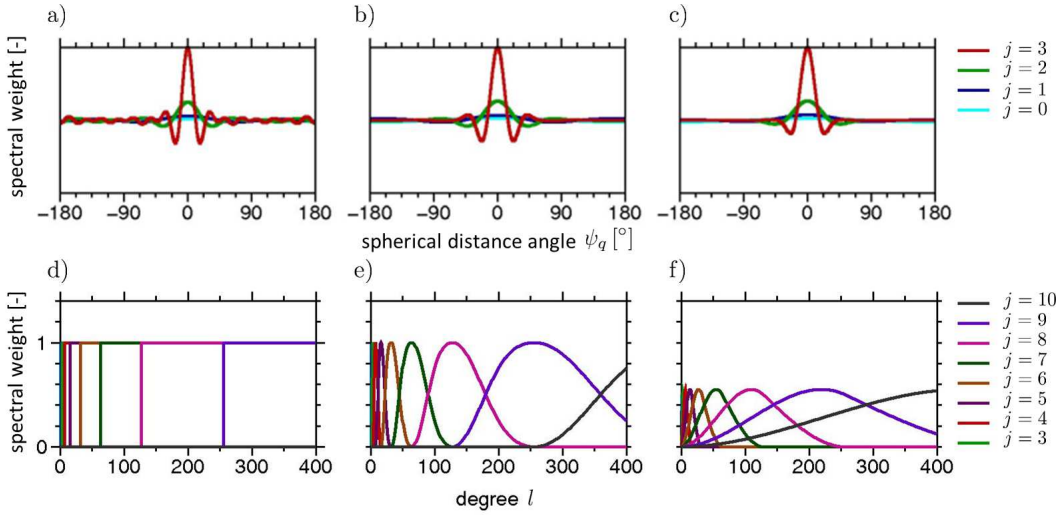

Figure 4.10: Different types of wavelet functions in the spatial domain (one-dimensional w.r.t. spherical distance angle ψ_q): (a) Shannon, (b) Blackman, (c) Cubic Polynomial, and referring wavelet coefficients (d), (e), (f) in the spectral domain, for several exemplarily chosen resolution levels j. Note, the colors in Fig. 4.9 refer to different levels.

In order to extract single frequency bands j, i. e. splitting $Z_j(\boldsymbol{x})$ in several detail signals $G_j(\boldsymbol{x})$, the SBFs are applied as band-pass filters. Following *Schmidt et al.* (2007), band-pass filters are generated by subtracting the Legendre coefficients of two low-pass filtering SBFs. For neighboring levels j and $j - 1$, the differential Legendre coefficients yield

$$\psi_{l,j} = \phi_{l,j} - \phi_{l,j-1}\,. \tag{4.35}$$

In analogy to Fig. 4.9, the wavelet functions and their wavelet coefficients are presented in Fig. 4.10 for the types (a, d) Shannon, (b, e) Blackman, and (c, f) Cubic Polynomial in the (a – c) spatial and (d – f) spectral domain. Note, the colors of scaling and wavelet functions (respectively coefficients) refer to different levels in both Figs. 4.9 and 4.10. The differences of Legendre coefficients, cf. Eq. (4.35), then read

$$\psi_{l,j}^{\mathrm{Sha}} = \phi_{l,j}^{\mathrm{Sha}} - \phi_{l,j-1}^{\mathrm{Sha}} \tag{4.36}$$

$$\psi_{l,j}^{\mathrm{Bla}} = \phi_{l,j}^{\mathrm{Bla}} - \phi_{l,j-1}^{\mathrm{Bla}} \tag{4.37}$$

$$\psi_{l,j}^{\mathrm{CuP}} = \phi_{l,j}^{\mathrm{CuP}} - \phi_{l,j-1}^{\mathrm{CuP}} \tag{4.38}$$

for the specific cases of Shannon, Blackman and Cubic Polynomial, cf. Eqs. (4.29) to (4.31). As discussed above, the Shannon wavelet ranges in the spectral domain the full bandwidth $l_{j-1}+1, ..., l_j$ of one resolution level j without any smoothing behavior. Consequently, the frequency bands and, thus, the corresponding detail signals G_j, cf. Eq. (4.40), (1) do not overlap in the spectral domain, and (2) contain full spectral information. These beneficial properties are used in this work for (de)composing the multi-resolution signals.
In contrast, the bandwidth which is extracted by a Blackman band-pass filter, cf. Fig. 4.10 b) and e), comprises the spectral domain $l_{j-2}+1, ..., l_j$ of two levels, i. e. j and $j-1$. The spectral weight, defined by the coefficients (e), increases from $l_{j-2}+1$ to l_{j-1}, and decreases from $l_{j-1}+1$ to l_j. Each frequency band has an overlap with the lower and the upper one. Hence, the referring detail signals are not independent of each other.
The coefficients of Cubic Polynomial wavelets, cf. Fig. 4.10 f), show the strongest smoothing behavior of the three examples, with increasing spectral weights from $l > 0$ to l_{j-1}, and decreasing values from $l_{j-1}+1$ to l_j. All spectral bands overlap and the spectral information of the detail signals is not uniquely separated.
Inserting Eq. (4.35) in Eq. (4.33), results in the band-pass filtering (spherical) wavelet function

$$\Psi_{q,j} = \Psi_j(\boldsymbol{x}, \boldsymbol{x}_q) = \sum_{l=0}^{l_j} \frac{2l+1}{4\pi R^2} \left(\frac{R}{r}\right)^{l+1} \psi_{l,j}\, P_l(\boldsymbol{r}^T \boldsymbol{r}_q)\ . \tag{4.39}$$

According to Eq. (4.32), the detail signal G_j is obtained from the spherical convolution

$$G_j = G_j(\boldsymbol{x}) = (\Psi_{q,j} * Z')_{\Omega_R}(\boldsymbol{x}) = \sum_{q=1}^{Q_j} d_{q,j} \Psi_j(\boldsymbol{x}, \boldsymbol{x}_q)\,, \tag{4.40}$$

and according to Eq. (4.34), the series expansion in terms of wavelet functions $\Psi_{q,j}$ reads

$$G_j = G_j(\boldsymbol{x}) = \sum_{q=1}^{Q_j} d_{q,j} \sum_{l=0}^{L_j} \frac{2l+1}{4\pi R^2} \left(\frac{R}{r}\right)^{l+1} \psi_{l,j}\, P_l(\boldsymbol{r}^T \boldsymbol{r}_q)\ . \tag{4.41}$$

Hereby, the scaling coefficients $d_{q,j}$ from the series expansion (4.32), can be inserted in Eq. (4.41) referring to the statement from Eq. (4.11). The number Q_j of terms of the series expansion (4.40), expressing a band-pass filtered detail signal G_j in terms of wavelet functions, corresponds to the number of terms in the series expansion (4.32), expressing a low-pass filtered signal Z_j up to the same resolution level j in terms of scaling functions. In both linear combinations (4.32), and (4.40), an identical admissible point system $S_{Q_j} = \left\{\boldsymbol{x}_q \in \Omega_R | q = 1, 2, ..., Q_j\right\}$ has to be chosen w.r.t. level j, and the same number $Q_j \geq N_{l_j}$ of scaling coefficients $d_{q,j}$ has to be determined.
The number Q_{j-1} of the next lower level decreases by the power of 2, cf. Eq. (4.24). *Freeden* (1999), pp. 219, show, that coefficients $d_{q,j}$ and $d_{q,j-1}$ of neighboring levels depend linearly on each other, and can be successively computed. This feature is of great importance for setting up a **pyramid algorithm**. The key benefits are (1) the down-sampling of the number of scaling coefficients from level to level in a top-down MRR, and thus the reduction of parameters to be estimated (saving numerical and time-intensive computational expense), and (2) the connection of the detail signals by relating spectral and covariance information from higher and lower levels. The pyramid algorithm is not part of this work. However, the principle of MRR is presented and applied, delivering the fundamentals for connecting the resolutions levels in future work.

High-pass filtering

The naturally non-bandlimited signal Z' can be reproduced by spherical convolution

$$Z' = Z'(\boldsymbol{x}) = \left(k'_q * Z'\right)_{\Omega_R}(\boldsymbol{x})\,, \tag{4.42}$$

according to Eq. (4.4), with the non-bandlimiting Abel-Poisson kernel k'_q, defined in Eq. (4.3). Z' is low-pass filtered in Eq. (4.32) with scaling function $\Phi_{q,J}$, Eq. (4.33), up to maximum level J. The high-resolution part $Z'_{>J}(\boldsymbol{x})$ from Eq. (4.27), comprising the spectral domain above level J, can be expressed by the difference

$$Z'_{>J}(\boldsymbol{x}) = Z'(\boldsymbol{x}) - Z_J(\boldsymbol{x})$$

$$= \left(k'_q * Z'\right)_{\Omega_R}(\boldsymbol{x}) - \left(\Phi_{q,J} * Z'\right)_{\Omega_R}(\boldsymbol{x})$$
$$= \left((k'_q - \Phi_{q,J}) * Z'\right)_{\Omega_R}(\boldsymbol{x}). \tag{4.43}$$

Factoring out identical terms of the difference $k'_q - \Phi_{q,J}$ yields the differential Legendre coefficients

$$\phi'_{l,>J} = 1 - \phi_{l,J} \tag{4.44}$$

(*Schmidt et al.*, 2005b), since the Legendre coefficients of the Abel-Poisson kernel k'_q read $B_l = 1$, cf. Sec. 4.1.1. For $\lim_{J\to\infty} \phi_{l,J} = 1$ (p. 155 *Freeden*, 1999), the coefficients $\phi'_{l,>J}$ become zero. Inserting Eq. (4.44) in Eq. (4.33) defines the high-pass filtering basis function

$$\Phi'_{q,>J} = \Phi'_{>J}(\boldsymbol{x}, \boldsymbol{x}_q) = \sum_{l=l_J+1}^{\infty} \frac{2l+1}{4\pi R^2} \left(\frac{R}{r}\right)^{l+1} (1 - \phi_{l,J})\, P_l(\boldsymbol{r}^T \boldsymbol{r}_q), \tag{4.45}$$

and finally, inserting Eq. (4.45) in (4.43), describes

$$Z'_{>J} = Z'_{>J}(\boldsymbol{x}) = (\Phi'_{q,>J} * Z')_{\Omega_R}(\boldsymbol{x}). \tag{4.46}$$

As mentioned above, the Legendre coefficients act as spectral weights and describe the magnitude of scaling functions in the spectral domain. Hence, the neglected signal content $> J$, expressed by Eq. (4.46), corresponds to the omission error σ^2_{om} according to Eq. (4.18). In Sec. 4.2.4, the latter was derived from the difference of energy content: For the non-bandlimited signal Z' and the bandlimited signal Z, it yields $E_{Z'} - E_Z$. Consequently, this difference refers to the same spectral domain as the one of the omission error, and the one described by the difference $(1 - \phi_{l,j})$ from Eq. (4.44). Inserting $\phi'_{l,>J} = B_l$, for instance, in Eq. (4.8), yields the set of high-pass filtered SH coefficients $G_{l,m}$. For a known set of SH coefficients $F_{l,m}$, the signal content $> J$, thus, can be expressed in terms of SBFs following the relations from Tab. 4.3.

The composition of diverse spectral domains, extracted by appropriate Legendre coefficients $\phi_{l,j}$ (4.29) – (4.31), $\psi_{l,j}$ (4.35), and $\phi'_{l,>J}$ (4.44), is visualized in Fig. 4.11 exemplarily for the Shannon kernel. $\phi^{\text{Sha}}_{l,j'}$ serve as low-, and $\psi^{\text{Sha}}_{l,j'+1}$, $\psi^{\text{Sha}}_{l,j'+2}, \ldots, \psi^{\text{Sha}}_{l,J}$ as band-pass filtering Legendre coefficients, defining the scaling $\Phi_{l,j'}$ (4.33) and wavelet $\Psi_{l,j'+1}$, $\Psi_{l,j'+2}, \ldots, \Psi_{l,J}$ (4.39) functions. According to Eq. (4.28), the summation of referring bandlimited signals $Z_{j'}$ and G_j yields the signal Z_J, which is equivalently described by the scaling function $\Phi_{q,J}$ with coefficients $\phi^{\text{Sha}}_{l,J}$ (lowest row) in Fig. 4.11. The complementary high-pass filtering function $\Phi'_{q,>J}$, according to Eq. (4.45), is indicated by the differential coefficients $(1 - \phi^{\text{Sha}}_{l,J})$.

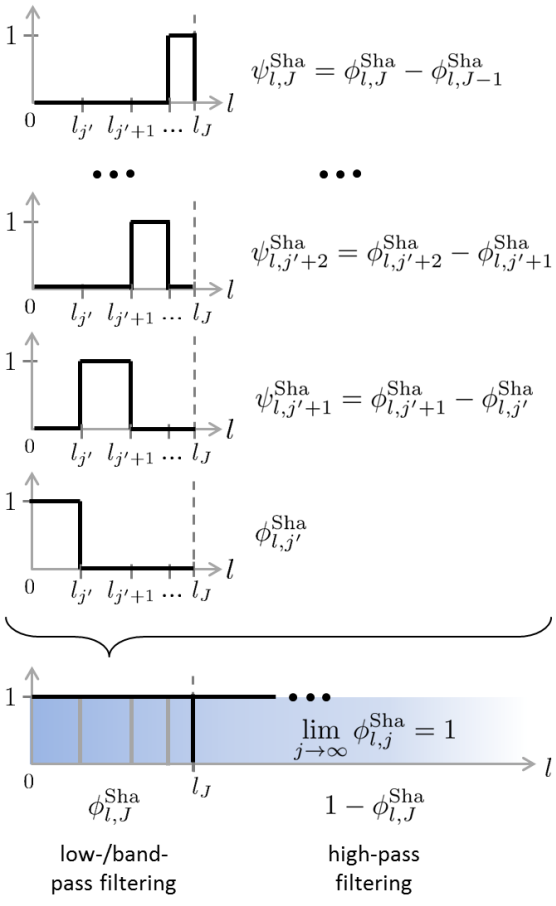

Figure 4.11: Legendre coefficients, exemplarily displayed for the Shannon kernel, acting as low-, band-, and high-pass filter in a MRR. The limit of the coefficients yields 1 (blue shaded) for infinite high spectral resolution.

5 Methodical settings, estimation model and spectral combination

The regional gravity modeling approach via radial basis functions enables an efficient combination of heterogeneous data in selected areas. Main criterion is the availability of high-resolution data. Within the geographical choice, the spectral domain where observations contribute most information shall be exploited as optimally as possible. As the different techniques provide various gravitational functionals, respective observation equations have to be specified.
In the first part of this chapter, the chosen tools and settings of an enhanced regional gravity modeling approach are presented by giving a kind of "recipe" for a reasonable parametrization. Hereby the relations, derived from global gravity field representations in the previous Chapters 2 and 4, are used as fundamental base, and adapted to the data from Chapter 3. Restricting those investigations to regional applications and related difficulties are discussed in detail. In the second part, the estimation model is set up, computing gravitational functionals from a combination of various observations in specified regions at one resolution level. The spectral combination at different resolution levels is presented in the third part within the framework of a MRR.

5.1 Methodical settings

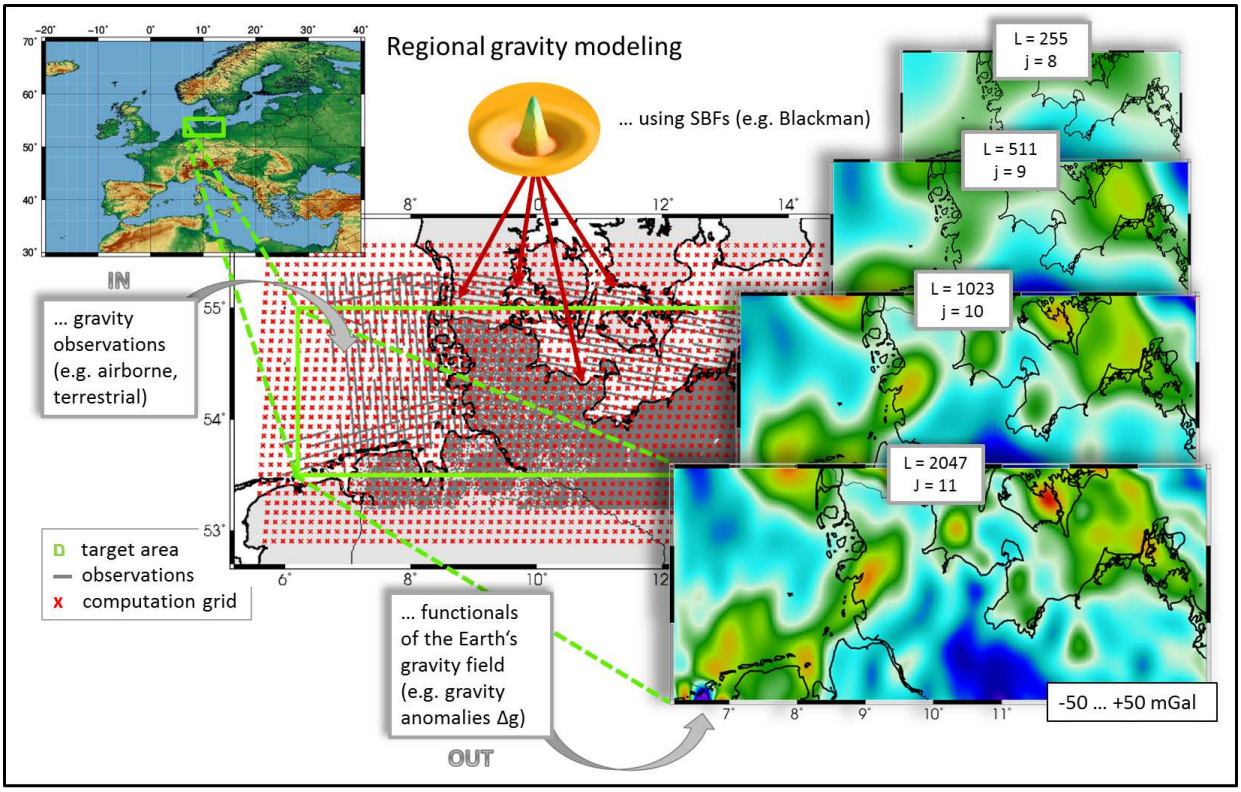

Figure 5.1: Settings of the regional gravity modeling approach.

The settings of the regional gravity modeling approach, established and enhanced within this thesis, are explained by means of Fig. 5.1, following the studies of *Lieb et al.* (2016). Input are the diverse observations,

presented in Sec. 3.3 (here, in Northern Germany). The target area, i. e. the region of interest, is green bordered in the upper left and in the middle of Fig. 5.1. Within this region, the gravity field shall be gained by the regional modeling approach using SBFs (e. g. Blackman functions). They are located at points (red crosses) of an appropriate computation grid, displayed in the middle of Fig. 5.1. Further, the target area is selected corresponding to the spatially limited observations (exemplarily gray colored airborne tracks and terrestrial observation sites). The aim is extracting most information from the data, i. e. fitting them as optimally as possible at different resolution levels. A selection of resulting regional models ($j = 8, \ldots, 11$) is shown in terms of gravity anomalies Δg on the right side. Vice versa to selecting the target area w.r.t. the spatial distribution of available observations, in practice, often the target area is predefined and appropriate data sets have to be collected. This case could be motivated by applications, as e. g. deriving a national height reference within the borderlines of a country.
In the sequel, after globally defining an appropriate computation grid in Sec. 5.1.1, all further methodical settings (Secs. 5.1.2 - 5.1.6) refer explicitly to regional investigations and aim to set up the enhanced regional gravity modeling approach, the core of this thesis.

5.1.1 Computation grid and global rank deficiency

The role of a computation grid (red-marked crosses in the middle part of Fig. 5.1) is to locate the SBFs. As mentioned before, in contrast to SH functions, the two-point functions $b(\boldsymbol{x}, \boldsymbol{x}_q)$, Eq. (4.14), are isotropic and centered in points P_q, with $\boldsymbol{x}_q \in \Omega_R$. For instance, *Freeden et al.* (1998), pp. 171, defined several mathematical grids; *Eicker* (2008), *Wittwer* (2009), *Klees and Haagmanns* (2008) discussed their applicability for locating basis functions in regional gravity modeling.
The main aspects for the choice of the computation grid are

- type: irregular (signal-related) vs. regular, i. e. mathematically described (equidistributed, -angular, Icosahedron, ...),
- admissibility w.r.t. Eq. (4.10),
- resolution: grid spacing (density of grid points), related to model resolution.

Reuter grid

In this work, a globally defined, regular grid, namely the *Reuter* grid (*Reuter*, 1982), is used. The points are equidistributed on Ω_R and, thus, allow a homogeneous coverage of the sphere. *Cui and Freeden* (1995) investigated several equidistributed point grids on a sphere and conclude that none of the types takes an exceptional role. *Bentel et al.* (2013b) showed, that the choice of different grid types influences resulting regional gravity models only marginally, compared with the impact of other parameters, as e. g. the choice of the basis functions. The number $N_L^{\max}$ of points is regulated by the control parameter γ_L, in this work depending on maximum degree L, namely

$$N_L^{\max} = 2 + \frac{4}{\pi}\gamma_L^2 \ . \tag{5.1}$$

It yields an upper estimate of the number of grid points in the global (glob) case. Mathematical formulas for generating the geographical distribution can be found e. g. in *Freeden et al.* (1998), pp. 171.

Global rank deficiency and admissibility

The total global number $Q_L^{\text{glob}} \leq N_L^{\max}$ of grid points equals the global number $Q_L =: Q_L^{\text{glob}}$ of unknown coefficients d_q in the series expansion (4.15). On the one hand, the number of grid points follows mathematical relations. On the other hand, the SBFs span the space $H_{0,\ldots,L}(\Omega_R^{\text{ext}})$ of dimension $N_L = (L+1)^2$, cf. Eq. (4.13). Two general questions arise and are answered in the following:

1. How to find a grid with appropriate number of points adopting as optimally as possible the dimension of the space spanned by the basis functions?
2. How to minimize the potentially resulting global rank deficiencies?

For $Q_L^{\text{glob}} \geq N_L$ the point system, cf. Eq. (4.10) becomes admissible. The number Q_L^{glob} usually exceeds the dimension N_L of the space $H_{0,\ldots,L}(\Omega_R)$ (*Lieb et al.*, 2016), since generating a computation grid with an appropriate number N_L^{glob} of points usually cannot be realized in practical applications. Consequently, there exist $Q_L^{\text{glob}} - (L+1)^2$ linear dependencies among the basis functions. It yields the global rank deficiency

$$k_L^{\text{glob}} = Q_L^{\text{glob}} - (L+1)^2 \,. \tag{5.2}$$

In order to minimize k_L^{glob}, to ensure an admissible point system, and to ensure covering the frequency domain up to L, the total number Q_L^{glob} of coefficients, respectively N_L^{glob} of Reuter grid points, is chosen in-between

$$(L+1)^2 \leq Q_L^{\text{glob}} \leq N_L^{\max} \,, \tag{5.3}$$

Grid spacing

Lieb et al. (2016) define the characteristic control parameter γ_L of the Reuter grid as a resolution-depending parameter for the maximum degree L (highest spectral resolution, respectively). It yields

$$\gamma_L^2 = (L+1)^2 \,, \tag{5.4}$$

for $L \geq 2$, according to the dimension N_L of the space $H_{0,\ldots,L}(\Omega_R)$. Hence, the total global number N_L^{glob} of Reuter grid points approximates (and is ensured to be smaller than) the estimate $N_L^{\max}$, cf. Eq. (5.1), and an admissible point system is guaranteed. Table 5.1 lists N_L^{glob} and $N_L^{\max}$ w.r.t. γ_L for different examples of maximum spectral degree L. In Fig. 5.2 selected point distributions are plotted. With rising maximum resolution L, the number and density of grid points increases. Consequently, by locating more and more SBFs on the grid points, expanded in series which are accordingly increasing up to L, more and more details can be modeled.

Table 5.1: Global number of Reuter grid points.

max. degree L	control parameter γ_L	total number N_L^{glob}	estimated number $N_L^{\max}$
2	9	12	13
4	25	30	33
8	81	98	105
16	289	358	368
32	1089	1379	1388
64	4225	5364	5381
128	16641	21126	21189
256	66949	83966	84098
280	78961	100394	100538
2048	4198401	5344564	5345572
2190	4800481	6111064	6112164

↪ In the following, all investigations are transferred from global to regional settings.

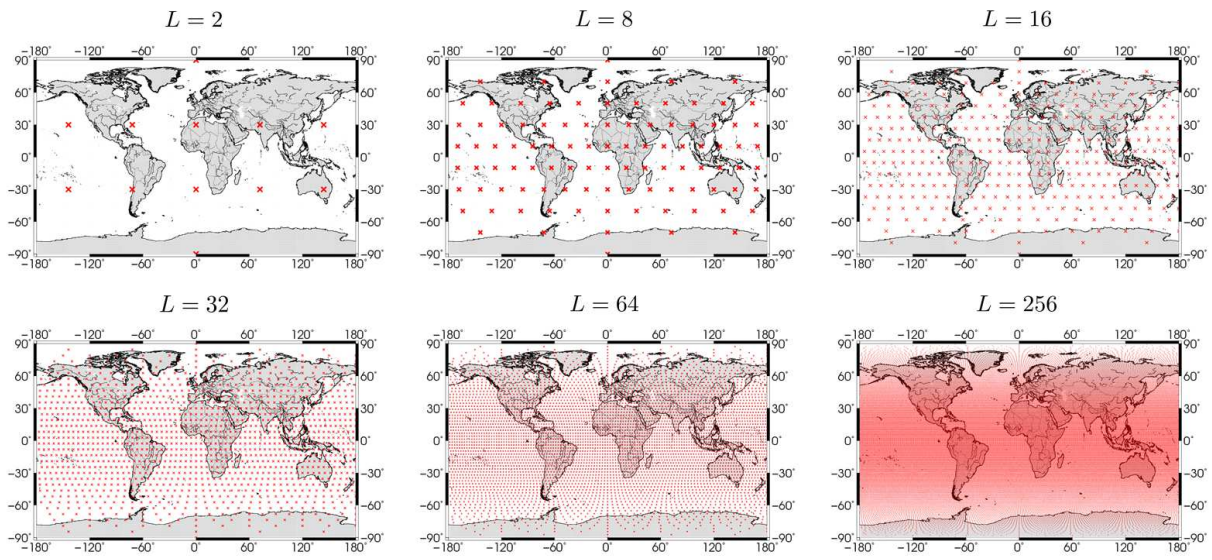

Figure 5.2: Global distribution of Reuter grid points w.r.t. different maximum degree values L. The total numbers N_L^{glob} of grid points are listed in Tab. 5.1.

5.1.2 Definition of regional target, observation and computation area

In contrast to global applications, several additional challenges arise in the regional case – above all, the extension of the region has to be defined, depending on the given observations. In the here presented approach, three areas with different extensions are distinguished, cf. Fig. 5.3:

1. computation area $\partial\Omega_C \subset \Omega_R$,
2. observation area $\partial\Omega_O \subset \partial\Omega_C$,
3. area of investigation $\partial\Omega_I \subset \partial\Omega_O$.

The computation area $\partial\Omega_C \subset \Omega_R$ (red rectangle in Fig. 5.3) serves for locating the basis functions $b(\boldsymbol{x}, \boldsymbol{x}_q)$, Eq. (4.14), at the grid points P_q. Therefore, the previously introduced Reuter grid is used, cf. Sec. 5.1.1. The observation area $\partial\Omega_O$ (gray rectangle) is the area of given observations; the area of investigation $\partial\Omega_I$ (green rectangle) is the target area of the final output gravity model.

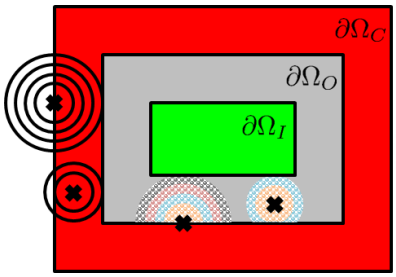

Figure 5.3: Different extensions of computation ($\partial\Omega_C$), observation ($\partial\Omega_O$), and target ($\partial\Omega_I$) area. Side lobes are indicated as black circles, edge effects as colored rings around exemplarily chosen positions (black crosses) of SBFs.

The need of different extensions of the areas is studied, for instance, by *Bentel et al.* (2013b). On the one hand, starting from the given observations, their spatial distribution has to be embedded in the computation area, in order to fit the observations as optimally as possible by a regional model, i. e. the computation area is chosen to be larger than the observation area with $\partial\Omega_O \subset \partial\Omega_C$. The reason results from restricting the global functions $b(\boldsymbol{x}, \boldsymbol{x}_q)$ to a specific region, which provokes side lobes, visualized in Fig. 5.3 by black circles. Globally, the oscillations of SBFs, overlap and balance each other; hence, a global gravity field representation in terms of SBFs and SHs is equivalent, cf. Tab. 4.3. Since regionally, the number of basis functions is reduced and refers to $\partial\Omega_C$, the neglect of SBFs outside $\partial\Omega_C$ causes modeling errors. (An estimate of the regional rank deficiency is derived in Sec. 5.1.4.) The modeling errors are small due to the localizing character of SBFs in the spatial domain. Depending on the type of SBF, the higher their spatial localization, the smaller their side lobes, cf. Fig. 4.9 (a – c). However, especially the basis functions which are located at positions $\boldsymbol{x}_q$ (black crosses in Fig. 5.3) at the boundary of $\partial\Omega_C$, experience less overlap by neighboring SBFs, than the ones which are completely surrounded by SBFs. The oscillations of the latter are more and more compensated (decreasing number of black circles).
On the other hand, the corresponding coefficients d_q can only be estimated properly if their locations are

covered by observations in a certain surrounding zone of influence. Thus, missing observations lead to insufficiently estimated coefficients and provoke edge effects, displayed in Fig. 5.3 by colored rings. Again, the effects appear at positions along the borderline of the area, now $\partial\Omega_O$, where the coefficients are not supported by observations, and decrease with more and more surrounding observations. Consequently, the area of investigation has to be chosen $\partial\Omega_I \subset \partial\Omega_O$ (*Lieb et al.*, 2016).
The three areas are displayed, as well, in Fig. 5.1: the gray observation sites (here exemplarily airborne tracks and terrestrial point stations) define the observation area of the input data; they cover except for some data gaps the green-bordered smaller target area, which finally is modeled by placing scaling functions at the Reuter grid points in the largest computation area (red crosses).

5.1.3 Choice of area margins

For a practicable implementation, the size of the resolution-depending margins are defined stepwise according to the level-discretization of the frequency domain, cf. Eq. (4.25), and coupled with the choice of the basis functions. From the selection of SBFs, exemplarily displayed in Fig. 4.9, the Shannon function (a) has the strongest spatial oscillations due to its exact band limitation in the frequency domain, cf. Fig. 4.9 (a, d). The side lobes depend on the spectral resolution and are amplified with increasing degree $l' = l_j$, respectively level j. However, in the same manner, the peak becomes sharper, i. e. the local support decreases, as visualized in Fig. 5.5. Taking the latter aspect of resolution-depending side lobes into account, *Lieb et al.* (2016) define the margins between the different areas for the maximum resolution level J according to Eq. (4.21), with $l = 2^{J-1}$, as

$$\eta^J = \eta^J_{I,O} = \eta^J_{O,C} = \frac{180^\circ}{2^{J-1}\,\cos(|\varphi|_{\max})}\,. \tag{5.5}$$

Hereby, the width $\eta^J_{O,C}$ of the margin between the observation area $\partial\Omega_O$ and the computation area $\partial\Omega_C$ equals the width $\eta^J_{I,O}$ of the margin between the target area $\partial\Omega_I$ and the observation area $\partial\Omega_O$. Consequently, both, the effects of the side lobes in Fig. 5.3 within the overhanging margin of $\partial\Omega_C$ (red), as well as the artificial edge effects within the margin of $\partial\Omega_O$ (gray) are reduced within the resulting regional gravity model in $\partial\Omega_I$. The extension η^J of the margins further depends on the maximum absolute value $|\varphi|_{\max}$ of the latitude of $\partial\Omega_I$. The reason is, that the margins are geographically defined with meridian convergence towards the poles, while the Reuter grid points of $\partial\Omega_C$ are equidistributed, cf. Fig. 5.2.
For a study area in *Northern Germany*, cf. Fig. 5.1, the extensions of the three areas are depicted in Fig 5.4. With $|\varphi|_{\max} = 55^\circ$ and $J = 11$, the width counts $\eta^{11} \approx 0.3^\circ$. From the coverage of all available data sets, (1) $\partial\Omega_O$ is chosen, and (2) $\partial\Omega_C$ and (3) $\partial\Omega_I$ are adapted with equal margins. In Fig. 5.4, exemplarily the observations from spatially limited available airborne, terrestrial and altimetry data sets are displayed by gray-shaded tracks and dots within $\partial\Omega_O$. The extension of $\partial\Omega_I$ is green bordered; $\partial\Omega_C$ is visualized by red crosses. For maximum degree of $L = 2190$, e. g., the regional number Q_L of *Reuter* grid points counts $Q_L = 2118$ within this area.

5.1.4 Estimate of the regional rank deficiency

As mentioned above, a regional computation area $\partial\Omega_C$ with a corresponding number of Reuter grid points is obtained by extracting an appropriate geographical area from the globally (glob) defined Reuter grid with Q_L^{glob} points. The number Q_L^{reg} of regionally (reg) enclosed grid points, thus, depends on the extension of $\partial\Omega_C$. In analogy to the global rank deficiency k_L^{glob}, defined in Eq. (5.2), there exists a regional rank deficiency k_L^{reg}. It can be estimated from the ratio $A_{\partial\Omega_C}/A_{\Omega_R}$ of areas, and the ratio $Q_L^{\text{reg}}/Q_L^{\text{glob}}$ of computation points, and is assumed to be proportional to the global rank deficiency k_L^{glob}, i. e.

$$\frac{A_{\partial\Omega_C}}{A_{\Omega_R}} = \frac{Q_L^{\text{reg}}}{Q_L^{\text{glob}}} = \frac{k_L^{\text{reg}}}{k_L^{\text{glob}}} \tag{5.6}$$

The area of the sphere Ω_R with radius R yields $A_{\Omega_R} = 4\pi R^2$; the surface element of the computation area $\partial\Omega_C$ with minimum and maximum geographical coordinates $(\lambda_{\min}, \varphi_{\min})$ and $(\lambda_{\max}, \varphi_{\max})$ on the same sphere

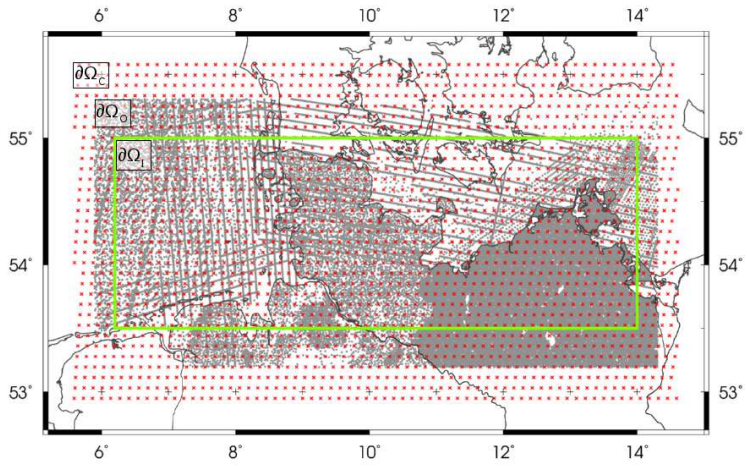

Figure 5.4: Study region in *Northern Germany*: the green-bordered area defines the area of investigation $\partial\Omega_I$, the gray lines represent exemplarily altimetry, airborne and terrestrial measurement sites within the observation area $\partial\Omega_O$. The red crosses mark the *Reuter* grid points P_q within the computation area $\partial\Omega_C$ (regional number $Q_L = 2118$, $L = 2190$). The margins between the areas amount each around 0.3°.

yields

$$A_{\partial\Omega_C} = (\lambda_{\max} - \lambda_{\min})\,(|\sin\varphi_{\max} - \sin\varphi_{\min}|)\,R^2\,. \tag{5.7}$$

Referring to the initial guess of the rank by *Naeimi* (2013)[21], *Lieb et al.* (2016) derive the rank deficiency approximately by

$$k_L^{\text{reg}} \cong \frac{A_{\partial\Omega_C}}{A_{\Omega_R}}\left[Q_L^{\text{glob}} - (L+1)^2\right]. \tag{5.8}$$

In order to minimize the regional rank deficiency problem, the choice of an appropriate maximum degree L of the basis functions b_q according to Eq. (4.14), is discussed in the next Sec. 5.1.5. Additional problems might appear due to inhomogeneous data distribution. Their reduction is discussed in Sec. 5.2 by introducing prior information within the estimation model.

5.1.5 Choice of modeling resolution

From (1) the spectral and spatial resolution of the input data, according to their attribution to the frequency spectrum as shown in Fig. 4.8, and (2) the spatial extension of the observed area $\partial\Omega_O$, both a minimum and maximum modeling resolution can be derived, in terms of spectral degrees $l_{\min}$ and L. Further, $l_{\min}$ and L are related to the local support of SBFs.

Local support of SBFs

In Fig. 5.5 (i), the local support of SBFs on Ω_R is schematically displayed depending on the maximum modeling resolution in terms of degree L and will be explained based on two examples.

Modeling resolution $L = 1$ A basis function up to degree $L = 1$ is related to the spectral resolution $\lambda_1 = 2\pi R$ (blue-colored wavelength) and spatial resolution $\rho_1 = \pi R$, cf. Eq. (4.21). The corresponding local support ranges from a spherical distance of $-180°$ to $180°$, covering the whole sphere Ω_R with circumference $2\pi R$. Note, the origin Q of each basis function is located along the L-axis, i. e. spherical distance of 0°. For $L = 1$, the origin Q is indicated by a blue bullet.

Modeling resolution $L = 7$ A basis function up to degree $L = 7$ yields a wavelength of $\lambda_7 \approx 0.3\pi R$ (red-colored in Fig. 5.5). With mean value $R = 6378.137$ km the spatial resolution, Eq. (4.20), results to $\rho_7 \approx 2862$ km or $\approx 26°$, indicating the local support of the basis function. Relating (i) the local support at degree $L = 7$ to (ii) the spatial representation of the Shannon function at level $j = 3$, cf. Fig. 4.9 a), the latter represents the main signal content within the spherical distance of ±26° (red-dashed lines).

[21] The rank can only be estimated, e. g. by the determination of eigenvalues, and not exactly be determined because of computational limitations.

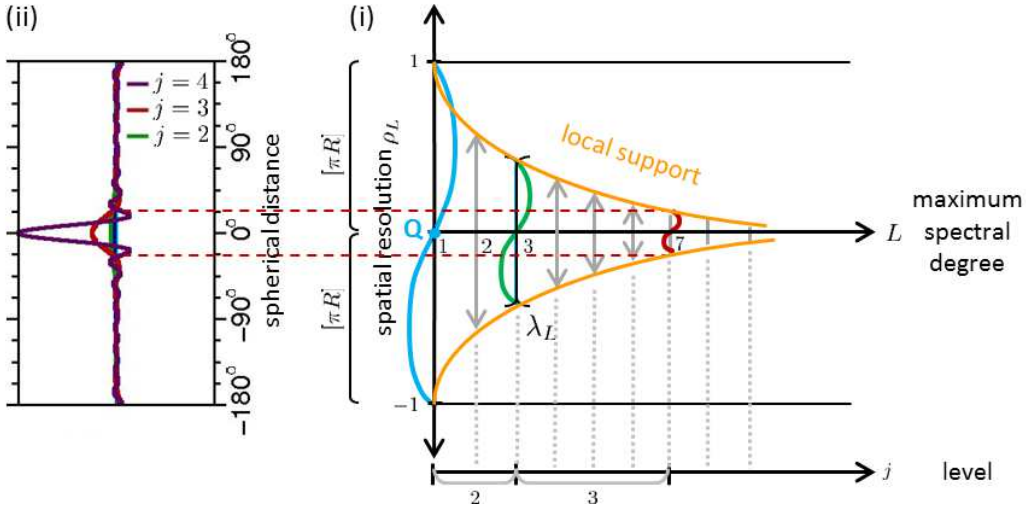

Figure 5.5: Local support of SBFs on a sphere Ω_R. (i) The decreasing local support with increasing spectral degree L is visualized in the spectral domain. The decreasing wavelength λ_L relates to (ii) a sharper peak of the SBF in the spatial domain (red-dashed lines). The gray arrows in (i) indicate decreasing local support with increasing spherical distance for each degree L. The frequency domain is further discretized by level j.

With increasing spectral degree L, the amplitude of SBFs, cf. Fig. 5.5 (ii), becomes sharper in the spatial domain and their local support decreases, i. e. the first zero crossing of the Shannon function appears at a smaller spherical distance from the center of the SBFs, and the wavelengths become shorter (indicated for $L = 7$ with red-dashed lines in Fig. 5.5). Further, for each modeling resolution up to degree L, the local support of a SBF decreases with increasing spherical distance from its origin (the gray arrows in (i) symbolize decreasing local support). The decline of the spatial influence for both, increasing spectral degree, and increasing spherical distance, is indicated by the yellow curve in Fig. 5.5 (i).
Haagmans et al. (2002) propose a limited capsize, i. e. truncating the SBFs in the spatial domain at their first zero crossing, counted radially outwards from the center, in order to remove the side lobes, and estimate the omission error. Due to the loss of spectral information and additional truncation errors, it is not pursued in this work.

Minimum spectral resolution

The minimum spectral resolution of a regional gravity model depends on the average spatial extension Π of the observed area $\partial\Omega_O$, i. e. on the maximum gravitational wavelength $\lambda_{l,\max}$, cf. Eq. (4.21), which can be resolved. According to the Nyquist theorem, the minimum spectral resolution in terms of degree $l_{\min}$ and level j' reads

$$l_{\min} = \left\lfloor \frac{2\pi R[\mathrm{km}]}{\Pi[\mathrm{km}]} \right\rfloor , \tag{5.9}$$

$$j' = \lfloor \log_2(l_{\min} + 1) \rfloor \ . \tag{5.10}$$

The maximum degree of the minimum level j' is defined as $l_{j'}$ according to Eq. (4.24). For instance, in terms of global modeling with an average area extent of $\Pi = 40\,000$ km and $R = 6378.137$ km, the minimum resolution results to $l_{\min} = 1$, $j' = 1$; for an area extent of $\Pi = 13\,200$ km, it yields $l_{\min} = 3$, $j' = 2$ (visualized as red circle in Fig. 5.6, in analogy to Fig. 5.5); for $\Pi = 4000$ km, it yields $l_{\min} = 10$, $j' = 3$.

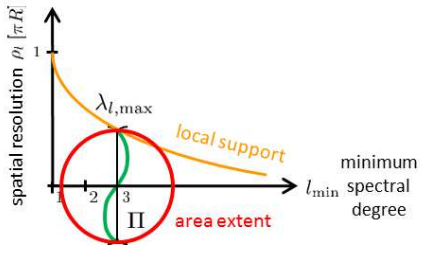

Figure 5.6: Relation of area extent Π = 13 200 km (red circle) and resulting minimum modeling resolution $l_{\min} = 3$, w.r.t. maximum resolvable $\lambda_{l,\max}$.

A selection of minimum resolutions w.r.t. the extent Π of the observation area is listed in Tab. 5.2. For the example in Fig. 5.1, the area extent of $\partial\Omega_O$ averages Π =550 km. It yields a minimum resolution of degree $l_{\min} = 36$ and level $j' = 5$.

Table 5.2: Minimum modeling resolution degree and level w.r.t. the extent Π of the observation area $\partial\Omega_O$.

average area extent Π[km]	minimum spectral degree $l_{\min}$	minimum resolution level j'
20000	1	1
6600	3	2
5000	4	2
4000	5	2
3000	6	2
2000	10	3
1000	20	4
900	22	4
800	25	4
700	28	4
600	33	5
550	36	5
500	40	5
400	50	5
300	66	6
200	100	6
100	200	7

Maximum spectral resolution

In Sec. 4.3.1, the modeling resolution was introduced in terms of a maximum spectral degree L, depending on the spectral content of the observations. Referring to the level-j-fragmentation in Tab. 4.8, the highest resolution level J is defined up to spectral degree l_J. The choice of $l_J \leq L$ allows to minimize influences of omission errors stemming from the truncation of the infinite series expansion, discussed in Sec. 4.2.4. This first aspect is visualized in Fig. 5.7, as extension to Fig. 4.4:

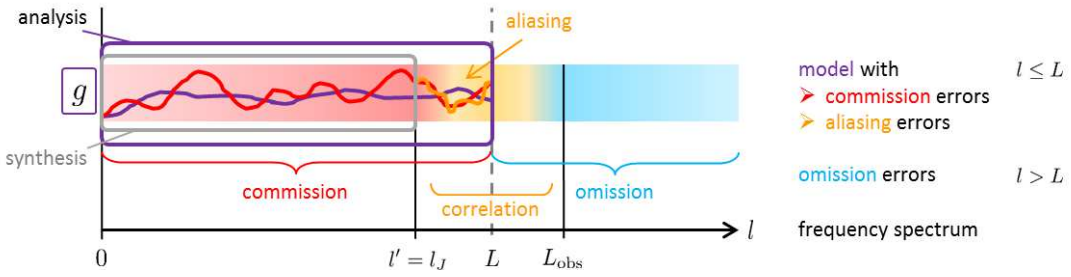

Figure 5.7: Observations with maximum resolution up to degree L^{obs} are represented by the bandlimited function g up to degree L (modeling resolution in the analysis; purple bordered). Aliasing errors are reduced by a reasonable choice of modeling resolution l_J in the synthesis (gray bordered), cf. Fig. 4.4.

- As the maximum resolution, i. e. maximum spectral degree L_{obs}, of real observations is generally not known, the SBFs are expanded in a series (4.14) up to maximum degree $L \leq L_{\max}$. The modeled, bandlimited signal g, cf. Eq. (4.15), is indicated in purple.

- The truncation of the non-bandlimited, observed signal yields an omission error (blue). As already discussed, the latter is correlated with the commission error due to aliasing effects (yellow) in the high frequencies.

- In order to reduce the aliasing error, the maximum resolution level J is chosen such, that $l_J \leq L$. Appropriate scaling functions with Legendre coefficients $\phi_{l,J}$, cf. Eqs. (4.29) – (4.31), enable the corresponding low-pass filtering within the synthesis of a MRR, resulting in a smoothed signal up to degree l_J (gray-bordered spectral domain).

Referring to the four options of band limitation and truncation of SBFs in the frequency domain, expressed by the general Legendre coefficients B_l in Fig. 4.1, an additional case (e) is introduced in Fig. 5.8. In terms of a MRR up to J, the Legendre coefficients $B_l = \phi_{l,j}$, Eqs. (4.29) – (4.31), are bandlimiting at $l' = l_j = l_J$. The referring SBFs are truncated at L, but bandlimiting at the lower degree $l_J < L$.
Besides the adaption of $l_J \leq L$, the maximum modeling degree L itself is chosen such that the regional rank deficiency k_L^{reg}, cf. Eq. (5.8), shall be minimized. In the ideal case, $k_L^{\text{reg}} = k_{l_J}^{\text{reg}}$ becomes zero. *Lieb et al.* (2016) derive an upper estimate of the maximum modeling degree, i. e.

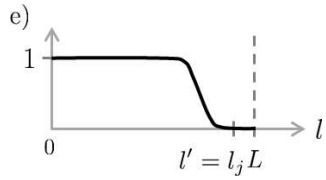

Figure 5.8: Legendre coefficients $B_l = \phi_{l,j}$ of SBFs, bandlimiting at degree $l' = l_j$ and truncated at a different degree $L > l_j$.

$$L^{\text{rank}} = \left\lfloor \sqrt{Q_{l_J}^{\text{glob}}} - 1 \right\rfloor, \tag{5.11}$$

from $Q_{l_J}^{\text{glob}} - (L^{\text{rank}} + 1)^2 = 0$, with $Q_L^{\text{glob}} = Q_{l_J}^{\text{glob}}$, and $l_J = L^{\text{rank}}$. Hence, L^{rank} depends on the maximum number $Q_{l_J}^{\text{glob}}$ of corresponding Reuter grid points within the computation area $\partial\Omega_C$. In order to account for both aspects, minimizing the aliasing error and further the regional rank deficiency, the maximum modeling resolution in terms of spectral degree L is chosen in-between

$$l_J \leq L \leq L^{\text{rank}}\,. \tag{5.12}$$

For the example in Fig. 5.1, the lower boundary yields $l_{11} = 2047$, cf. Eq. (4.24), and the upper boundary $L^{\text{rank}} = 2310$, with $J = 11$ and $Q_{l_J}^{\text{glob}} = N_L^{\text{glob}} = 5\,344\,564$, cf. Tab. 5.1.

5.1.6 Choice of background model

Before any estimation model will be set up, a global background model is subtracted from each input data set, listed in Tab. 3.7. The main reasons are:

1. As mentioned in the context of normal potential (Sec. 2.3.4), dealing with small input quantities enables a more accurate model representation, than fitting large values. However, the errors contained in the long wavelengths of observables are not captured by the background model and have to be taken into account (cf. discussion in Sec. 6, study case (e)).
2. Global background models cover the low frequencies, while the corresponding long wavelengths cannot be resolved by regional observations. The minimum spectral resolution of a regional approach down to degree l_{min}, Eq. (5.9), refers to the average extension of the observed area $\partial\Omega_O$.
3. The low frequency part is very well approximated in existing global models based on global satellite observations. Thus, the background model can be assumed to be noise-free.

The background model serves in the here presented approach additionally as prior information, see Sec. 5.2.1. Hence, the choice of its type and resolution depends on the issues of correlation and regularization:
On the one hand, global models should contain data that are independent of the input observations to avoid correlations. The spectral resolution of the global model then is chosen lower than the maximum modeling resolution (L), and thus, lower than the maximum resolution of the observations ($L \leq L_{\text{obs}}$), in order to extract the highest spectral content of the observations, which is the primary aim. Further, it should be chosen as least as high as the minimum modeling resolution (l_{min}) depending on the average spatial extension Π of the observed area according to Eq. (5.9), and thus, as least as high as the minimum resolution of the observations, in order cover the full frequency domain. In terms of a MRR composition as visualized in Fig. 4.5, the choice of a level-depending resolution ($l_{j'}$) is appropriate, cf. Eq. (5.10). Several examples are investigated in Chapter 6.
On the other hand, subtracting a global background model containing explicitly the same data as the input observations, allows, e. g., rating the model fit of the data within simulation studies, see Sec. 6.1.1. Further, subtracting the same data types from real observations up to the same resolution, enables, for instance, analyzing time variations. However, these applications are not part of this thesis.
As mentioned before, introducing additional long wavelength global gravity information stabilizes the solution of regional modeling approaches. In case of unstable solutions where regularization is needed, i. e. for filling data gaps, the resolution of the prior information should approximate the one of the observations. In most

cases, a compromise has to be found between choosing a model of high resolution in order to overcome data gaps, but taking correlations of equivalent input data into account, versus choosing a model of low resolution for not subtracting too much valuable information from the observations. Several study cases are investigated in Chapter 6.
The different input observables, according to Fig. 2.9, are summarized by $\mathcal{Y}[\,\tilde{V}\,]$ as functionals of the (differential) gravitational potential $\tilde{V}$. Subtracting a background model, thus, requires the adaptation to the appropriate functional. A differential observable $\mathcal{Y}[\,\Delta\tilde{V}(\boldsymbol{x})\,]$ at location $\boldsymbol{x} \in \Omega_R^{\text{ext}}$, then reads

$$\mathcal{Y}[\,\Delta\tilde{V}(\boldsymbol{x})\,] = \mathcal{Y}[\,\tilde{V}(\boldsymbol{x})\,] - \mathcal{Y}[\,\tilde{V}_{\text{back}}(\boldsymbol{x})\,]\,. \tag{5.13}$$

$\mathcal{Y}[\,\tilde{V}_{\text{back}}\,]$ is obtained from the given global background model. The models are typically provided in terms of Stokes coefficients $F_{l,m}$, Eq. (2.39). In order to ensure consistency w.r.t. the reference potential of the observations, the SH coefficients are rescaled according to Eq. (2.42), i. e. adapted to the reference potential of the input data. The regional data sets presented in Tab. 3.7 refer, for instance, to GRS80, cf. Sec. 3.2.1. The various functionals, e. g. δg (2.66) or Δg (2.69), then are modeled in terms of SHs by using the relations in Tab. 2.3.
According to the remove-restore principle, the subtracted background model can be added in the end to the estimated differential gravity signal, yielding a total gravity model of broad spectral range. Or, in other words, placing the estimated regional signal on top of a global model, might indicate additional signal and be used for regional refinements of global models.

5.2 Estimation model

One possibility to determine the unknown coefficients of a series expansion, i. e. for example the Stokes or scaling coefficients, is the method of **parameter estimation**. Besides this method, numerical integration is another very prominent approach. For the task of this thesis, regional gravity field modeling in terms of SBFs from a combination of heterogeneous real data, the computation of the unknown scaling coefficients via parameter estimation has essential advantages. As summarized by *Bentel et al.* (2013a), this technique enables not only the estimation of the unknown coefficients, but delivers also their covariance matrix, containing information about their standard deviations and correlations. Further, parameter estimation allows to keep the observations at their original observation sites, whereas numerical integration requires data provided on a regular grid, i. e. in most cases a pre-processing procedure in terms of interpolation and, thus, manipulation of the data.
Schmidt et al. (2006) discuss the suitability of parameter estimation, in contrast to numerical integration, for regional MRR gravity modeling in terms of SBFs in detail. Based on the findings, the principle of parameter estimation is adapted to the specific requirements of this work and applied within an (extended) GMM, cf. Fig. 5.9:

- In a first step, the fundamental Gauß-Markov model is defined for regional gravity modeling from one observation group. The estimation model is successively established by setting up a linear model for one single observation (white), and for $\bar{n}$ observations belonging to one observation type (yellow). Introducing additional prior information (green) enables to determine the unknown parameters by VCE.

- In a second step, the GMM then is extended to $K + 1$ observation equations, allowing regional modeling from the combination of several (K) observation groups and the prior information (red). Herein, the combination at one resolution level is denoted as "single-level estimation" or "single-level combination" and summarized within the light blue analysis box in Fig. 5.9. (In contrast, the "multi-level estimation/combination" by MRR is explained in the Sec. 5.3.) From the estimated scaling coefficients, any output functional can be computed in the synthesis (dark blue box on the right side), either from one (yellow), or from various (red) observation groups. The covariance information of the estimated coefficients, as well as of the modeled parameters is derived.

Details are explained in the following.

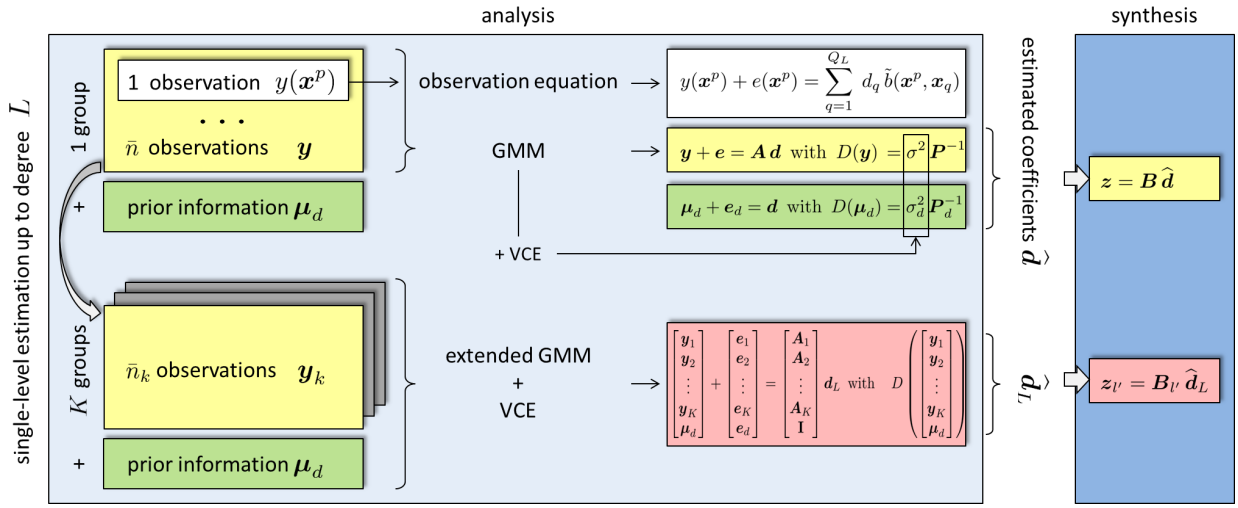

Figure 5.9: Analysis and synthesis from a single-level estimation of unknowns at one resolution level within an (extended) GMM and VCE.

5.2.1 Gauß-Markov model

As mentioned, parameter estimation within an appropriate GMM, provides both results, and accuracies, from one observation type, as well as from several types (extended model). Further, it allows to introduce prior information in order to overcome singularity problems in case of an ill-conditioned system. Applying VCE for the relative weighting of the heterogeneous data sets enables their efficient combination on normal equation level.
Based on the fundamentals and settings derived in the previous sections, the rigorous estimation model is set up in order to compute regional gravity fields at any resolution level j from the combination of appropriate input data. In this section, only components of the light blue analysis box in Fig. 5.9 are discussed.

Observation equation

For one single observation

$$y(\boldsymbol{x}^p) = \mathcal{Y}[\,\tilde{V}(\boldsymbol{x}^p)\,] - \mathcal{Y}[\,\tilde{V}_{\text{back}}(\boldsymbol{x}^p)\,] \tag{5.14}$$

with measurement error $e(\boldsymbol{x}^p)$, at observation site $P(\boldsymbol{x}^p)$, $p \in \{1, \ldots, \bar{n}\}$, expressing any functional $\mathcal{Y}[\,\tilde{V}(\boldsymbol{x}^p)\,]$, reduced by the appropriate functional $\mathcal{Y}[\,\tilde{V}_{\text{back}}(\boldsymbol{x}^p)\,]$ of a background model according to Eq. (5.13), the **observation equation** reads

$$y(\boldsymbol{x}^p) + e(\boldsymbol{x}^p) = \sum_{q=1}^{Q_L} d_q\, \tilde{b}(\boldsymbol{x}^p, \boldsymbol{x}_q)\,, \tag{5.15}$$

according to Eq. (4.15). $\tilde{b}_q$ represent the adapted SBFs of Tab. 4.7. This fundamental relation is displayed within the white box in Fig. 5.9. In order to estimate the unknown scaling coefficients d_q from, in total, $\bar{n}$ observations, vector notation is used in the sequel. $\boldsymbol{y} = [y(\boldsymbol{x}^1), \ldots, y(\boldsymbol{x}^{\bar{n}})]^T$ identifies the $\bar{n} \times 1$ observation vector, $\boldsymbol{e} = [e(\boldsymbol{x}^1), \ldots, e(\boldsymbol{x}^{\bar{n}})]^T$ the $\bar{n} \times 1$ vector of measurement errors, and $\boldsymbol{d} = [d_1, \ldots, d_{Q_L}]^T$ the $Q_L \times 1$ vector of unknown coefficients. The **GMM** then is defined as

$$\underbrace{\boldsymbol{y} + \boldsymbol{e} = \boldsymbol{A}\,\boldsymbol{d}}_{\text{deterministic part}} \quad \text{with} \quad \underbrace{D(\boldsymbol{y}) = \sigma^2\,\boldsymbol{P}^{-1}}_{\text{stochastic part}} \tag{5.16}$$

(*Koch*, 1999, p. 153). It is visualized within the yellow box in Fig. 5.9. In the deterministic part, $\boldsymbol{A} = \left[\,\tilde{b}(\boldsymbol{x}^p, \boldsymbol{x}_q)\,\right]$ represents the $\bar{n} \times Q_L$ design matrix, containing the adapted basis functions $\tilde{b}(\boldsymbol{x}^p, \boldsymbol{x}_q)$. In the stochastic part, $D(\boldsymbol{y})$ denotes the $\bar{n} \times \bar{n}$ covariance matrix of the observation vector $\boldsymbol{y}$, σ^2 the unknown variance factor, and $\boldsymbol{P}$ is the given $\bar{n} \times \bar{n}$ positive definite weight matrix. Following *Koch* (1999, p. 154), $\boldsymbol{P} = \mathbf{I}$ is

introduced as identity matrix, assuming the measurement errors to be uncorrelated and the observations to have similar accuracies. This simplification is made due to considerably smaller computational expense and due to insufficient information about the quality of most of the data sets, listed in Tab. 3.7.

Least-squares adjustment

The primary aim of setting up the observation equations within the deterministic part of the GMM (5.16) is to describe the original data by an appropriate model and to compute the unknown parameters, in the sequel denoted as analysis. Hereby, the GMM (5.16) is a linear adjustment model, i. e. the adjusted observations with measurement errors can be expressed by a linear combination of the given design matrix $\boldsymbol{A}$ and the unknown parameters, i. e. the vector $\boldsymbol{d}$ of coefficients. *Koch* (1999), pp. 150, presents several methods for estimating the parameters. Among them, **least-squares adjustment** is applied in the sequel. Hereby, the estimation $\widehat{\boldsymbol{d}}$ of the vector of coefficients has to be determined such that the sum of squares $\left(\boldsymbol{y} - \boldsymbol{A}\widehat{\boldsymbol{d}}\right)^T \boldsymbol{P} \left(\boldsymbol{y} - \boldsymbol{A}\widehat{\boldsymbol{d}}\right)$ becomes a minimum (*Koch*, 1999, pp. 158). This process leads to the **normal equation system**

$$\left(\boldsymbol{A}^T\boldsymbol{P}\boldsymbol{A}\right)\widehat{\boldsymbol{d}} = \boldsymbol{A}^T\boldsymbol{P}\boldsymbol{y} \tag{5.17}$$

with the solution

$$\widehat{\boldsymbol{d}} = \left(\boldsymbol{A}^T\boldsymbol{P}\boldsymbol{A}\right)^{-1}\boldsymbol{A}^T\boldsymbol{P}\boldsymbol{y} \tag{5.18}$$

in case that $\boldsymbol{A}^T\boldsymbol{P}\boldsymbol{A}$ is of full rank. The coefficients d_q are point parameters belonging to the altogether Q_L grid points $P_q \in \partial\Omega_C$. As already mentioned, the values of d_q represent in the spatial domain the amplitude of the (adapted) basis functions b_q, Eq. (4.14), respectively $\tilde{b}_q$, Tab. 4.7, and thus have a geophysical meaning.

Prior information

Due to linear dependencies among radial basis functions, the design matrix $\boldsymbol{A}$ in Eq. (5.16) usually reveals a rank deficiency. In the regional case, k_L^{reg} can be estimated according to Eq. (5.8). Besides this (1) rank deficiency problem, the normal equation system in Eq. (5.17) might be ill-conditioned and cause singularities due to (2) downward continuation problems, and (3) data gaps. For handling these difficulties an additional linear model

$$\boldsymbol{\mu}_d + \boldsymbol{e}_d = \boldsymbol{d} \quad \text{with} \quad D(\boldsymbol{\mu}_d) = \sigma_d^2\,\boldsymbol{P}_d^{-1} \tag{5.19}$$

is introduced as prior information, cf. green box in Fig. 5.9. $\boldsymbol{\mu}_d$ is the $Q_L \times 1$ expectation vector of the scaling coefficients, and $\boldsymbol{e}_d$ the corresponding unknown $Q_L \times 1$ error vector. $D(\boldsymbol{\mu}_d)$ is the $Q_L \times Q_L$ covariance matrix of the prior information, including the variance factor σ_d^2 and the inverse of the $Q_L \times Q_L$ weight matrix $\boldsymbol{P}_d$. In case of using the background model as prior information as mentioned in Sec. 5.1.6, i. e. subtracting according to Eq. (5.13) the same information as additionally supplied, the expectation vector $\boldsymbol{\mu}_d$ can be introduced as zero vector. This beneficial choice is applied in all numerical studies and studied in the next Chapter 6. Further, assuming that the coefficients have the same accuracies and are not correlated, the weight matrix $\boldsymbol{P}_d = \mathbf{I}$ yields the identity matrix.

The variance factors σ^2 and σ_d^2 in Eqs. (5.16) and (5.19) can either be given a priori or estimated, for instance, by VCE (cf. black arrow in Fig. 5.9). The combination of the two linear models (5.16), cf. yellow box in Fig. 5.9, and (5.19), green box in Fig. 5.9, then yields an unique solution for $\widehat{\boldsymbol{d}}$, as suggested and applied, e. g., by *Koch and Kusche* (2002) and *Schmidt et al.* (2007). Details are explained in the next section.

Modeling equation

In analogy to the system of observation equations for one single observation group, i. e. the deterministic part in the GMM (5.16) within the analysis, the system of modeling equations for any output functional $\mathcal{Y}[\tilde{V}] = z(\boldsymbol{x}^c)$, $\boldsymbol{x}^c \in \Omega_R^{\text{ext}}$ reads

$$z = \boldsymbol{B}\,\widehat{\boldsymbol{d}} \tag{5.20}$$

in the synthesis. It is indicated in yellow within the blue synthesis box in Fig. 5.9. The $C \times 1$ vector $z = \left[z(\boldsymbol{x}^1), \ldots, z(\boldsymbol{x}^C)\right]^T$ contains the output functional values, the $C \times Q_L$ matrix $\boldsymbol{B} = \left[\tilde{b}(\boldsymbol{x}^c, \boldsymbol{x}_q)\right]$ the adapted SBFs, and the $Q_L \times 1$ vector $\widehat{\boldsymbol{d}}$ the estimated coefficients from Eq. (5.18).

5.2.2 Extended Gauß-Markov model

Based on the above introduced principles of parameter estimation within a GMM by means of one observation type, an extended GMM now is set up in order to derive regional gravity models from the combination of heterogeneous data. The different observation types are distinguished and collected in groups, following the criteria of

- measurement system (satellite, absolute/relative terrestrial, ship-/airborne gravimetry, ...),
- observed functional ($\Delta V, \boldsymbol{V}_{ab}, T, \Delta g, \delta g, \ldots$),
- observation height (orbit height of satellite, measurements at the Earth's surface, at a platform, ...),
- spectral resolution (depending on functional, measurement system, ...),
- accuracy (e. g. externally influenced by the climate, humans, ...),
- observation epoch (hours, months, consideration of seasonal variations, ...),
- sampling rate (of one or several measurement campaigns, ...),
- pre-processing (application of reductions, corrections, elimination of outliers, ...),
- reference (height, gravity, ...),
- spatial distribution,
- ...

For the combination of the different groups within an appropriate estimation model, especially the first three aspects are challenging, i. e. handling a variety of functionals and observation heights from diverse measurement systems. For the different functionals $\mathcal{Y}[V] \in \{\Delta V, \boldsymbol{V}_{ab}, T, \Delta g, \delta g, \ldots\}$, different observation equations (5.15) have to be formulated. The design matrix in Eq. (5.16) then contains the correspondingly adapted basis functions $\tilde{b}(\boldsymbol{x}^p, \boldsymbol{x}_q)$ from Tab. 4.7 with $\boldsymbol{x} = \boldsymbol{x}^p$. The varying observation heights are taken into account by the downward continuation term $(R/r)^{l+1}$, cf. Tab. 2.2, within the observation equations. *Bouman et al.* (2013) study signal and degree RMS at different observation heights; *Kern* (2003), pp. 105, studies the effect of attenuation and amplification of gravitational functionals and their errors at different heights. The remaining criteria which classify the diverse observation groups, depend on the specific data sets, cf. Sec. 3.3. Examples are given in the next chapter. In the following, components of the single-level combination are studied, referring to the two boxes of analysis and synthesis in Fig. 5.9.

Analysis: Estimation of coefficients

Within the analysis step (light blue box in Fig 5.9), the unknown scaling coefficients are estimated. They describe the amplitudes of basis functions in the spatial domain. In Fig. 5.1, it would mean to locate Shannon SBFs at the Reuter grid points (red crosses) in $\partial\Omega_C$, and to multiply them with the estimated coefficients.

Choice of basis functions

The basis functions $\tilde{b}_q$ are defined as Shannon functions, cf. Eq. (4.6), i. e. inserting $B_l = 1$ in the expressions of Tab. 4.7. For the simplest functional, T, the basis function yields

$$\tilde{b}_L(\boldsymbol{x}^p, \boldsymbol{x}_q) = \sum_{l=0}^{L} \frac{2l+1}{4\pi R^2} \left(\frac{R}{r}\right)^{l+1} P_l\left((\boldsymbol{r}^p)^T \boldsymbol{r}_q\right), \tag{5.21}$$

based on Legendre polynomials P_l w.r.t. the spherical distance angle between observed point $P^p = P(\boldsymbol{x}^p)$ and computation point $P_q = P(\boldsymbol{x}_q)$, i. e. $\boldsymbol{r}^p$ and $\boldsymbol{r}_q$ as introduced in Eq. (4.2). The bandlimiting maximum degree L corresponds to the chosen maximum degree of the modeling resolution, cf. Eq. (5.12). As discussed before, the Shannon kernel ensures an exact band limitation at degree L without any smoothing behavior.

Observation equations

For the combination of different observation techniques, the parameter estimation model (5.16) is extended from one observation group to K groups with observation vectors $\boldsymbol{y} = \boldsymbol{y}_k$, $k = 1, \ldots, K$. Next, an appropriate background model is selected and subtracted according to Eq. (5.13) from the elements of all observation vectors $\boldsymbol{y}_k$. It yields the differential $\bar{n}_k \times 1$ observation vector $\boldsymbol{y}_k$ of the k^{th} measurement technique with differential elements $y(\boldsymbol{x}^p) = y_k(\boldsymbol{x}^p)$ according to Eq. (5.14). $\boldsymbol{e}_k$ and $\boldsymbol{A}_k$ are the corresponding $\bar{n}_k \times 1$ error vector and the $\bar{n}_k \times Q_L$ design matrix. For the combination of the altogether K observation techniques including the additional model (5.19) for the prior information, the **extended GMM** reads

$$\begin{bmatrix} \boldsymbol{y}_1 \\ \boldsymbol{y}_2 \\ \vdots \\ \boldsymbol{y}_K \\ \boldsymbol{\mu}_d \end{bmatrix} + \begin{bmatrix} \boldsymbol{e}_1 \\ \boldsymbol{e}_2 \\ \vdots \\ \boldsymbol{e}_K \\ \boldsymbol{e}_d \end{bmatrix} = \begin{bmatrix} \boldsymbol{A}_1 \\ \boldsymbol{A}_2 \\ \vdots \\ \boldsymbol{A}_K \\ \mathbf{I} \end{bmatrix} \boldsymbol{d}_L \quad \text{with} \quad D\left(\begin{bmatrix} \boldsymbol{y}_1 \\ \boldsymbol{y}_2 \\ \vdots \\ \boldsymbol{y}_K \\ \boldsymbol{\mu}_d \end{bmatrix}\right) = \begin{bmatrix} \sigma_1^2 \boldsymbol{P}_1^{-1} & \mathbf{0} & \ldots & \mathbf{0} & \mathbf{0} \\ \mathbf{0} & \sigma_2^2 \boldsymbol{P}_2^{-1} & \ldots & \mathbf{0} & \mathbf{0} \\ \vdots & \vdots & \ddots & \vdots & \vdots \\ \mathbf{0} & \mathbf{0} & \ldots & \sigma_K^2 \boldsymbol{P}_K^{-1} & \mathbf{0} \\ \mathbf{0} & \mathbf{0} & \ldots & \mathbf{0} & \sigma_d^2 \boldsymbol{P}_d^{-1} \end{bmatrix} \tag{5.22}$$

(*Schmidt et al.*, 2007). It is displayed within the red box in Fig. 5.9. The design matrices $\boldsymbol{A}_k$ contain the adapted basis functions from Eq. (5.21). Each covariance block matrix $D(\boldsymbol{y}_k) = \sigma_k^2 \boldsymbol{P}_k^{-1}$ consists of an unknown Variance Component (VC) σ_k^2 and the inverse of a given $\bar{n}_k \times \bar{n}_k$ positive definite weight matrix $\boldsymbol{P}_k$. Those block matrices, and the covariance matrix $D(\boldsymbol{\mu}_d)$ of the prior information, are located on the main diagonal of the covariance matrix $D([\boldsymbol{y}_1^T, \ldots, \boldsymbol{y}_K^T, \boldsymbol{\mu}_d^T])$, cf. Eq. (5.22). The off-diagonal block elements are zero-matrices, assuming that the observation groups $\boldsymbol{y}_k$ and the prior information $\boldsymbol{\mu}_d$ are uncorrelated.
Further, as mentioned in the context of Eq. (5.16), in all numerical investigations in Chapter 6, the measurement errors are assumed to be uncorrelated and the observations are assumed to have similar accuracies within one observation group k. Thus, identity matrices can be introduced for the weight matrices $\boldsymbol{P}_k$ in Eq. (5.22).

Least-squares adjustment

Following *Lieb et al.* (2016), the K observation techniques with each $\bar{n}_k$ ($k = 1, \ldots, K$) observations are combined at normal equation level. A combination at observation equation level instantly delivered residuals of the observations, which are necessary for VCE. However, the size and, thus, the computation time of the linear equation systems restrict a practical realization within the scope of this work. According to the normal equation system (5.17) for one observation group, the observation equation system (5.22) for K groups and the prior information yields

$$\left(\sum_{k=1}^{K}\left(\frac{1}{\sigma_k^2}\boldsymbol{A}_k^T\boldsymbol{P}_k\boldsymbol{A}_k\right) + \frac{1}{\sigma_d^2}\boldsymbol{P}_d\right)\widehat{\boldsymbol{d}}_L = \sum_{k=1}^{K}\left(\frac{1}{\sigma_k^2}\boldsymbol{A}_k^T\boldsymbol{P}_k\boldsymbol{y}_k\right) + \frac{1}{\sigma_d^2}\boldsymbol{P}_d\boldsymbol{\mu}_d \ . \tag{5.23}$$

This system of normal equations is independent of the number of observations. The estimated coefficients $\widehat{d}_q$, collected in the vector $\widehat{\boldsymbol{d}}_L$ up to degree L, are computed from

$$\widehat{\boldsymbol{d}}_L = \left(\sum_{k=1}^{K}\left(\frac{1}{\widehat{\sigma}_k^2}\boldsymbol{A}_k^T\boldsymbol{P}_k\boldsymbol{A}_k\right) + \frac{1}{\widehat{\sigma}_d^2}\boldsymbol{P}_d\right)^{-1}\left(\sum_{k=1}^{K}\left(\frac{1}{\widehat{\sigma}_k^2}\boldsymbol{A}_k^T\boldsymbol{P}_k\boldsymbol{y}_k\right) + \frac{1}{\widehat{\sigma}_d^2}\boldsymbol{P}_d\boldsymbol{\mu}_d\right), \tag{5.24}$$

cf. Eq. (5.18). The components $\widehat{d}_q$ have the SI-unit $\mathrm{m}^2/\mathrm{s}^2$ of the gravitational potential; the elements of the design matrix $\boldsymbol{A}$ contain the corresponding conversion factors for the particular functionals.

Variance component estimation

In this work, VCE is used for regulating (1) the relative weighting of heterogeneous observation groups and (2) the amount of regularization by prior information. The variance components are iteratively estimated to $\widehat{\sigma}_k^2$ and $\widehat{\sigma}_d^2$, as suggested by *Koch and Kusche* (2002). The regularization parameter yields $\lambda_\sigma = \widehat{\sigma}_k^2/\widehat{\sigma}_d^2$. Hereby, the estimates are computed based on stochastic information, i. e. using the residuals of the observations. The iteration starts from an initial value and ends in the point of convergence (the first three digits of two successive

iterations must not change any more).
The reciprocals $\widehat{\sigma}_k^{-2}$ and $\widehat{\sigma}_d^{-2}$ of the estimated VCs in Eq. (5.24) determine the relative weight of each observation group $\boldsymbol{y}_k$, and hence, regulate the contribution of each measurement technique to the overall combination result. The influence depends on the accuracy of the observation data, the spectral resolution and the spatial distribution (*Lieb et al.*, 2016). Since low-resolution signal is smoother in the spatial domain, i. e. it shows large scale-variations, and high-resolution signal represents short-scale variations. Further, the spatial distribution and the spectral content of the observations are related to each other, cf. Eq. (4.21). Data which cover wide areas enable to recover medium down to long wavelengths. The spectral content of measurements also depends on the type of the gravitational functional and the aspect of downward continuation. According to the Meissl scheme (Fig. 2.7), different functionals have different spectral sensitivities to high-frequency variations and the downward continuation, e. g. of satellite measurements down to the Earth's surface, amplifies high frequencies. All those aspects are connected with the need of regularization by prior information $\boldsymbol{\mu}_d$. Details are studied and discussed by means of numerical applications in Chapter 6.

Covariance information of the unknowns

The full covariance information of the vector $\widehat{\boldsymbol{d}}_L$ of estimated coefficients is obtained by applying error propagation on Eq. (5.24).[22] The covariance matrix

$$D\left(\widehat{\boldsymbol{d}}_L\right) = \boldsymbol{Q}_{dd}^{-1} = \begin{bmatrix} v(\widehat{d}_1) & c(\widehat{d}_1,\widehat{d}_2) & \dots & c(\widehat{d}_1,\widehat{d}_{Q_L}) \\ c(\widehat{d}_2,\widehat{d}_1) & v(\widehat{d}_2) & & \vdots \\ \vdots & & \ddots & \\ c(\widehat{d}_{Q_L},\widehat{d}_1) & \dots & & v(\widehat{d}_{Q_L}) \end{bmatrix}^{-1}, \tag{5.25}$$

contains information about the uncertainty of the estimated coefficients (*Lieb et al.*, 2016). The diagonal elements are the variances $v(\widehat{d}_q)$ of the estimated coefficients. The off-diagonal elements represent the covariances between two coefficients, for instance, $c(\widehat{d}_1,\widehat{d}_2)$ between $\widehat{d}_1$ and $\widehat{d}_2$. $\boldsymbol{Q}_{dd}$ is the $Q_L \times Q_L$ normal equation matrix

$$\boldsymbol{Q}_{dd} = \sum_{k=1}^{K}\left(\frac{1}{\sigma_k^2}\boldsymbol{A}_k^T\boldsymbol{P}_k\boldsymbol{A}_k\right) + \frac{1}{\sigma_d^2}\boldsymbol{P}_d \tag{5.26}$$

expressed on the left side of Eq. (5.23), and inverted in Eq. (5.24).

Synthesis: Computation of gravity field functionals

In order to express different functionals of the Earth's gravity field, the observation equations (5.15) serve as modeling equations in the synthesis. The elements of the vector $\widehat{\boldsymbol{d}}_L$ of estimated coefficients from Eq. (5.24) are again multiplied with adapted scaling functions from Tab. 4.7. However, the functions $\tilde{b}_{l'}(\boldsymbol{x}^c,\boldsymbol{x}_q) = \tilde{\Phi}_{q,J}(\boldsymbol{x}^c,\boldsymbol{x}_q)$ now are related to a maximum resolution level J, as introduced Sec. 4.3.3, and the function values are computed at locations $\boldsymbol{x} = \boldsymbol{x}^c$, $c = 1,\dots,C$, inside a target area $\partial\Omega_I$. Therefore, the SBFs are located, for instance, on a regular grid or along flight tracks in any height on or above the Earth's surface. For the example in Fig. 5.1, Blackman SBFs are located on a regular geographical grid in the study area in Northern Germany, multiplied with the estimated coefficients from the analysis, and visualized up to $J = 11$ in terms of Δg (lower right). The functional relations in Tab. 4.7 can be further complemented by other functionals, e. g. quasi-geoid heights ζ according to Eq. (2.63) or deflections of the vertical ξ,η according to (2.70).

[22] In analogy, error propagation can equivalently be applied to the scaling coefficients Eq. (5.18), estimated from one observation group. Since the combination of several observation groups is in the focus of this work, its description was neglected in Sec. 5.2.1.

Choice of basis functions

According to Eq. (4.33), the adapted scaling function yields

$$\tilde{\Phi}_{q,J} = \Phi_J(\boldsymbol{x}^c, \boldsymbol{x}_q) = \sum_{l=0}^{l_J} \frac{2l+1}{4\pi R^2} \left(\frac{R}{r}\right)^{l+1} \phi_{l,J}\, P_l\left((\boldsymbol{r}^c)^T \boldsymbol{r}_q\right) . \tag{5.27}$$

Since the components of $\widehat{\boldsymbol{d}}_L$ are estimated in the analysis step by strictly bandlimiting non-smoothing Shannon kernels, it is possible to multiply them in the synthesis with a different kernel function (*Schreiner*, 1996), cf. Eqs. (4.11). The use of different functions, defined by $\phi_{l,j} \in \left\{\phi_{l,j}^{\mathrm{Sha}}, \phi_{l,j}^{\mathrm{Bla}}, \phi_{l,j}^{\mathrm{CuP}}\right\}$ according to Eqs. (4.29) – (4.31), is analyzed in Sec. 6.1.1.
The bandlimiting maximum degree $l_J \leq L$ is chosen smaller than the maximum degree L of the analysis in order to reduce aliasing errors in the frequency domain, and thus, erroneous side lobes in the spatial domain, cf. Fig. 5.8. Figure. 5.7 visualizes the principle: Modeling a bandlimited signal g (purple curve) according to Eq. (4.15) up to maximum degree L within the analysis (purple box) from a finite set of function values, yields aliasing errors due to frequency folding (yellow) of the originally infinite signal f (*Jekeli*, 1996). Expanding the series of $\tilde{\Phi}_{q,J}$ in the synthesis (gray box) up to $l_J \leq L$, acting as low-pass filter, here depending on a maximum resolution level J, reduces those aliasing errors (*Schmidt et al.*, 2007).

Modeling equations

In analogy to Eq. (5.20), the system

$$\boldsymbol{z}_J = \boldsymbol{B}_J\, \widehat{\boldsymbol{d}}_L \;\rightarrow \Delta Z_J, \tag{5.28}$$

of modeling equations can be set up by means of $\widehat{\boldsymbol{d}}_L$, estimated from K observation groups according to the extended GMM (5.22), and $\boldsymbol{B}_J$, containing the chosen low-pass filtering SBFs $\tilde{\Phi}_{q,J}$, Eq. (5.27). The output functional values $z_J(\boldsymbol{x}^c)$, collected in the $C \times 1$ vector $\boldsymbol{z}_J$, contain information up to maximum spectral degree l_J and describe the "differential signal" ΔZ_J w.r.t. the background model. The system of modeling equations is highlighted in red in the synthesis box of Fig. 5.9.
Restoring the previously subtracted background model at the modeling positions $\boldsymbol{x}^c$ delivers the "total signal"

$$Z_J = Z_{\mathrm{back}} + \Delta Z_J \tag{5.29}$$

with $Z_{\mathrm{back}} = \mathcal{Y}[\,\tilde{V}_{\mathrm{back}}\,]$. In analogy to computing the differences at locations $\boldsymbol{x}^p$, cf. Eq. (5.13), the functional values Z_{back} at positions $\boldsymbol{x}^c$ are obtained from series expansion (2.40) in terms of SHs. Note, in this work, "total signal" means that the (low up to medium) frequency information of the previously subtracted background model has been restored, in contrast to the "differential signal", where the referring spectral content is missing.

Covariance information of the output functionals

Information about the accuracy and the dependencies of the resulting functionals $z_J(\boldsymbol{x}^c)$ from Eq. (5.28) is obtained by computing the variances and covariances at the output positions $P(\boldsymbol{x}^c)$. Applying error propagation on the modeling equation (5.28)[23], the $C \times C$ covariance matrix $D(\boldsymbol{z}_J)$ reads

$$\begin{aligned} D(\boldsymbol{z}_J) &= \boldsymbol{B}_J D\left(\widehat{\boldsymbol{d}}_L\right) \boldsymbol{B}_J^T \\ &= \begin{bmatrix} v\left(z_J\left(\boldsymbol{x}^1\right)\right) & c\left(z_J\left(\boldsymbol{x}^1\right), z_J\left(\boldsymbol{x}^2\right)\right) & \dots & c\left(z_J\left(\boldsymbol{x}^1\right), z_J\left(\boldsymbol{x}^C\right)\right) \\ c\left(z_J\left(\boldsymbol{x}^2\right), z_J\left(\boldsymbol{x}^1\right)\right) & v\left(z_J\left(\boldsymbol{x}^2\right)\right) & & \vdots \\ \vdots & & \ddots & \\ c\left(z_J\left(\boldsymbol{x}^C\right), z_J\left(\boldsymbol{x}^1\right)\right) & \dots & & v\left(z_J\left(\boldsymbol{x}^C\right)\right) \end{bmatrix} . \end{aligned} \tag{5.30}$$

It contains on the diagonal the variances $v\left(z_J\left(\boldsymbol{x}^c\right)\right)$, now indicating the accuracy of the resulting functional $z_J(\boldsymbol{x}^c)$ up to spectral degree l_J at point P^c, cf. Eq. (5.25). The off-diagonal elements represent the covariances

[23] In analogy, error propagation can be applied to the modeling equation (5.20).

between two values, for instance, $c(z_J(\boldsymbol{x}^1), z_J(\boldsymbol{x}^2))$ at the output grid points P^1 and P^2. They give a measure for the dependency, i. e. the correlation, between the values of both points.

↪ In the following, all investigations are transferred from single-level to multi-level combination via MRR.

5.3 Spectral combination via MRR

Spectral combination of heterogeneous gravity data within a MRR enables (1) capturing as optimally as possible information from each data set and (2) increasing the information content of the resulting regional models. Due to those beneficial advantages, the spectral combination via MRR is realized in this work. *Kern* (2003), pp. 81, discusses further methods, as e. g. LSC, one of the most prominent approaches.
In Fig. 5.10, the general principle of the spectral combination is visualized as an upgrade of Fig. 5.9: The single-level combination of several observation groups, presented in the previous section, now is applied at different resolution levels. Hereby, the data of various measurement techniques contribute at the levels where they show their highest sensitivity. It is implemented by filling several analysis boxes (blue boxes, collected in the light orange box on the lower left in Fig. 5.10) and connect them by a MRR bottom-up approach according to Fig. 4.7, left side. Vice versa, the synthesis boxes (light purple boxes in the dark orange box on the lower right in Fig. 5.10) of the resulting output functionals at different spectral domains can be connected in a MRR top-down approach according to Fig. 4.7, right side.

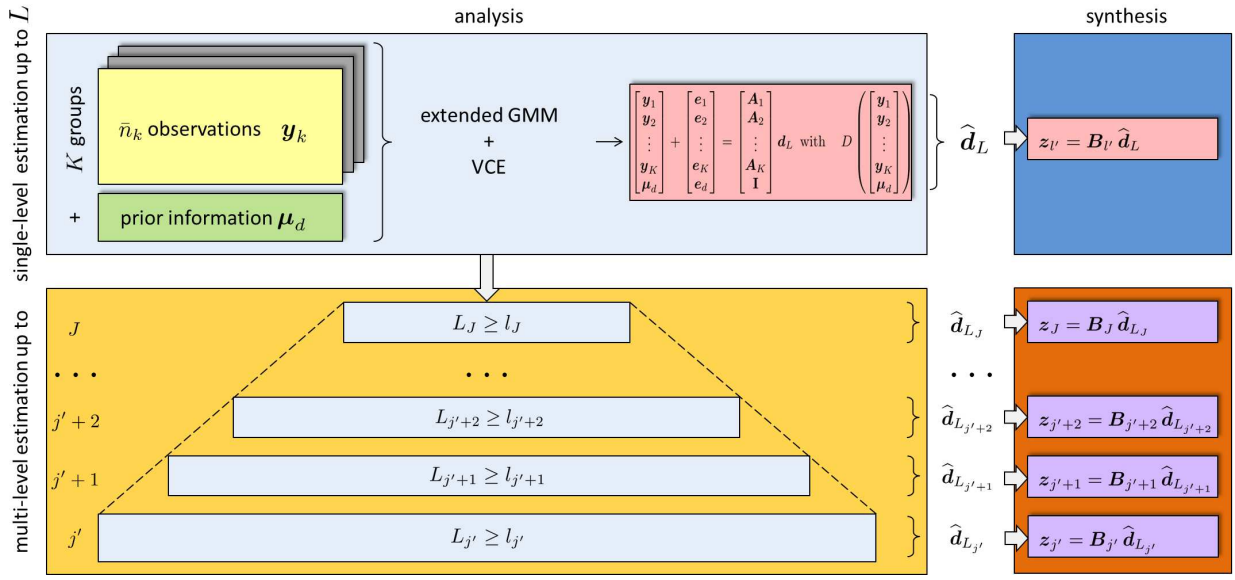

Figure 5.10: Analysis and synthesis from a single-level estimation of unknowns at one resolution level within an extended GMM and VCE (blue boxes; upper row); MRR from several single-level estimation models (several blue analysis boxes are set up) at different levels j yield a multi-level estimation up to level J (orange boxes; lower row).

5.3.1 Analysis and choice of observation groups

In order to fill the blue analysis boxes within the MRR as displayed in Fig. 5.10, the estimation of the coefficient vector $\widehat{\boldsymbol{d}}_L$ from a single-level combination of heterogeneous data in the extended GMM according to Eq. (5.24), is applied at different resolution levels j. For the connection of the levels, specific settings are required and discussed in the following.

Choice of basis functions

The choice of Shannon SBFs within the analysis, is appropriate for a spectral combination of diverse observation data. The functions ensure the exact splitting of frequency bands and enable to extract signal content at each resolution level without any loss or overlap. The characteristic Legendre coefficients, cf. Eq. (4.29), now are defined as $\phi^{\mathrm{Sha}}_{l,L_j}$, for $j = j'+1, j'+2, \ldots, J$, with a bandlimiting degree $L_j \geq l_j$, e. g. $L = 140$ at $j = 7$, $L = 280$ at $j = 8 \ldots$, referring to Fig. 5.5. If L_J is chosen higher than the maximum degree l_j of each resolution level j, aliasing errors due to frequency folding can be reduced in the synthesis, as discussed in the context of Fig. 5.7. The series of corresponding SBFs are truncated at the same level-depending bandlimiting degree L_j, cf. case (d) in Fig. 4.1. Further, the functions have to be adapted to the different gravitational functionals according to Tab. 4.7. It yields

$$\tilde{\Phi}_{L_j}(\boldsymbol{x}^p, \boldsymbol{x}_q) = \sum_{l=0}^{L_j} \frac{2l+1}{4\pi R^2} \left(\frac{R}{r}\right)^{l+1} \phi^{\mathrm{Sha}}_{l,L_j} \, P_l\left((\boldsymbol{r}^p)^T \boldsymbol{r}_q\right) . \tag{5.31}$$

for the Shannon function up to level j, adapted to $\mathcal{Y}[\,\tilde{V}\,] = T$. These scaling functions are the components of the design matrices $\boldsymbol{A}_k$ (e. g. for one observation group k) in the extended GMM (5.22), which is set up at each level. In Fig. 5.10, every blue box represents one of those single-level estimations; the decreasing size bottom-up indicates decreasing spectral bandwidths at increasing resolution levels. The resulting estimated coefficient vectors $\widehat{\boldsymbol{d}}_{L_j}$ from Eq. (5.24), cf. Fig. 5.10, contain information each up to $L_j \geq l_j$

Choice of observation groups

In analogy to Eq. (5.13), an appropriate background model is selected and subtracted from all observations as discussed above, now up to resolution level j', cf. Eq. (5.10). At each level $j = j'+1, \ldots, J$ the observation groups which contribute most spectral information relatively to the others have to be identified. In this work, the choice follows the three-step strategy displayed in Fig. 5.11:

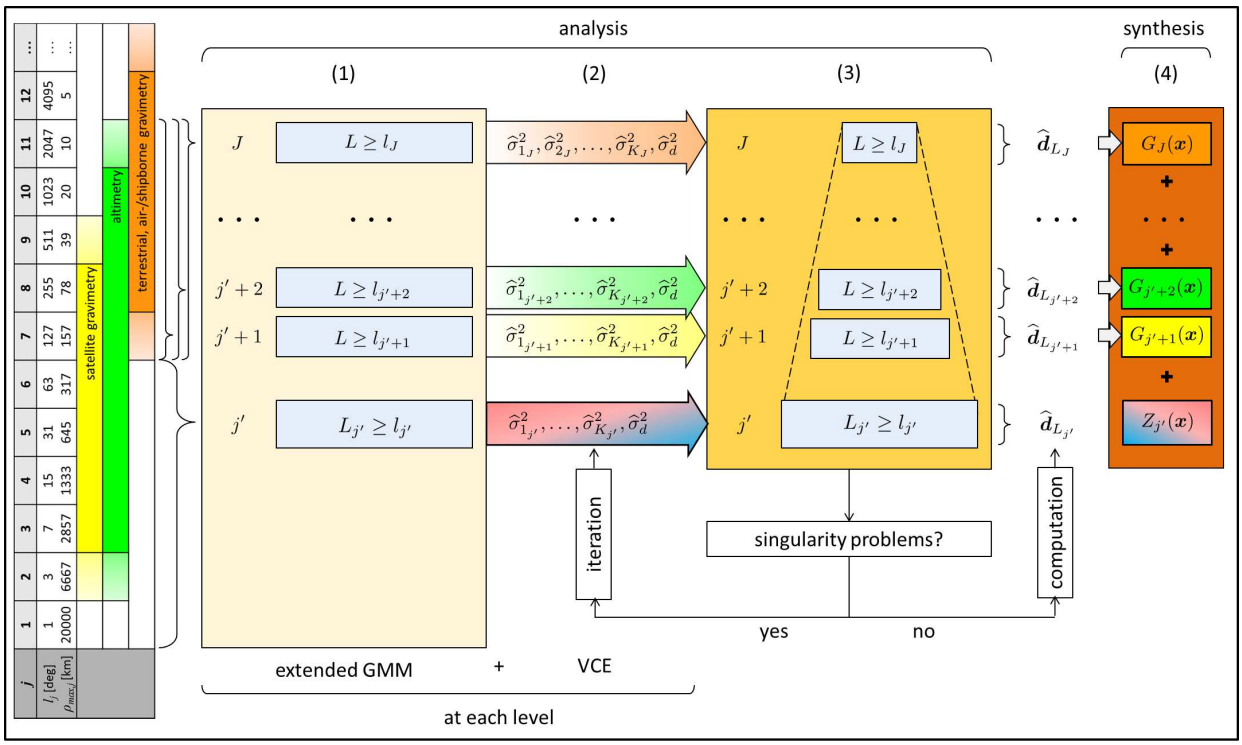

Figure 5.11: Choice of observation groups for the spectral combination via MRR.

(1) Single-level estimation at each level with all observation groups The extended GMM is set up according to Eq. (5.22) at each level, using all observation groups K. In Fig. 5.11 it is indicated by introducing the classified observations according to Tab. 4.8 at level $j', j'+1, j'+2, \ldots, J$ in the blue analysis boxes with according maximum degrees $l_{j'}, l_{j'+1}, l_{j'+2}, \ldots, l_J$. The maximum resolution level of the resulting regional model is exemplarily chosen with $J = 11$, the minimum level with $j' = 6$, cf. Eq. (5.10). Thus, a background model is subtracted from the observations up to $j = 6$ with maximum degree $l_6 = 63$, serving further as prior information $\boldsymbol{\mu}_d$, as introduced in Eq. (5.19).

(2) Relative weighting of observation groups at each level The observation groups are weighted relatively to each other by VCE following *Koch and Kusche* (2002), in analogy to the single-level combination presented above. As the influence of the K single groups to the resulting regional model is regulated by the variance factors $\widehat{\sigma}^2_{1_j}, \widehat{\sigma}^2_{2_j}, \ldots, \widehat{\sigma}^2_{K_j}, \widehat{\sigma}^2_d$, the latter are used as indicators for the choice of the observation groups, which contribute relatively to each other the most spectral information at each level j. In Fig. 5.11, the estimated VCs of step (2) are the output of the analysis boxes of step (1), arranged in colored arrows. The colors indicate, referring to the classification of data types (orange for high-resolution terrestrial, air- and shipborne gravimetry, green for high- down to medium-resolution altimetry, and yellow for mid- down to low-resolution satellite gravimetry data), the dominant type of observation groups which typically get the highest relative weights at the according levels. At lowest resolution level j' (red-blue shaded), most of the information is removed from the observations by the subtracted background model. The relative weighting of the K groups depends above all on the availability of data, on their spectral content (i. e. resolution), accuracy and spatial distribution – hence, on the individual modeling task.

(3) MRR composition from single-level estimations Besides using the VCs from step (2) as first criterion, two further criteria are defined for selecting appropriate observation groups at each level:

- High sensitivity: Observation groups with smallest VCs are supposed to show the highest sensitivity and deliver the most spectral information at the corresponding level. It is the main criterion, see step (2).
- No correlations: Referring to the introduction of the weight matrices $\boldsymbol{P}_k$ and $\boldsymbol{P}_d$ in Eq. (5.22) as identity matrices, the observation groups are assumed to be uncorrelated, i. e. their information should contribute only to one level.
- Spectral range and spatial distribution (prior information not sufficient): The second criterion is not strictly kept, if spectral or spatial data gaps lead to singularity problems when solving the normal equations (5.23). Especially at higher resolution levels, the low spectral content of the prior information $\boldsymbol{\mu}_d$ up to degree $l_{j'}$ might not be sufficient to overcome the gaps.

The third criterion requires the introduction of further observation groups, i. e. repeated contribution of the same data sets at different levels. Consequently, the modeling results (i. e. the detail signals G_j) of neighboring levels, obtained from the synthesis, are no longer independent of each other and contain superposing information when summing them up within the MRR, cf. step (4) in Fig. 5.11. (Note, this step (4) is identical to step (d) in Fig. 4.5.) The effects and the role of the prior information is discussed in Sec. 6, by means of numerical results.
The here presented approach of selecting observation groups according to the three criteria yields an iterative process of steps (2) and (3) until no more singularities appear in the normal equations, trying to avoid as much correlations as possible. This strategy is not as efficient, but quite effective, as which can be seen from the numerical applications in the next chapter.

Estimation of unknowns and their covariance information

Step (3) of Fig. 5.11 schematically indicates the spectral combination of the selected observation groups (cf. light orange analysis box in Fig. 5.10): By serving as input at each level, the estimates $\widehat{\boldsymbol{d}}_{L_j}$ of the coefficient vectors (output of analysis) can be computed according to Eq. (5.24); here $\widehat{\boldsymbol{d}}_{L_6}, \widehat{\boldsymbol{d}}_{L_7}, \ldots, \widehat{\boldsymbol{d}}_{L_11}$. The covariance information $D(\widehat{\boldsymbol{d}}_{L_j})$, cf. Eq. (5.25), is obtained from the inverse normal equation matrices $\boldsymbol{Q}_{dd,j}$, Eq. (5.26),

computed at at each level j. It yields

$$D\left(\widehat{\boldsymbol{d}}_{L_j}\right) = \boldsymbol{Q}_{dd,j}^{-1} = \begin{bmatrix} v(\widehat{d}_{L_j,1}) & \dots & c(\widehat{d}_{L_j,1}, \widehat{d}_{L_j,Q_L}) \\ c(\widehat{d}_{L_j,2}, \widehat{d}_{L_j,1}) & & \vdots \\ \vdots & \ddots & \\ c(\widehat{d}_{L_j,Q_L}, \widehat{d}_{L_j,1}) & \dots & v(\widehat{d}_{L_j,Q_L}) \end{bmatrix}^{-1} . \tag{5.32}$$

5.3.2 Synthesis and spectral composition

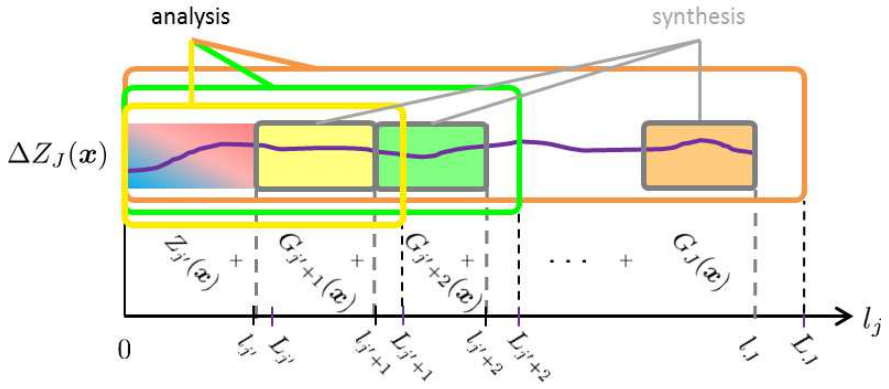

Figure 5.12: Synthesis (gray boxes) of MRR low- (yellow-shaded), mid- (green-shaded), up to high- (orange-shaded) resolution detail signals G_j, and the low-resolution signal $Z_{j'}$ up to degree $l_j < L_j$ in the spectral domain. The analysis comprises the frequency spectrum up to a higher degree L_j (red/blue, yellow, green, orange boxes). Adding G_j and Zj' yields the differential bandlimited signal ΔZ_J w.r.t. the background model (one-dimensional representation in purple).

The synthesis of the estimation models (5.22), set up at the corresponding resolution levels, finally yields the low-pass filtered signal $Z_{j'}$ and the band-pass filtered detail signals $G_{j'+1}$, $G_{j'+2}, \dots, G_J$ of the differential signal ΔZ_J. Adding them, and restoring the background model results in the total signal Z_J, according to the MRR defined in Eq. (4.28).

Choice of basis functions

In order to spectrally combine the signal content as visualized in Fig. 4.5 (c), Shannon wavelet functions $\Psi_j(\boldsymbol{x}^c, \boldsymbol{x}_q)$, Eq. (4.39), are used with Legendre coefficients $\psi_{l,j}^{\text{Sha}}$ according to Eq. (4.36) for the levels $j = j' + 1, \dots, J$, i. e.

$$\tilde{\Psi}_j(\boldsymbol{x}^c, \boldsymbol{x}_q) = \sum_{l=0}^{l_j} \frac{2l+1}{4\pi R^2} \left(\frac{R}{r}\right)^{l+1} \psi_{l,j}^{\text{Sha}} \, P_l\left((\boldsymbol{r}^c)^T \boldsymbol{r}_q\right) . \tag{5.33}$$

At the lowest level j', the low-pass filtering scaling function

$$\tilde{\Phi}_{j'}(\boldsymbol{x}^c, \boldsymbol{x}_q) = \sum_{l=0}^{L_{j'}} \frac{2l+1}{4\pi R^2} \left(\frac{R}{r}\right)^{l+1} \phi_{l,j'}^{\text{Sha}} \, P_l\left((\boldsymbol{r}^c)^T \boldsymbol{r}_q\right) . \tag{5.34}$$

is formulated according to Eq. (4.33). The adapted scaling ($\tilde{\Phi}_{j'}(\boldsymbol{x}^c, \boldsymbol{x}_q)$) and wavelet ($\tilde{\Psi}_j(\boldsymbol{x}^c, \boldsymbol{x}_q)$) functions can express any output functional, according to the relations from Tab. 4.7. The bandlimiting maximum degree $l_j \leq L_j$ refers to the level-discretization defined in Eq. (4.24), and is chosen smaller than the maximum degree L_j of the analysis in order to avoid aliasing errors, cf. Fig. 5.7. The principle is exemplarily displayed in Fig. 5.12 for three detail signals: the yellow-, green- and orange-bordered boxes contain the spectral content of the estimated coefficients from the analysis up to L_j; the gray boxes depict the spectral domain of the yellow-, green-, and orange-shaded detail signals, obtained from the synthesis by the band-pass filtering

wavelet functions up to degree l_j. The colors again correspond to the spectral classification of input data in Fig. 4.5 (b).

Modeling equations

The low-resolution signal $Z_{j'}$ and the detail signals G_j are obtained setting up the modeling equations (purple boxes in the synthesis step, Fig. 5.10 dark orange)

$$\begin{aligned} z_{j'} &= \boldsymbol{B}_{j'}\,\widehat{\boldsymbol{d}}_{L_{j'}} \rightarrow Z_{j'} \\ z_{j'+1} &= \boldsymbol{B}_{j'+1}\,\widehat{\boldsymbol{d}}_{L_{j'+1}} \rightarrow G_{j'+1} \\ z_{j'+2} &= \boldsymbol{B}_{j'+2}\,\widehat{\boldsymbol{d}}_{L_{j'+2}} \rightarrow G_{j'+2} \\ &\vdots \\ z_J &= \boldsymbol{B}_J\,\widehat{\boldsymbol{d}}_{L_J} \rightarrow G_J\,, \end{aligned} \tag{5.35}$$

according to Eq. (5.28) of a single-level combination. The $C\times 1$ vectors $\boldsymbol{z}_j$ contain the output functional values $\left[z_j(\boldsymbol{x}^c)\right]$, $\boldsymbol{x}^c \in \Omega_I$, $c = 1, 2, \ldots, C$ of any desired functional $\mathcal{Y}[\,\tilde{V}\,]$. They are computed by means of the estimated coefficient vectors $\widehat{\boldsymbol{d}}_{L_j}$, cf. orange box (4) in Fig. 5.11. The $C \times Q_{L_j}$ matrices $\boldsymbol{B}_j$ are set up by the adapted wavelet functions from Eq. (5.33) for the levels $j = j' + 1, \ldots, J$, and by the adapted scaling function from Eq. (5.34) for level j'. For each vector $\boldsymbol{z}_j$, cf. Eq. (5.35), the covariance information $D(\boldsymbol{z}_j(\boldsymbol{x}^c))$ can be obtained according to Eq. (5.30): Applying error propagation on the covariance matrix $D(\widehat{\boldsymbol{d}}_{L_j})$, Eq. (5.32), of the estimated parameters, yields the $C \times C$ covariance matrix $D(\boldsymbol{z}_j)$ of the output signal $\boldsymbol{z}_j$ at each modeling point $P(\boldsymbol{x}^c)$ w.r.t. level j, i. e.

$$D\left(z_j(\boldsymbol{x}^c)\right) = \boldsymbol{B}_j D\left(\widehat{\boldsymbol{d}}_{L_j}\right)\boldsymbol{B}_j^T = \begin{bmatrix} v\left(z_j(\boldsymbol{x}^1)\right) & \ldots & c\left(z_j(\boldsymbol{x}^1), z_j(\boldsymbol{x}^C)\right) \\ c\left(z_j(\boldsymbol{x}^2), z_j(\boldsymbol{x}^1)\right) & & \vdots \\ \vdots & \ddots & \\ c\left(z_j(\boldsymbol{x}^C), z_j(\boldsymbol{x}^1)\right) & \ldots & v\left(z_j(\boldsymbol{x}^C)\right) \end{bmatrix}, \tag{5.36}$$

according to Eq. (5.30).

Spectral composition and error propagation

Adding the low-resolution signal $Z_{j'}$ and the detail signals G_j of successive resolution levels j, obtained from the synthesis according to Eqs. (5.35), describes the so-called **differential signal**

$$\Delta Z_J = \Delta Z_J(\boldsymbol{x}^c) = Z_{j'} + \sum_{j=j'+1}^{J} G_j(\boldsymbol{x}^c)\,, \tag{5.37}$$

of any gravitational functional $\mathcal{Y}[\,\tilde{V}\,]$ at a modeling point $P(\boldsymbol{x}^c)$ w.r.t. the background model. ΔZ_J is bandlimited, comprising the low-, medium- and high-resolution levels up to J. This differential MRR-output signal ΔZ_J represents the result of the spectral combination of diverse heterogeneous observation groups according to Eq. (4.28).
Restoring the the background model $Z_{\text{back}} = \mathcal{Y}[\,\tilde{V}_{\text{back}}(\boldsymbol{x}^c)\,]$ – vice versa to Eq. (5.14) – now to the estimated differential signal ΔZ_J, results in the **total signal** $Z_J = Z_J(\boldsymbol{x}^c)$, cf. Eq. (5.29). Vice versa to the spectral composition (bottom-up), the signal Z_J can also be decomposed (top-down) into several detail signals by successively low-pass filtering, as schematically displayed in Fig. 4.7 and exemplarily visualized in Fig. 5.1. Both scenarios are studied by numerical applications in Sec. 6.2.
In analogy to summing up the low-resolution signal $Z_{j'}$ and the detail signals G_j of the levels $j', j'+1, \ldots, J$ yielding the spectrally combined output signal ΔZ_J, the corresponding accuracy of the differential signal is

obtained by adding the variances $v(z_j(\boldsymbol{x}^c))$ of $\boldsymbol{z}_j$, referring to one modeling point $P(\boldsymbol{x}^c)$, i. e.

$$v_J(z(\boldsymbol{x}^c)) = \sum_{j=j'}^{J} v(z_j(\boldsymbol{x}^c)) \,. \tag{5.38}$$

Since the background model was assumed to be noise free, the restored low-resolution signal Z_{back} is also assumed to be noise free. Consequently, the variances $v_J(z(\boldsymbol{x}^c))$, cf. Eq. (5.38), derived for the differential signal $\Delta Z_J(\boldsymbol{x}^c)$, cf. Eq. (5.37), account for the total signal $Z_J(\boldsymbol{x}^c)$ as well. They give an estimate of the accuracy of the regional model w.r.t. the spectral domain of the estimated levels. Hereby, the assumptions are:

- The signal values of $Z_{j'}$ and G_j are uncorrelated in case of Shannon, i. e.
- the covariances, e. g. $c(z_j(\boldsymbol{x}^1), z_{j+1}(\boldsymbol{x}^1))$ between the signal of one point $P(\boldsymbol{x}^1)$ at two different levels, j and $j+1$, are zero (respectively, the covariance $c(z_j(\boldsymbol{x}^1), z_{j+1}(\boldsymbol{x}^2)) = 0$ between the signal of different points, $P(\boldsymbol{x}^1)$ and $P(\boldsymbol{x}^2)$, at different levels), i. e.
- the signals are estimated from different input data,
- the different input data groups provide independent data sets, and
- their long-wavelength errors are small.

Hence, special attention has to be paid to step (3) in Fig. 5.11, the choice of independent input data at each level, as discussed above. Further, the effect of regularization has to be taken into account depending on the relative weight of the prior information. Details and the reliability of the assumptions are studied by means of numerical applications in Sec. 6. Remaining error influences and uncertainties are summarized in Tab. 7.1 in the end.

6 Results, Validation and Discussion

The primary aim of this thesis is the development of a proper, stable and efficient regional gravity modeling approach in order to combine heterogeneous real data via MRR. Three secondary aims can be derived, i. e.

1. verification and judgment of properness, stability and efficiency of the approach,
2. computation of very high-resolution regional gravity fields, and thus,
3. regional refinements of existing global models.

The first point includes the questions, how accurately the approach fits simulated as well as real data, single as well as multiple data sets, and if the chosen estimation model (cf. Sec. 5.2) and settings (cf. Sec. 5.1) are appropriate. The covariance information of estimated parameters and output functionals gives a measure for the model accuracy, correlations, and the handling of noise. From simulation studies in terms of closed-loop (CL) tests (Sec. 6.1.1), the consistency and stability of the approach may be rated (in the sequel, denoted as "internal validation"), while the efficiency can be evaluated from comparisons with other approaches.
Taking the findings into account, the approach then is applied using real observations (6.1.2). High-resolution regional gravity field models and their accuracy can be derived. An "external validation" shall prove the accuracy. By validating the regional results against global models or against further data sets in terms of a cross-validation, issues, as e. g. if the stochastic model is realistic, can be addressed.
In Sec. 6.2, the spectral combination of real data via MRR is applied. The beneficial peculiarities of the MRR approach enable detecting data gaps and closing them spectrally by merging information from appropriate measurement techniques. The resulting regional models may provide, for instance, the basis for national height systems (second secondary aim), serve as regional refinements of global models (third secondary aim), or can be used for many geophysical applications at different spectral domains, as e. g., studying density variations of the Earth's interior.

The primary, as well as the three secondary aims, shall be discussed in the following by means of selected study results. In principle, two categories are distinguished: Section 6.1 investigates results from the single-level estimation model, set up at one resolution level according to Sec. 5.2.2; Section 6.2 investigates results from the spectral combination model via MRR, according to Sec. 5.3. Table 6.1 gives an overview of the classification of the different study cases. The arrangement of options to study follows a top-down flow chart. The selection of parameters (light gray shaded) is arranged along the vertical axis w.r.t. their "influence on the target achievement"; The "complexity" of options is arranged along the horizontal axis. The chosen parameters turned out to have the largest influence within the here presented modeling approach.

Number of levels The first parameter, i. e. setting up the approach at one or at multiple resolution levels, separates the two general categories, Sec. 6.1 and Sec. 6.2, and thus, has the largest influence.

Type of data sets Second, results obtained from simulated and real data are distinguished. While simulation studies in Sec. 6.1.1 serve especially to achieve the first secondary aim as mentioned above, the studies on real data in Secs. 6.1.2 and 6.2 mostly relate on specific applications, see second and third secondary aim.

Number of data sets Before the combination of heterogeneous data sets is explored, the approach is tested by using single data sets.

Stochastic information Distinguishing between noise-free and noisy data restricts to simulated data sets, as all real data naturally show a stochastic behavior. The noise-free case further is tested only for one single data set.

Variety of functionals Consequently, referring to the selection above, several different functionals (at different observation heights) and their field transformations can only be studied for multiple data sets.

Data set The data sets (dark gray shaded) and the referring study cases (a) – (g) are classified w.r.t. the different options to investigate. Their arrangement along the horizontal axis symbolizes increasing complexity from left to right.

The light-purple boxes in the background visualize validation and comparison strategies applied for one or several results: For the simulation studies (a) – (c) closed-loop tests are appropriate, while the accuracy of real data results is verified by trace criterion (d) for GOCE GGs, or X-calibration (e). The results (e) – (g) further are compared with global SH models.

6.1 Single-level approach

6.1.1 Simulation studies

The central question to be answered in this section is: How well does the regional model fit the input data? Therefore, simulation studies are appropriate: From an existing global gravity model observations are simulated, which then are used as input for the regional modeling approach. The output model should deliver the same values as the input model, i. e. optimally fit the known input data. The simulation data are obtained from the analysis of a global SH model by computing different gravitational functionals in a certain study area, e. g. at the grid points of a geographic grid. Modeling as output the same gravitational functional and at the same locations, cf. study cases (a) and (b), allows to compute their differences; they should converge to zero in the frame of computational accuracy of 1×10^{-16}. (For all numerical investigations, a computer applying 16 digits is used.) If variations of the closed-loop settings, cf. case (c), as e. g. comparing the in- and output functional in another altitude, deliver similar accuracy by the CL differences, the approach is assumed to be consistent and stable and, thus, verified for the application of real data.

Study cases (a) and (b): One in-/output functional

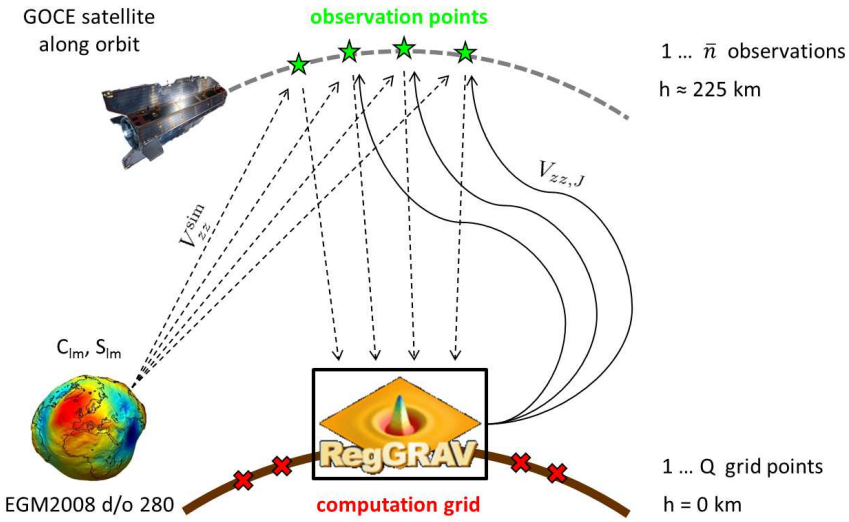

Figure 6.1: Closed-loop scenario using simulated V_{zz}^{sim} GOCE data from EGM2008 up to d/o 280: The differences $V_{zz}^{\text{sim}} - V_{zz,8}$ of the simulated observations and modeled output values are computed at the observation points (green stars) along the gray-dashed GOCE orbit ($h \approx 225\,\text{km}$). The computation grid (red crosses) of the RegGRAV approach is located at the Earth's surface (brown solid line at $h = 0\,\text{km}$). Simulations are visualized by black-dashed arrows, regionally modeled values by solid black ones.

Table 6.1: Classification of study cases from single-level approach (a) – (e) and from spectral combination via MRR (f) – (g).

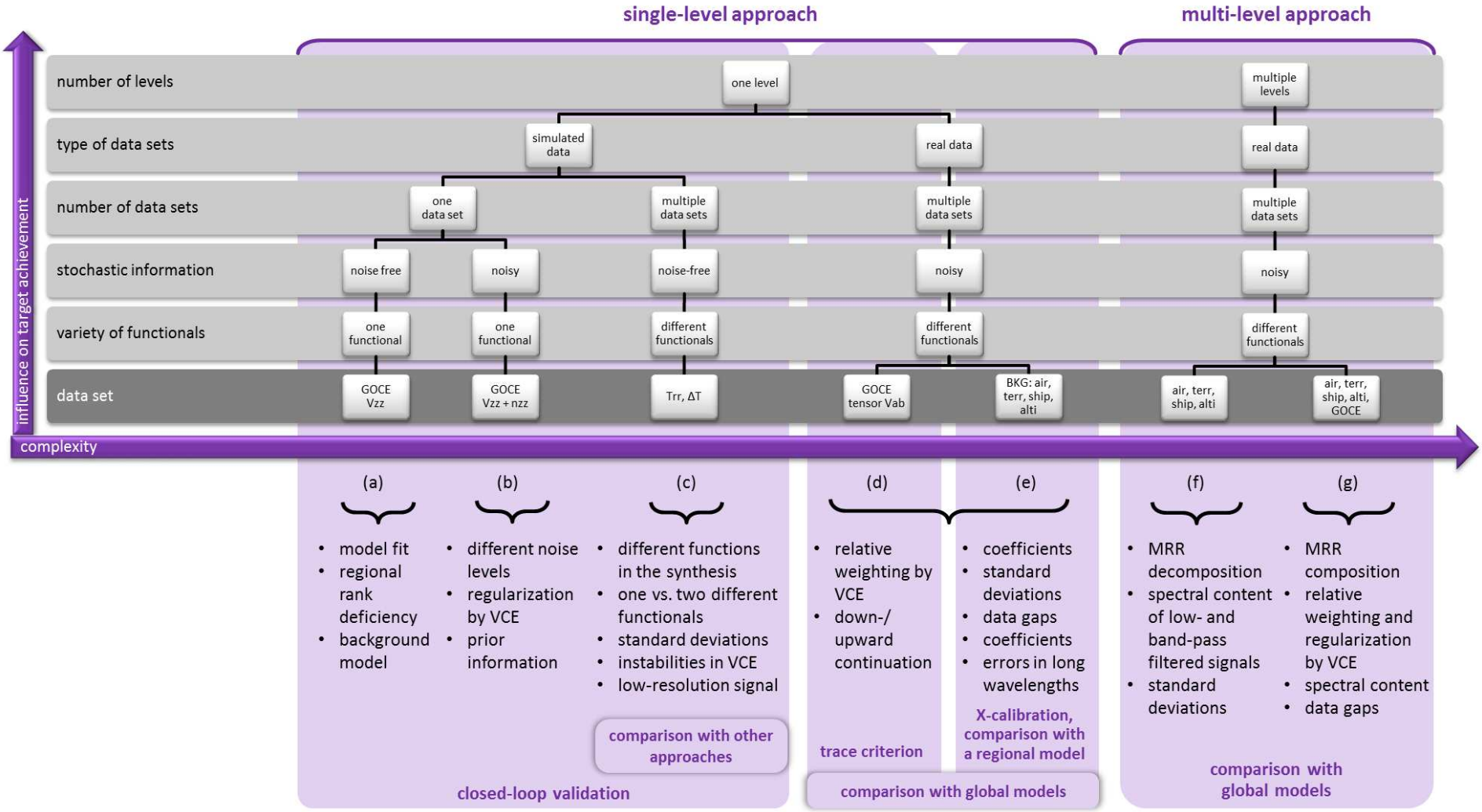

Different closed-loop scenarios are discussed in the following in order to validate the regional output models and rate the methodical settings. Due to the large variety of options, only a selection can be investigated. According to Tab. 6.1, the study cases (a) and (b), w.r.t. one and the same in-/output gravitational functional, consider:

Study case (a) CL differences at observation points at satellite altitude: How well does the regional model fit noise-free data?

Study case (b) CL differences using noisy observations. How strong is the model fit influenced by noisy observations?

(a) and (b) How large is the regional rank deficiency? How strong is the regularization and the corresponding influence of the prior information?

Figure 6.1 shows the principle of the closed-loop scenario using one and the same gravitational functional as in- and output. The regional gravity modeling approach is set up in the study area of Northern Germany, cf. Fig. 5.1, based on the methodical settings from Sec. 5.1. The chosen specifications are listed in Tab. 6.2 for a maximum resolution level $J = 8$ and are explained in the following.

Table 6.2: Study cases (a) and (b): Specifications.

Input $\partial\Omega_O$	(a)	· V_{zz}^{sim} simulated from EGM2008
		· $L_{\text{obs}} = 280$
		· $\bar{n}$ =34 680 measurement positions (λ, φ, r) from lower orbit phase, time span 08/2012 - 11/2013
	(b)	· V_{zz}^{sim} + white noise $n_{zz}^{0.01}$
		· V_{zz}^{sim} + white noise $n_{zz}^{0.1}$
		· V_{zz}^{sim} + white noise $n_{zz}^{0.5}$
		· V_{zz}^{sim} + white noise $n_{zz}^{1.0}$
Approach $\partial\Omega_C$		· $V_{\text{zz,back}}$: EGM2008, $l_{j'} = 127$ ($j' = 7$)
		· prior information: EGM2008, $l_{j'} = 127$
		· $L = 280$ (analysis, Shannon)
		· $Q_L = 282$ unknowns, Reuter grid points respectively
		· $R_{\text{Reuter}} = 6378.137$ km grid radius
		· $l_J = 255$ ($J = 8$, synthesis, Shannon)
Output $\partial\Omega_I$	(a)	· $\Delta V_{zz,8}$
	(b)	· $\Delta V_{zz,8}^{\alpha}$
	(a), (b)	· at original positions (λ, ϕ, r) ($C = 4981$)

Simulated input data The global SH model EGM2008, described in Sec. 3.2.2, serves as basis for the simulation: From the given set of SH coefficients $C_{l,m}$, $S_{l,m}$, the radial gravity gradient V_{zz}^{sim} is computed along the GOCE tracks according to Eq. (2.79) by expanding the series (2.40) of SHs up to degree and order 280. The positions $\boldsymbol{x}^p \in \Omega_O$ are represented by green stars along the gray dashed orbit in Fig. 6.1, for further information see Tab. 6.2. Since the observations are simulated up to $L_{\text{obs}} = 280$, resolution level $J = 8$ is the highest level which is completely covered by their spectral information, cf. Tab. 4.8. Using those simulated V_{zz}^{sim} observations, a first **study case (a)** is investigated at the positions $\boldsymbol{x}^p = \boldsymbol{x}^c \in \Omega_I$ of the original GOCE observations, discussing the model fit and the regional rank deficiency.
In order to approximate simulation studies to real data studies, the influence of noise shall be investigated. GOCE GGs are assumed to be overlaid by Gaussian white noise in the MBW (*Haberkorn et al.*, 2014).[24] Hence, in a more realistic **study case (b)**, simulated noise is added on top of the noise-free observations V_{zz}^{sim}, i. e.

$$V_{zz}^{\text{sim},\alpha} = V_{zz}^{\text{sim}} + n_{zz}^{\alpha} \,. \tag{6.1}$$

Hereby, the factor α allows to regulate the noise level. In this study, the values $\alpha \in \{0, 0.01, 0.1, 0.5, 1.0\}$ are exemplarily chosen for simulating an increasing noise level in order to test the stability of the regional

[24] Colored noise predominates the noise characteristic in the spectral domain below the MBW. The spectrum of white noise is characterized by a constant power spectral density over a certain frequency domain, i. e. by a continuum of frequencies equally distributed over a certain frequency spectrum, here the MBW of GOCE.

modeling approach. The noise n_{zz}^{α} corresponds to around 0.08 mE ($\alpha = 0.01$), 0.81 mE ($\alpha = 0.1$), 4.07 mE ($\alpha = 0.5$), 8.14 mE ($\alpha = 1.0$); $\alpha = 0$ means the noise-free case (a) with $n_{zz}^{\alpha=0} = 0$.[25]

Methodical settings The "RegGRAV" box in Fig. 6.1 symbolizes the regional gravity modeling approach in analogy to Fig. 2.9), established by the methodical settings in Sec. 5.1, and including the (extended) GMM estimation model presented in Sec. 5.2 as core component. The computation grid (Reuter grid at $J = 8$, cf. Sec. 5.1.1) is located near the Earth's surface (red crosses along brown solid line) at $h = 0$ km.
The three areas are defined according to Sec. 5.1.2 and displayed in Fig. 6.3: $\partial\Omega_O$ (with input GOCE tracks in gray), $\partial\Omega_C$ (with red Reuter grid points at level $J = 8$), and $\partial\Omega_I$ (for the regional output model in Northern Germany, green bordered). The area margins count $\eta^8 \approx 2.5$ ($\varphi_{\max} = 55°$), cf. Eq. (5.5).

Regional rank deficiency The regional rank deficiency k_L^{reg}, cf. Eq. (5.8), can be computed from the relation of the regional to the global area ratio, respectively the ratio of the regional to global number of Reuter grid points according to Eq. (5.6):

- Computing the observation area $A_{\partial\Omega_C}$ with minimum and maximum geographical coordinates ($\lambda_{\min}$, $\varphi_{\min}$) = (1.297°,48.597°) and ($\lambda_{\max}, \varphi_{\max}$) = (18.903°,59.903°) according to Eq. (5.7), the area ratio yields $A_{\partial\Omega_C}/A_{\Omega_R} \approx 0.0028$, cf. Eq. (5.6).
- With $N_{280}^{\text{glob}} = Q_{280}^{\text{glob}} = 100\,394$ from Tab. 5.1 and $Q_L = 282$ from Tab. 6.2, the ratio of number of grid points yields $Q_L/Q_L^{\text{glob}} \approx 0.0028$. Thus, as postulated, both the area and the grid point ratio deliver the same value.
- Inserting the latter and Q_{280}^{glob} in Eq. (5.8) delivers the estimate $k_{280}^{\text{reg}} \approx 60$ of the regional rank deficiency.
- With Q_{255}^{glob} at level $J = 8$ ($l_J = 255$), according to Tab. 5.1, the upper estimate L^{rank} of the maximum modeling degree L yields $L^{\text{rank}} \approx 288$, cf. Eq. (5.11).

Background model As discussed in Sec. 5.1.6, in simulation studies it is appropriate to subtract the same background model from the input data as which is used for generating the latter, i. e. here EGM2008. Consequently, in the noise-free case (a), the low-resolution information is completely removed from the observations V_{zz}^{sim}; for noisy observations (b) $V_{zz}^{\text{sim},\alpha}$, the added white noise remains in the low spectral domain.
The resolution of the background model depends on different aspects, as discussed in Sec. 5.1.6: From the average spatial extension $\Pi = 550$ km of the test region in Northern Germany, a minimum modeling resolution level of $j' = 5$ is estimated by Eq. (5.10). This defines the maximum spectral resolution of the background model in order to ensure spectral consistency. However, since dealing with small quantities allows a more accurate model fit, the background model EGM2008 is computed up to level $j' = 7$ (degree $l_{j'} = 127$) in terms of $V_{zz,\text{back}}$. It is displayed in Fig. 6.2 at a constant height of $h = 225$ km; the values range from 2778.84 E to 2779.20 E. Removing $V_{zz,\text{back}}$ according to Eq. (5.14) from the simulated input data yields the differential observations

$$\Delta V_{zz}^{\text{sim},\alpha} = (V_{zz}^{\text{sim}} + n_{zz}^{\alpha}) - V_{zz,\text{back}} \tag{6.2}$$

[25] The values of $\Delta Z_J = \Delta V_{zz,8}$, i. e. of the modeled differential output functional $\mathcal{Y}[\tilde{V}] = \Delta V_{zz,8}$ up to level 8 according to Eq. (5.37) from noise-free input data $\Delta V_{zz}^{\text{sim}}$, satisfy the normal distribution $\mathcal{N}\left(\bar{V}_{zz}^{\text{sim}}; v(\Delta V_{zz,8})\right)$, with mean value $\Delta\bar{V}_{zz,8} = 0.390$ mE and variance $v(\Delta V_{zz,8}) = (8.143\,\text{mE})^2$ within the frequency domain of spectral degrees $l = 128, \ldots, 255$. The Gaussian white noise n_{zz}^{α} then is produced w.r.t. $\mathcal{N}\left(\bar{V}_{zz}^{\text{sim}}; \alpha \cdot v(\Delta V_{zz,8})\right)$ by a Gaussian random number generator (source: `https://www.random.org/gaussian-distributions/`).

for the (a) noise-free ($\alpha = 0$; $n_{zz}^{\alpha=0} = 0$) and (b) noisy cases. The corresponding differential EGM2008 model, containing spectral content of degree $l = 128, \ldots, 280$, is displayed in Fig. 6.3 (i) in the target area $\partial\Omega_I$. For visualization purposes, EGM is plotted in $\partial\Omega_I$ at constant height $h = 225$ km. A plot of the simulated input observations $\Delta V_{zz}^{\mathrm{sim},\alpha}$ at their original positions $\boldsymbol{x}^p$ would be dominated by the gravitational variations w.r.t. the radial distance $r = R_{\mathrm{Reuter}} + h$. Using this spectral input information, the regional modeling approach is set up, as described below, at the Reuter grid points, cf. (ii). Plot (iii) shows the resulting differential output model $\Delta V_{zz,8}$ along the GOCE tracks at constant height $h = 225$ km.

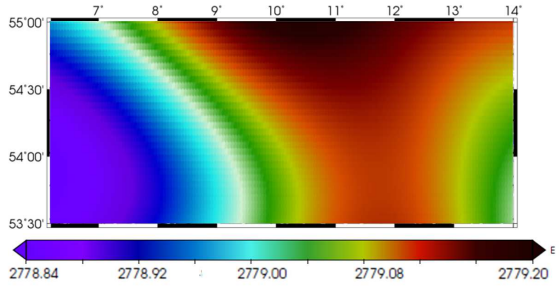

Figure 6.2: Study cases (a) and (b): Background model $V_{zz,\mathrm{back}}$ up to $l_7 = 127$ at $h = 225$ km.

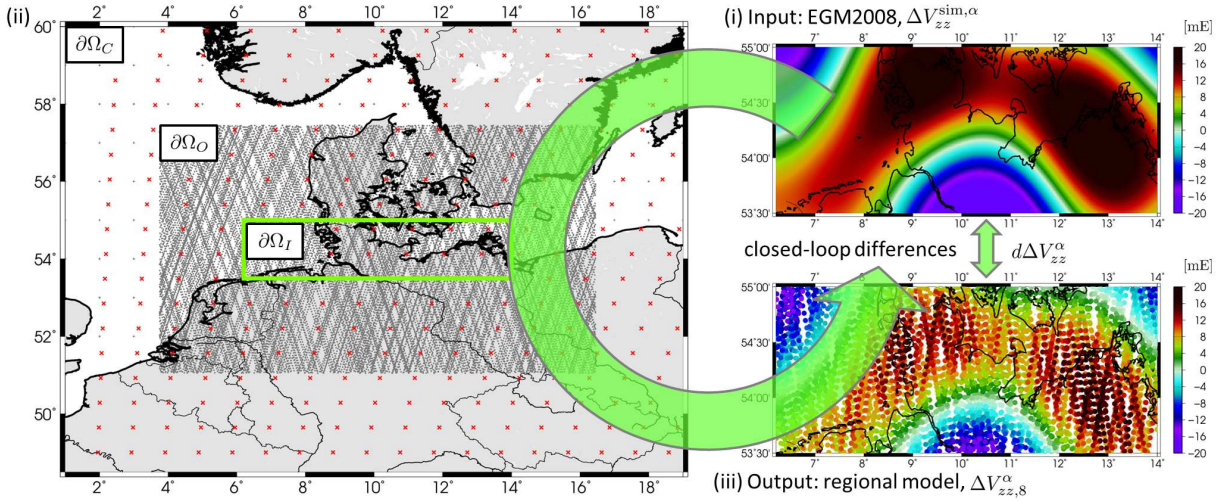

Figure 6.3: Simulation study in Northern Germany at level $J = 8$: (i) The differential input simulation (sim) data $\Delta V_{zz}^{\mathrm{sim},\alpha}$ (noise-free case, $\alpha = 0$) stem from EGM2008 up to d/o 280 (here displayed at $h = 225$ km w.r.t. background model). (ii) Three areas are defined: computation area $\partial\Omega_C$ (with Reuter grid points, red crosses), observation area $\partial\Omega_O$ (with input GOCE tracks in gray), and area of investigation $\partial\Omega_I$ (for the regional output model, green bordered); area margins $\eta^8 \approx 2.5$. (iii) The resulting differential output $\Delta V_{zz,8}^{\alpha}$ ($\alpha = 0$) up to $l_8 = 255$ is plotted along the GOCE tracks at $h = 225$ km w.r.t. background model. The difference between (i) and (iii) is denoted as closed-loop difference $d\Delta V_{zz}^{\alpha}$.

Estimation model For the functional $V_{zz}^{\mathrm{sim},\alpha}$ ($\alpha \in \{0, 0.01, 0.1, 0.5, 1.0\}$) an observation equation (5.15) is formulated according to Tab. 4.7. The above discussed regional rank deficiency and the downward continuation of the observations to the Earth's surface where the Reuter grid is located, cause amongst others a singular normal equation system (5.17). Those instabilities are reduced by introducing additional prior information $\boldsymbol{\mu}_d$, cf. Eq. (5.19). Since the prior information stems from the previously subtracted background model EGM2008 up to $l_7 = 127$, cf. Tab. 6.2, $\boldsymbol{\mu}_d$ yields a zero vector, as mentioned in the context of Eq. (5.19). Consequently, the extended GMM (5.22) is set up and the normal equations (5.23) can be solved. Within the analysis step, the series (5.21) is expanded up to degree $L = 280$ using Shannon basis functions. Hereby, the modeling degree L, defined in Eq. (5.12), is adapted to the maximum spectral content of the observations (degree $L^{\mathrm{obs}} = 280$). As the latter equals the maximum modeling degree $L = 280$ in the analysis, cf. Eq. (5.21), and the observations are noise-free, aliasing errors as displayed in Fig.5.7, vanish. The non-smoothing Shannon function ensures the estimated coefficients $\widehat{d}_q$, cf. Eq. (5.24), to contain full information up to degree $L = 280$. Within the synthesis, the series (5.27) is expanded up to degree $l_8 = 255$, adapted to the level-discretization of the frequency spectrum, cf. Tab. 4.8. Again, the Shannon function is used. (Alternative filter functions are discussed in study case (c).) The modeling equations (5.28) deliver the differential output functional $\Delta V_{zz,8}^{\alpha=0}$,

Table 6.3: Study cases (a) and (b): Estimated variance components (VC) and order of magnitude of relative weights (RW; w.r.t. $\Delta V_{zz}^{\text{sim},\alpha=0}$) for $\Delta V_{zz}^{\text{sim},\alpha}$ at different noise levels α.

observation group		$\alpha = 0$	$\alpha = 0.01$	$\alpha = 0.1$	$\alpha = 0.5$	$\alpha = 1.0$
$\Delta V_{zz}^{\text{sim},\alpha}$	VC	0.157×10^{-9}	0.170×10^{-9}	0.244×10^{-9}	0.957×10^{-9}	0.161×10^{-8}
	RW	1	1	1	1	10^{-1}
prior information	VC	0.305×10^{-6}	0.309×10^{-6}	0.305×10^{-6}	0.316×10^{-6}	0.323×10^{-6}
	RW	10^{-3}	10^{-3}	10^{-3}	10^{-3}	10^{-3}

cf. Fig. 6.3 (iii), from the noise-free input data $\Delta V_{zz}^{\text{sim},\alpha=0}$, and $\Delta V_{zz,8}^{\alpha\neq0}$ from the noisy input data $\Delta V_{zz}^{\text{sim},\alpha\neq0}$, at positions $\boldsymbol{x}^c = \boldsymbol{x}^p \in \partial\Omega_I$, $c = p = 1, \ldots, C$.

Variance components The iteratively estimated VCs, cf. Sec. 5.2.2, are listed in Tab. 6.3 for the simulated input data $\Delta V_{zz}^{\text{sim},\alpha}$ at the different noise levels $\alpha \in \{0, 0.01, 0.1, 0.5, 1.0\}$ and the prior information. In each case, convergence is already obtained after four to five iterations, indicating that the initial values of the VCs are chosen appropriate. Further, in Tab. 6.3, the orders of magnitude of the relative weights (RW) are listed, referenced to the noise-free input data set $\Delta V_{zz}^{\text{sim},\alpha}$. At all noise levels, the simulated input data obtain a smaller VC than the prior information. Thus, the resulting models $\Delta V_{zz,8}^{\alpha}$ contain mainly information from $\Delta V_{zz}^{\text{sim},\alpha}$. In Fig. 6.3 (ii) and (iii), the structures of the in- and output models look very similar; differences are analyzed below. The VCs of the simulated observations increase with augmenting noise level. The VCs of the prior information increase as well, except for the noise level $\alpha = 0.1$ where the estimated VC is identical to the one of $\alpha = 0$. However, the relative weight of the prior information is only two to three orders of magnitude smaller w.r.t. the input data at all noise levels $\alpha \in \{0, 0.01, 0.1, 0.5, 1.0\}$.
The regularization parameter $\lambda_\sigma = \widehat{\sigma}^2/\widehat{\sigma}_d^2$ is plotted in Fig. 6.4. With augmenting noise level, λ_σ increases and indicates a stronger regularization, which seems reasonable. The smoother increase of λ_σ for noise level $\alpha = 0.1$ results from the smaller VC of the prior information, cf. Tab. 6.3. All values λ_σ are in the order of magnitude of 10^{-4} to 10^{-3}, i. e. strong regularization is needed for fitting the simulated data at all noise levels, even for fitting noise-free data, due to the regional rank deficiency of $k_L^{\text{reg}} \approx 60$. The consequences of the strong regularization and the influence of the prior information on the regional modeling results are studied in the sequel by means of the closed-loop differences. Possible effects due to the downward continuation of the observables are investigated in study case (d).

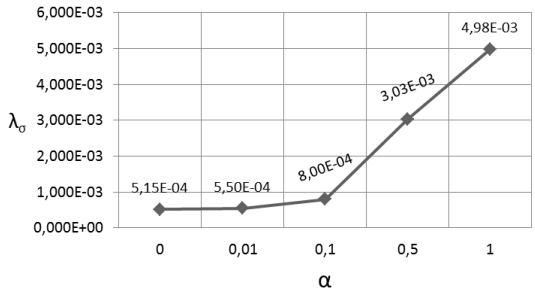

Figure 6.4: Regularization parameter $\lambda_\sigma = \widehat{\sigma}^2/\widehat{\sigma}_d^2$ w.r.t. different noise levels α.

Closed-loop differences

By computing closed-loop (CL) differences, the regional model fit can be rated. The validation data set $\Delta V_{zz,8}^{\text{sim}}$ ($\Delta V_{zz}^{\text{sim},\alpha=0} \rightarrow \Delta V_{zz,8}^{\text{sim}}$) corresponds to the simulated input data set (generated from EGM2008), and further is consistently filtered to the spectral domain (degree $l = 128, \ldots, 255$) of the resulting differential output model up to level $J = 8$. The differences

$$d\Delta V_{zz,8}^{\alpha} = \Delta V_{zz,8}^{\alpha} - \Delta V_{zz,8}^{\text{sim}}, \tag{6.3}$$

then are computed at positions $\boldsymbol{x}^c = \boldsymbol{x}^p \in \Omega_I$, $c = p = 1, \ldots, C$.

Statistics The mean values (mean), and standard deviations (SD) of the differences are listed in Tab. 6.4. Further, the statistics range (min ... max), mean value and SD of the output signal $\Delta V_{zz,8}^{\alpha}$, cf. Fig. 6.3 (iii), are given (vertically arranged), as well as the statistics (horizontally arranged) of the validation data $\Delta V_{zz,8}^{\text{sim}}$ (i. e smoothed input signal in Fig. 6.3 ii), to which the differences are computed.
In principle, the mean values and SDs of all CL differences $d\Delta V_{zz,8}^{\alpha}$ are smaller than 1 mE (except for

$\alpha = 1.0$). The SDs range from 0.146 mE in the noise-free case (a), up to 0.394 mE for $\alpha = 0.5$ (corresponding to around 4 mE) in case (b), i. e. in the order of magnitude of 10^{-13} (with $1\,\mathrm{E} = 1 \times 10^{-9}\,1/\mathrm{s}^2$). Only for input data of noise level $\alpha = 1.0$ (corresponding to around 8 mE), the SD of the mean difference increases up to 0.510 E. Consequently, for the regional models from noisy input data up to the noise level $\alpha = 0.5$, the SDs of the mean CL differences are smaller than the variations of the white noise. In those cases (b) and in the noise-free case (a), the SD values are close to the computational accuracy of 10^{-16} and indicate a high regional modeling accuracy. Consequently, the regional model approximates the gravitational signal within the equivalent frequency domain, here spectral degree $l = 128, \ldots, 255$, very well up to a noise level of $\alpha = 0.5$.
Relating the variance $v\left(d\Delta V^{\alpha}_{zz,8}\right)$ of the mean difference to the variance $v\left(\Delta V^{\mathrm{sim}}_{zz,8}\right) = 41.757\,\mathrm{mE}$ of the validation data with mean value 4.684 mE and SD 6.462 mE, yields the relative differences, cf. Tab. 6.4, lowest row. They range from 5.105×10^{-4} ($\alpha = 0$) up to 3.718×10^{-3} ($\alpha = 0.5$). The values augment approximately proportional with the noise level, which seems reasonable. For instance, a five times higher noise level from $\alpha = 0.1$ to $\alpha = 0.5$ yields approximately a five times higher relative variance from 7.418×10^{-4} to 37.176×10^{-4}.

Table 6.4: Statistics of study cases (a) and (b), distinguished by input data of different noise levels. The range (min ... max), the mean value (mean) and its standard deviation (SD) of the referring regional output models are listed below; the statistics of the validation data $\Delta V^{\mathrm{sim}}_{zz,8}$ are listed on the left side. The resulting mean values and SD of the closed-loop (CL) differences (a) and (b), are presented in the middle, relative variances (w.r.t. the variance of $\Delta V^{\mathrm{sim}}_{zz,8}$) are given below.

		case	(a)	(b)	(b)	(b)	(b)	
		output	$\Delta V^{0}_{zz,8}$	$\Delta V^{0.01}_{zz,8}$	$\Delta V^{0.1}_{zz,8}$	$\Delta V^{0.5}_{zz,8}$	$\Delta V^{1.0}_{zz,8}$	
		min ...	−18.702	−18.740	−18.679	−18.381	−19.282	
		max [mE]	... 18.957	... 19.003	... 19.163	... 19.583	... 18.860	
difference	min ...	mean,	4.724	4.712	4.797	4.738	4.537	CL
to	max [mE]	SD [mE]	6.456	6.460	6.454	6.462	6.391	difference
$\Delta V^{\mathrm{sim}}_{zz,8}$	−18.812	4.684	0.040	0.028	0.113	0.054	−0.147	$d\Delta V^{\alpha}_{zz,8}$
	...18.670	6.462	0.146	0.150	0.176	0.394	510	
	relative		5.105	5.388	7.418	3.718	6.229	$\frac{v\left(d\Delta V^{\alpha}_{zz,8}\right)}{v\left(\Delta V^{\mathrm{sim}}_{zz}\right)}$
	difference		$\times 10^{-4}$	$\times 10^{-4}$	$\times 10^{-4}$	$\times 10^{-3}$	$\times 10^{3}$	

Geographical distribution The differences $d\Delta V^{\alpha}_{zz,8}$ from Eq. (6.3) between the estimated output model and the simulated input data are geographically plotted in Fig. 6.5 (i). With increasing noise level from $\alpha = 0$ (case a) to $\alpha = 1.0$ (cases b), the range of the amplitudes augments from around ±0.1 mE in the lower right plot up to more than ±1.0 mE in the upper left plot. The geographical structures remain about the same, indicating the presence of systematic effects. Negative differences appear in the middle of the study area, while positive differences are located in the western and eastern areas. Those systematic differences stem from the regularization: As discussed above, strong regularization is needed for solving the normal equation systems at all noise levels. Since the prior information w.r.t. the background model $V_{zz,\mathrm{back}}$ is introduced as zero vector, the regional models $\Delta V^{\alpha}_{zz,8}$ can be interpreted to contain "zero-signal", i. e. to be smoothed. At highest noise level $\alpha = 1.0$, strongest regularization is needed, i. e. the output model $\Delta V^{1.0}_{zz,8}$ contains the most information from the zero-vector $\boldsymbol{\mu}_d$. Comparing, for instance, the geographical structure of the differences $d\Delta V^{1.0}_{zz,8}$ with those of $V_{zz,\mathrm{back}}$ from Fig. 6.2, intensifies the assumption: $V_{zz,\mathrm{back}}$ shows largest amplitudes in the middle of the area of investigation, and lower ones in the western and eastern parts. If the output functionals $\Delta V^{\alpha}_{zz,8}$ are smoothed and thus adapted to the low-resolution signal, they delivered too large values in the middle and too small values in the western and eastern parts. This would result in corresponding negative (middle) and positive (western/eastern) differences to the validation data $\Delta V^{\mathrm{sim}}_{zz,8}$.

Histogram The presence of "zero-signal" w.r.t. the background model in the estimated output models and the effects of noise amplification further are visible in the referring histograms of the differences $d\Delta V^{\alpha}_{zz,8}$, cf. Fig. 6.5 (ii). In a perfect model fit of noise-free data, the curves are expected to represent sharp peaks w.r.t. the

computational accuracy. In this study, they approximately extend to ±1.0 mE, except the peak of noise level $\alpha = 1.0$ (dark blue curve), which extends to around ±1.5 mE. The sharpest peak results for the differences $d\Delta V^{0.1}_{zz,8}$ of noise level $\alpha = 0.1$ (pink curve). As discussed above, in this case, the VC of the prior information (and thus, the regularization parameter) did not increase compared with the behavior of σ^2_d at other noise levels, cf. Tab. 6.3 (Fig. 6.4). Thus, the corresponding curve of the histogram of the differences confirms this slightly weaker influence of regularization in the regional model $\Delta V^{0.1}_{zz,8}$. Further, all peaks of the differences are centered at around 0 mE, except of case $\alpha = 1.0$. The latter was indicated by the negative mean value in Tab. 6.4, causing a small shift of the histogram to the negative domain. Since both the simulated input observations, as well as the output models have a shifted mean value at about 5 mE (cf. Tab. 6.2), it can be concluded that the regional modeling approach is able to capture this shift of observations up to noise level $\alpha = 0.5$ (corresponding to around 4 mE).

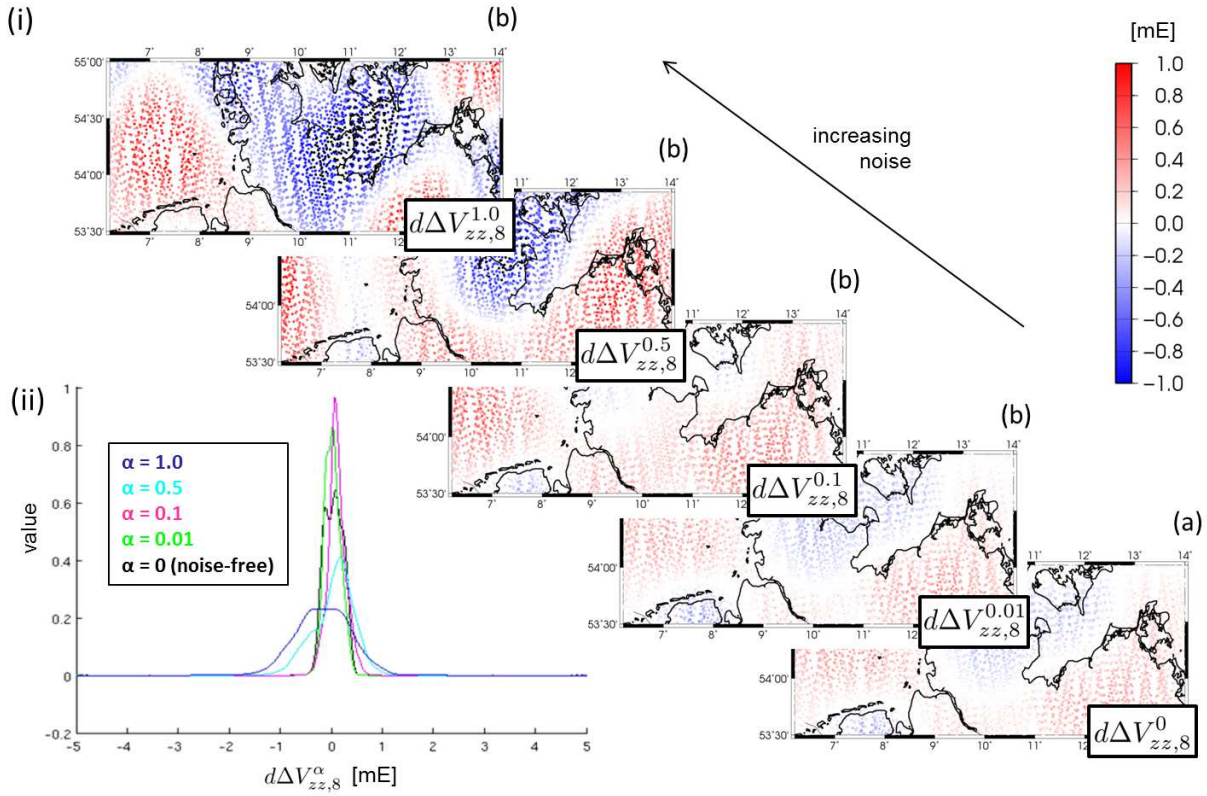

Figure 6.5: Study cases (a) and (b): Differences $d\Delta V^{\alpha}_{zz,8}$ at different noise levels: case (a) noise-free ($\alpha = 0$), and case (b) Gaussian white noise ($\alpha = 0.01, 0.1, 0.5, 1.0$). Displayed are (i) the geographical distribution and (ii) the histograms of the differences.

Summary and discussion of study cases (a) and (b)

The remaining different shapes and magnitudes of the histogram peaks, the range and the geographical distribution of minimum and maximum differences in Fig. 6.5, as well as the (relative) SDs of the mean differences indicate some weaknesses in the modeling approach: Especially the regional rank deficiency and the downward continuation cause instabilities in the normal equation system and require strong regularization. Consequently, the prior information, introduced as zero-vector, has large influence on the regional solutions. Further modeling errors are contained due to artificial structures from the oscillating Shannon function in the spatial domain. Taking those aspects into account, the regional modeling approach can be assumed to be consistent, in conclusion of study cases (a) and (b). The above all small closed-loop differences w.r.t. the validation data indicate a high internal accuracy of the regional modeling approach and a proper handling of noise-free and noisy input data.

The remaining weaknesses in cases (a) and (b) could be reduced, either by (1) introducing additional and/or

more realistic prior information, (2) investigating alternative regularization strategies, or (3) minimize the regional rank deficiency.

(1) Additional and/or alternative prior information Introducing a higher-resolution background model, and thus, a higher-resolution prior information, delivered a more realistic "zero-signal", but the instabilities in the VCE due to the missing residuals of the global model remain. Instead, the prior information could be replaced by alternative information, e. g. stemming from synthetic Earth models taking into account the Earth's topography. Introducing the latter as stochastic observation group in the extended GMM in terms of a relative gravitational functional might stabilize the method of VCE.
In order to further ensure the relation of the regional model to the long wavelengths of the Earth's gravity field, the synthetic model could also be introduced in addition to the prior information w.r.t. the background model. Hence, on the one hand, the output model is referenced to a low- up to medium-resolution global SH model, and on the other hand, the estimation model is be stabilized by a higher-resolution synthetic model. A possible realization within the approach of this work is discussed in the Outlook 7.

(2) Alternative regularization strategies As discussed above, for the combination of heterogeneous data sets, VCE is appropriate to manage their relative weighting. However, the weaknesses of regularization by VCE are shown in the study cases (a) and (b) if strong regularization is needed and the prior information is not realistic enough. *Naeimi* (2013) compares different regularization strategies and parameters for regional gravity modeling by SBFs. Besides VCE, generalized cross validation, L-curve analysis and Parameter-Signal-Correlation (PSC) are investigated for different settings in closed-loop scenarios. In the most cases, the method of PSC delivers the smallest RMS values of CL differences, while the method of VCE delivers the largest RMS values. Hence, alternative regularization strategies could reduce the CL differences, obtained in study cases (a) and (b). However, *Naeimi* (2013) tested only regional models, using either simulated GRACE, or simulated GOCE data, but no combined models, which would be relevant for the following case studies of this work.

(3) Reduction of rank deficiency The global rank deficiency k_L^{glob} becomes zero, if the number Q_L^{glob} of grid points of the computation grid equals the dimension $N_L = (L+1)^2$ of the space $H_{0,\ldots,L}(\Omega_R)$, spanned by the SBFs. It was discussed in the context of Eq. (5.2). However, due to the choice of the Reuter grid with a defined number of grid points, this cannot be realized in the most cases. As mentioned in Sec. 5.1.1, alternative point grids were studied by several research groups, but finding a "perfect" computation grid is quite challenging. Irregular grids might be manually adapted such that the global number of grid points equals the dimension N_L of the space $H_{0,\ldots,L}(\Omega_R)$, which is very time consuming. However, even if the global number of grid points equals the N_L, linear dependencies could remain in the normal equation system, for instance, due to an unfavorable geographical data distribution. Since usually, those linear dependencies occur very rarely for heterogeneously distributed real data, a fixed Reuter grid enhances in the most cases the stability of the approach.
In contrast to the global rank deficiency, the regional rank deficiency furthermore depends on several aspects, as e. g. regionally limiting the number of SBFs. Since the latter are globally defined, spectral information is missing in the resulting regional models. The larger the extent of the computation area $\partial\Omega_C$, i. e. the less basis functions are neglected. However, the spatial extent of the observation data limits the size of $\partial\Omega_C$. By an appropriate choice of areas and area margins, as discussed in Secs. 5.1.2 and 5.1.3, the local support of SBFs is tried to be captured as optimally as possible. Note, that k_L^{reg} gives only a rough estimate of the regional rank deficiency, cf. Sec. 5.1.4. The actual value is unknown, as e. g. discussed by *Naeimi* (2013).

Study case (c): Different input functionals

In contrast to the above presented study cases (a) and (b), different gravitational functionals now serve as input for regional gravity modeling in case (c). According to the classification of study cases in Tab. 6.1, the complexity increases. The main aspects to be answered read:

Study case (c1) What is the effect of using different basis functions in the synthesis? How well do combined models from heterogeneous data with different gravitational functionals and spatial distributions fit validation data?

Study case (c2) What is the effect of a non-combined solution (c2) in contrast to the combined solution (c1)?

The following investigations are studied in the frame of the International Association of Geodesy (IAG) Inter-Commission Committee on Theory (ICCT) JSG (Joint Study Group) 0.3 "Comparison of Current Methodologies in Regional Gravity Field Modeling" (`http://jsg03.dgfi.tum.de/index.php?id=5`). Some of the results were presented by *Lieb et al.* (2014).

Table 6.5: Study case (c): Specifications.

Input $\partial\Omega_O$,	(c1)	· ΔT^{sim} GRACE simulated from EGM2008 · $L_{\text{obs}} = 250$ · 4355 observations along flight tracks of one month
	(c1), (c2)	· T_{rr}^{sim} GOCE simulated from EGM2008 · $L_{\text{obs}} = 250$ · 9295 observations along flight tracks of 61 days
Approach $\partial\Omega_C$,	(c1), (c2)	· $J = 8$ · ΔT_{back}, $T_{\text{rr,back}}$: GOCO03s, d/o 60 · prior information: GOCO03s, d/o 60 · $L = 280$ (analysis, Shannon) · $Q_L = 796$ unknowns · $R_{\text{Reuter}} = 6378.137$ km grid radius · $l_J = 255$ ($J = 8$, synthesis using Shannon, Blackman, Cubic Polynomial)
Output $\partial\Omega_I$,	(c1), (c2) (c2)	· T_8^{Sha}, T_8^{Bla}, T_8^{CuP} up to $l_8 = 255$ · T_8^{Bla} up to $l_8 = 255$ · validation sites, geographical grid (spacing $30' \times 30'$)
Validation	(c1), (c2)	· T_{250}^{sim} up to d/o 250 · validation sites, geographical grid (spacing $30' \times 30'$)

Simulated input data According to the suggestion of JSG0.3, a test area in Europe is chosen, see Fig. 6.6 (i). The color-encoding topography is visualized based on the Digital Topographic Model 2006.0 (DTM2006.0) (*Pavlis et al.*, 2007). Several data sets are available within this area and provided on the website of JSG0.3, simulated from EGM2008 (cf. Sec. 3.2.2). In study case (c1) the filtering with different basis functions in the synthesis shall be investigated, and in case (c2) the combination of GRACE and GOCE vs. a GOCE-only solution. The specifications of the modeling approach are listed in Tab. 6.5.
The input data are given in the observation area $\partial\Omega_O$ along real orbits of the GRACE and GOCE satellite missions. The spatial extent of the simulated data is visualized in Fig. 6.6 (i). The GRACE and GOCE observations cover the gray-bordered observation area $\partial\Omega_O$ for a regional modeling approach set up at level $J = 8$. White dots indicate the geographic distribution of the data and are equivalent to the gray dots (GRACE) and lines (GOCE) in (ii). The red- and the larger green-bordered area in (i) are the referring computation and modeling area, $\partial\Omega_C$ and $\partial\Omega_I$, cf. Sec. 5.1.2.
The simulated data refer to the disturbing potential T, Eq. (2.53), w.r.t. the normal reference field GRS80, cf. Sec. 3.2.1. Thus, GRACE observations are provided in terms of disturbing potential differences ΔT^{sim}, cf. Eq. (2.61). The data set covers a time period of one month. Simulated GOCE observations describe radial gravity gradients T_{rr}^{sim}, cf. Eq. (2.79), of the disturbing potential and cover a full 61-days repeat cycle.[26] Both data sets are noise free and given with spectral resolution up to SH degree $L_{\text{obs}} = 250$.

Methodical settings The modeling approach is set up at level $J = 8$. According to Tab. 4.8 the maximum spectral resolution of the input data is close to the upper boundary $l_8 = 255$ of this level. The basis functions are located at Reuter grid points (red crosses in Fig. 6.6 ii) within the computation area $\partial\Omega_C \in \Omega_R$ with $R = R_{\text{Reuter}} = 6378.137$ km, i. e. at $h = 0$ km near the Earth's surface. GOCO03s serves as background model up to d/o 60. The choice was made in the frame of a variety of comparisons with other research groups in the ICCT JSG0.3. The input data are reduced by the background model according to Eq. (5.13). Note, EGM2008 was used for the simulation of the input data.

[26] As mentioned in Sec. 3.1.4, the small angular deviation of the GOCE T_{zz} component in GRF, to the radial direction r from the geocenter to the center of the satellite, is neglected in this work and it yields $T_{zz} \approx T_{rr}$.

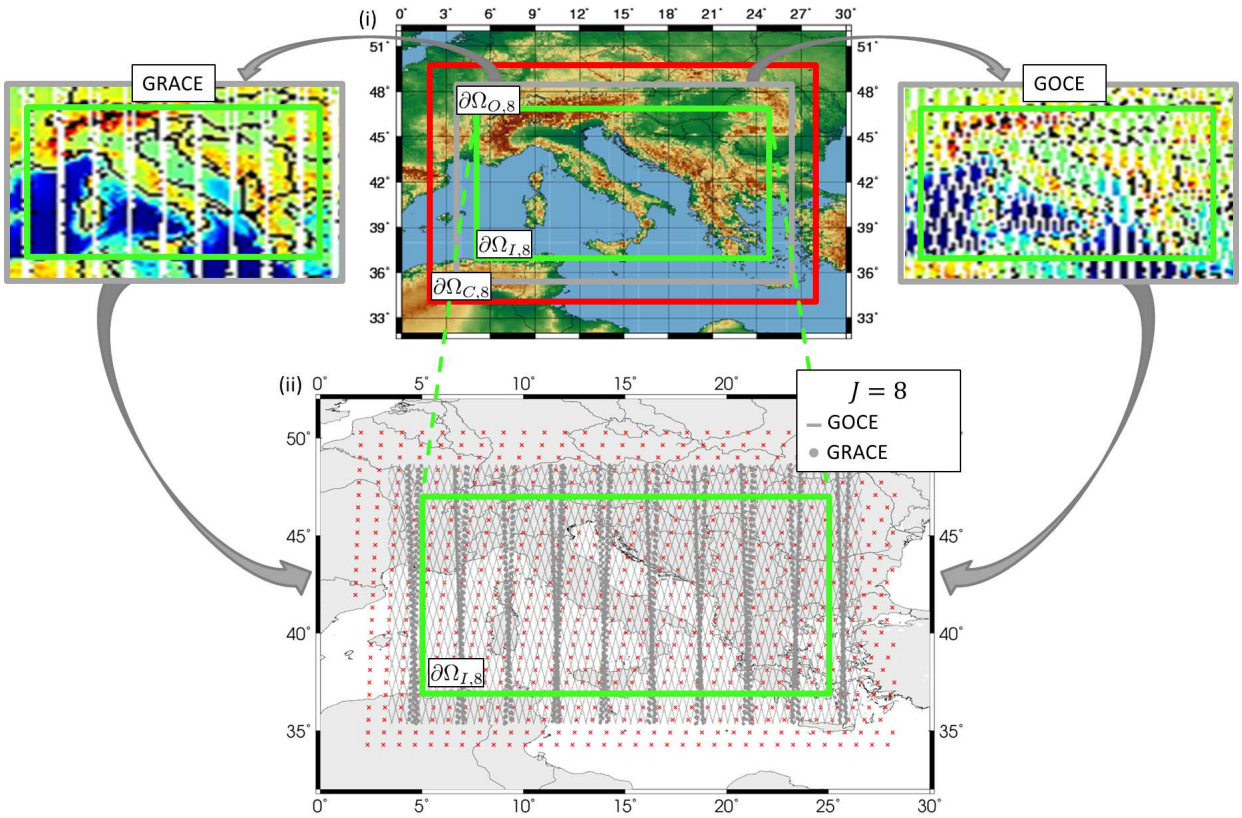

Figure 6.6: Study case (c): Closed-loop scenarios in (i) a test area in the Mediterranean Sea in Europe (altitude encoding topography from DTM2006.0), set up at level $J = 8$, using different input functionals (simulated GOCE, GRACE observations). In (i), computation, observation and modeling area are bordered in red ($\partial\Omega_C$), gray ($\partial\Omega_O$) and green ($\partial\Omega_I$). The spatial distribution of "GOCE" and "GRACE" is visualized within $\partial\Omega_O$ in terms of white dots, and symbolized as gray lines (GOCE) and bullets (GRACE) in (ii); the red crosses symbolize Reuter grid points within $\partial\Omega_C$.

Estimation model In order to compute regional gravity field models from a combination of different functionals, the extended GMM (5.22) is set up. The observation equations are formulated in the analysis step for each input functional ΔT^{sim} and T_{rr}^{sim} by means of adapted basis functions from Eq. (5.21). Hereby, the expressions of Tab. 4.7, formulated w.r.t. V, can be equivalently applied for $\mathcal{Y}[\tilde{V}] = T$. All simulated observations consistently refer to the same normal potential reference GRS80, and are subtracted by the same background model according to Eq. (5.14). The design matrix $\boldsymbol{A}$ in the extended GMM (5.22) comprises the field transformations which are necessary to enable a combination of different gravitational functionals. Further, prior information $\boldsymbol{\mu}_d$ (zero-vector w.r.t. the background model GOCO03s up to d/o 60) is introduced as additional observation group, cf. Eq. (5.19), in order to handle singularity problems when solving the normal equation system (5.23), as exemplarily discussed in study cases (a) and (b).
The series (5.21) is developed in terms of the non-smoothing Shannon functions up to degree $L = 280$, i. e. higher than the upper boundary ($l_8 = 255$) of the maximum resolution level $J = 8$, and smaller than $L^{\text{rank}} = 288$, in order to reduce the regional rank deficiency. ($L^{\text{rank}} = 288$ is estimated by Eq. (5.11), with $Q_{256}^{\text{glob}} = 83966$ from Tab. 5.1.) Since $L_{\text{obs}} < L$, the estimated scaling coefficients, cf. Eq. (5.24), contain only information up to degree 250.

Different filter kernels

In the synthesis, the low-pass filtering SBFs $\Phi_8(\boldsymbol{x}^c, \boldsymbol{x}_q)$, Eq. (5.27), are adapted to T, cf. Tab. 4.7. While in the analysis, Shannon functions, defined by Eq. (4.29), are used due to their ideal filter characteristic in the spectral domain, different filter kernels now shall be investigated in the synthesis in **study case (c1)**. The uncertainty of the Shannon functions in the spatial domain provokes erroneous side lobes in the output models. In order to study those effects, the three different low-pass filtering functions Shannon (Sha), Blackman (Bla), Cubic Polynomial (CuP) from Fig. 4.9, are compared in the sequel. They are defined by setting the Legendre coefficients in Eq. (5.27) to $\phi_{l,j}^{\text{Sha}}$, Eq. (4.29), $\phi_{l,j}^{\text{Bla}}$, Eq. (4.30), $\phi_{l,j}^{\text{CuP}}$, Eq. (4.31). As explained in the context

Table 6.6: Study case (c1): Range (min... max), mean value (mean) and referring standard deviation (SD) of the output models T_8 obtained by different filter kernels (Sha, Bla, CuP) in the synthesis. The statistics of the estimated standard deviations sT_8 are listed below.

		Shannon (Sha)	**Blackman (Bla)**	**Cubic Polynomial (CuP)**
T_8	min ... max [m^2/s^2]	−64.58 ... 47.89	−58.31 ... 49.28	−37.49 ... 37.55
	mean +/- SD [m^2/s^2]	−0.07±20.24	0.02±19.11	−0.09±13.29
sT_8	min ... max [m^2/s^2]	0.157 ... 0.527	0.006 ... 0.047	0.006 ... 0.035
	mean +/- SD [m^2/s^2]	0.266±0.0750	0.014±0.0073	0.010±0.0044

of Eq. (4.11), it is possible to multiply the scaling coefficients in the modeling equations (5.28) with different basis functions. The resulting differential models T_8^{Sha}, T_8^{Bla}, T_8^{CuP} of the disturbing potential up to level $J = 8$ (degree $l_8 = 255$) refer to the background model GOCO03s up to d/o 60. They are computed at the given validation sites $\boldsymbol{x}^c$ of a regular grid, cf. Tab. 6.5.

Output models and standard deviations Figure 6.7 shows the geographical structures of the regional models (i) T_8^{Sha}, (ii) T_8^{Bla}, (iii) T_8^{CuP}, computed at validation sites $\boldsymbol{x}^c \in \partial\Omega_I$. The referring statistics are listed in Tab. 6.6. As expected, the gravitational variations are similar in all three cases and a smoothing behavior is visible for the Blackman and CuP-filtered solutions w.r.t. the non-smoothed Shannon-solution. The statistics in Tab. 6.6 confirm the decrease of the amplitudes: While for Shannon, they range from $-64.58\,m^2/s^2$ to $47.89\,m^2/s^2$ (with a standard deviation of $20.24\,m^2/s^2$), for Blackman the range is smaller with values from $-58.31\,m^2/s^2$ to $49.28\,m^2/s^2$ (and a SD of $19.11\,m^2/s^2$), and for CuP the smallest range is obtained with amplitudes from $-37.49\,m^2/s^2$ to $37.55\,m^2/s^2$ (SD $13.29\,m^2/s^2$). The characteristic Legendre coefficients, cf. Fig. 4.9 (d) – (f), define this smoothing effect especially in the high frequencies when using Blackman and CuP functions. Since the resulting gravitational structures are of minor interest in this study case (c1), they are not further analyzed.

The standard deviations sT_8^{Sha}, sT_8^{Bla}, sT_8^{CuP} of the resulting differential models are estimated according to Eq. (5.30) with $sT(\boldsymbol{x}^c) = \sqrt{v\left(T_8\left(\boldsymbol{x}^c\right)\right)}$ at validation sites $\boldsymbol{x}^c \in \partial\Omega_I$. They are visualized in Fig. 6.8 for the three different filter kernels (i) Shannon, (ii) Blackman, (iii) CuP; the statistics are further listed in Tab. 6.6.

As expected, the SD values increase in all three cases close to the borderlines of $\partial\Omega_I$ due to remaining edge effects, cf. discussion in Sec. 5.1.3. The latter have been reduced by choosing different extensions of $\partial\Omega_I$, $\partial\Omega_O$, $\partial\Omega_C$, cf. Fig. 6.6. With $|\varphi|_{\max} = 47°$ and $J = 8$, the margin from Eq. (5.5) counts $\eta^8 \approx 2.0°$.

For Shannon the standard deviations are around one order of magnitude larger than for Blackman and CuP (different color bars are used in Fig. 6.8). The maximum SD of sT_8^{Sha} yields with $0.53\,m^2/s^2$ around 1 % of the maximum (positive) signal amplitude of T_8^{Sha}, cf. Tab. 6.6. Both, the signal and the SD maxima, are reached at the northern boundary of the test area, cf. Figs. 6.7 (i) (orange colored at around 12° longitude) and 6.8 (i) (red colored along the northern borderline). However, the SD seems not to be correlated with the signal for the Shannon-, as well as for the Blackman- and CuP-solutions. In the latter two cases, the maximum SD values reach $0.047\,m^2/s^2$ (Bla) and $0.035\,m^2/s^2$ (CuP) at the north-western and north-eastern edges of $\partial\Omega_I$. Consequently those maxima yield only around 0.1 % of the largest (positive) signal amplitudes of T_8^{Bla} and T_8^{CuP}, cf. Fig. 6.7 (i) and (ii).

Choosing wider margins between the three areas depending on the choice of basis function (e. g. for Shannon) might further reduce the edge effects at the expense of reducing the size of the study area $\partial\Omega_I$. The here selected width of the margins tries to balance the reduction of edge effects and a spatial extent of $\partial\Omega_I$ as wide as possible adapted to the spatial extent of the observations in $\partial\Omega_O$.

Compared with Shannon, the smaller SDs of the Blackman- and CuP-filtered regional models could, on the one hand, indicate a higher modeling accuracy, since the Shannon function shows strong oscillations in the spatial domain. This would further explain the strong increase of the SD values along the borderlines. On the other hand, the smaller SD values of the Blackman- and CuP-solutions could result from smoothing the signal; thus, smaller standard deviations are obtained. A comprehensive study of a variety of SBFs and their standard deviations is investigated by *Bentel et al.* (2013a). The smaller SD values of the Blackman kernel compared with the SD values of the Shannon function are in agreement.

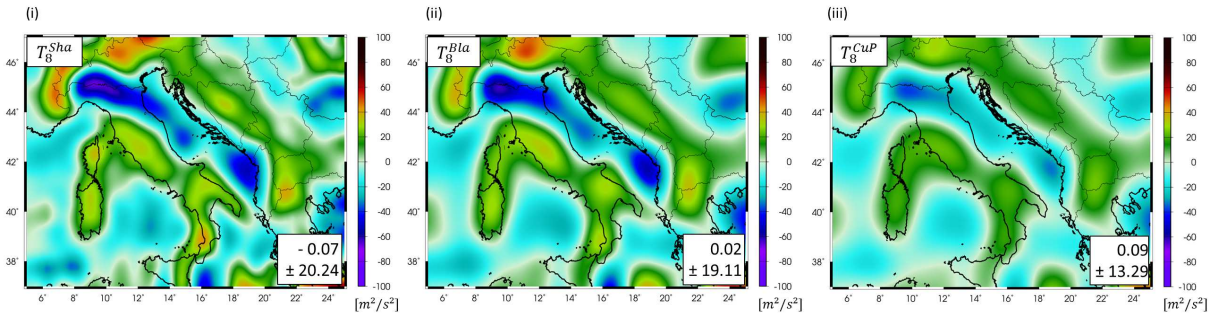

Figure 6.7: Study case (c1): Estimated disturbing potential (i) T_8^{Sha}, (ii) T_8^{Bla}, (iii) T_8^{CuP}, up to spectral resolution level $J = 8$, modeled from simulated GRACE and GOCE, using Shannon (Sha), Blackman (Bla), Cubic Polynomial (CuP) functions in the synthesis. Mean value and SD are depicted in the white boxes; unit $[\mathrm{m}^2/\mathrm{s}^2]$.

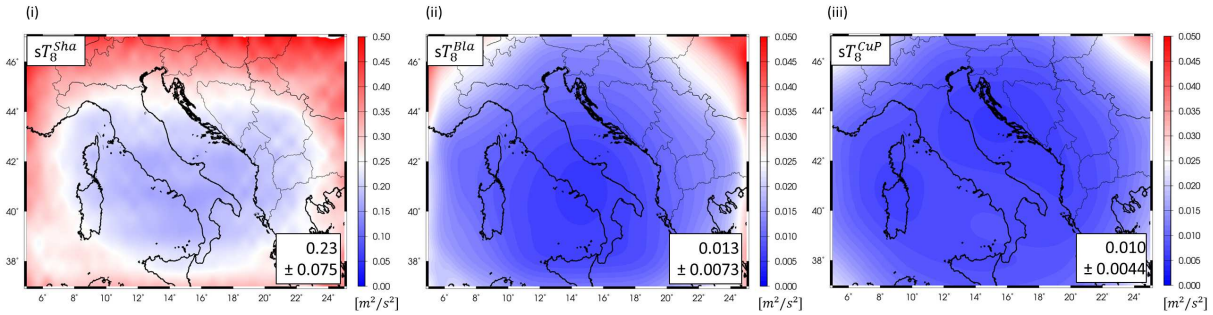

Figure 6.8: Study case (c1): Standard deviations (i) sT_8^{Sha}, (ii) sT_8^{Bla}, (iii) sT_8^{CuP}, of the differential signals, using Shannon (Sha), Blackman (Bla), Cubic Polynomial (CuP) functions in the synthesis. Mean value and SD are depicted in the white boxes; $[\mathrm{m}^2/\mathrm{s}^2]$.

CL differences In order to analyze the smoothing behavior of the basis functions and to rate the model fit of all three versions T_8^{Sha}, T_8^{Bla}, T_8^{CuP}, they are compared with the validation data T_{250}^{sim}, cf. Tab. 6.5. Note, the same non-smoothed validation data set is used for all three cases. The differences

$$
\begin{aligned}
dT_8^{\mathrm{Sha}} &= T_8^{\mathrm{Sha}} - T_{250}^{\mathrm{sim}}\,,\\
dT_8^{\mathrm{Bla}} &= T_8^{\mathrm{Bla}} - T_{250}^{\mathrm{sim}}\,,\\
dT_8^{\mathrm{CuP}} &= T_8^{\mathrm{CuP}} - T_{250}^{\mathrm{sim}}\,,
\end{aligned}
$$

are computed at validation sites $\boldsymbol{x}^c$ and displayed in Fig. 6.9. The values (i) dT_8^{Sha} range between around $-30\,\mathrm{m}^2/\mathrm{s}^2$ to $30\,\mathrm{m}^2/\mathrm{s}^2$ and seem to be randomly distributed. Compared with the range of the estimated signal T_8^{Sha} between around $-50\,\mathrm{m}^2/\mathrm{s}^2$ to $50\,\mathrm{m}^2/\mathrm{s}^2$, cf. Fig. 6.7 (i), the differences dT_8^{Sha} are in the same order of magnitude, cf. Fig. 6.9 (i). The SD of the mean difference counts $7.87\,\mathrm{m}^2/\mathrm{s}^2$. In contrast, the amplitudes and the SD of the mean of the differences dT_8^{Bla} (ii) are much smaller. They range approximately between $-20\,\mathrm{m}^2/\mathrm{s}^2$ to $20\,\mathrm{m}^2/\mathrm{s}^2$ with a SD of $4.01\,\mathrm{m}^2/\mathrm{s}^2$. However, the extreme values are supposed to be correlated with the topography, cf. Fig. 6.6 (ii), which becomes especially apparent for the mountainous regions of the Alps and of South Italy and Sicily. As the Blackman filter smoothes the high frequencies of each resolution level, cf. Fig. 4.9 (e), the referring spectral content is missing in the regional model T_8^{Bla}, cf. Fig. 6.7 (ii). The validation data set T_{250}^{sim} contains complete spectral information up to degree $l = 250$, and thus, the closed-loop differences are assumed to result mainly from the spectral inconsistency. This aspect is manifested by the investigating the differences dT_8^{CuP}, using Cubic Polynomial functions. In Fig. 6.9 (iii), topographic correlations are clearly visible. The extreme values of the differences range between $-40\,\mathrm{m}^2/\mathrm{s}^2$ to $40\,\mathrm{m}^2/\mathrm{s}^2$ and the SD of the mean difference counts $10.14\,\mathrm{m}^2/\mathrm{s}^2$. The strong smoothing behavior of CuP, cf. Fig. 4.9 (f), seems to remove valuable high-resolution information in the regional model of T_8^{CuP}.
Comparing the CL differences with the standard deviations from Fig. 6.8, the CL differences are for all three cases, Shannon, Blackman and CuP, around two to three orders of magnitude larger. This indicates too optimistic error estimates due to incomplete stochastic models. Further, low-resolution errors are not considered in the stochastic model. However, the larger CL differences mainly refer to the different characteristics of the

filter kernels: In case of Shannon, the large values dT_8^{Sha} and sT_8^{Sha} indicate erroneous effects in T_8^{Sha} stemming from the oscillations of the function in the spatial domain, cf. Fig. 4.9 a). The CL differences dT_8^{Bla} and dT_8^{CuP} are computed between smoothed regional models and non-smoothed validation data. In case of CuP, the values sT_8^{CuP} are very small, but the differences dT_8^{CuP} are strongly correlated with the topography and the SD of the mean difference is even larger than in case of Shannon. Hence, the small values sT_8^{CuP} may be owed to the smoothing in the high frequency domain of the modeled signal T_8^{CuP}. Blackman scaling functions deliver the smallest closed-loop differences (smallest range and smallest SD of the mean difference) compared with Shannon and CuP. Further, the values sT_8^{Bla} are one order of magnitude smaller than for Shannon and in the same order of magnitude as for CuP. Together with the small CL differences dT_8^{Bla}, the small values of sT_8^{Bla} indicate the most accurate model fit w.r.t. the three selected cases T_8^{Sha}, T_8^{Bla}, T_8^{CuP}. In conclusion, Blackman SBFs are verified to be a good compromise between smoothing functions in the frequency domain and oscillating functions in the spatial domain (*Lieb et al.*, 2014).
The however relatively large CL difference of around 5 % for Blackman (w.r.t. the range of approximately $\pm 40\,\mathrm{m}^2/\mathrm{s}^2$ of T_8^{Bla}, cf. Tab. 6.6), which mainly stems from missing signal content in the high frequencies of level $J = 8$, further results from regularization in order to stabilize the ill-conditioned normal equation system (5.23), as discussed in study cases (a) and (b). The relative weight of $\boldsymbol{\mu}_d$ counts 1×10^{-10} w.r.t. the simulated data T_{rr}^{sim}; the regularization parameter λ_σ yields 6.09×10^{-10} (with an estimated VC of 8.87×10^{-14} for the GOCE observations and 1.46×10^{-4} for the prior information).

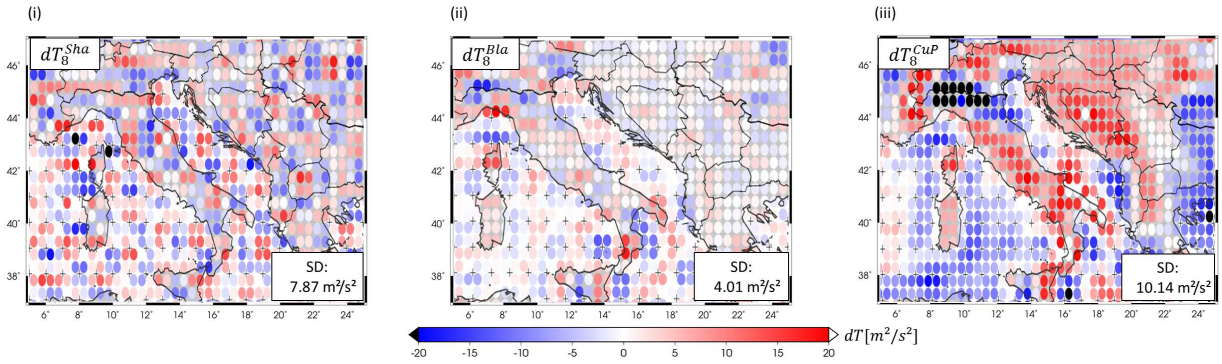

Figure 6.9: Study case (c1): Closed-loop differences (i) dT_8^{Sha}, (ii) dT_8^{Bla}, (iii) dT_8^{CuP}, w.r.t. the validation data set T_{250}^{sim}, using Shannon (Sha), Blackman (Bla), Cubic Polynomial (CuP) functions in the synthesis.

Different functionals

In the following, the combination of the two data sets GRACE and GOCE from study case (c1) shall be compared with a GOCE-only solution, study case (c2). The modeling approach using just one observation group T_{rr}^{sim} is set up at level $J = 8$ in analogy to study case (c1). The specifications are listed in Tab. 6.5. Further, prior information in terms of GOCO03s up to d/o 60 is introduced in order to solve the normal equation (5.17). Consequently, the extended GMM (5.22) is set up for T_{rr}^{sim} and $\boldsymbol{\mu}_d$ (zero vector).

Variance component estimation In Tab. 6.7, the estimated VCs, the order of magnitude of relative weights (RL) w.r.t. T_{rr}^{sim}, and the regularization parameter λ_σ are listed, both for the combined (c1) and the only (c2) case. The values of the estimated VCs for T_{rr}^{sim} are very similar: (c1) 8.87×10^{-14} and (c2) 8.81×10^{-14}. The VC of the prior information gets a slightly higher value of 1.46×10^{-4} in the combined case (c1), i. e. a lower relative weight, than in the only case (c2) 1.06×10^{-4}. The corresponding smaller regularization parameters (c1) $\lambda_\sigma = 6.09 \times 10^{-10}$ and (c2) $\lambda_\sigma = 8.30 \times 10^{-10}$ affirm a stronger regularization in the GOCE-only scenario (c2).
In the GRACE-GOCE combination, the simulated GRACE observations ΔT^{sim} obtain a relatively high VC; the relative weight w.r.t. T_{rr}^{sim} is 7 orders of magnitude lower (the RW of the prior information is 10 orders of magnitude lower). Consequently, the contribution of GRACE to the modeling solution T_8^{Bla} from Fig. 6.7 (ii)

Table 6.7: Study cases (c1) and (c2): Variance components (VC), order of magnitude of relative weights (RW; w.r.t. T_{rr}^{sim}), and regularization parameter λ_σ for the (c1) combined and (c2) only solution.

case	(c1)			(c2)		
observation group	**VC**	**RW**	λ_σ	**VC**	**RW**	λ_σ
T_{rr}^{sim}	8.87×10^{-14}	1	6.09×10^{-10}	8.81×10^{-14}	1	8.30×10^{-10}
ΔT^{sim}	3.24×10^{-7}	10^{-7}				
prior information	1.46×10^{-4}	10^{-10}		1.06×10^{-4}	10^{-10}	

is relatively weak compared with the one of GOCE. The Reason originates from the spatial distribution of the observations: While the GOCE observations cover $\partial\Omega_O$ homogeneously and are equally distributed (cross-track distances smaller than 0.5°), the GRACE tracks are concentrated and yield cross-track distances of around 2.5°, as displayed in Fig. 6.6 (ii). The corresponding lower spectral resolution is reasonably considered within the VCE.
Comparing the regularization parameter of the GOCE-only case (c2) with the one of the GOCE-only case from study (a), cf. Tab. 6.3, the latter was around 6 orders of magnitude larger, i. e. the regularization much stronger. Influences stem from different regional rank deficiencies, different resolution of the background models, or instabilities and uncertainties in the procedure of VCE due to the use of noise-free data. Consequently, the normal equation system of case (a) is less stable than in case (c2). A more detailed comparison is difficult due to the different parametrization.

Output models and differences In the synthesis, Blackman functions are used due to the favorable characteristics as discussed in case (c1). The modeling equation (5.28) is set up for $J = 8$ and yields the regional GOCE-only model T_8^{Bla}(c2) of the disturbing potential. It ranges from $-58.21\,\text{m}^2/\text{s}^2$ to $49.39\,\text{m}^2/\text{s}^2$. The mean value counts $0.097\,\text{m}^2/\text{s}^2$ and the referring standard deviation $19.994\,\text{m}^2/\text{s}^2$. Consequently, the values are very similar to the statistics of the combined model T_8^{Bla} in Tab. 6.6.

Due to the weak contribution of GRACE information in case (c1), the GOCE-only solution (c2) is expected to be very similar. The difference of the resulting differential models of case (c1) and (c2) ranges from $-0.24\,\text{m}^2/\text{s}^2$ to $0.58\,\text{m}^2/\text{s}^2$ with a mean difference of $0.077\,\text{m}^2/\text{s}^2$ and a SD of $0.058\,\text{m}^2/\text{s}^2$. Hence, the difference counts around 1 % of the maximum modeled signal amplitude and is one order of magnitude larger than the SD sT_8^{Bla}, cf. Fig. 6.8 (ii). The difference is plotted in Fig. 6.10. Hereby, especially the decreasing slope in south-northern direction, and the negative and positive slopes towards the south-eastern and north-eastern corners are noticeable. This could be due to correlations of low-resolution GRACE information in case (c1), if the background model GOCO03s up to d/o 60 did not completely remove the long frequencies. As mentioned in Sec. 3.2.2, the low-resolution information of both models, GOCO03s and EGM2008, mainly stems from GRACE observations.

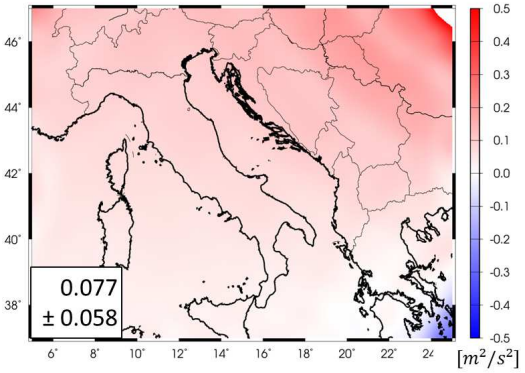

Figure 6.10: Study cases (c1) and (c2): Difference of the combined GRACE/GOCE and the GOCE-only models of the disturbing potential up to level $J = 8$. Mean difference and SD are depicted in the white box; $[\text{m}^2/\text{s}^2]$.

The closed-loop differences dT of the combined case (c1) and the GOCE-only case (c2) are very similar. The SD of the above presented difference $dT_8^{\mathrm{Bla}} = dT(\mathrm{c1})$ yields 4.01 $\mathrm{m}^2/\mathrm{s}^2$, cf. Fig. 6.9 (ii). The SD of $dT(\mathrm{c2})$ reaches a marginally larger value of 4.02 $\mathrm{m}^2/\mathrm{s}^2$, cf. Tab. 6.8. Hence, the SD values differ in the second digit, which is in the order of magnitude of the SD (0.058 $\mathrm{m}^2/\mathrm{s}^2$) of the mean difference between the resulting models (c1) and (c2), cf. Fig. 6.10. Consequently, the missing GRACE information in (c2) seems to be less relevant for the CL difference. This is reasonable, since the contribution of GRACE is very weak in case (c1), expressed by the small RW in Tab. 6.7.

Table 6.8: Study cases (c1) and (c2): Specifications and SD of the mean CL difference dT in terms of disturbing potential T.

	IN	specifications of study case (c)				CL
case	**obs.**	**spectral res.**	**spatial res.**	**noise**	**T_{back}**	**dT: SD [m²/s²]**
c1	GOCE+ GRACE	j = 8	30′	-	GOCO03s d/o 60	4.01
c2	GOCE	j = 8	30′	-	GOCO03s d/o 60	4.02

Discussion of study case (c)

The SD values of a few $\mathrm{m}^2/\mathrm{s}^2$ of the CL differences in the studies (c1) and (c2), cf. Tab. 6.8, stem amongst others from rank deficiency problems which are not captured by the regularization and unrealistic prior information (”zero-signal“), both as discussed in study cases (a) and (b). Further instabilities in the procedure of VCE in case of noise-free data, and remaining low-resolution signal which is not removed by the background model influence the CL differences, as well.

Instabilities of VCE As mentioned in Sec. 5.2.2 the variance factors are computed based on stochastic information, i. e. using the residuals of the observations. However, in this study case (c), noise-free data are used. In case (c1), convergence in the VCs is reached after 21, in case (c2) after 22 iterations. The number of iterations, depends on the initial values of the VCs and the chosen point of convergence. In this work, the parameters are empirical values. Consequently, the estimated VCs might be unrealistic and the regularization parameter not large enough to stabilize the normal equation system. Choosing a more realistic approximate value for the beginning of the iterations and/or a defining a more realistic stop criterion could help to stabilize the procedure. Further investigations follow in real data scenarios by means of noisy data, where VCE is more appropriate.

Influence of low-resolution signal In order to consistently reduce the simulated data from the EGM2008 by the chosen background model GOCO03s, the SH coefficients of GOCO03s are rescaled according to Eq. (2.42), i. e. adapted to EGM2008. Note, both SH models refer to GRACE in the low frequencies, cf. Sec. 3.2.2. However, some signal remains in the long wavelengths of the simulated input data ΔT^{sim} and T_{rr}^{sim}. The differences between the chosen background model GOCO03s and the simulation model EGM2008 range from $-0.19\,\mathrm{m}^2/\mathrm{s}^2$ to $0.00\,\mathrm{m}^2/\mathrm{s}^2$ in the spectral domain up to degree 60 (for the functional T) with a mean value of $-0.10\,\mathrm{m}^2/\mathrm{s}^2$ and a SD of $0.046\,\mathrm{m}^2/\mathrm{s}^2$. Thus, the differences yield an offset of around $-0.1\,\mathrm{m}^2/\mathrm{s}^2$. Consequently, this low-resolution signal remains in the simulated input data (w.r.t. EGM2008) after subtracting the background model GOCO03s. Further, the regional models of the study cases (c1) and (c2) describe differential signal w.r.t. the background model, while the validation data refer to EGM2008. Both aspects explain to some extent the CL differences.

Comparison with studies from other research groups

By the above discussed closed-loop simulations, the regional gravity modeling approach presented in this thesis, is tested for diverse parametrization and input data. According to Tab. 6.1, main aspects are the need of regularization in connection with different stochastic information (study cases (a) and (b)) and the use of appropriate basis functions in the synthesis (study case (c)). Hereby, the complexity of the scenarios increases. In the simplest test case (a), the internal accuracy reaches almost the level of computational accuracy. Thus, the internal stability of the approach is rated. Within the more complex cases (b) and (c), the noise behavior and some of the methodical settings are tested. From the plausible in- and decrease of standard deviations and CL differences, the chosen settings seem to be appropriate and the consistency of the resulting models can be

approved.
The choice of appropriate SBFs is always a compromise between spectral and spatial localization due to the uncertainty principle of frequency and space, as visualized in Fig. 4.8. The approach, using Shannon SBFs in the analysis and Blackman SBFs in the synthesis, turns out to be a good compromise by means of small standard deviations of the modeled signal, and small CL differences. Further research groups use different basis functions or different methods for regional gravity modeling. The main motivation of the JSG0.3 was to compare those approaches; an overview of some examples was given in the Introduction. As outcome, the accuracy and the efficiency of different strategies can be evaluated.
The here presented modeling approach using SBFs was compared with approaches using spherical wavelets, spherical splines, reduced point masses, least-squares collocation and Slepian functions, cf. Tab. 1.1. The results are summarized by *Schmidt et al.* (2014). The closed-loop settings are comparable with the one of study case (c). All approaches achieve closed-loop differences, i. e. mean standard deviations, in the order of a few m^2/s^2. None of the approaches consistently reaches the smallest differences. In general, the efficiency varies for different applications and comparisons are difficult. However, it is approved that the approach of this work fits simulated data with analog accuracy as the other approaches. Taking the previously discussed modeling errors of the case studies (a) – (c) into account, the first secondary aim, mentioned at the beginning of this chapter, is fulfilled.

6.1.2 Real data studies

The application of the regional modeling approach on real data, is one of the main targets in this work. Based on the findings of the above discussed simulation studies, further settings and specifications have to be tested. While simulation studies enable to fit the data as close as possible, real data applications suffer from the lack of knowledge of the exact spectral content of the measurements. Further, stochastic information might be missing, and especially data gaps tend to provoke instabilities in the estimation model. Consequently, regularization is necessary. According to Tab. 6.1, the study cases (d) and (e) are set up, in order to investigate the combination of real data

Study case (d) ... particularly with different functionals and accuracies.

(d1) Is the relative weighting by VCE appropriate and reasonable? Is the Laplace condition valid in terms of tensor computations?

(d2) What is the effect of up-/downward continuation?

Study case (e) ... particularly with different observation heights and spatial distributions.

(e1) What is the effect of data gaps on the relative weighting? What is the contribution of prior information which is used for regularization?

(e2) How accurate and plausible are the estimated scaling coefficients?

(e3) What is the effect of data gaps in resulting regional models? How do they influence the accuracy? What is the effect of field transformations?

(e4) What is the added value of the regional model w.r.t. global SH models?

(e5) How plausible is the regional result w.r.t. another regional model?

(e6) How well does the regional model fit external data?

Study case (d): GOCE gravity gradients

As already mentioned, gravity field modeling from non-rotated GOCE gravity gradients, obtained w.r.t. GRF, requires special emphasis, cf. Sec. 3.1.4. In order to derive gravitational information in Earth-bound coordinate systems and, further, to consistently combine GOCE measurements with other observation types, the adapted basis functions, cf. Tab. 4.7, which are used for setting up the observation equations in the extended GMM (5.22), contain transformation terms between GRF and the Earth-bound spherical coordinate system, cf. Sec. 2.2.2. Since the GOCE GGs embody directional information of the Earth's gravity field, each individual gravity gradient is treated as separate observation group assuming them to be uncorrelated. Details are

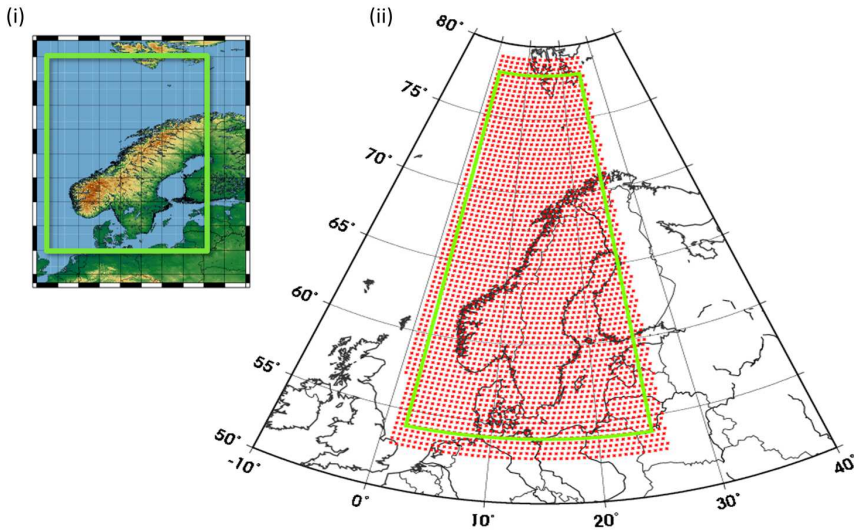

Figure 6.11: (i) Geographical location of the test area Scandinavia (green bordered) with altitude encoding topography. (ii) Distribution of the Reuter grid points (red dots).

Table 6.9: Study case (d): Specifications.

Input $\partial\Omega_O$	(d1), (d2)	· $V_{xx}, V_{xy}, V_{xz}, V_{yy}, V_{yz}, V_{zz}$ in GRF · re-processed release 2 (level-2 products), time span 03/2010 - 05/2012 · pre-processing according to Sec. 3.3.5
Approach $\partial\Omega_C$	 (d1) (d1)	· $V_{ab,\text{back}}$: GOCO03s, d/o 250 · prior information: GOCO03s, d/o 250 · $L = 280$ (analysis, Shannon) · $R_{\text{Reuter}} = 6378.137$ km grid radius · $R_{\text{Reuter}} = 6648.137$ km grid radius
Output $\partial\Omega_I$	(d1), (d2)	· $T_{xx,8}, T_{xy,8}, T_{xz,8}, T_{yy,8}, T_{yz,8}, T_{zz,8}$ in LNCS · at regular grid (spacing $0.2° \times 0.2°$), $h = 270$ km

explained by *Lieb et al.* (2015). The numerical investigations and the outcome are summarized in the following.

The specifications of the modeling approach are listed in Tab. 6.9. The approach is set up at level $J = 8$, as this is the maximum level which is completely located within the sensitivity domain (MBW) of GOCE, cf. Sec. 3.1.4. The area of investigation $\partial\Omega_I$ is chosen in the Scandinavian region, see Fig. 6.11 (i), green-bordered. The level depending Reuter grid points within $\partial\Omega_C$ can be seen in Fig. 6.11 (ii), red crosses. In study case (d1), the Reuter grid refers to a sphere with grid radius $R_{\text{Reuter}} = 6378.137$ km, in case (d2) with grid radius $R_{\text{Reuter}} = 6648.137$ km. The observations cover the time span 03/2010 - 05/2012 of the re-processed release 2 (level-2 products), cf. Sec 3.3.
All measurements are reduced by the global background model GOCO03s ($V_{ab,\text{back}}$). Exactly the same model is used, as for filling up the low frequencies of the observations in the pre-processing step, cf. Sec. 3.3.5, to be consistent. Further, since GOCO03s contains full signal up to approximately degree 200, cf. 3.2.2, the differential observations $dV_{\text{ab}} = V_{ab} - V_{ab,\text{back}}$ comprise mainly spectral information above degree $l = 200$ (no information below approximately $l = 40$ due to the pre-processing, and white noise in-between $l \approx 40, \ldots, 200$). They are approximated in the estimation model, cf. Eq. (5.22), at level $J = 8$. Additionally, in order to avoid singularities in the normal equation system (5.23), prior information is introduced according to Eq. (5.19) and yields a zero vector $\boldsymbol{\mu}_d$ w.r.t. the background model, cf. Tab. 6.9.
As output, the gradients $T_{ab,8}$ ($a, b \in \{x, y, z\}$) of the disturbing potential are computed by formulating appropriate modeling equations (5.28), and restoring the background model according to Eq. (5.29). The modeling height of 270 km is adapted to the mean GOCE orbit height within the Northern test area for the selected time span of observations.

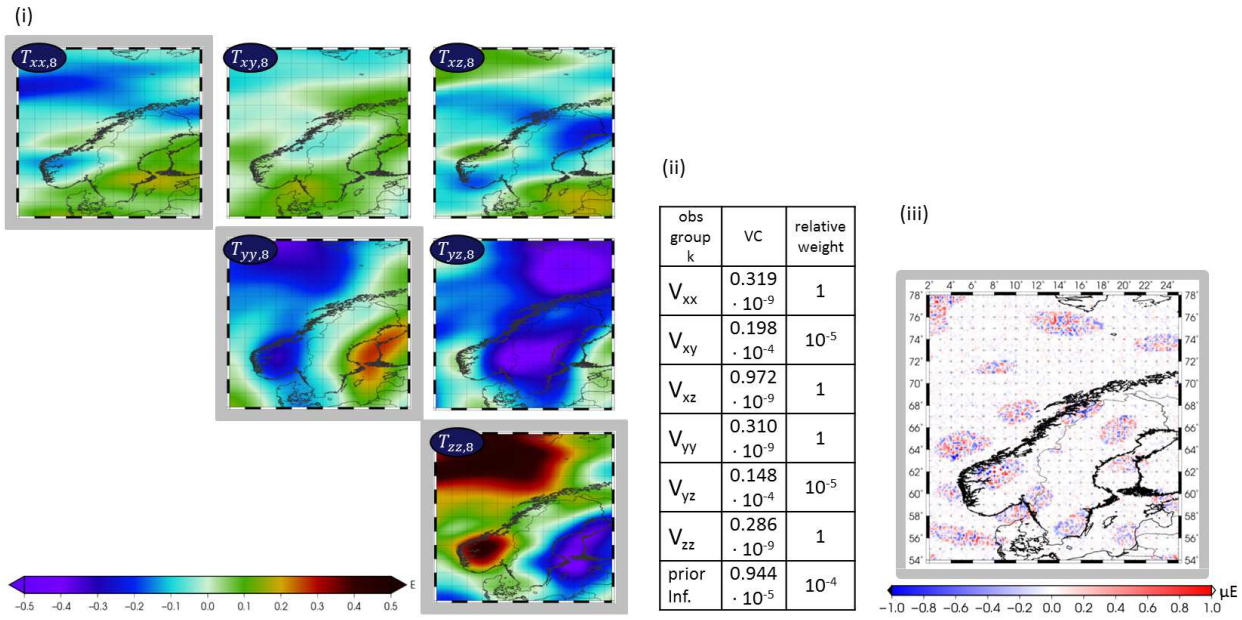

obs group k	VC	relative weight
V_{xx}	$0.319 \cdot 10^{-9}$	1
V_{xy}	$0.198 \cdot 10^{-4}$	10^{-5}
V_{xz}	$0.972 \cdot 10^{-9}$	1
V_{yy}	$0.310 \cdot 10^{-9}$	1
V_{yz}	$0.148 \cdot 10^{-4}$	10^{-5}
V_{zz}	$0.286 \cdot 10^{-9}$	1
prior Inf.	$0.944 \cdot 10^{-5}$	10^{-4}

Figure 6.12: Study case (d): (i) Gravity gradient grids of the 2nd derivatives of the disturbing potential modeled at 270 km height in LNCS from GOCE GG measurements. (ii) VCs and corresponding order of magnitude of the relative weights for each observation group k and the prior information GOCO03s, referenced to V_{zz} with highest relative weight. (iii) Trace of the tensor $\boldsymbol{T}_{ab}$ (gray shaded).

Figure 6.12 (i) presents the results of **study case (d1)** according to the xyz tensor arrangement in LNCS. The gradients T_{ab} of the disturbing potential show clearly different structures depending on the different spatial directions. As expected, the radial pointing zz component observes the strongest gravitational signal between ± 0.5 E, since it is isotropic as the Laplace equation is valid (proof see below). The variations of the xx component (pointing in flight direction) dominate in North-South direction. The high sensitivity is explained by the high inclination of the satellite, such that the flight tracks are almost oriented in direction of the meridians (*Bouman et al.*, 2016). In contrast, the yy component (cross-track) is more sensitive into East-West direction (along the latitudes), cf. referring variations in $T_{yy,8}$ Fig. 6.12 (ii).

Relative weighting by VCE The contribution of the individual GOCE GGs is regulated by VCE, cf. Sec. 5.2.2. Within Eq. (5.24), i. e. the computation of the unknown scaling coefficients, the estimated variance factors $\widehat{\sigma}_k^2$ (here $k = 1, 2, \ldots, 6$ for the six tensor components) and $\widehat{\sigma}_d^2$ indicate the relative weighting of the different observation groups V_{xx}, V_{xy}, V_{xz}, V_{yy}, V_{yz}, V_{zz}, depending on their quality. Table (ii) in Fig. 6.12 lists the estimated variance components of study case (d1), and respectively the orders of magnitude of the relative weights, $\widehat{\sigma}_k^{-2}$ and $\widehat{\sigma}_d^{-2}$, w.r.t. the zz component which points in the direction of highest signal amplitude. The referring observation group V_{zz} obtains the smallest VC, iteratively determined as described in Sec. 5.2.2, i. e., the highest relative weight. The VCs of V_{xx} and V_{yy} are only marginally larger. Those gradients have the smallest errors, since the GOCE gradiometer was most sensitive along the X- and Y-axes. Hence, the systematic errors in the V_{yy} component due to anomalous signal close to the magnetic poles, which applies for the chosen study area in Scandinavia, cf. Fig. 6.11, are obviously removed by appropriate filtering in the pre-processing procedure, cf. Sec. 3.3.5. As expected, the four accurate components V_{xx}, V_{yy}, V_{zz}, V_{xz}, obtain relative weights in the same order of magnitude. The less accurate components V_{xy} and V_{yz} are down-weighted by five orders of magnitude. Thus, their influence on the resulting models converges to zero. The prior information GOCO03s is down-weighted by four orders of magnitude indicating that regularization is very weak. This appears intuitively due to the high accuracy of the observables, their homogeneous spatial distribution and their spectral resolution, which covers the chosen modeling resolution level $J = 8$. In conclusion, the method of VCE seems to handle the observation groups in a reasonable way, by down-weighting less accurate data sets. Together with the findings from case studies (a) – (c), it is appropriate for the combination of heterogeneous data with different functionals, accuracies, spatial distributions and number of observations.

Validation by trace criterion A validation of the estimated gravity gradients $T_{ab,8}$, displayed in Fig. 6.12 (i), can be obtained by the Laplace condition (trace $(\mathbf{T}_{ab}) = 0$). The sum of the diagonal elements (gray shaded) must be zero. The trace criterion gives a mean value of 0.000 µE and a SD of 0.147 µE. Since 1 µE = 1×10^{-15} 1/s^2, and since the remaining structures, displayed in Fig. 6.12 (iii) have artificial character, the Laplace condition is valid in the frame of computational accuracy (10^{-16}). Consequently, it is proved, that the rotation of the observation equations in the GRF is implemented in a proper way, and that the regional approach delivers reasonable GG grids, cf. 6.12 (i).

Up-/downward continuation Within study **case (d2)**, the influence of the up- and downward continuation is investigated. Since the modeling approach from case (d1) uses a Reuter grid with $R_{\text{Reuter}} = 6378.137$ km grid radius, the basis functions are located near the Earth's surface ($h = 0$ km). Down- and upward continuation terms, cf. series expansions in Tab. 4.7, are applied in the observation (analysis in terms of Eq. (5.21)) and modeling (synthesis in terms of Eq. (5.27)) equations.
In case (d2), the level $J = 8$ computations are repeated according to the specifications from Tab. 6.9, now with basis functions located on a sphere with Reuter grid radius $R_{\text{Reuter}} = 6648.137$ km, i. e. approximately 270 km above the Earth's surface, close to the mean observation height. In order to investigate the influence of down- and upward continuation, the resulting GG grids of tensor $\boldsymbol{T}_{ab,8}$, case (d1), and $\boldsymbol{T}^{270\text{km}}_{ab,8}$, case (d2), are compared with GOCO03s (d/o 250). The statistics (mean, SD) of the referring differences $d\boldsymbol{T}_{ab,8}$, $d\boldsymbol{T}^{270\text{km}}_{ab,8}$, are listed in Tab. 6.10 for the single tensor components.

Table 6.10: Study case (d2): Mean value and SD of the differences $d\boldsymbol{T}_{ab,8}$ and $d\boldsymbol{T}^{270\text{km}}_{ab,8}$ to GOCO03s up to d/o 250.

	case (d1) $R_{\text{Reuter}} = 6378.137$ km			**case (d2)** $R_{\text{Reuter}} = 6648.137$ km	
difference	mean [mE]	SD [mE]	**difference**	mean [mE]	SD [mE]
$dT_{xx,8}$	0.014	0.098	$dT^{270\text{km}}_{xx,8}$	0.012	0.089
$dT_{xy,8}$	−0.002	0.070	$dT^{270\text{km}}_{xy,8}$	0.000	0.033
$dT_{xz,8}$	−0.001	0.132	$dT^{270\text{km}}_{xz,8}$	0.003	0.078
$dT_{yy,8}$	0.014	0.214	$dT^{270\text{km}}_{yy,8}$	0.003	0.077
$dT_{yz,8}$	0.020	0.230	$dT^{270\text{km}}_{yz,8}$	−0.003	0.086
$dT_{zz,8}$	−0.018	0.280	$dT^{270\text{km}}_{zz,8}$	−0.001	0.129

The mean values of $d\boldsymbol{T}^{270\text{km}}_{ab,8}$ are smaller than 0.02 mE, the corresponding SD values smaller than 0.13 mE, cf. Tab. 6.10. The largest SD 0.129 mE is obtained for $d\boldsymbol{T}^{270\text{km}}_{zz,8}$. In a rough estimate, it is for instance in the same order of magnitude as the maximum omission error 0.1 mE of V_{zz} at altitude of $h = 225$ km, assessed by *Bouman et al.* (2016) (using EGM2008 between SH degree $l = 361, \ldots, 2190$), taking different grid altitudes and spectral resolutions into account. The differences $d\boldsymbol{T}_{ab,8}$ at $h = 0$ km are slightly larger. Similar differences between the tensor components of the main diagonal and GOCO03s are discussed in the supplementary material of *Bouman et al.* (2016).
Comparing the SD values of (d1) and (d2) relatively to each other, the value of the zz component distinguishes the most. However, the difference is in the same order of magnitude as the above mentioned maximum omission error of 0.1 mE for V_{zz} from EGM2008 (again, taking into account the different spectral resolutions and altitudes). It can be concluded, that the grids of both approaches (d1) set up at $h = 0$ km, and (d2) set up at $h = 270$ km, deliver similar modeling results at satellite altitude. The effect of down- and upward continuation is marginal and does not seem to have an essential influence on the results of (d1).
Moreover, setting up the approach at $h = 0$ km increases the flexibility and is beneficial for the combination with terrestrial, air-/shipborne and altimetry data sets, observed at lower heights. Further, in most applications, one is interested in variations of the Earth's gravitational field at or close to the Earth's surface, e. g. for referencing height systems, analyzing structures of the crust or the lithosphere (*Bouman et al.*, 2013). Differences of GOCE GGs and GOCO03s at $h = 0$ km, i. e. applying just downward continuation in the analysis, but avoiding upward continuation in the synthesis, reach a few E in the Scandinavian test area, the SD of the mean difference counts around 1 E. Those differences might either indicate modeling errors or different signal in the regional models w.r.t. global SH models.

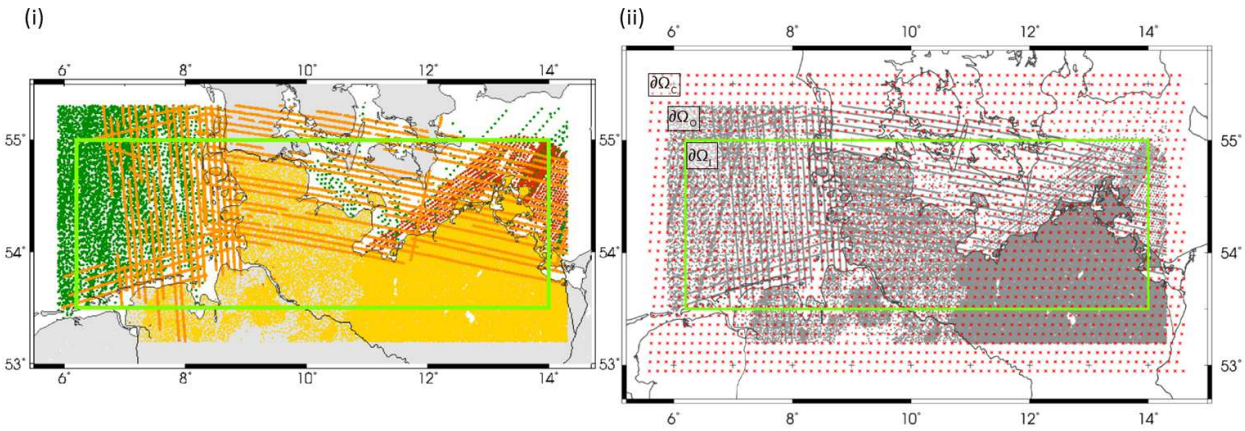

Figure 6.13: Study case (e): Test area (green bordered) in Northern Germany: (i) Spatial distribution of the terrestrial (yellow), air- (orange), shipborne (red), and altimetry (green) observations. (ii) Computation $\partial\Omega_C$ (Reuter grid, red crosses), observation $\partial\Omega_O$ (gray dots and lines), and modeling $\partial\Omega_I$ (green bordered) area. Source: *Lieb et al.* (2016), Figs. 1 and 2.

Study case (e): Terrestrial, air-/shipborne and altimetry data

The investigations and results of study case (e) are published by *Lieb et al.* (2016). The most relevant aspects to be discussed in this section are cited below. Figure 6.13 depicts (i) the heterogeneous spatial distribution of observations according to Fig. 3.9, (ii) the three areas of computation, observation and investigation, cf. Fig. 5.1. The specifications are summarized in Tab. 6.11. From the average point, along- and cross-track distances of the measurements presented in Sec. 3.3 and the overall spatial distribution, a mean spatial resolution of 10 km is derived, cf. Fig. 6.13 (i). According to Tab. 4.8, the modeling approach then is set up at level $J = 11$. The pre-processing steps, further described in in Sec. 3.3, ensure a homogenization of the data sets w.r.t. GRS80, cf. Tab. 3.7.

Table 6.11: Study case (e): Specifications.

Input $\partial\Omega_O$		· δg_{ter} gravity disturbances, terrestrial (ter) data · 5 km average point distance · pre-processing according to Sec. 3.3.1
		· δg_{air} gravity disturbances, airborne (air) data · 10 km average along-/cross-track resolution · pre-processing according to Sec. 3.3.3
		· δg_{ship} gravity disturbances, shipborne (ship) data · 4 km average along-/cross-track resolution · pre-processing according to Sec. 3.3.2
		· T disturbing potential, derived from altimetry SSH · 10 km average along-/cross-track resolution · pre-processing according to Sec. 3.3.4
Approach $\partial\Omega_C$		· $\delta g_{\text{back}}, T_{\text{back}}$: GOCO05s, $l_{j'} = 127$ ($j' = 127$) · prior information: GOCO05s, $l_{j'} = 127$ · $L = 2190$ (analysis, Shannon) · $Q_L = 2118$ unknowns, Reuter grid points respectively · $R_{\text{Reuter}} = 6378.137$ km grid radius · $l_J = 2047$ ($J = 11$, synthesis, Blackman)
Output $\partial\Omega_I$	(e1) (e1), (e2)	· Δg gravity anomalies · ζ quasigeoid heights · at regular grid (spacing $0.2° \times 0.2°$), $h = 270$ km

The estimation model [Eq. (5.22)] contains the functional relationships for the $K = 9$ different observation groups from terrestrial [1], airborne (two campaigns: *North Sea* [2], *Baltic Sea* [3]), and shipborne [4] gravimetry, as well as from altimetry (missions: ERS-1e [5], ERS-

Table 6.12: [Study case (e1):] Relative weights for each observation group k and the prior information, referenced to group [1] with highest relative weight [...]. Source: *Lieb et al.* (2016), Tab. 2.

observation group k	**observation type**	**data set**	**relative weight**
[1]	terrestrial	BKG	1
[2]	airborne	*North Sea*	1
[3]		*Baltic Sea*	1
[4]	shipborne	BKG	10^{-1}
[5]	altimetry	ERS-1e	10^{-3}
[6]		ERS-1f	10^{-3}
[7]		Cryosat RADS	10^{-3}
[8]		Envisat EM	10^{-3}
[9]		Jason-1 GM	10^{-3}
	prior information	GOCO05s	10^{-5}

1f [6], Cryosat [7], Envisat EM [8], Jason-1 GM [9]), see [Tab. 4.7]. As prior information we introduce the same global SH model as the subtracted background model GOCO05s up to [$l_7 = 127$], contributing low-resolution information mainly stemming from satellite gravimetry [cf. Sec. 3.2.2]. Thus, the expectation [vector] can be set to $\boldsymbol{\mu}_d = \mathbf{0}$ and [$\boldsymbol{P}_d = \boldsymbol{I}$] (identity matrix), assuming the SH model as noise-free. We further treat all $K = 9$ groups as independent data sets. Both, due to the variety of different measurement systems and due to the unrelated observation time spans, it is justified to neglect the correlations between the observation groups k, [cf. Sec. 3.3]. Further, we introduce identity matrices $\boldsymbol{P}_k = \boldsymbol{I}$, assuming no correlations and similar accuracies of the measurements $\boldsymbol{y}_k$ of one data type, due to insufficient information about the data quality and due to considerably smaller computational expense. (*Lieb et al.*, 2016)

The external accuracy of the computed functionals can be assessed e. g. by comparing the regional results [... in study **case (e5)**] with an existing regional model computed by a different approach and/or from different input data, or [in **case (e6)**] by composing a cross-validation, i. e. extracting some input data from the estimation and comparing the modeling results finally with those data. A comparison with regional models should [prove] the plausibility of our solution while differences to existing global models [in **case (e4)**] identify supplementary significant signal content in our model and thus the additional value of the chosen approach. However, we have to take into account correlations between identical input data in the different models. The cross-validation further allows rating the model fit of the data and thus the external accuracy. (*Lieb et al.*, 2016)

Relative weighting of input data In a first study **case (e1)**, the relative weighting of the heterogeneous data sets listed in Tab. 6.11 is discussed.

[Table 6.12] lists the relative weights [...], i. e. the reciprocal [values] of the VCs, for all observation groups k referred to the observation group [1] ($k = 1$). This terrestrial data set obtains the smallest VC, i. e. the highest relative weight due to several positive features, such as high data quality and quantity: the observations show a good signal to noise (s/n) ratio, few data gaps, homogeneous and wide-spread distribution, and high spectral resolution [cf. Sec. 3.3.1]. [...]
The off-shore shipborne measurements [4] are down-weighted relatively to [1] by one order of magnitude, due to their spatial limitation and lower accuracy [cf. Sec. 3.3.2]. The downward continuation of the airborne measurements [2] and [3] may reduce their s/n ratio as well, but the effect is marginal [cf. Study case (d),] so that [2] and [3] get the same high relative weights as [1].
The altimetry measurements [5] to [9] get each similar weights, but they are down-weighted three orders of magnitude compared to [1]: Especially the limited spatial resolution [cf. Sec. 3.3.4] reduces their signal content and contribution to the combined solution here; the low influence in contrast to [4] probably stems from the strong pre-processing of the originally less accurate

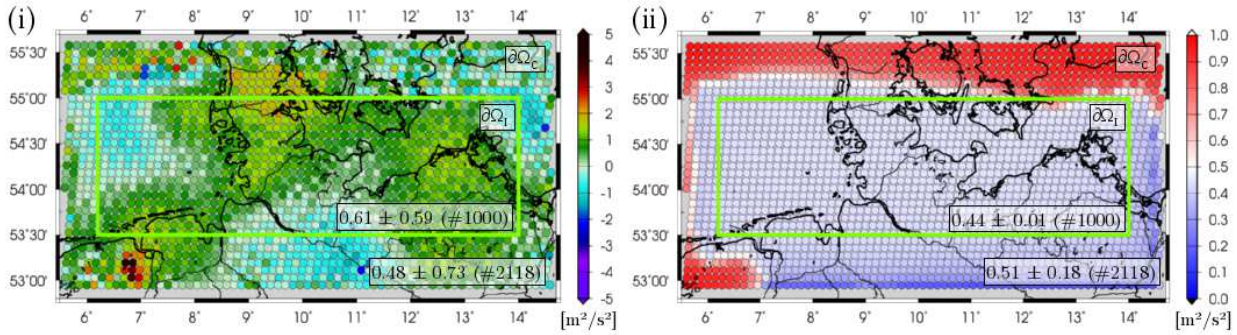

Figure 6.14: [Study case (e2): (i)] Estimated coefficients [...] and [(ii)] their standard deviations up to $L = 2190$ within the computation area $\partial\Omega_C$. The area of investigation $\partial\Omega_I$ is bordered in green. For each area the mean value and its standard deviation (of the 2118, 1000 coefficients) are displayed in the boxes. All numbers are given in m^2/s^2 [...]. Source: *Lieb et al.* (2016), Fig. 5.

> shipborne data.
> The impact of the prior information $\boldsymbol{\mu}_d$ is very weak, indicated by a 5 times lower weight compared with the terrestrial data [1]. As in general, the target area is well observed by high- and [medium]-resolution measurement systems, there is only little need for filling in data gaps, but the low-resolution prior information from GOCO05s [cf. Sec. 3.2.2] mainly serves for stabilizing the inversion and downward continuation process, in order to reduce rank deficiency and singularity problems [cf. Sec. 5.1.4]. (*Lieb et al.*, 2016)

The relative weighing of heterogeneous data sets by VCE is influenced by their accuracy, cf. study case (d), as well as by their spectral resolution, and thus, spatial distribution and size of data gaps. According to the Nyquist theorem, data sets with large spatial extent enable to resolve medium wavelengths while the latter cannot be resolved by spatially limited observations. However, for the estimation at level $J = 11$, high-frequency information is more relevant. Consequently, regionally more limited data sets, as e. g. the shipborne measurements [4], contribute in almost the same measure to the modeling solution, as spatially better distributed terrestrial measurements [1]. Even if the accuracy of observation group [4] is assumed to be lower, it supplements the spatial distribution of group [1] in the Baltic Sea, cf. Fig. 6.13 (i). Further, the airborne data set [3] gets a relative weight in the same order of magnitude as [1], despite data gaps and lower accuracy. The size of the large data gap at around 54.8° latitude, 12° longitude, seems only marginally cause a down-weighting. The data gap might be balanced by the overall spatial contribution of data set [3] in the Baltic Sea, where [3] is not overlaid by other data sets.

Accuracy and plausibility of scaling coefficients In study **case (e2)** the accuracy and plausibility of the estimated scaling coefficients up to degree $L = 2190$ is investigated.

> The unknown coefficients d_q are [...] estimated by inserting the iterated VCs $\widehat{\sigma}_k^2$ and $\widehat{\sigma}_d^2$ into [Eq. (5.24)]. [... Figure 6.14 (i)] shows the 2118 coefficients covering the computation area $\partial\Omega_C$. Inside $\partial\Omega_I$ (green bordered) the 1000 coefficients themselves already represent the gravitational structures. Consequently they have a physical meaning: large (positive or negative) values indicate additional gravity signal w.r.t. the background model. Inside $\partial\Omega_I$ the coefficients vary between $-1.31\,m^2/s^2$ and $2.15\,m^2/s^2$; their standard deviations [Fig. 6.14 (ii)], obtained from the main diagonal elements of $\boldsymbol{Q}_{dd}^{-1}$ [cf. Eq. (5.25)], between $0.39\,m^2/s^2$ and $0.65\,m^2/s^2$. [...] The standard deviations are about one order of magnitude smaller than the coefficients, indicating a good s/n ratio and thus a well-balanced combination of the data sets.
> As expected, the coefficients outside from the target area $\partial\Omega_I$ alternate and get an artificial character. Values from $-2.15\,m^2/s^2$ to $4.34\,m^2/s^2$ are reached in the margin between $\partial\Omega_I$ and $\partial\Omega_C$ and the standard deviations increase up to $0.97\,m^2/s^2$. (*Lieb et al.*, 2016)

Consequently, the structure and the accuracy of the estimated scaling coefficients inside $\partial\Omega_I$ seem plausible. An external validation is indirectly obtained after the synthesis in the next step, i. e. multiplying $\widehat{\boldsymbol{d}}_L$ with adapted basis functions from Eq. (5.27) up to degree $l_{11} = 2047$.

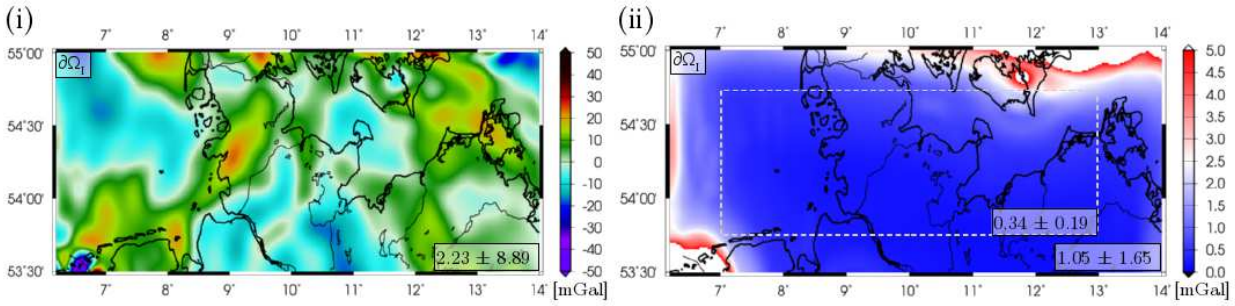

Figure 6.15: [Study case (e3): (i)] Differential gravity anomalies [Δg] up to level $J = 11$, referenced to GOCO05s up to $j' = 7$, and [(ii)] the corresponding standard deviations. Mean values and their standard deviations (depicted in boxes, given in mGal) are computed for $\partial\Omega_I$ in [(i) and (ii)], and for an inner region in [(ii)] (dashed box) representing the above all well-observed study area. Source: *Lieb et al.* (2016), Fig. 6.

Output model and its accuracy w.r.t. two different gravitational functionals By setting up the modeling equations according to (5.28), two output models are obtained for the gravitational functionals Δg and ζ. Their accuracy is investigated in this study **case (e3)** with special emphasis on the effect of data gaps.

> The resulting gravity anomalies [Δg], shown in [Fig. 6.15 (i)] vary in a range of around ±30 mGal w.r.t. GOCO05s (d/o 127), except in the southwest corner, where edge effects with values down to −57.22 mGal prevail due to data gaps. In principle, the largest negative anomalies of the differential signal are located in the South of the target area at around 11° longitude, and in the northwestern edge of $\partial\Omega_I$. [...] The respective standard deviations in [Fig. 6.15 (ii)] show here [...] their largest values with amplitudes of >5 mGal, indicating a low precision of the modeling result. This might be an artifact resulting from data gaps in the airborne measurements: [Fig. 6.13 (i)] shows clearly missing tracks in these regions. Large standard deviations further appear in the southwest corner because of missing observations in the *Netherlands* (NL). Data sets should overlap the target area in general [cf. Sec. 5.1.2] to avoid such erroneous edge effects. However, within the mainly well-observed area (dashed line in [Fig. 6.15 (ii)], the standard deviations are very small: we obtain on average 0.34 mGal (maximum 1.76 mGal). As we introduced [...] all weighting matrices as unit matrices in the estimation model [in Eq. (5.22], we have to take into account that the error propagation [cf. Eq. 5.30] might deliver too positive error estimates by neglecting possibly correlations between the measurements. A more realistic stochastic model could further marginally change the relative weighting between the observation groups. However, we conclude that we derive a modeling result with high internal precision. (*Lieb et al.*, 2016)

> The differential quasi-geoid heights ζ (w.r.t. GOCO05s, d/o 127) in [Fig. 6.16 (i)] show similar structures as the differential gravity anomalies [Fig. 6.15 (i)], since they are related to the same set of coefficients $\widehat{\boldsymbol{d}}_L$. However, the field transformation smooth[e]s the gravity signal: the functional ζ is normalized by a normal gravity γ (here w.r.t. GRS80) [...]. Minimum values are reached in the German lowlands down to −0.48 m w.r.t. GOCO05s. Maximum values up to 1.06 m appear mainly at the same locations as the maximum values of gravity anomalies. The corresponding standard deviations [Fig. 6.16 (ii)] increase up to maximum 0.12 m along the northern borderline and in the southwest corner due to the data gaps, as discussed [above]. Within the well-observed inner area (dashed box), the mean [SD] of only 1 cm (maximum 2.2 cm) approves the high internal precision of the modeling approach, taking into account feasibly too positive error estimates. (*Lieb et al.*, 2016)

In conclusion, data gaps provoke a less accurate model fit in the referring areas, indicated by the larger standard deviations. The modeling approach seems to reasonably identify missing gravitational information. The field transformation according to the Meissl scheme in Fig. 2.7, affects a smoothing of the ζ-signal, compared to gravity anomalies. The referring standard deviations in Fig. 6.16 (ii) are slightly smaller relatively to the signal values in (i), than it is in case of gravity anomalies, cf. Fig.6.15. In both Figs. 6.15 and 6.16, the signal values (i) are plotted within a range of one order of magnitude larger than the range of their standard deviations (ii).

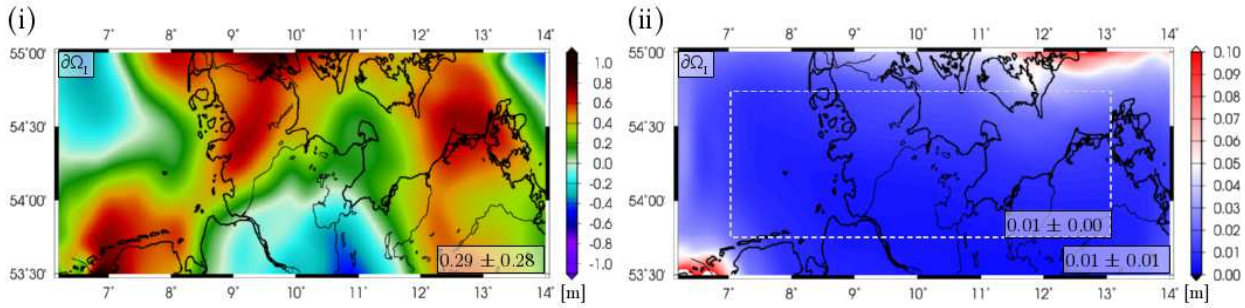

Figure 6.16: [Study case (e3): (i)] Differential quasi-geoid heights [ζ] up to level $J = 11$, w.r.t. GOCO05s up to $j' = 7$, and [(ii)] their standard deviations. The statistics (depicted in boxes) are given accordingly to [Fig. 6.15]. Source: *Lieb et al.* (2016), Fig. 7.

In order to investigate the effect of field transformations, a comparison of the regional model to global SH models is studied w.r.t. both functionals, Δg and ζ, see below.

Added value w.r.t. global SH models Potential added value contained in the regional model is rated by a comparison with global SH models in study **case (c4)**. Therefore, the erroneous edge effects are removed in the data gap areas according to the standard deviations. (*Lieb et al.* (2016) use a 3-sigma threshold.) The background model GOCO05s then is restored to the regional solution, obtaining the total signals of Δg and ζ according to Eq. (5.29). The total signal of ζ is displayed in Fig. 6.18 (i).

> We choose two global high-resolution models, EGM2008 (EGM), available up to d/o 2190, and EIGEN-6c (EIG), available up to d/o 1949, [cf. Sec 3.2.2,] and computed the differences $[d\Delta g]$ and $[d\zeta]$ to our total regional (reg) results [...]. For spectral consistency, we smoothed the equivalent functionals of the global SH models with the same *Blackman* filter up to degree $l_{11} = 2047$, as we used in the regional synthesis [cf. Eq. (5.27)]. (The missing high frequencies $l = 1950, \ldots, 2047$ in the EIGEN-6c model are set to zero and do not influence the applied *Blackman* filter.) [Table 6.13] lists the range, the mean values and the corresponding (relative) standard deviations of the differences (reg - EGM) and (reg - EIG) for the target area $\partial\Omega_I$. In general, the differences to EGM2008 and to EIGEN-6c are comparable. (The difference between both global models counts $[d\Delta g]$ (EGM - EIG) = 0.07 ± 0.94 mGal, $\Delta\zeta$ (EGM - EIG) = 0.5 ± 3.0 cm respectively, resulting mainly from the different spectral resolution.) The mean values of the differences of −0.68 mGal for $[d\Delta g]$ (reg - EGM) (−0.61 mGal for $[d\Delta g]$ (reg - EIG)), and 0.09 m for $[d\zeta]$ (reg - EGM) (0.10 m for $[d\zeta]$ (reg - EIG)) indicate a small offset, probably stemming from the spatially limited data sets used in the regional solution and from insufficient prior information, and thus missing information in the [medium] frequencies.
> The according standard deviations of 2.30 mGal and 2.41 mGal (corresponding to EGM2008 and EIGEN-6c) from the mean value of the gravity anomaly differences are one order of magnitude larger than the mean values themselves. For quasi-geoid heights they are with 6 cm (EGM) and 5 cm (EIG) similar to the mean values. In order to compare the different output functionals, we computed relative standard deviations related to the standard deviation (12.67 mGal for $[\Delta g]$ and 1.32 m for ζ) of the mean value of the EGM2008 signal as well. Thus, the relative standard deviation counts around 18.1 % for gravity anomaly differences $[d\Delta g]$ (reg - EGM), but just around 4.3 % for quasi-geoid height differences $[d\zeta]$ (reg - EGM). We explain the lower relative standard deviation of $[d\zeta]$ by the smoothness of the functional ζ itself (cf. Sec. 2.5.3), whereas the differential gravity quantity $[\Delta g]$ shows much more detailed structures. [...]
> To further [prove the signal content in our regional model], we study the spatial pattern of the differences $[d\Delta g]$ and $[d\zeta]$ to EGM2008 (reg - EGM), [see Fig. 6.17 (i) and (ii)]. As expected, the largest deviations (down to −22 mGal for gravity anomalies and up to around 40 cm for quasi-geoid heights) occur in the southwest corner where our regional model contains erroneous edge effects due to the lack of data. Comparing the spatial pattern with the observations in [Fig. 6.13 (i)] we notice that the terrestrial data end up along the borderline of the *Netherlands*, and the airborne tracks do not overlap $\partial\Omega_I$ along the northern margin. Those dominant local effects coincide with the largest standard deviations in [Figs. 6.15 (ii) and 6.16 (ii)]. Thus, we

Table 6.13: [Study case (e4):] Differences between regional results (reg) at level $J = 11$, *Blackman* filtered up to $l = 2047$, outliers removed, and the corresponding functionals Dg and ζ computed from EGM2008 (EGM) and EIGEN-6c (EIG), both *Blackman* filtered up to level $J = 11$. The relative standard deviation (SD) is referenced to the standard deviation of the mean value of EGM2008 in $\partial\Omega_I$. Source: *Lieb et al.* (2016), Tab. 3.

difference	**range**	**mean**	**SD**	**relative SD**
$d\Delta g$ (reg - EGM)	−21.96 to 14.46 mGal	−0.68 mGal	2.30 mGal	18.1 %
$d\Delta g$ (reg - EIG)	−20.97 to 15.46 mGal	−0.61 mGal	2.41 mGal	19.0 %
$d\zeta$ (reg - EGM)	−0.08 to 0.40 m	0.09 m	0.06 m	4.3 %
$d\zeta$ (reg - EIG)	−0.04 to 0.43 m	0.10 m	0.05 m	4.1 %

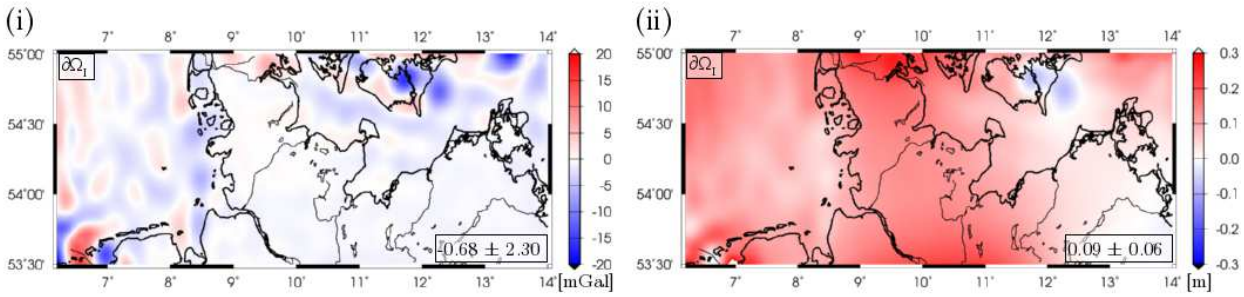

Figure 6.17: [Study case (e4)]: [(i)] Differences $[d\Delta g]$ and [(ii) $d\zeta$] of the resulting total gravity anomalies and quasi-geoid heights ([...] background model GOCO05s restored) to the global model EGM2008, consistently filtered with *Blackman* kernel up to degree $l_{11} = 2047$. Mean values and standard deviations from the mean values are given for $\partial\Omega_I$ in the corresponding units. Source: *Lieb et al.* (2016), Fig. 9.

conclude a lack of signal content in our [...] model [in this region]. The low-resolution prior information obtained from GOCO05s up to d/o 127 cannot provide enough spectral information to overcome these edge effects. For $[d\zeta]$ the offset of around 10 cm predominates the remaining small standard deviations [Fig. 6.17 (ii)], while for the more sensitive differences $[d\Delta g]$ some small-scale structures occur especially in the off-shore areas. We interpret those deviations as additional signal in our regional model, stemming especially from altimetry observations (mainly Cryosat an Jason-1 GM), and from airborne measurements, which overcome the altimetry data gaps near the coastlines. They are not part of the global model EGM2008. Over land, our regional model and the global EGM2008 model fit better. For the remaining deviations, correlations stemming from terrestrial and airborne data sets can be excluded, as we used recently collected data which are not contained in the existing global models (EGM2008 relies on older data with less accuracy). Hence, we interpret the differences as supplementary information in our regional model [... with the] potential to improve the existing global models in selected regions. (*Lieb et al.*, 2016)

Plausibility of the regional result w.r.t. another regional model

In order to validate our regional modeling result, we thus compare it [in study **case (e5)**] to an existing regional model, the *German Combined Quasigeoid 2011* (GCG2011) [cf. Fig. 3.8]. It is provided [...] with an off-shore precision of 4 cm to 10 cm and an on-shore precision of 1 cm to 2 cm in the German lowlands [cf. Sec. 3.2.3]. Thus, the precision is comparable with the obtained mean standard deviation of 1 cm of our regional model, [cf. Fig. 6.16 (ii)].
The statistics of all differences are listed in [Tab. 6.14]. The mean value of the difference $[d\zeta]$ (reg - GCG) between our regional estimation (reg) and the GCG2011 model (GCG) predominates with −18 cm the small standard deviations of ≤5 %, relatively to the mean standard deviation of EGM2008. Comparing the global EGM2008 model (EGM) with GCG2011 delivers a larger offset of -28 ± 3 cm, but an even smaller relative standard deviation of 2.3 %. The difference seems to originate from the GCG2011 model, as the difference $[d\zeta]$ (reg - EGM) at exactly the same grid points counts a mean value of 9 ± 6 cm, equivalent to the corresponding statistics in [Tab. 6.13]: In contrast to our regional model, the GCG2011 is not a pure gravimetric geoid model, as it is adapted to a number of GNSS (Global Navigation Satellite System) leveling points

Table 6.14: [Study case (e5):] Differences of the quasi-geoid heights obtained by our regional approach (reg) up to level $J = 11$, *Blackman* filtered up to $l_{11} = 2047$, to GCG2011 (GCG), as well as to EGM2008 (EGM), also *Blackman* filtered up to $l_{11} = 2047$. The values $[d\zeta]$ are computed at the given $1' \times 1.5'$ GCG2011 grid. The relative standard deviation is referenced to the standard deviation of the mean value of EGM2008. Source: *Lieb et al.* (2016), Tab. 4.

difference	**range**	**mean**	**SD**	**relative SD**
$d\zeta$ (reg - GCG)	−0.38 to 0.20 m	−0.18 m	0.06 m	4.8 %
$d\zeta$ (EGM - GCG)	−0.38 to −0.15 m	−0.28 m	0.03 m	2.3 %

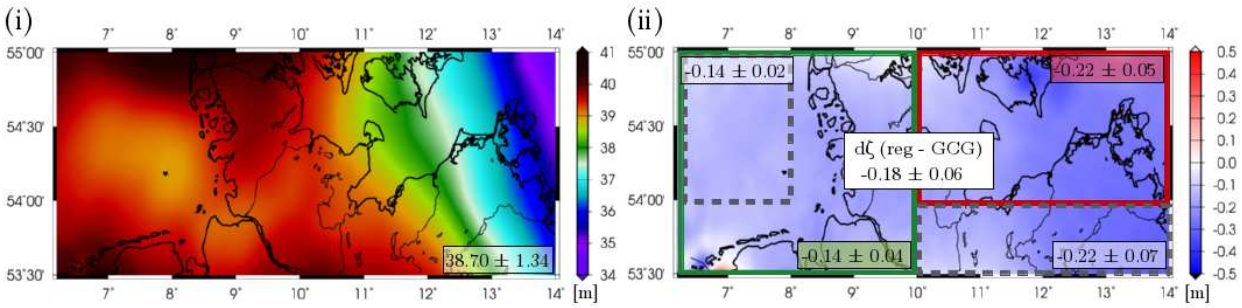

Figure 6.18: Study case (e5): (i) Total signal ζ up to level $J = 11$ (GOCO05s restored) and (ii) differences $d\zeta$ to GCG2011. Mean values and their SD are given for the entire area, the red-bordered altimetry validation area, the green-bordered shipborne validation area, and two gray-dashed-bordered pure off-/on-shore areas. Source: *Lieb et al.* (2016), Figs. 8 b and 10.

in order to allow transformations to geometric reference frames [(*BKG*, 2011)].
We further evaluate the differences for different sub-regions, shown in [Fig. 6.18 (ii)]. The offset increases between the western (green-bordered box from 6.2° to 10° longitude) and the eastern part (10° to 14° longitude) from −14 cm to −22 cm. The mean standard deviations of the differences increase as well, but they differ additionally between off- and on-shore regions: Over the *North Sea*, mainly observed by altimetry (gray-dashed box from 6.2° to 8° longitude), they count 2 cm from the mean value, and 4 cm for the entire green-bordered western part, containing both off- and on-shore areas. Over the *Baltic Sea* they rise up to 5 cm and we obtain finally 7 cm over the south-east "terrestrial-only" area (gray-dashed box). Comparing those values with the given precision of the GCG2011 model, the differences $[d\zeta]$ (reg - GCG) are not significant in off-shore areas, but over land. As the GCG2011 relates to the same terrestrial, air- and shipborne input data sets as our regional model, the deviations may result from topographic corrections which have been applied to the GCG2011 model [(*BKG*, 2011)].
However, regarding the whole area $\partial\Omega_I$, both regional models fit very well to each other and the small standard deviation (6 cm) of the mean difference confirms the high precision [and plausibility] of our modeling result.

External accuracy of the resulting models

In order to evaluate the external accuracy of our regional model, we set up a cross-validation [in study **case (e6)**]: we excluded the altimetry Envisat EM observations and recomputed quasi-geoid heights at their 1029 positions. We choose Envisat EM among all altimetry missions as it does not affect the spatial extent of the satellite data, especially the coverage of the *Baltic Sea* and the areas along the coastlines. The differences $[d\zeta^{\#}]$ to the eliminated altimeter observations are displayed in [Fig. 6.19 (i)]. Further, we excluded each 10th shipborne and each 10th terrestrial observation and recomputed gravity anomalies at their locations. The plots [(iii) and (ii)] show the corresponding differences $[d\Delta g^{\#}]$ (reg - ship) and $[d\Delta g^{\#}]$ (reg - terr) at the 101 and 1807 data points. [Table 6.15] lists the statistics of the cross-validation.

Envisat EM data For the cross-validation with Envisat EM (reg - Env) we notice a very homogeneous structure of the differences [cf. Fig. 6.19 (i)] with a mean value of -2 ± 5 cm, excluding a few outliers >30 cm, close to the islands in the south. In this coastal area, we assume the altimeter data to be erroneous [cf. Sec. 3.3.4]. The standard deviations of the mean

Table 6.15: [Study case (e6):] Statistics of the cross-validation: Differences $[d\zeta]$ and $[d\Delta g]$ between the total regional model (reg) and the previously excluded [(i)] 1037 Envisat EM (Env), [(ii)] 1807 terrestrial (terr), and [(iii)] 101 shipborne (ship) data [cf. Fig. 6.19]. Additionally we compare the global model EGM2008 (EGM) with both the data sets and the regional results. Relative standard deviations are referenced to the [SD] of the mean value of EGM2008 in $\partial\Omega_I$. Source: *Lieb et al.* (2016), Tab. 5.

difference	**range**	**mean**	**SD**	**relative SD**
$d\zeta^{\#}$ (reg - Env)	−0.28 to 0.25 m	−0.02 m	0.05 m	4.1 %
$d\zeta^{\#}$ (EGM - Env)	−0.36 to 0.15 m	−0.12 m	0.05 m	4.1 %
$d\zeta^{\#}$ (reg - EGM)	0.05 to 0.17 m	0.10 m	0.03 m	2.3 %
$d\Delta g^{\#}$ (reg - terr)	−9.02 to 6.97 mGal	0.00 mGal	1.62 mGal	12.8 %
$d\Delta g^{\#}$ (EGM - terr)	−7.79 to 5.60 mGal	0.52 mGal	1.59 mGal	12.5 %
$d\Delta g^{\#}$ (reg - EGM)	−3.36 to 5.18 mGal	−0.52 mGal	0.48 mGal	3.8 %
$d\Delta g^{\#}$ (reg - ship)	−7.55 to 5.50 mGal	0.85 mGal	2.12 mGal	16.7 %
$d\Delta g^{\#}$ (EGM - ship)	−2.32 to 5.69 mGal	2.46 mGal	1.62 mGal	12.8 %
$d\Delta g^{\#}$ (reg - EGM)	−10.11 to 3.44 mGal	−1.61 mGal	1.77 mGal	14.0 %

values of both differences (reg - Env) and (EGM - Env) count 5 cm, i. e. 4.1 % of the mean standard deviation of the EGM2008 signal, [see Tab. 6.15]. The small relative deviation states a high external precision of our regional model w.r.t. Envisat EM observations. To consistently compare the cross-validation with the validation against EGM2008 [cf. study case (e4)], we recomputed the differences along the Envisat EM tracks and obtain a relative standard deviation (reg - EGM) of 2.3 %. We conclude that over the ocean our regional model fits better to the global model EGM2008 than to the Envisat EM observations, but both models, the global EGM2008 and our regional model, fit the altimetry observations similarly. We do not achieve an improvement with our regional approach in the case of fitting altimeter data sets, but we reach comparable precision as with a global approach, and even higher accuracy comparing the mean values of the differences of −2 cm for (reg - Env) vs. −12 cm for (EGM - Env).

Terrestrial data In the case of fitting regional data sets, we reach similar relative approximations: In a second cross-validation we compare our regional model with the excluded 1807 (10 %) terrestrial observation sites. From [Tab. 6.15] we infer that our regional model (reg) fits the terrestrial data (terr) again equivalently to the global EGM2008 model (EGM) (relative standard deviations of 12.8 % and 12.5 %). However, mean value of the differences $[d\Delta g^{\#}]$ (reg - terr) counts 0.00 ± 1.62 mGal, whereas $[d\Delta g^{\#}]$ (EGM - terr) delivers 0.52 ± 1.59 mGal. As the differences $[d\Delta g^{\#}]$ (reg - terr), displayed in [Fig. 6.19 (ii)], do not show any systematic, we conclude that our model confidently extracts as much information as possible from the regional data set.

Shipborne data From the cross-validations with Envisat EM and with terrestrial data we conclude a similar modeling precision both by a global and by a regional approach. To further [prove], if the model approximations are independently from on- or off-shore areas, we set up a cross-validation with 101 shipborne data, [see Fig. 6.19 (iii)]. The corresponding statistics of the differences $[d\Delta g^{\#}]$ (reg - ship) in [Tab. 6.15] show a larger relative standard deviation (16.7 %), than the differences (reg - terr) to terrestrial data. It seems reasonable, as the shipborne data have [lower] accuracy than the terrestrial and thus get a smaller weight in the VCE, [cf. Tab. 6.12]. The data fit by our regional model is less close than the data fit by the EGM2008 model (12.8 % relative standard deviation of the differences). Assuming the large differences in the north-east corner stemming from erroneous edge effects (cf. large standard deviations in [Fig. 6.15 (ii)]) and excluding them, delivers a standard deviation of 1.24 mGal (9.8 %). (*Lieb et al.*, 2016)

In conclusion, all three cross-validations confirm a high external accuracy of the regional modeling results obtained in the test area in Northern Germany. Together with the high internal precision, discussed in case (e3), the approach is verified to manage the consistent combination of real data sets with different observation heights and spatial distributions in this study case (e).

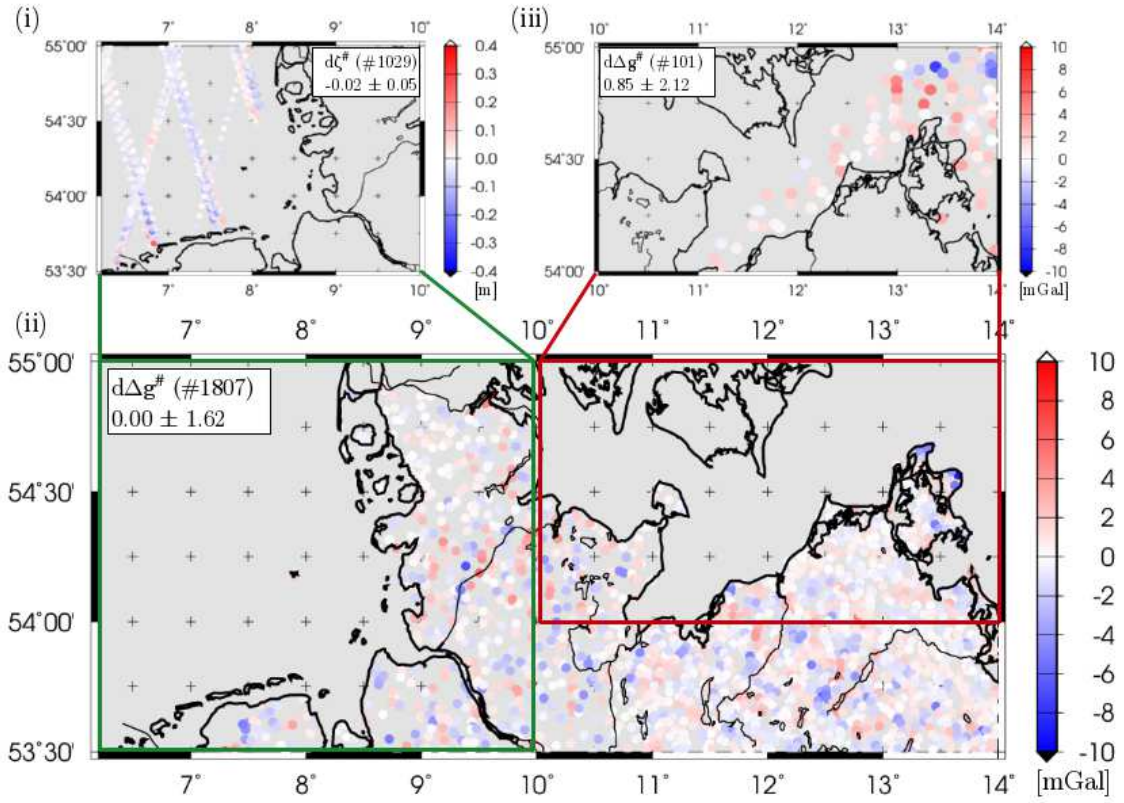

Figure 6.19: Study case (e6): Cross-validation with [(i)] 1029 Envisat EM (Env), [(iii)] 101 shipborne (ship) and [(ii)] 1807 terrestrial (terr) observations. Displayed are the differences [(i) $d\zeta^{\#}$] (reg - Env), [(iii) [$d\Delta g^{\#}$] (reg - ship), and [(ii) $d\Delta g^{\#}$] (reg - terr) between the observations and the modeled total gravity functionals (reg), computed without these observations, at locations of the validation data sets. Mean values and their standard deviations are given in the corresponding units m [(i)], and mGal [(ii), (iii)]. Source: *Lieb et al.* (2016), Fig. 11.

Remaining long-wavelength signal and errors

As discussed in study case (c) by means of simulated noise-free data, low-resolution signal remains after removing the data by a global background model which contains different information. In case of real data, long-wavelength errors remain as well. For instance in study case (e), the background model GOCO05s up to $l_{j'} = 127$ is mainly computed from GRACE data, while the regional model uses terrestrial, air-/shipborne and altimetry data. Those erroneous measurements contain different low-resolution information than GOCO05s. Figure 6.20 visualizes the aspect referring to Fig. 4.4: The observations, cf. black curve in (i), contain low- up to high-resolution errors (red-yellow curve). Subtracting $\mathcal{Y}[\,\tilde{V}_{\text{back}}(\boldsymbol{x})\,]$ up to degree $l_{j'}$ according to Eq. (5.13) from the observations (at location $\boldsymbol{x}$), yields remaining long-wavelength errors and signal, indicated in (ii) as red curve in the frequency spectrum up to $l_{j'}$. In the analysis, the model g (purple curve) is computed by series expansion up to degree L (purple box) and in the synthesis up to $l' < L$ (gray box). Aliasing errors by frequency folding (yellow) are reduced, as discussed in the context of Fig. 4.4; long-wavelength errors and signal (red-purple curve) at degrees $< l_{j'}$ remain, cf. Fig. 6.20. In the MRR approach which is applied in Sec. 6.2, the bandpass filtering wavelet functions (cf. gray boxes in Fig. 5.12) reduce in the synthesis the remaining influence of long wavelengths in the detail signals.
Since low-resolution errors are mainly of systematic nature, they are visible in terms of an offset or a slope of the data sets and cannot be captured by VCE. However, they are assumed to be small, as the pre-processing of the data sets according to Sec. 3.3, and the rescaling of the SH coefficients of the background model, cf. Sec. 5.1.6, ensure consistency w.r.t. a reference potential. Possibilities of estimating the values of the systematic errors and taking them into account are discussed in the Outlook 7.

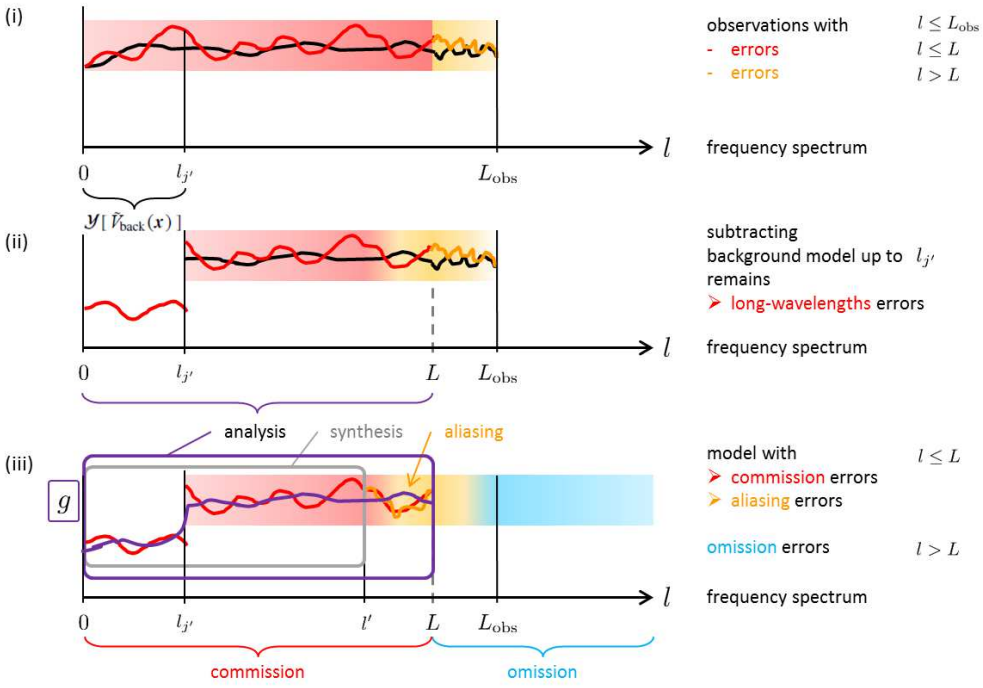

Figure 6.20: (i) Observations in the spectral domain containing signal (black curve) up to degree L_{obs}, and low-/medium-frequency (red) up to high-frequency (yellow) errors. (ii) Subtracting a background model $\mathcal{Y}[\,\tilde{V}_{\text{back}}(\boldsymbol{x})\,]$ up to degree $l_{j'}$ yields remaining long-wavelength errors and signal (truncated red curve $< l_{j'}$). (iii) The model g (purple curve) is in the analysis computed by series expansion up to degree L (purple box) and in the synthesis up to $l' < L$ (gray box). Aliasing errors by frequency folding (yellow) are reduced, but long-wavelength errors and signal (red-purple curve) at degrees $< l_{j'}$ remain.

Summary and conclusion of the real data studies at one resolution level

From both study cases (d) and (e) using a variety of heterogeneous real data, it is shown, that the regional modeling approach manages different accuracies, observation heights, functionals, field transformations and

spatial distributions in a proper and consistent way; the error propagation and the different validation strategies confirm the high accuracy and stability of the resulting models. Further it is demonstrated, that high-resolution models deliver the potential for regionally refining global models. Taking the findings from the simulation studies (a) – (c) into account, the three secondary aims, listed at the beginning of this chapter, are achieved for the presented study cases.
However, especially the data gaps in case (e) indicate weaknesses and limits of the approach. The data gaps in high-resolution observation groups can be compensated by surrounding observations inside the target area. In contrast, at the edges, erroneous oscillations predominate data gaps. The prior information, introduced for regularization purposes, is not sufficient to compensate the lack of measurements at high resolution levels, since it is a "zero-signal" w.r.t. the lower-resolution background model. Further, the above discussed errors in the long wavelengths are not taken into account.
Since dealing with high-resolution real data implies in the most cases the problem of data gaps, it is imperative to address their proper handling and to overcome the difficulties in the resulting models. Introducing additional high resolution prior information from topography models, as mentioned in study cases (a) and (b), might help to fill those gaps, see Sec. 7 as well. Further, in both case studies (d) and (e), the maximum resolution level ($J = 8$ and $J = 11$) was adapted to the mean spatial, and thus, spectral resolution of the different observation groups. This choice is beneficial, as long as the different groups have similar spectral resolutions according to the classification in Fig. 4.8. However, the introduction of GOCE GGs, which are most sensitive at resolution levels $j = 5, \ldots, 8$, as additional observation groups in study case (e), where the estimation model is set up at level $J = 11$, fails. In conclusion, the approach applied at resolution level $J = 11$ is not appropriate for a combination of observation groups with lower spectral resolution in case of data gaps. (Note, in contrast to a homogeneous spatial data distribution, the simulation study in case (c2) indicated, that the solution might be stabilized by appropriate information in the low frequency domain.)
The spectral combination via MRR, presented in Sec. 5.3, provides the potential to overcome those difficulties since it allows a flexible combination of heterogeneous data sets according to their different spectral content, i. e. it enables to extract as optimally as possible the spectral information out of each observation group.

6.2 Spectral combination via MRR

In order to enrich the regional model at each resolution level as optimally as possible with information stemming from sensitive measurement techniques, a spectral combination via MRR is set up. Hereby, the use of real data requires specific considerations. Following the definition of the three areas in Fig. 5.3, which is the above all methodical setting by the transition from global to regional in Sec. 5.1.2, the aspects are distinguished by

- data depending considerations w.r.t. the observation area $\partial\Omega_O$, i. e. spatial distribution, type, spectral resolution, number, functional, observation height and stochastic information of data sets;
- model depending considerations w.r.t. the computation area $\partial\Omega_C$, i. e. type, resolution, weighting of prior information, modeling height, functional, resolution level and basis function within the synthesis;
- area depending considerations w.r.t. the target area $\partial\Omega_I$, i. e. type (oceanic vs. terrestrial) or topography.

Further, selecting the target area requires not only the availability of observations, but also the study of more details: Which area is "sufficiently" covered by data? What means "sufficient" in order to achieve the chosen modeling resolution L according to Eq. (5.12)? How large is the effect of data gaps within the MRR at different levels, i. e. the spatial influence of edge effects?

Study case (f) : MRR decomposition: How does the information vary at different levels? Up to which level does the prior information fill data gaps?

Study case (g) : MRR composition: Which observation group contributes at which level most spectral information?

(g1) Avoiding correlations between detail signals. Is the signal content sufficient?

(g2) Multiple (decomposed) single-level estimations. What is the added value w.r.t. the single-level combination?

6.2.1 MRR decomposition

In Fig. 4.7, the MRR decomposition is described by successively low-pass filtering a high-resolution signal Z_J level by level "top-down" to a low-resolution signal $Z_{j'}$. This filter procedure is applied to the signal of differential gravity anomalies Δg from case study (e), displayed in Fig. 6.15 (i). The approach was set up at level $J = 11$, and the background model GOCO05s subtracted up to degree $l_7 = 127$. The latter defines the minimum resolution level $j' = 7$, cf. Eq. (5.10), since up to its maximum degree l'_j, most of the signal is removed from the observations. Consequently, the fundamental equation (4.28) of MRR reads for the following study case (f)

$$\Delta Z_{11}(\boldsymbol{x}) = \Delta Z_{j'=7}(\boldsymbol{x}) + \sum_{j=8}^{11} G_j(\boldsymbol{x})\,. \tag{6.4}$$

The detail signals G_j are computed according to the modeling equations (5.35) for $j = 8, \ldots, 11$. Herein, the wavelet functions $\tilde{\Psi}_j$ are formulated for gravity anomalies Δg and expanded in a series up to the maximum degree l_j of the particular resolution level j according to Eq. (5.33). Since in the approach of study case (e), Blackman scaling functions are used in the synthesis, cf. Tab. 6.11, the referring Blackman wavelet functions now are applied in study case (f). They are defined by the band-pass filtering Legendre coefficients $\psi^{\mathrm{Bla}}_{l,j}$ according to Eq. (4.37), as displayed in Fig. 4.10 (e). In the top-down approach, the detail signals are successively subtracted from ΔZ_J and yield the low-pass filtered signals

$$\begin{aligned}
\Delta Z_{10}(\boldsymbol{x}) &= \Delta Z_{11}(\boldsymbol{x}) - G_{11}(\boldsymbol{x})\,,\\
\Delta Z_{9}(\boldsymbol{x}) &= \Delta Z_{10}(\boldsymbol{x}) - G_{10}(\boldsymbol{x})\,,\\
\Delta Z_{8}(\boldsymbol{x}) &= \Delta Z_{9}(\boldsymbol{x}) - G_{9}(\boldsymbol{x})\,,\\
\Delta Z_{7}(\boldsymbol{x}) &= \Delta Z_{8}(\boldsymbol{x}) - G_{8}(\boldsymbol{x})\,.
\end{aligned}$$

Low- and band-pass filtered signals

The low- and band-pass filtered signals ΔZ_j and G_j, as well as the initial signal ΔZ_{11} at highest resolution level, are displayed in Fig. 6.21 in terms of gravity anomalies w.r.t. GOCO05s up to $l_7 = 127$. The referring statistics (range, mean value, SD) are listed in Tab. 6.16; outliers have been removed. As expected, the successive low-pass filtering of the initial signal from level $J = 11$ down to level $j = 8$ is clearly visible: While the signal ΔZ_{11} shows a lot of geographical structures, the latter become smoother and smoother for decreasing resolution levels. The information of the low-resolution signal $\Delta Z_{j'=7}(\boldsymbol{x})$ is almost completely reduced by the background model, and thus, as good as no gravitational variations are visible.
The statistics (range and SD of the signals ΔZ_j) establish the considerations. The range of ΔZ_{11} counts about ±30 mGal, the SD around 10 mGal, whereas ΔZ_8 ranges between ±10 mGal and yields a SD of approximately 4 mGal. The remaining differences of ΔZ_7 w.r.t. GOCO05s at level $j' = 7$ yield 0.29 mGal to 1.64 mGal. For the levels $j = 8, \ldots, 11$, the mean values of ΔZ_j are very similar; they slightly increase from around 2.18 mGal ($j = 8$) to 2.61 mGal ($J = 11$). For ΔZ_7, the mean value is with 1.11 mGal only approximately half as large. As expected, the mean values of G_j are close to zero[27] for the levels $j = 9, \ldots, 11$, while for G_8 the mean value counts 1.07 mGal, i. e. this detail signal contains information of an offset w.r.t. GOCO05s. Since long wavelengths cannot be resolved by regional models, the appearance of offsets w.r.t. global models is explicable.
In analogy to ΔZ_{11}, the detail signal G_{11} shows very fine structures in Fig. 6.21; the latter become rougher for G_{10}, G_9, and G_8. Those signals contain the spectral information of the frequency bands, described by the Legendre coefficients from Fig. 4.10 (e). For the band-pass filtering Blackman wavelet, the frequency bands overlap due to the smoothing behavior. Consequently, the detail signals are correlated and not independent from each other. The corresponding ranges and SD values in Tab. 6.16 decrease as well together with the resolution level.
The erroneous effects, which are visible in the south-western edge and along the northern borderline in Fig. 6.15 (i) have been discussed in study case (e). They result from data gaps. The missing information is filled up by prior information, i. e. with "zero-signal" w.r.t. GOCO05s up to $l_7 = 127$. The higher-resolution detail signals G_{11} and G_{10} show corresponding erroneous structures in Fig. 6.21; G_9 is still affected by the

[27] The detail signals are globally per definition zero.

data gap in the south-western corner. In G_8 (respectively Z_8), the data gaps are not longer apparent; the "zero-signal" from the prior information seems to be sufficient to fill them up.

Table 6.16: Study case (f): Range (min... max), mean value and SD of low- (ΔZ_j) and band- (G_j) pass filtered signals, as well as of the background model GOCO05s up to $l_7 = 127$.

ΔZ_j	range [mGal]	mean [mGal]	SD [mGal]	G_j	range [mGal]	mean [mGal]	SD [mGal]
ΔZ_{11}	−33.81 to 40.42	2.61	11.169	G_{11}	−26.91 to 31.83	0.28	6.850
ΔZ_{10}	−20.47 to 24.17	2.36	8.841	G_{10}	−13.67 to 13.27	0.05	4.568
ΔZ_9	−13.83 to 15.97	2.31	6.697	G_9	−9.87 to 13.16	0.13	4.291
ΔZ_8	−7.38 to 7.80	2.18	3.551	G_8	−8.02 to 6.51	1.07	3.389
ΔZ_7	0.29 to 1.64	1.11	0.332				
GOCO05s	−28.20 to 16.85	−6.16	11.161				

Standard deviations

In Fig. 6.22 the referring standard deviations $s\Delta Z_j$ of the low-, and sG_j of the band-pass filtered signals are visualized. Note, $s\Delta Z_8$, $s\Delta Z_7$ and sG_7 refer to different color bars. The statistics (maximum, mean, and SD values) are listed in Tab. 6.17. As discussed in the context of study case (e), the values of $s\Delta Z_{11}$ enormously increase in the corresponding south-western corner and along the northern borderline due to the edge effects. The standard deviations reach up to around 30 mGal. Low-pass filtering the initial signal ΔZ_{11} provokes a smoothing of the signal, as well as of the standard deviations. Consequently, the structures in Fig. 6.22 become also smoother, especially for the levels $j = 8$ and $j = 9$. The referring mean standard deviations then are smaller than 0.5 mGal, cf. Tab. 6.17.
The standard deviations $s\Delta Z_7$ refer to the low-resolution signal ΔZ_7 stemming from the remaining observations which have not been completely removed by the background model. Consequently, those standard deviations could give a rough measure of the long-wavelength errors, discussed in the context of Fig. 6.20. The maximum and mean values are in the order of 0.08 mGal and 0.05 mGal. However, those estimates are obtained via error propagation from the initial standard deviations at level $J = 11$. A more realistic estimate of the long-wavelength errors might be obtained by setting up the modeling approach (with specifications of Tab. 6.11) at level $J = 7$, see next section. In general, the standard deviations might be too optimistic, especially since correlations and realistic accuracies of the observations are not considered in the stochastic model, as discussed in the previous study cases.

Table 6.17: Study case (f): Maximum , mean value and SD of the standard deviations $s\Delta Z_j$ of the low-, and sG_j of the band-pass filtered signals w.r.t. GOCO05s up to $l_7 = 127$.

	max [mGal]	mean [mGal]	SD [mGal]
$s\Delta Z_{11}$	30.144	1.64	3.534
$s\Delta Z_{10}$	6.483	0.98	1.279
$s\Delta Z_9$	1.726	0.45	0.352
$s\Delta Z_8$	0.379	0.16	0.070
$s\Delta Z_7$	0.084	0.05	0.017

	max [mGal]	mean [mGal]	SD [mGal]
sG_{11}	29.586	1.20	3.336
sG_{10}	6.250	0.83	1.258
sG_9	1.684	0.41	0.353
sG_8	0.369	0.15	0.068

Discussion of study case (f)

Besides the previously discussed weaknesses of the regional modeling approach, cf. study cases (a) – (e), the MRR decomposition in this study case (f) reinforces data gaps to be one of the major problems. As already

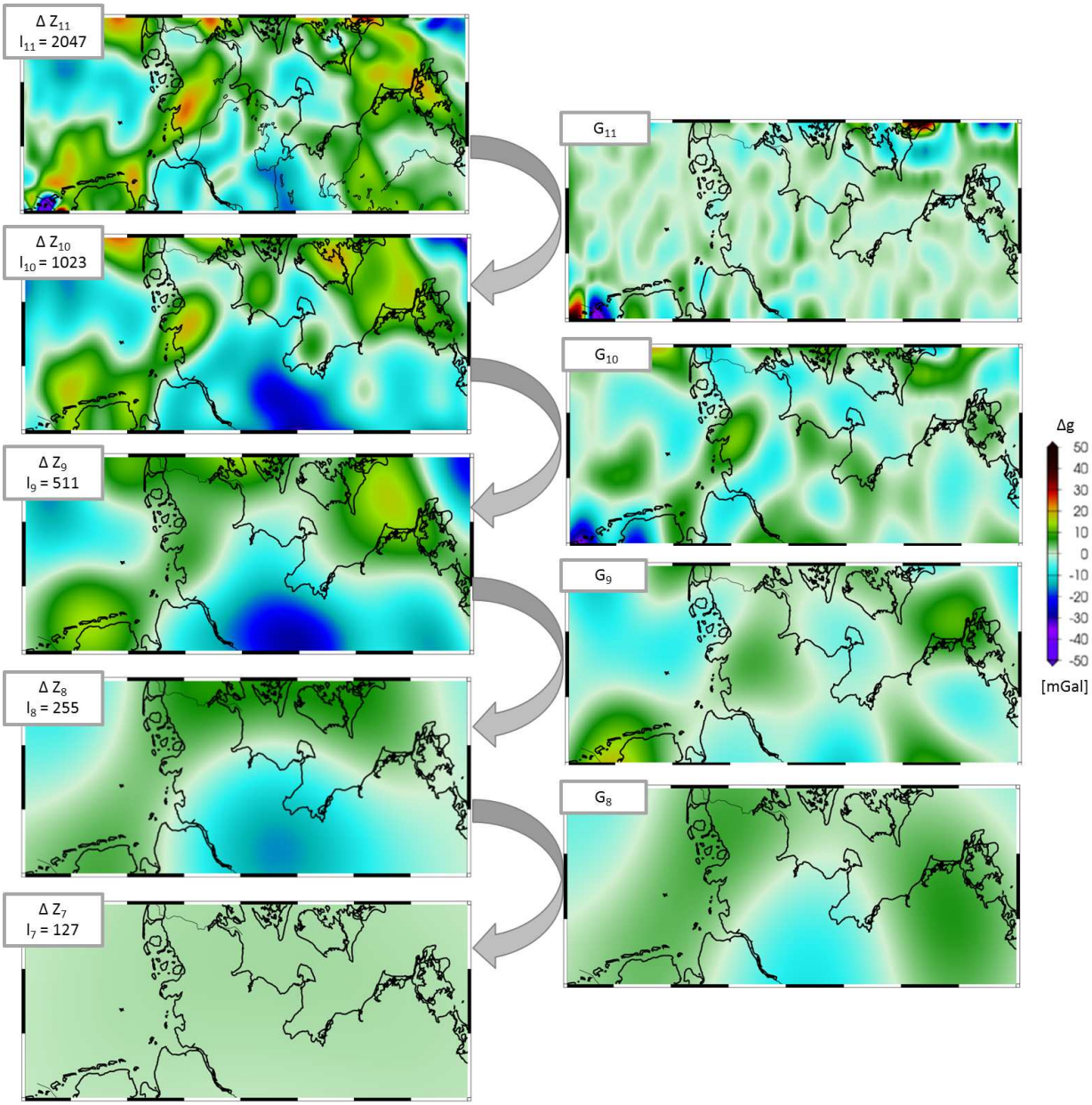

Figure 6.21: Study case (f): MRR decomposition of the signal ΔZ_{11} of differential gravity anomalies from Fig. 6.15 (i) (w.r.t. GOCO05s up to $l_7 = 127$) down to ΔZ_7 by successively subtracting band-pass filtered detail signals G_j.

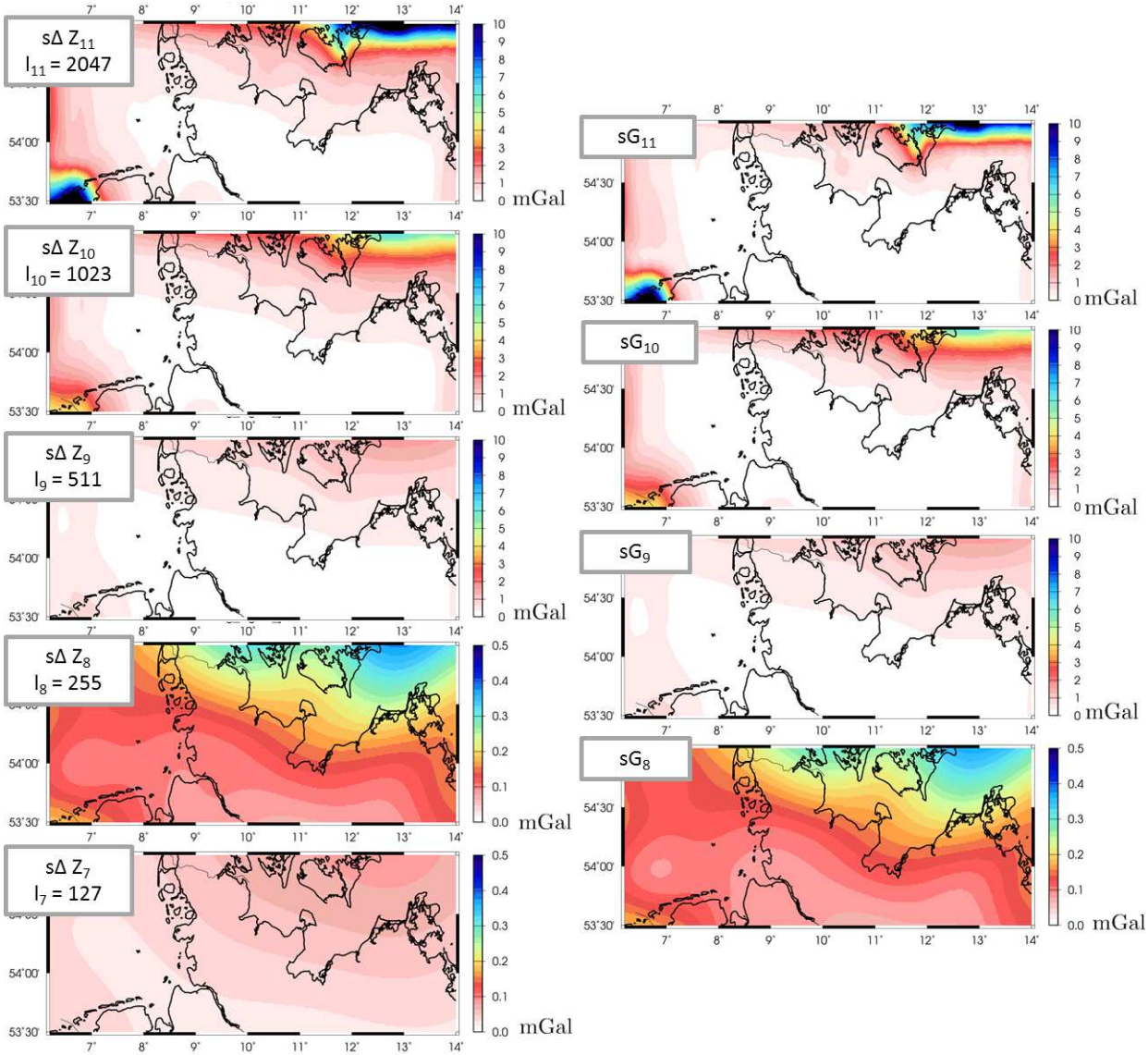

Figure 6.22: Study case (f): Standard deviations $s\Delta Z_j$ of low-, and sG_j of band-pass filtered signals w.r.t. GOCO05s up to $l_7 = 127$.

assumed, the low-resolution prior information seems not appropriate to overcome data gaps in high-resolution regional gravity field models and provokes large erroneous effects. The VCE regulates the regularization, and thus, the relative weighting of the prior information w.r.t. the whole observation area $\partial\Omega_O$. This regularization might be too weak for single data gaps, if most of the area is well-observed, as in study case (e), respectively (f). An alternative handling will be discussed in the sequel. Further, since the approach seems to be sensitive to data gaps, this property is useful, vice versa, in order to detect data gaps of existing gravitational models.

Observation depending weighting of prior information Instead of introducing the additional observation $\boldsymbol{\mu}_d$ with unit matrix $\boldsymbol{P}_d = \boldsymbol{I}$ in Eq. (5.19), the stochastic model could be adapted to the heterogeneous spatial distribution of the observations. Hereby, the main diagonal elements of $\boldsymbol{P}_d$ can vary depending on the number of observations, counted in a specific circle around each grid point $P_q \in \partial\Omega_C$. The principle is schematically displayed in Fig. 6.23. In the left red-colored circle with radius ρ around a grid point (red cross), only two observations are available, here e. g. terrestrial measurements (green triangles). Consequently, the unknown coefficient to be estimated at this grid point, is only weakly supported by information. Additional prior information would be necessary. It could be considered by setting the corresponding value at the main diagonal of $\boldsymbol{P}_d$ smaller than one, depending on the counted number of data points. In contrast, in the right red-colored circle, there are several terrestrial (green) and satellite (gray-dashed tracks) observations and the corresponding coefficient located at the right red cross is sufficiently supported by observed signal; less prior information is necessary and the corresponding value at the main diagonal of $\boldsymbol{P}_d$ could remain one. Consequently, the estimation model might be purposefully stabilized at data gaps. However, the spectral content of the prior information refers to the background model, and thus, appropriate high-resolution information still is missing in the resulting regional model.

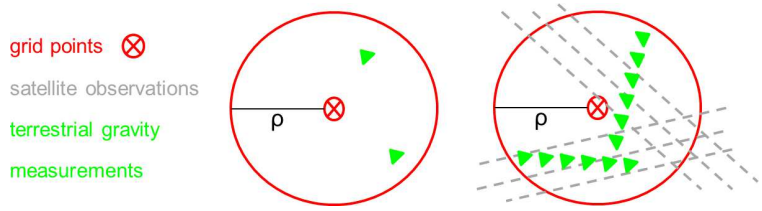

Figure 6.23: Observation depending weighting of prior information depending on the number of observations (gray, green) in a specific influence zone (spherical radius ρ) of each grid point (red cross).

Detecting data gaps in existing models Vice versa to setting up a MRR decomposition by subtracting the detail signals, the same results can be obtained by successively low-pass filtering the initial signal. As mentioned in the context of Eq. (4.35) band-pass filters are generated by subtracting the Legendre coefficients of two low-pass filtering SBFs. Consequently, the subtraction of two consecutive low-pass filtered models, e. g. ΔZ_j and ΔZ_{j-1}, yields the detail signal G_j, according to the general Eq. (4.28) of MRR (de)composition. This aspect is of beneficial relevance, e. g. for spectrally decomposing an arbitrary given model, and thus, visualizing the signal w.r.t. different spectral domains (*Schmidt et al.*, 2007): Data gaps can be detected at different resolution levels, if they were filled up with synthetic information. Further applications of a MRR decomposition arise, for instance, in order to analyze coarser structures as mass variations in the Earth's interior, the density of the Earth's crust and lithosphere (*Bouman et al.*, 2013; *Ebbing et al.*, 2013; *Bouman et al.*, 2016).

6.2.2 MRR composition

The MRR composition, e. g. in terms of a bottom-up approach as described in Fig. 4.7, aims to estimate detail signals G_j from those input data, which contribute at the corresponding resolution levels j a high measure of spectral information. Therefore, the spectral sensitivity of the observation groups has to be investigated w.r.t. j and relatively to each other. From a reasonable choice of observation groups, the detail signals can be modeled and composed according to the MRR equation (4.28).

In this **study case (g)**, the data types from cases (d) and (e) shall be combined. The specifications are listed in Tab. 6.18. The terrestrial (δg_{ter}), the two airborne (δg_{air}), the shipborne (δg_{ship}), and the five altimetry (T) data sets correspond to the ones from study (e), listed in Tab. 6.11. Their spatial distribution is displayed in Fig. 6.13 (i). The elements V_{ab} of the GOCE tensor refer to the time span 08/2012 - 11/2013, i. e. the lower orbit phase with $h \approx 225\,\text{km}$. The spatial distribution is similar to the data set from the nominal phase, cf. Fig. 6.3 (ii), which was used in study case (d). In total, it yields $K = 15$ observation groups. The assignment of the groups ([k] with $k = 1, \ldots, 9$) refers to Tab. 6.12. The six GOCE GGs obtain the numbers $k = 10, \ldots, 15$. GOCO05s serves as background model up to $l_7 = 127$, i. e. it is subtracted from all observations and defines the lowest level $j' = 7$ of the MRR; $J = 11$ is the highest level of the MRR in analogy to study case (e). While the area of investigation $\partial\Omega_I$ is the same at all resolution levels (green bordered in Fig. 6.13), the areas of observation $\partial\Omega_O$ and of computation $\partial\Omega_C$ are adapted with level-depending margins according to Eq. (5.5).

Table 6.18: Study case (g): Specifications.

Input		· δg_{ter} gravity disturbances, terrestrial (ter) data set [1] · 5 km average point distance · pre-processing according to Sec. 3.3.1
		· δg_{air} gravity disturbances, airborne (air) data sets [2], [3] · 10 km average along-/cross-track resolution · pre-processing according to Sec. 3.3.3
		· δg_{ship} gravity disturbances, shipborne (ship) data set [4] · 4 km average along-/cross-track resolution · pre-processing according to Sec. 3.3.2
		· T disturbing potential, derived from altimetry SSH, data sets [5 – 9] · 10 km average along-/cross-track resolution · pre-processing according to Sec. 3.3.4
		· $V_{xx}, V_{xy}, V_{xz}, V_{yy}, V_{yz}, V_{zz}$ in GRF, data sets [10 – 15] · re-processed release 2 (level-2 products), time span 08/2012 - 11/2013 ($h \approx 225\,\text{km}$) · pre-processing according to Sec. 3.3.5
Approach		· background model GOCO05s, $l_{j'} = 127$ ($j' = 7$) · prior information: GOCO05s, $l_{j'} = 127$ · $R_{\text{Reuter}} = 6378.137\,\text{km}$ grid radius
	(g1)	· $L_j = 140$ (analysis, Shannon)
		· $l_j = 127$ ($j = 7$, synthesis, Blackman)
	(g1), (g2)	· $L_j = 280$ (analysis, Shannon)
		· $l_j = 255$ ($j = 8$, synthesis, Blackman)
	(g1)	· $L_j 550$ (analysis, Shannon)
		· $l_j = 511$ ($j = 9$, synthesis, Blackman)
	(g1)	· $L_j = 1100$ (analysis, Shannon)
		· $l_j = 1023$ ($j = 10$, synthesis, Blackman)
	(g1), (g2)	· $L_J = 2190$ (analysis, Shannon)
		· $l_J = 2047$ ($J = 11$, synthesis, Blackman)
Output $\partial\Omega_I$	(g2)	· Δg gravity anomalies at each level via multi-level estimation and MRR decomposition · Δg gravity anomalies at highest level $J = 11$ via MRR composition

Step (1): Single-level estimations using all observation groups

The choice of appropriate observation groups which are sensitive at different spectral domains follows the strategy presented in Fig. 5.11. In step (1), at each resolution level j a single-level estimation model is set up from the combination of all available data sets.

Table 6.19: Study case (g1): VCE for all $K = 15$ observation groups at different resolution levels $j = 8, \ldots, 11$, step (1). The groups with smallest VCs are highlighted in color referring to the spectral classification in Tab. 4.8. Study case (g2): VCE for selected groups (bordered in color) at levels $j = 8$ and maximum MRR level $J = 11$, step (2). The spectral content then is transferred to the lower levels (colored arrows) via MRR decomposition.

observation group [k]		j = 7 (L_7 = 140)		j = 8 (L_8 = 280)		j = 9 (L_9 = 550)		j = 10 (L_{10} = 1100)		J = 11 (L_{11} = 2190)	
		step (1)	step (2)	step (1)	step (2)	step (1)	step (2)	step (1)	step (2)	step (1)	step (2)
[1]	terrestrial BKG	10^{-7}		10^{-9}		10^{-11}		10^{-13}		10^{-14}	10^{-14}
[2]	airborne North Sea	10^{-6}		10^{-9}		10^{-10}		10^{-12}		10^{-13}	10^{-14}
[3]	airborne Baltic Sea	10^{-6}		10^{-8}		10^{-10}		10^{-12}		10^{-14}	10^{-14}
[4]	shipborne BKG	10^{-5}		10^{-8}		10^{-9}		10^{-11}		10^{-13}	10^{-13}
[5]	ERS-1e	10^{-7}		10^{-9}		10^{-10}		10^{-10}		10^{-11}	10^{-11}
[6]	ERS-1f	10^{-7}		10^{-9}		10^{-10}		10^{-10}		10^{-11}	10^{-11}
[7]	Cryosat RADS	10^{-8}		10^{-9}		10^{-10}		10^{-10}		10^{-11}	10^{-11}
[8]	Envisat EM	10^{-8}		10^{-9}		10^{-10}		10^{-11}		10^{-11}	10^{-11}
[9]	Jason-1 GM	10^{-8}		10^{-9}		10^{-10}		10^{-11}		10^{-12}	10^{-11}
[10]	GOCE V_{xx}	10^{-9}		10^{-9}	10^{-9}	10^{-9}		10^{-9}		10^{-9}	
[11]	GOCE V_{xy}	10^{-4}		10^{-5}	10^{-5}	10^{-5}		10^{-4}		10^{-4}	
[12]	GOCE V_{xz}	10^{-8}		10^{-8}	10^{-8}	10^{-8}		10^{-8}		10^{-8}	
[13]	GOCE V_{yy}	10^{-9}		10^{-9}	10^{-9}	10^{-9}		10^{-9}		10^{-9}	
[14]	GOCE V_{yz}	10^{-4}		10^{-5}	10^{-5}	10^{-5}		10^{-5}		10^{-5}	
[15]	GOCE V_{zz}	10^{-9}		10^{-9}	10^{-9}	10^{-9}		10^{-9}		10^{-9}	
	prior information GOCO05s d/o 127	10^{+2}		10^{+2}	10^{-6}	10^{-1}		10^{-5}		10^{-7}	10^{-9}

The observation equations of this **study case (g1)** are formulated according to Tab. 4.7 and the series (5.31) are expanded in terms of Shannon functions up to a maximum degree $L_j > l_j$ in the analysis. In addition, prior information is introduced for regularization purposes. The VCs are iteratively computed for the $K = 15$ different observation groups. The orders of magnitude of the VCs are listed in Tab. 6.19 for the single levels $j = 7, \ldots, 11$. Further, the chosen maximum degree $L_j > l_j$ of the analysis is given w.r.t. j. Figure 6.24 shows the referring regularization parameter $\lambda_j = \widehat{\sigma}^2_{k_j}/\widehat{\sigma}^2_d$ (logarithmic representation) w.r.t. the observation group $k = k_j$, which obtains the smallest VC at level j.

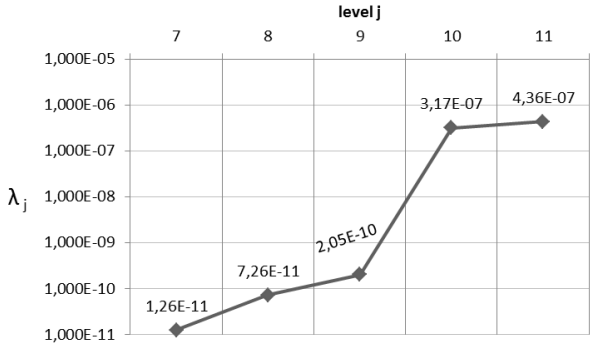

Figure 6.24: Study case (g1): Regularization parameter λ_j w.r.t. different resolution levels j.

Relative weighting and regularization in step (1)

Level 7 Referring to Tab. 4.8, satellite data are expected to contribute spectral information at $j = 7$, while regional observations are expected to contain less signal depending on their spatial resolution and extent. Since most of the information (if available at all) is reduced by the background model GOCO05s, the spectral content of all observation groups is low. As mentioned in Sec. 3.2.2, GOCO05s contains GRACE information up to degree 150, and GOCE predominates from degree 120 on. Hence, low up to medium resolution information remains in the altimetry and GOCE observations. (The long-wavelength errors of GOCE below the MBW, and the offsets of the altimetry missions have been reduced by appropriate pre-processing and should be small.)

The VCE yields for the main diagonal elements [10] V_{xx}, [13] V_{yy}, [15] V_{zz} of the GOCE GG tensor the smallest variance factors in the order of magnitude of 10×10^{-9}, cf. Tab. 6.19. Those observation groups (highlighted in blue) are identified to deliver the most valuable information compared with the other groups. The reasons are (i) the long and medium wavelengths information of global satellite data together with the high spectral sensitivity of GOCE within the MBW (cf. Sec. 3.1.4) which covers this frequency domain in contrast to terrestrial, air-/shipborne and altimetry measurements, (ii) the high accuracy (V_{xx}, V_{yy}) and the high sensitivity (V_{zz}; direction with largest signal amplitude) of the three main diagonal elements of the GOCE tensor in contrast to the off-diagonal elements, and (iii) the homogeneous spatial distribution over the whole area.
The prior information obtains a very large VC, and indicates less need of regularization due to the sufficient spectral content and the good spatial distribution of the data sets; the regularization parameter λ_7 w.r.t. $k = 10$ yields a small value of 1.26×10^{-11}, cf. Fig. 6.24.

Level 8 At level $j = 8$, ten observation groups are identified with the smallest variance factors: The three GOCE GGs [10] V_{xx}, [13] V_{yy}, [15] V_{zz}, as well as the five altimetry groups [5 – 9], the [1] terrestrial, and the airborne data [2] in the North Sea obtain similar VCs in the order of magnitude of 10×10^{-9}. They are highlighted in Tab. 6.19 in yellow [1], orange [2] and green [5 – 9] according to the classification in Tab. 4.8, and in blue for GOCE [10, 13, 15]. For the latter, the same aspects can be assumed as discussed at level $j = 7$. The altimetry data also stem from global satellite observations, and thus, contain information in the long and medium wavelengths, i. e. they are spectrally sensitive at this level $j = 8$. However, only over the ocean, altimetry measurements can be used for gravity field recovery. Their spatial distribution is restricted to the North and just few parts of the Baltic Sea, as displayed in Fig. 6.13 (i) (green dots). The VCE balances the spectral resolution and spatial extent according to Eq. (4.22).
The similarly low VC of the [1] terrestrial data results from the spatial distribution of the observations. The extent of [1] ranges over wide parts of the area of investigation, and thus, medium wavelengths are contained in the data set. Further, the airborne measurements [2] over the North Sea seem to be relevant for a stable solution at level $j = 8$. Corresponding spectral content and probably the need of closing the data gap between the terrestrial and the altimetry measurements in the North Sea stabilize the constellation.
The large VC of the prior information in the order of magnitude of 10×10^2 indicates low need of regularization in analogy to the estimation at $j = 7$. However, the regularization parameter $\lambda_8 = 7.26 \times 10^{-11}$ w.r.t. $k = 5$ is around seven times larger than λ_7. Hence, singularity problems slightly increase at level $j = 8$. Since for both levels, the same observation groups are used, the problems seem to originate from the regional rank deficiency k_L^{reg} discussed in study case (a). The size of k_L^{reg} depending on the resolution level j is investigated below.

Level 9 The terrestrial data set (yellow highlighted in Tab. 6.19) obtains the smallest VC in step (1) at this level $j = 9$ (order of magnitude of 10×10^{-11}) in contrast to the other observation groups due to the previously mentioned characteristics of this data set. The GOCE GG groups are, for instance, down-weighted by two orders of magnitude relatively to the terrestrial data, since the MBW covers the spectral domain of level $j = 9$ only partially; the errors increase at the high frequencies above the MBW and predominate the GOCE signal, cf. Sec. 3.1.4.
The [5 – 9] altimetry and the [2 – 3] shipborne groups are down-weighted just by one order of magnitude w.r.t. [1]. Consequently, they deliver valuable spectral information within the bandwidth of $j = 9$, and further balance the spatial restriction of the terrestrial data (south-eastern area; yellow in Fig. 6.13 i) in the western (especially [5 – 9]; green observation sites) and in the northern (especially [3]; orange-colored flight tracks) parts of $\partial\Omega_I$, cf. 6.13 (i).
The regularization parameter w.r.t. group [1] increases up to 2.05×10^{-10}, cf. Fig. 6.24, and thus, around one order of magnitude compared with λ_7. The stabilization of the normal equation system becomes more and more important for higher resolution levels.

Level 10 At level $j = 10$ again, the terrestrial data [1] contribute the most valuable content relatively to the other observation groups; [1] obtains the smallest VC and is yellow highlighted in Tab. 6.19. The airborne data sets [2] and [3] are down-weighted by one order of magnitude, and thus, contain also spectral information referring to the frequency band of level $j = 10$. The [8] Envisat-EM and the [9] Jason-1 GM missions, as well as the [4] shipborne data provide slightly less spectral content (two orders of magnitude w.r.t. [1]).

The regularization parameter λ_{10} increases from λ_9 by two orders of magnitude up to a value of 4.33×10^{-8}. This jump in the curve of Fig. 6.4 stems from the missing GOCE information at this level $j = 10$. While GOCE contributed as global observation type with the very accurate tensor measurements relevant signal in the medium resolution levels $j = 7, 8, 9$, it is not longer sensitive at the higher level $j = 10$. Consequently, stronger regularization is needed for stabilizing the normal equation system.

Level 11 At level $J = 11$, the contrast between global and regional data sets enhances. The VCs of almost all observation groups obtain smaller values compared with $j = 10$, while the VCs of the global GOCE gradients [10 – 15] yield values in the same order of magnitude. The most valuable signal stems from [1] terrestrial and [3] airborne data; they are highlighted in yellow and orange in Tab. 6.19. As mentioned at level $j = 10$, due to the low support of global observations, the prior information becomes more important for stabilization purposes. It is expressed by the largest regularization parameter $\lambda_{11} = 4.36 \times 10^{-7}$ w.r.t. [3], compared to the one of the lower levels in Fig. 6.4. The increase from λ_{10} to λ_{11} is smoother again, indicating a similar spectral contribution of the (regional) observation groups at levels $j = 10$ and $j = 11$.
While for the GOCE GGs [10 – 15], the estimated variance factors remain about the same at all resolution levels, the VCs of the altimetry groups [5 – 9] decrease by around two orders of magnitude, and the VC of the terrestrial data [1] by five orders of magnitude from the lowest to the highest level, relatively to their estimates at $j = 7$.
In analogy to computing the regularization parameter λ_j w.r.t. the smallest VC at each level, it can be computed w.r.t. one and the same observation group over all levels. It is displayed in Appendix B, Fig. B.1, exemplarily for the observation groups [1], [3], [5] and [15]. A more detailed study of the contribution of the single observation types depending on their spectral sensitivity, e. g. by means of Fourier analysis, would go beyond the scope of this thesis.

Summary: Need for regularization in step (1)

Regional rank deficiency The estimate k_L^{reg}, Eq. (5.8), depends on the maximum resolution L_j, i. e. on the level j, and on the area ratio of the computation area w.r.t. the area of the whole globe. The area ratio, Eq. (5.6), is the same at all resolution levels j due to the definition of the level-depending margin width η^j in Eq. (5.5), i. e. $A_{\partial\Omega_C}/A_{\Omega_R} \approx 0.0028$, cf. study case (a). For instance, with a maximum degree $L_8 = 280$ at level $j = 8$, k_{280}^{reg} yields approximately 60. Up to level $J = 11$, the estimate k_{2190}^{reg} enormously increases up to 3669. Consequently, with augmenting resolution level, singularity problems increase and more regularization is needed. Besides the possibilities of reducing the regional rank deficiency discussed in study case (a), another option would be to define a decreasing area ratio $A_{\partial\Omega_C}/A_{\Omega_R}$, i. e. a smoother increase of η^j with increasing level j. However, since the margin width is adapted to the side lobes of the SBFs, smaller computation areas could provoke more edge effects in the resulting models. Above all, the the regional rank deficiency k_L^{reg} is just an estimate, and thus, difficult to rate.

Data gaps If regularization depended only on the regional rank deficiency, the curve in Fig. 6.4 would be expected to have a continuous increase. However, there is a jump between level $j = 9$ and level $j = 10$, as discussed above. At the lower levels $j = 7, 8, 9$, the spectral content as well as the spatial distribution of all observation groups balance each other, and thus, there are no data gaps at those resolution levels. At the higher levels $j = 10, 11$, less observation groups contribute sufficient spectral information, and additionally, the spatial distribution of appropriate data sets is fragmentary within $\partial\Omega_I$, cf. 6.13 (i), i. e. data gaps appear, and regularization becomes more important.

As discussed in study case (f), with increasing resolution level, the "zero-signal" of the prior information w.r.t. the minimum level $j' = 7$, becomes less appropriate and provokes erroneous effects in the resulting model in case of data gaps. Since regularization is as good as in all regional modeling approaches needed, realistic prior information is required. Alternatives to the "zero-signal" have been discussed in study case (a).

Step (2): Choice of observation groups

Even if the VCE in step (1) delivers a reasonable relative weighting of the observation groups, using them for regional gravity field solutions would provoke strong erroneous effects at all levels due to data gaps, as described in study case (f). Except at level $j = 8$, where the prior information is appropriate to overcome the data gaps. Moreover, the aim is to emphasize the strengths of each data set by their flexible combination within a MRR approach. Hence, three criteria are defined in Sec. 5.3.1 for a reasonable selection of observation groups at the different resolution levels:

- high sensitivity,
- no correlations,
- spectral range and spatial distribution.

The observation groups of highest sensitivity relatively to each other are identified within step (1) w.r.t. the different resolution levels. In Tab. 6.19 they are marked in color. Some data sets obtain the lowest VC at several levels: The GOCE groups [10], [13] and [15] are expected to contribute most information at levels $j = 7$ and $j = 8$, and the terrestrial data [1] at levels $j = 8, 9, 10, 11$.
Strictly following the first criterion, i. e. setting up the estimation models at each level by using just the input data of highest relative weights, yielded correlated detail signals. Further, composing the latter via MRR, delivered a regional model with multiple presence of one and the same information at several resolution levels. In this work, hence, the second criterion applies: avoiding correlations by introducing different observation types at different levels.
Strictly following this second criterion means introducing each data set just once within the MRR composition. However, strong regularization then is needed at each level for the here available data sets. Due to their limited spatial extent, cf. 6.13 (i), the single data sets do not sufficiently cover $\partial\Omega_I$, and thus, spectral information is missing. In Appendix B, some tests are summarized in terms of estimated VCs in Tab. B.1, and corresponding estimated scaling coefficients in Fig. B.2. The data gap areas have to be filled with prior information, but the "zero-signal" w.r.t. GOCO05s up to $l_{j'} = 127$ is not sufficient, especially at higher resolution levels as mentioned above, and large erroneous effects predominated the output signals. Consequently, the spectral content, the spatial distribution, and the avoidance of multiple presence of the observation groups require a compromise in the MRR approach. As mentioned in the context of Fig. 5.11, the correlation-criterion has to be balanced very carefully with the third criterion: ensuring "sufficient" spectral range and spatial distribution. Another possibility would be to consider the presence of multiple information by connecting the consecutive low- and band-pass filtered signals and their stochastic information. This is the core of a pyramid algorithm, mentioned in Sec. 4.3.5. Some ideas for its realization are discussed in the Outlook 7.

Multi-level estimation Taking all three criteria into account, the following multi-level estimation is applied in a **study case (g2)**, in order to combine the data sets and capture their highest measure of information depending on the spectral sensitivity. Referring to the above identified contrast between the behavior of regional and global data sets in the VCE, cf. Tab. 6.19, step (1), two levels now are chosen: one estimation model (5.22) is set up at level $j = 8$, where the globally observed GOCE GGs [10 – 15] contribute valuable spectral information, and one is set up at highest level $J = 11$, where the "semi-global" altimetry [5 – 9], as well as the regional terrestrial [1], air- [2,3] and shipborne [4] data sets deliver appropriate gravitational content.
In the analysis, the adapted basis functions are expanded for the different functionals each in a series (5.31) up to $L_8 = 280$ for $j = 8$, and up to $L_{11} = 2190$ for $j = 11$. The level-8-solution later will be used to describe the spectral domain of levels $j = 8$ and $j = 7$. In analogy, the level-11-solution, which is equivalent to the solution from study case (e), will be used in order to describe the spectral content of levels $J = 11$, $j = 10$ and $j = 9$. The "multi-level" combination of Fig. 5.10, thus, becomes a "two-level" combination in this study case (g2).

Relative weighting and regularization in step (2)

Level 8 According to Tab. 6.19, step (2), the GOCE groups (blue-bordered) show at level $j = 8$ similar VCs as in step (1). However, the prior information gets a considerably smaller VC value in the order of 10^{-6}, which is even smaller than the variance factors of the less-accurate gradients [11] and [14] in the order of 10^{-5}. This

stronger need for regularization in this study case (g2) might stem from the downward continuation which causes instabilities in the system (5.23) of normal equations. The chosen GOCE data sets, cf. Tab. 6.18, refer to an average measurement height of 225 km. Thus, the signal has to be amplified down to the Earth's surface where the Reuter grid is set up with a grid radius of $R_{\text{Reuter}} = 6378.137\,\text{km}$; referring noise is amplified as well. (Note, in study case (d1), similar VCs were obtained for the six GOCE GGs, cf. Fig. 6.12 (ii), taking into account the different test areas and the different time spans of the data sets.)
In contrast to the GOCE-only combination in step (2), in step (1) the "near-Earth" observations stabilize the solution: Only small signal amplification is needed for the observation groups [2] and [3] (measurement height of around 30 m, cf. Sec. 3.3.3). Moreover, all data sets contribute valuable spectral information in study case (g1), and thus, less regularization is necessary than in (g2).

Level 11 The VC values at level $j = 11$, cf. Tab. 6.19, step (2), refer to the reciprocal relative weights which have been discussed in detail in the context of Tab. 6.12 in study case (e). The VC σ_d^2 of the prior information (in the order of magnitude of 10^{-9}) decreases compared with the value of σ_d^2 in step (1). However, the decrease yields only around two orders of magnitude; in contrast, at level $j = 8$, σ_d^2 decreases by eight orders of magnitude. As discussed before, the different need of regularization results from the spectral content of the corresponding data sets, taking the aspect of downward continuation into account: While in step (1), the regional data sets (with low need for downward continuation) contain high and medium resolution information down to level $j = 8$, vice versa, GOCE does not contribute high-resolution information for the combined solution at level $J = 11$. Consequently in step (2), at level $J = 11$, neglecting the groups [10 – 15] has less negative influence on the stability of the solution than neglecting groups [1 – 9] at level $j = 8$.

Summary: Main reasons for regularization

Within step (1) it is shown, that for a large variety of heterogeneous data sets, regularization becomes more important with increasing resolution level j. The reasons originate from regional rank deficiency problems and from data gaps. In step (2), the observation groups are divided in two categories: global vs. regional. In principle, the reduction of data sets at each level requires stronger regularization. However, the latter increases by a different amount due to the specific spectral contents of the observation groups and the aspect of downward continuation which causes instabilities in the estimation model, as discussed before.
The higher the influence of the prior information ("zero-signal" w.r.t. the background model; weight matrix is the unit matrix), the stronger is the influence of the unit matrix in the stochastic model, i. e. the less correlations are considered between the scaling coefficients at one level. Consequently, the error estimates are too optimistic.

MRR composition from (decomposed) single-level estimations

In the following, a combination of MRR-composition and -decomposition are applied. The principle is visualized in Tab. 6.19: The scaling coefficients are estimated in the synthesis at the specified levels ($j = 8$ and $J = 11$) by appropriate observations (blue bordered and yellow-/orange-/green-bordered; step 2). The spectral information then is used to model the referring detail signals at those levels, and further, it is transferred to the lower levels, in order to compute the low-resolution signal at $j' = 7$ (decomposition of the level-8 signal; blue-colored arrow), and the detail signals at $j = 9, 10$ (decomposition of the level-11 signal; yellow-orange-green-colored arrows). The composition of the signals at each resolution level finally delivers the spectrally combined level-11 signal.

Estimated scaling coefficients By means of the estimated VCs from Tab. 6.19, the normal equations (5.23) can be solved at level $j = 8$ and $J = 11$. The (i) resulting vectors $\widehat{\boldsymbol{d}}_{L_8}$ and $\widehat{\boldsymbol{d}}_{L_{11}}$ of estimated coefficients in step (2), and (ii) their standard deviations, obtained by Eq. (5.25), are displayed in Fig. 6.25. Note, the level-11 solution (upper row) is identical to the solution from study case (e), displayed in Fig. 6.14, but different color bars are used. In the sequel, more focus is on the level-8 solution in the lower row. The estimated coefficients and standard deviations at $j = 8$ refer to a scaling factor of $10^{-3}\,\text{m}^2/\text{s}^2$. The different orders of magnitude refer to the different spectral resolution: In contrast to the larger signal amplitudes at the higher level $J = 11$ (respectively larger amplitudes of $\widehat{d}_{q_{11}}$), the amplitudes of $\widehat{d}_{q_8}$ vary less since they refer to the

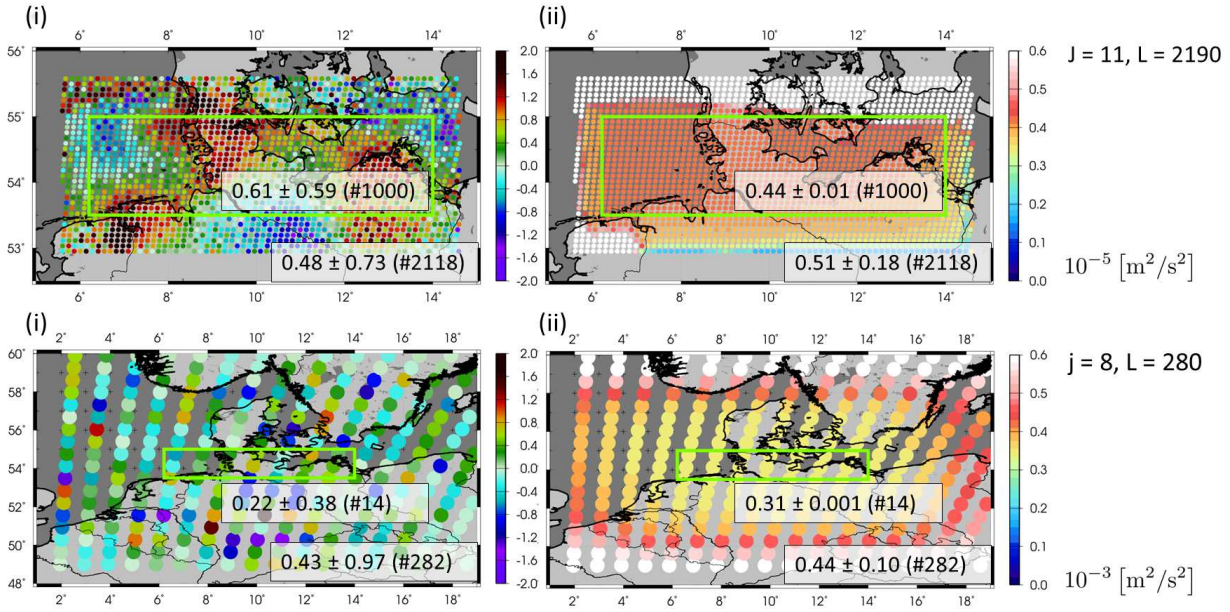

Figure 6.25: Study case (g2): (i) Scaling coefficients and (ii) referring standard deviations from two single-level estimations at levels $j = 8$ (maximum degree $L = 280$) and $J = 11$ ($L = 2190$). Mean values and SDs are depicted in boxes for the entire computation area and the target area (green-bordered); unit [m^2/s^2].

medium frequency domain of $j = 8$. Further, the extent of the computation areas is different at both levels: While the computation area at level $J = 11$ comprises 2118 coefficients, 282 coefficients are estimated at level $j = 8$. The area of investigation $\partial\Omega_I$ (green-bordered) comprises 1000 coefficients at level $J = 11$, and 14 coefficients at level $j = 8$. As expected and already discussed for $J = 11$ in the context of Fig. 6.14 (i), the amplitudes of the coefficients $\widehat{d}_{q_8}$ oscillate outside $\partial\Omega_I$ since they are less supported by observations and less compensated by side lobes from neighboring SBFs; inside $\partial\Omega_I$, they represent gravitational structures. The statistics (mean ± SD) are depicted in the boxes in Fig. 6.25 for the different computation areas and the green-bordered target area. Hereby, the signal-related variations of $\widehat{d}_{q_8}$ inside $\partial\Omega_I$ deliver a smaller SD of $0.38\,m^2/s^2$ than the erroneous variations outside with a larger SD of $0.97\,m^2/s^2$. (At level $J = 11$ the behavior is similar.) The referring standard deviations in plot (ii) confirm the considerations. They reach the smallest values in the green-bordered target area and increase towards the borderlines of $\partial\Omega_C$ due to missing observations. At each level, the SD values are only slightly smaller than the coefficients. It can be explained by the side lobes of the SBFs: In the analysis, Shannon functions with strong spatial oscillations are used in favor of ideal filter characteristics in the spectral domain.

Low-resolution and detail signals Using the vectors $\widehat{\boldsymbol{d}}_{L_8}$ and $\widehat{\boldsymbol{d}}_{L_{11}}$ of estimated coefficients from the analysis, they are multiplied with low- and band-pass filtering scaling functions in the synthesis in order to obtain the low-resolution signal $Z_{j'=7}$, and the detail signals G_j ($j = 8, \ldots, 11$). According to the two-level estimation, the system of modeling equations (5.35) is set up in terms of gravity anomalies Δg: The detail signal G_8 is computed by expanding the adapted wavelet functions $\tilde{\Psi}_8$, Eq. (5.33), up to $l_8 = 255$. The low-resolution signal Z_7 is obtained from the same set of coefficients ($\widehat{\boldsymbol{d}}_{L_8}$) by expanding the adapted scaling functions $\tilde{\Phi}_7$, Eq. (5.34), up to $l_7 = 127$.

The detail signals G_9, G_{10}, G_{11} refer to the estimated coefficients at level $J = 11$. Therefore, the wavelet functions $\tilde{\Psi}_8$, Eq. (5.33), are expanded up to $l_9 = 511$, $l_{10} = 1023$, $l_{11} = 2047$, cf. Tab. 4.8. While in the analysis, the Shannon kernels ensure that no signal is lost up to $L_8 = 280$ for $\widehat{\boldsymbol{d}}_{L_8}$ and up to L_{2190} for $\widehat{\boldsymbol{d}}_{L_{11}}$, in the synthesis, Blackman kernels smooth the high frequencies of each level in favor of reducing erroneous effects in the spatial domain, as discussed in study case (c).

The detail signals G_9, G_{10}, G_{11} have been discussed in study case (f) in the context of Fig. 6.21, the corresponding standard deviations sG_9, sG_{10}, sG_{11} by means of Fig. 6.22. There, the (i) detail signal $d_{11} \rightarrow G_8$ was computed from the vector $\widehat{\boldsymbol{d}}_{L_{11}}$ of coefficients, the (ii) standard deviations $sd_{11} \rightarrow sG_8$ by appropriate error propagation. The results are again displayed in the upper row of Fig. 6.26. In contrast, in

study case (g2), the (i) detail signal G_8 and the (ii) standard deviations sG_8 are directly computed at level $j = 8$. The solutions are visualized in the middle row of Fig. 6.26. Further, the differences (i) ΔG_8 and (ii) ΔsG_8 between the low-pass filtered solution from study case (f) and the direct solution from (g2) are plotted in the lower row. The range (min ... max), the mean value and the standard deviation are depicted in white-shaded boxes for all results in the unit [mGal].
In general, the structures of $d_{11} \rightarrow G_8$ and G_8 are similar. The largest amplitudes (green colored), describe an arch from the south-western (passing the mid-northern) to the south-eastern part of the study area. The lowest amplitudes refer to the north-western, mid-southern, and north-eastern parts. However, G_8 contains obviously more signal than $d_{11} \rightarrow G_8$. The amplitudes range from -14.01 mGal to 12.51 mGal, i. e. they are around twice as high as the amplitudes of $d_{11} \rightarrow G_8$ (-8.02 mGal to 6.51 mGal). This is reasonable, since G_8 is directly computed at level $j = 8$ from appropriate data (GOCE is sensitive at level $j = 8$). In contrast, $d_{11} \rightarrow G_8$ is obtained by band-pass filtering the estimated signal at level $J = 11$ from higher-resolution regional data sets. Even if the decomposition in Sec. 6.2.1 enables the representation of $d_{11} \rightarrow G_8$, valuable GOCE information is missing in this solution.
The difference sG_8 indicates the added value of GOCE in G_8. Further, remaining aliasing and long-wavelength errors can be obtained, as discussed in the context of Fig. 6.20. However, due to appropriate filtering in the synthesis and the pre-processing of the GOCE GGs, both error influences are expected to be small. The differences range from -5.17 mGal to 6.48 mGal. The spatial extent of the largest amplitudes refer to the spatial extent of the largest signal values of G_8. In analogy, the spatial distribution of the smallest amplitudes corresponds to the one of the smallest signal values. Consequently, they confirm the signal amplification of G_8 in contrast to $d_{11} \rightarrow G_8$. The mean value of the difference (2.11 mGal) indicates an offset between the model G_8 obtained from global satellite observations, and the model $d_{11} \rightarrow G_8$ obtained from regional data sets due to the missing long-wavelength information, as mentioned in study case (f).
The (ii) standard deviations sG_8, displayed in the middle row of Fig 6.26, reach maximum values of 0.2 mGal at the borderlines of the target area due to edge effects. They originate from the limited extent of the computation area, i. e. the neglect of basis functions outside $\partial\Omega_C$. Since all SBFs are globally defined, the remaining SBFs inside $\partial\Omega_C$ suffer from the support of the neglected SBFs. These modeling errors increase towards the borderlines of $\partial\Omega_C$, respectively $\partial\Omega_I$. They are reduced by an appropriate choice of different area margins according to Eq. (5.5). On average, the SD values count 0.14 mGal. Thus, they are two orders of magnitude smaller than the signal values of G_8 and indicate an high internal accuracy of the detail signal. Further, they are smaller than the values $sd_{11} \rightarrow sG_8$ of the smoothed level-11 result, displayed in Fig 6.26 (ii), upper row. The latter are especially influenced by the data gaps at the northern borderline (SD values up to 0.37 mGal) while the level-8 results do not suffer from missing data. On average, the standard deviations differ by 0.01 mGal; in the north-eastern part they decrease down to -0.23 mGal. Compared with the signal amplitude of $d_{11} \rightarrow G_8$, the SD values of $sd_{11} \rightarrow sG_8$ are closer to the signal, than in case of the level-8 solution. Consequently, the ratio of G_8 to sG_8 indicates a higher internal accuracy.

External validation of the level-8 detail signal For an external validation of the detail signal G_8, the differences to a global GOCE-only model are computed. The latest release GOCE-TIM-R5 (*Brockmann et al.*, 2014) is chosen (source: `http://icgem.gfz-potsdam.de/ICGEM/`). For spectral consistency, the low-pass filtered signal ΔZ_7 is added to G_8 (cf. $G_8 + \Delta Z_7 = \Delta Z_8$ from Fig. 6.21), and GOCE-TIM-R5 ($l = 128$ up to $l_8 = 255$) is low-pass filtered with a Blackman kernel as well. The difference ΔZ_8 – GOCE-TIM-R5$_8$ w.r.t. GOCE-TIM-R5 (GOCE-TIM-R5$_8$) model is displayed in Fig. 6.27 (i) in terms of gravity anomalies. It ranges from -1.66 mGal to 1.00 mGal and counts approximately 10 % of the maximum signal amplitudes of G_8. It thus indicates different signal and error content in the regional and in the global model.
The geographical pattern of the difference, cf. Fig 6.27 (i), shows to some extent correlations with the structures of the detail signal (i) G_8, middle row. For instance, the spatial extent of the negative part of the G_8 signal in the mid-southern part is similar to the spatial extent of the positive differences in Fig. 6.27 (i). Here, the G_8 signal seems to show edge effects probably due to the limited size of the computation area, i. e. the neglect of basis functions outside $\partial\Omega_C$, as discussed before. Further regional modeling errors which cause the differences inside $\partial\Omega_I$, stem from spatial oscillations from the SBFs (the Blackman functions have less, but still apparent oscillations).
In addition, G_8 contains long-wavelength errors in the GOCE GGs, which are still present after the pre-processing and after subtracting the background model GOCO05s up to degree $l_{j'} = 127$. Since GOCO05s mainly consists of GRACE information in this spectral domain, low-resolution signal remains as well. The ref-

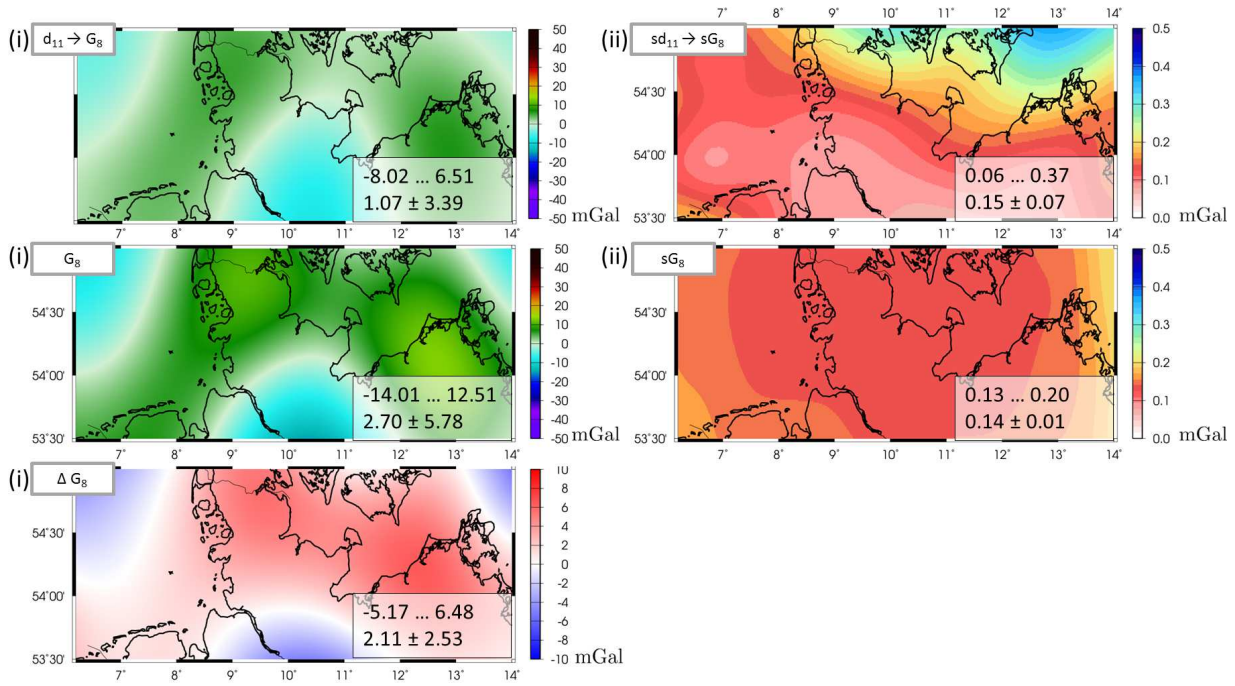

Figure 6.26: Study case (g2): (i) Detail signal $d_{11} \rightarrow G_8$ and (ii) standard deviation $sG_{11} \rightarrow sG_8$, obtained from the level-11 estimation (first row); (i) level-8 detail signal G_8 and (ii) standard deviation sG_8 (middle row); difference (i) ΔG_8 of the detail signals (lower row). Range, mean value and SD are depicted in boxes; unit [mGal].

erence of the detail signal G_8, respectively the low-resolution signal ΔZ_7, to the background model then causes the large-scale differences. They are quantified by computing the difference GOCO05s$_7$ − GOCE-TIM-R5$_7$ between the background model GOCO05s and GOCE-TIM-R5, both referring to the spectral domain of degree $l = 0, \ldots, 127$. The difference of the long wavelengths is visualized in Fig. 6.27 (ii) in terms of gravity anomalies (note the different color bar in contrast to (i)). It ranges from −0.24 mGal to 0.15 mGal with a mean value and SD of −0.05 mGal and 0.10 mGal. The SD of the mean difference GOCO05s$_7$ − GOCE-TIM-R5$_7$ of the low-resolution domain ($l = 0, \ldots, 127$), cf. Fig. 6.27 (ii), is around four times smaller than the SD of the mean difference ΔZ_8 − GOCE-TIM-R5$_8$ of the medium-resolution domain ($l = 128, \ldots, 255$), cf. Fig. 6.27 (i). However, especially the large-scale negative anomaly in Fig. 6.27 (ii) influences the low- and band-pass filtered signals ΔZ_7, G_8 of the regional model which refer to GOCO05s up to $l_7 = 127$, and explain to some extent the large-scale difference in Fig. 6.27 (i). Further, the input data of the here estimated regional model G_8 stem only from the lower orbit phase of the GOCE mission (time span 08/2012 - 11/2013), while the global GOCE-TIM-R5 model comprises the data from the whole satellite mission.
In total, the differences between the regional and the global GOCE-only models, expressed by Fig. 6.27 (i), are smaller than the differences ΔG_8 in Fig. 6.26 (i), lower row, between the G_8 signal and the one which is obtained from the level-11 estimation. Thus, G_8 contains additional GOCE signal in contrast to $d_{11} \rightarrow G_8$. Comparing the difference G_8 − GOCE-TIM-R5$_8$ with the previously discussed sG_8 from Fig. 6.26 (ii) in the middle row, the standard deviations reach values that are one order of magnitude smaller than the difference. Those too optimistic error estimates result again, as discussed before, from an incomplete stochastic model.

Differential signal According to the MRR equation (4.28), the composition of the low-resolution signal $Z_{j'=7}$ and the detail signals G_8, G_9, G_{10}, G_{11} finally delivers the differential signal $\Delta Z_{11,\mathrm{MRR}}$, cf. Eq. (5.37). The standard deviations $s\Delta Z_{11,\mathrm{MRR}} = \sqrt{v_{11}}$ are obtained by adding the variances of the low-resolution of the detail signals and according to Eq. (5.38). Figure 6.28 (i) shows the differential signal $\Delta Z_{11,\mathrm{MRR}}$ in terms of gravity anomalies Δg up to maximum MRR level $J = 11$, and (ii) the corresponding standard deviations $s\Delta Z_{11,\mathrm{MRR}}$. In (iii) the difference $\Delta Z_{11} - \Delta Z_{11,\mathrm{MRR}}$ between the single-level estimation from study case (e), cf. Fig. 6.15 (i), and the MRR-solution $\Delta Z_{11,\mathrm{MRR}}$ is visualized. The statistics are depicted in the white boxes, as mentioned above. On average, the differences count −0.99 ±4.09 mGal, i. e. less than 1 % of the signal range of $\Delta Z_{11,\mathrm{MRR}}$ and ΔZ_{11}. In general, the geographical pattern of $\Delta Z_{11,\mathrm{MRR}}$ is similar to ΔZ_{11}. However, the differences show largest amplitudes down to more than −50 mGal in the data gap area in the south-western

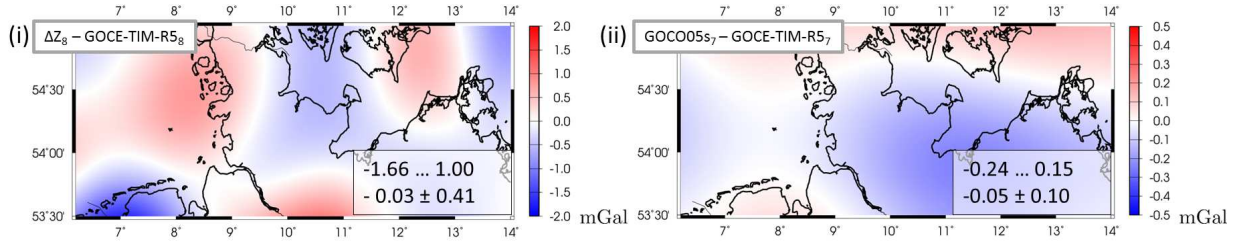

Figure 6.27: Study case (g2): (i) Difference $\Delta Z_8 - \text{GOCE-TIM-R5}_8$ between the low-pass filtered signal $\Delta Z_8 = \Delta Z_7 + G_8$ and the consistently filtered global GOCE-only model GOCE-TIM-R5 (GOCE-TIM-R5$_8$); (ii) Difference between GOCO05s and GOCE-TIM-R5 up to degree $l = 127$; Mean value and SD are depicted in the box in the unit [mGal].

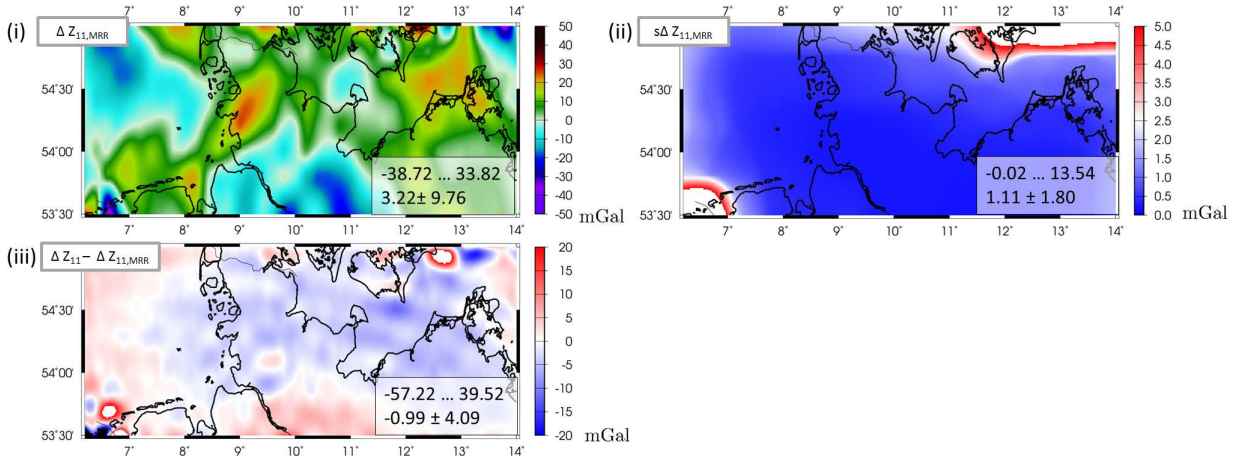

Figure 6.28: Study case (g2): (i) Differential signal $\Delta Z_{11,\text{MRR}}$, (ii) standard deviations $s\Delta Z_{11,\text{MRR}}$, and (iii) difference $\Delta Z_{11} - \Delta Z_{11,\text{MRR}}$ to the differential signal from the single-level estimation in Fig. 6.15 (i). The statistics (range, mean, SD) in the boxes are given in [mGal].

corner, and up to around 40 mGal in the same region and further at the north-eastern borderline where high-resolution observations are missing. Beside small-scale variations, the differential pattern shows above all large-scale variations: In the western and southern areas the differences are positive (around 5 mGal), while in the middle, negative differences of around −5 mGal extend to wide parts. Similar large-scale structures are represented by the difference ΔG_8 of the detail signals G_8 and $d_{11} \rightarrow G_8$ in Fig. 6.26 (i), middle row. In conclusion, the additional signal from GOCE at level 8 is represented in the MRR-solution $\Delta Z_{11,\text{MRR}}$ w.r.t. the regional modeling errors of around 10 %, approximately estimated from the difference $G_8 - \text{GOCE-TIM-R5}_8$ to the global GOCE-only model. Consequently, the enrichment of $\Delta Z_{11,\text{MRR}}$ in the medium wavelengths further explains the large-scale differences in Fig. 6.28 (iii) w.r.t. the single-level estimation ΔZ_{11}.

Total signal Restoring GOCO05s to the differential signal delivers the total MRR signal $Z_{11,\text{MRR}}$ in terms of gravity anomalies Δg up to level $J = 11$. It is displayed in Fig. 6.29 (i); outliers have been removed in the graphical representation w.r.t. a three-sigma threshold. In contrast to $\Delta Z_{11,\text{MRR}}$, the structures of $Z_{11,\text{MRR}}$ change especially in the North Sea, where negative anomalies overlay the small-scale variations from $\Delta Z_{11,\text{MRR}}$. (The difference $Z_{11} - Z_{11,\text{MRR}}$ to the total signal Z_{11} of the single-level estimation in study case (e) is expected to correspond to the difference $\Delta Z_{11} - \Delta Z_{11,\text{MRR}}$ to the differential signal, since the same constant background model GOCO05s was used.)
The difference $\text{EGM}_{11} - Z_{11,\text{MRR}}$ to the consistently filtered EGM2008 (EGM_{11}) is visualized in Fig. 6.29 (ii). It yields a similar large-scale geographical pattern as $\Delta Z_{11} - \Delta Z_{11,\text{MRR}}$ from Fig. 6.28 (iii). Since EGM2008 contains no GOCE information, cf. Sec. 3.2.2, the differences confirm the considerations from above: The large-scale differences in the medium wavelengths seem to stem from the additional GOCE observations, which are contained in the regional model $Z_{11,\text{MRR}}$. Comparing Fig. 6.29 (ii) with the differences between Z_{11} and EGM2008 from Fig. 6.17 (i), those large-scale structures do not appear.
Besides the beneficial aspect of additional information in $Z_{11,\text{MRR}}$, the differences in the data gap areas seem to be smaller in Fig. 6.29 (ii) than in Fig. 6.17 (i). While in study case (e), differences down to −22 mGal

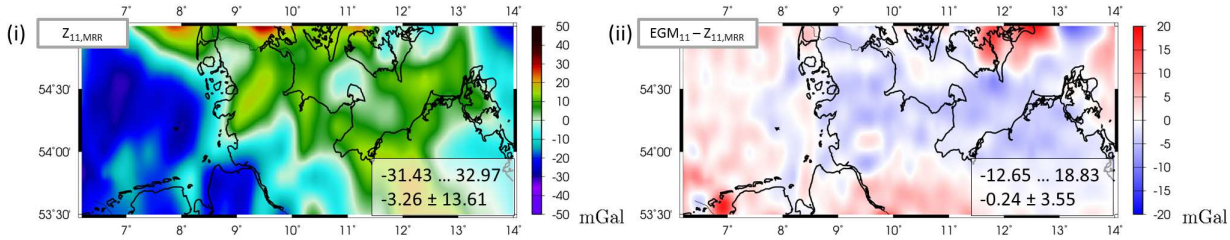

Figure 6.29: Study case (g2): total signal.

were obtained in the south-western corner, the amplitudes now range from −12.65 mGal to 18.83 mGal and vary around −0.24 mGal with a SD of 3.55 mGal. Note, in study case (e), the differences were computed vice versa, i. e. $Z_{11} - \mathrm{EGM}_{11}$; hence, large negative anomalies refer to large positive anomalies in this study case (g2). In conclusion, erroneous effects due to data gaps are obviously reduced in the MRR-solution. The contribution of GOCE delivers valuable spectral content in the medium-wavelengths domain and further stabilizes the regional model in case of missing high-resolution information.

Summary and discussion of study case (g)

- The comparison of the detail signals $d_{11} \rightarrow G_8$ and G_8 indicates additional signal in G_8, stemming from GOCE. Further, the internal accuracy is higher due to the ratio G_8/sG_8 of signal and standard deviation. However, the SDs are too optimistic (in all regional models), since the stochastic model does not consider correlations of the observations and assumes equal accuracies.
- The comparison of the regional GOCE-only low-resolution signal ΔZ_8 with the consistently filtered global GOCE-only model GOCE-TIM-R5 verifies the additional signal of G_8 to some extent. It further quantifies differences between the regional and the global model (around 10 % of the signal amplitude of G_8) due to different signal content (different time spans), the reference of G_8 w.r.t. GRACE signal (from the background model GOCO05s up to degree $l_{j'} = 127$), the influence of remaining long-wavelength signal and errors (which are not removed by the background model) and remaining modeling errors in the global model and in the regional approach.
- The differential MRR signal is enriched by the additional signal.
- The total MRR signal shows smaller edge effects in data gap areas than the signal from the previous single-level estimation.

In conclusion, computing detail signals from measurement techniques depending on their spectral sensitivity allows to extract at each level valuable information. The combination finally yields a regional model which is enriched by spectral information at all frequencies.
Besides the above discussed error influences, the MRR composition does not consider connections between the detail signals. The VCE yields the relative weighting of the observation groups w.r.t. one level j. The same prior information is introduced at each level for regularization. However, the amount of regularization varies from level to level so that the total influence of prior information cannot be quantified in the resulting MRR signal. In order to avoid the multiple presence of one and the same information at different resolution levels, the observation groups have to be chosen very carefully by balancing spectral content and spatial distribution. A pyramid algorithm could provide the potential to manage those difficulties, see Sec. 7.

7 Summary and Outlook

Summary

The enhanced regional gravity field modeling approach from the combination of real data via MRR is founded on the theory from Secs. 2 to 5. The application in Sec. 6 provides ground for rating the methodical settings and discussing the obtained results.

Theory of the approach

The Chapters 2, 4 and 5 describe the theory of the regional modeling approach. Hereby, fundamentals of gravity field representation, which are relevant for this work, are depicted in Sec. 2. Amongst others, diverse gravitational functionals are introduced w.r.t. their spectral sensitivity according to the Meissl scheme. For regionally modeling the Earth's gravity field, in Sec. 4, radial SBFs are specified. Especially the commonalities and differences between global modeling in terms of SH functions and regional modeling in terms of SBFs are studied. Section 5 finally investigates the choices of the methodical settings and of the estimation model for a spectral combination of heterogeneous data sets via MRR.
The diversity of measurement systems, the characteristics and reasonable pre-processing of corresponding observation types was discussed in Sec. 3.3. The properties manifest the need of carefully adapting the basis functions, the methodical settings, and the estimation model for an enhanced regional gravity field modeling from the combination of heterogeneous data by exploiting their strengths. The corresponding spectral classification of the data types w.r.t. resolution level j in Tab. 4.8 delivers the basis for setting up the approach.

Choice of SBFs The locally supporting SBFs provide a compromise between the uncertainty in the spectral and in the spatial domain. While in the analysis, Shannon functions with ideal filter characteristics are used for the determination of the unknown scaling coefficients, smoothing Blackman functions are used in the synthesis for modeling the output gravity fields. Those SBFs have smaller oscillations in the spatial domain, and thus, reduce erroneous effects.

Choice of methodical settings For installing the regional modeling approach, the specific methodical settings in Sec. 5.1 are chosen such, that they balance, e. g., edge effects due to the spatially limited computation area, aliasing problems due to the truncation of series expansions, minimum and maximum modeling resolution w.r.t. the spatial and spectral content of the observations. Edge effects are reduced by defining different spatial extents for the three areas, i. e. the area of computation, observation and investigation. Hereby, the margin width η^j decreases with increasing resolution level. The maximum modeling resolution L_j is chosen higher than the upper boundary of the desired resolution level of the output model in order to reduce aliasing errors from frequency folding. The minimum resolution level refers to the average extent of the observed area and further is related to the maximum resolution of the background model in order to ensure spectral consistency.

Choice of estimation model The unknown scaling coefficients are estimated in an extended GMM which enables the combination of diverse observation groups on normal equation level. Observation equations have to be formulated for each functional. Hereby, special emphasize is given to the representation of the measurements in their most original state. The pre-processing shall be kept as low as possible in order to capture a high measure of information out of the measurements. For instance, the observation equations for the GOCE tensor contain transformation terms from the Earth-bound modeling system to the satellite specific GRF where the gravity gradients were observed. For a multi-level estimation as visualized in Fig. 5.10, several single-level estimation models are set up. The composition then enables a MRR of the resulting gravitational signal.

Application of the approach

The application of the theory is demonstrated and discussed by means of several study cases in Chapter 6. Table 6.1 gives an overview of the main cases (a) – (g) w.r.t. to their complexity. Hereby, several categories are identified which influence the target achievement; above all, the number of levels, i. e. setting up the regional modeling approach in terms of a single-level (Sec. 6.1) or a multi-level estimation (Sec. 6.2), i. e. a spectral combination via MRR. Further, the types of simulated (Sec. 6.1.1) and real data (Sec. 6.1.2) are distinguished.

The method of VCE has two tasks in this work: It manages the relative weighting of the heterogeneous observation groups and, by introducing prior information as additional data set, the amount of regularization.

Regularization For a stable solution of the normal equation system in the GMM, regularization is necessary. By means of study cases (a), (b), (d) and (g), three main issues have been identified for its need: (1) regional rank deficiency, (2) data gaps, and (3) downward continuation. Hence, due to (1), regional approaches always require the stabilization of the estimation model in contrast to global approaches. In order to overcome the ill-conditioned normal equation system, prior information is necessary. It stems in the here presented approach from a global SH model.
The regional rank deficiency problem was especially investigated in cases (a,b) and (g1). An estimate k_L^{reg} for the quantification of the regional rank deficiency was derived in Sec. 5.1.4. k_L^{reg} increases with augmenting resolution level and requires a stronger regularization. However, the exact determination is not possible due to the spatial limitation of the computation area and the corresponding neglect of SBFs outside this area. A possible reduction of k_L^{reg} was discussed in study cases (a,b). However, the reduction comes along with taking either increasing edge effects into account (by reducing η^j), or increasing aliasing errors (by choosing a smaller modeling degree L_j). In this work, the regional rank deficiency is tried to be kept as small as possible by appropriate methodical settings.
An inhomogeneous spatial distribution of the observations and referring data gaps require regularization, as well. The missing spectral content is filled up by the additional prior information. The latter is introduced as zero-vector due to its dual role: it also serves as background model, i. e. the spectral content of all observation groups is reduced by the spectral information of this model. In all study cases, the prior information could stabilize the ill-conditioned normal equation systems. However, the "zero-signal" turned out to be not appropriate for filling in the data gaps at higher resolution levels. In study cases (e) and (g), erroneous effects predominate the areas of missing high-frequency information.
The third need for regularization due to downward continuation was discussed in study cases (d) and (g1). For modeling gravitational structures at the Earth's surface and/or for combining satellite data with near-Earth observations, downward continuation is necessary, and thus, a stronger regularization.

Relative weighting Since the iteratively estimated variance factors are computed based on the stochastic information of the observations, the method is appropriate for the relative weighting of noisy data, especially for real data which is the aim in this thesis. The residuals of the observations indicate the accuracy and the spectral resolution of the data sets. Low-resolution signal is smoother in the spatial domain, i. e. it shows large-scale variations, while high-resolution signal represents short-scale variations. Hence, the type of the gravitational functional and the aspect of downward continuation play a role, as well. According to the Meissl scheme (Fig. 2.7), different functionals are more or less sensitive to high-frequency variations of the Earth's gravity field and signal (e. g. from satellite measurements) is amplified in the high frequencies by downward continuation to the Earth's surface. Further, data sets with spatially limited extent cannot resolve long wavelengths while the latter can be resolved by spatially widespread observations. Thus, the spectral content of observations depends on the size of data gaps, as well.
The appropriate and reasonable relative weighting of heterogeneous data sets by VCE at one single resolution level, is shown in study cases (b), (d), (e) and (g1). In the multi-level combination in study case (g2), the VCs at different resolution levels then are used as indicators for the classification of the observation groups depending on their spectral sensitivities. This beneficial strategy allows to set up the MRR composition, which is one of the main tasks of this work.
In study cases (a) and (c), simulated noise-free data are used. Due to the missing stochastic information, instabilities appear in the method of VCE. They are especially discussed in study case (e). Further, long-wavelength errors cannot be considered, and the regularization by VCE in terms of prior information from a

noise-free global SH model is unstable as well. However, the iterations converge in all study cases and stable normal equation systems can be achieved.

In conclusion, VCE is appropriate for the relative weighting of real data. However, weaknesses appear when using the method for regularization by low-resolution prior information. Consequently, the choice of a more suitable strategy is recommended for future studies. In study case (a), alternative regularization methods, as well as the introduction of additional information from topography models are exemplarily mentioned. By formulating for the latter observation equations in terms of residual quantities and setting up an appropriate stochastic model, the influence of the synthetic model can be managed by VCE. Consequently, this high-frequency information could overcome data gaps at high resolution levels in addition to stabilizing the modeling approach by long-wavelength information from global SH models.

Results of the approach

Simulation studies by single-level estimation The simulation studies (a) – (c) confirm for various different settings the plausibility and stability of the approach by means of closed-loop scenarios. Especially different noise levels and the choice of SBFs in the synthesis are investigated. The method of VCE reasonably considers the different stochastic information in study case (b); in study case (c) the Blackman function is verified as a good compromise between a oscillating SBF in the spatial and a smoothing SBF in the spectral domain. In general, the closed-loop differences are small. However, they do not reach computational accuracy. In study cases (a,b), especially systematic errors dominate the CL differences, probably stemming from the prior information. By means of study case (c) additional modeling errors are identified, e. g. due to instabilities in the VCE or incomplete stochastic models. In Tab. 7.1, possible error influences are summarized.

Real data studies by single-level estimation Taking the findings from the simulation studies into account, the application of the single-level approach on real data is investigated within study cases (d) and (e). Hereby, the complexity w.r.t. the influence factors on the target achievement from Tab. 6.1 increases. Data types with different functionals and accuracies are especially discussed in case (d) by means of GOCE GGs. Hereby the method of VCE is verified by reasonable relative down-weighting of the less accurate GGs. Further, the trace criterion of the GOCE tensor is valid at computational accuracy and justifies the consistent rotation of the observation equations into the GRF. Besides the already identified weaknesses and regional modeling errors, instabilities in the estimation model due to downward continuation require regularization, as well. In study case (e), further, different observation heights, functionals, spatial distributions and resolutions of diverse data sets are investigated at a high spectral resolution level. The small standard deviations of the estimated parameters and models confirm a high internal accuracy; the small differences of the results to the regional GCG2011 model and in a cross-validation constitute a high external accuracy of the modeling approach, and thus, its plausibility. However, the incomplete stochastic model yields too optimistic standard deviations. A proper consideration of covariance information of the observations is recommended for future studies. From slightly larger differences to global models, additional resolution in the regional model is assumed. However, data gaps turn out as most negative aspect. While they can be compensated by surrounding observations inside the target area, erroneous oscillations predominate data gaps at the edges. Further, the combination of regional and global data sets, with considerably different spectral resolutions, cannot be properly handled within the single-level estimation model.

Multi-level estimation The main advantages of a multi-level estimation are that the observation techniques can contribute information exactly in the spectral domain of their highest sensitivity, and the resulting regional model is enriched by the spectral content from global low-resolution, as well as from regional high-resolution measurements. The spectral decomposition of an existing model in several low- and bandpass filtered signals in study case (f) emphasizes the potential of the MRR approach to detect data gaps w.r.t. the resolution level. Further applications of the spectral decomposition arise for neighboring disciplines, as e. g., studying large-scale variations in the Earth's interior. Vice versa, for the spectral combination, three criteria are specified in this work: (1) introducing data sets with highest spectral sensitivity, (2) avoiding correlations between detail signals, (3) ensuring "sufficient" spectral content, and thus, spatial distribution of the input data. In study case (g1), the VCE highlights especially the different nature of the here available global vs.

regional data sets from study cases (d) and (e). In study (g2), a two-level composition, incorporating further decomposition, is realized. In contrast to the single-level combination in (e), the MRR-model shows the enrichment by additional GOCE signal. The comparison with EGM2008 proves that the erroneous effects of data gaps is reduced compared with the model from study case (e). Further, the large-scale differences indicate the enrichment of the regional model through GOCE information. They are rated by a comparison to the global GOCE-only model GOCE-TIM-R5. Since the MRR composition of the high-resolution level-11 signal does not consider connections, correlations and error propagation between the detail signals, the amount of additional signal in the regional model compared with EGM2008 cannot exactly be quantified and approved. In conclusion, the spectral MRR composition enables to stabilize high-resolution regional models by the enrichment of medium-resolution spectral content and erroneous edge effects are reduced in data gap areas. The approach has the potential to deliver additional high-resolution information for existing global models.

Error influences and uncertainties

Table 7.1 summarizes the previously specified error influences and uncertainties in the regional modeling approach of this work. Hereby, their consideration in terms of quantification and/or reduction is assigned and further or alternative possibilities are suggested. Note, the applied reduction strategies and the (alternative) possibilities are contradictory in some cases and point out the need for compromises.

Table 7.1: Error influences or uncertainties, their quantification and/or reduction, and (alternative) possibilities, referring to settings w.r.t. $\partial\Omega_C$, input data w.r.t. $\partial\Omega_O$, and output models w.r.t. $\partial\Omega_I$.

	error influences and uncertainties	**quantification and/or reduction**	**(alternative) possibilities**
$\partial\Omega_C$	spatial oscillations of SBFs	reduction by choice of Blackman functions in the synthesis	alternative basis functions (*Bentel et al.*, 2013a)
	regional rank deficiency	regularization	smaller area margins, studying the amount by singular value decomposition (*Naeimi*, 2013), different point systems
	$\hookrightarrow$ linear dependencies due to unfavorable spatial distribution of the observations	regularization	alternative point grids
	$\hookrightarrow$ truncation of the series expansion of SBFs	estimation of omission error, reduction of aliasing errors by appropriate filtering in the analysis and synthesis	
	$\hookrightarrow$ truncation of the computation area, i. e. neglect of basis functions outside the computation area, and thus, missing support of those SBFs	estimating regional rank deficiency	smaller maximum modeling degree, alternative computation grids
	$\hookrightarrow$ truncation of SBFs in the spatial domain by the borderlines of the computation area (globally defined functions with local support)	appropriate area margins	estimating the truncation error, as e. g. suggested by *Haagmans et al.* (2002)
	singularities in the normal equation system due to downward continuation and inhomogeneous data distribution	regularization	
$\partial\Omega_O$	systematic errors stemming from prior information and/or observations	reduced by homogenization w.r.t. the normal potential	additional prior information, adapting parameter estimation model (additional unknown; complete stochastic model)
	unknown spectral content of observations	classification of observation types w.r.t. spatial resolution	spectral analysis
	inconsistencies in height and gravity datums of different data sets	homogenization w.r.t. normal potential, pre-processing	
	unknown height and gravity reference (systematic errors)		introducing an additional unknown in estimation model, deterministic estimation of systematic errors
	unknown accuracy, stochastic information of the observations	assuming the measurement errors to be uncorrelated and to have the same accuracies	considering more realistic covariance information in the weight matrix, deterministic estimation of stochastic and systematic errors
	missing stochastic information of the prior information		introducing covariance information in stochastic model, alternative prior information
	correlations of background model and observations		alternative background models
	data gaps	prior information	additional prior information, e. g. topography models
$\partial\Omega_I$	assuming the detail signals to be uncorrelated	Shannon filter functions in the analysis	connecting detail signals and applying error propagation within a pyramid algorithm

Outlook

From the indicated error sources in Tab. 7.1 and the discussions of the results in Sec. 6, the most relevant open questions yield consequential recommendations for future studies.

- Considering covariance information of the observations, i. e. formulating a complete stochastic model taking correlations and different accuracies into account or introducing additional unknowns in the estimation model.
- Considering covariance information of the prior information stemming from a global SH background model.
- Introducing additional observation groups with high-resolution information, e. g. from topography models of the Earth.
- Implementing the pyramid algorithm for a consistent spectral combination.
- Implementing a combined estimation in terms of SBFs and SHs.

Covariance information of the observations

Complete stochastic model For the consistent combination of different observation groups, stochastic and systematic error components have to be described within the estimation model. However, the information about the quality of (especially terrestrial, air-/shipborne) regional data sets is often not available. Thus, identity matrices describe the weight matrices in this thesis. *Fecher et al.* (2015) suggest an empirical derivation of the systematic errors from a validation of regional data against global gravity models. The resulting stochastic models then can be externally calibrated by means of the covariance information of the global SH models. A similar strategy, computing the differences between a low-pass filtered global SH model and low-pass filtered observations is described by *Wittwer* (2009), pp. 157. In the here presented approach, it could be realized as follows: The SH gravity models, which are introduced as background models up to degree $l_{j'}$, are assumed to be noise-free. The observations have to be low-pass filtered up to the same degree $l_{j'}$. The differences then give an estimate of the remaining long-wavelength errors.

Estimation of long-wavelength errors The estimation model (5.22) further can be extended by additional unknowns in order to handle long-wavelength errors. Since low-resolution errors are mainly of systematic nature, an additional parameter could be introduced in the GMM (5.22), e. g. in terms of a constant value or a regression surface, depending on the differences w.r.t. the background model. In altimetry applications, as e. g. determining the structure of marine gravity fields, systematic offsets are, for instance, considered by estimating a constant parameter in the estimation model (*Pimenova*, 2013).

Covariance information of SH background models

While for regional data sets error information is often missing, it is usually available for global gravity field models in terms of covariance matrices. In order to formulate an appropriate stochastic model, the covariance matrix has to be transformed into an appropriate weight matrix $\boldsymbol{P}_d$ in the extended GMM (5.22). In analogy to the transformation of SH coefficients into scaling coefficients (*Eicker et al.*, 2013), the transformation of covariance information is not unique and singularities have to be considered.

Additional prior information

As mentioned in study cases (a) and (b), additional prior information from synthetic Earth models, as e. g. topography models, might help to stabilize the method of VCE and overcome data gaps in the resulting regional model. In order to reduce the propagation of long-wavelength errors and uncertainties of topography models onto the regional models, the topographic information should be introduced in terms of relative quantities, representing derivatives of the gravitational potential. Deflections of the vertical η, ξ, cf. Sec. 2.5.6, or gravity gradients V_{ab}, cf. Sec. 2.5.7, are, for instance, appropriate gravitational functionals. As suggested by *DGFI-TUM* (2014), observation equations can be formulated in analogy to Tab. 4.7 and considered as

additional observation type in the extended GMM (5.22). In order to account for remaining uncertainties of the synthetic model, a reasonable weight matrix has to be chosen. The relative contribution to the regional model then is regulated by VCE. The topographic information might stabilize the regional modeling approach and reduce the presence of "zero-signal" w.r.t. the background model in the differential output signal. Especially at higher resolution levels, the high-resolution topographic information could be further beneficial in order to overcome data gaps.

Another aspect comes along with additional information from the Earth's topography: Instead of using spherical basis functions, a gravity field representation in terms of ellipsoidal basis functions, e. g. ellipsoidal harmonics (*Hofmann-Wellenhof and Moritz*, 2005) or ellipsoidal wavelets (*Schmidt et al.*, 2007), may be more appropriate in order to achieve a closer fit of the basis functions to the topographic structures of the Earth (*Rummel*, 2011). However, the computational effort then increased a lot.

Pyramid algorithm

As schematically displayed in Fig. 4.7, a signal Z_J can be decomposed (top-down) into several detail signals by successive low-pass filtering. Connecting the detail signals in the top-down decomposition is the core idea of a so-called pyramid algorithm, mentioned in Sec. 4.3.5. Hereby, the number of scaling coefficients and their corresponding spectral content are reduced level-by-level, and the spectral information and the covariance information of higher levels serve as input for lower levels.
The principle is visualized in Fig. 7.1. Starting from the highest level J, the referring detail signal G_J is computed from high-resolution data sets (e. g. observation group 1; orange) by estimating the unknown scaling coefficients (collected in the vector $\boldsymbol{d}_J$). In order to compute the smoother detail signal G_{J-1} of the next lower level $J-1$, the scaling coefficients ($\boldsymbol{d}_{J-1}$) of this level are computed from $\boldsymbol{d}_J$ by low-pass filtering. This has several advantages: (1) The coefficients of different levels do not have to be computed separately. Their estimation is very time-consuming especially at high levels. (2) The low-pass filter matrix $\boldsymbol{H}_{J-1}$, which connects the sets of coefficients $\boldsymbol{d}_J$ and $\boldsymbol{d}_{J-1}$, allows to take the estimated signal G_J and the covariance information from the higher level into account. (3) Appropriate observations (e. g. from group 2; green) can be introduced and their correlations can be considered in the low-pass filter matrix, as well. The spectral combination down to level $j'+1$ hence ensures consistency and full error propagation.
The practical realization of the pyramid algorithm, however, has several challenges: Hierarchical point grids do not exist on the sphere (*Freeden et al.*, 1998) (non-hierarchical point grids, as e. g. the Reuter grid, have to be used); The down-sampled scaling coefficients are not unique (a pseudoinverse would have to be introduced for solving the normal equation system); The area margins have to be adapted (lower levels require larger area margins due to edge effects); Setting up the low-pass filter matrix $\boldsymbol{H}_{j-1}$ for the regional case is still an open issue (*Schmidt and Fabert*, 2008). All those aspects are implicitly considered or mostly do not matter within the spectral composition, realized within this work following the bottom-up approach.

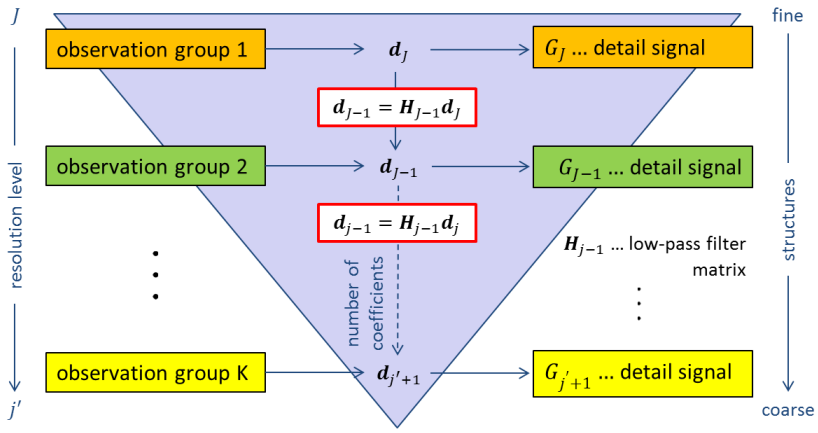

Figure 7.1: Pyramid algorithm.

Combined estimation in terms of SHs and SBFs

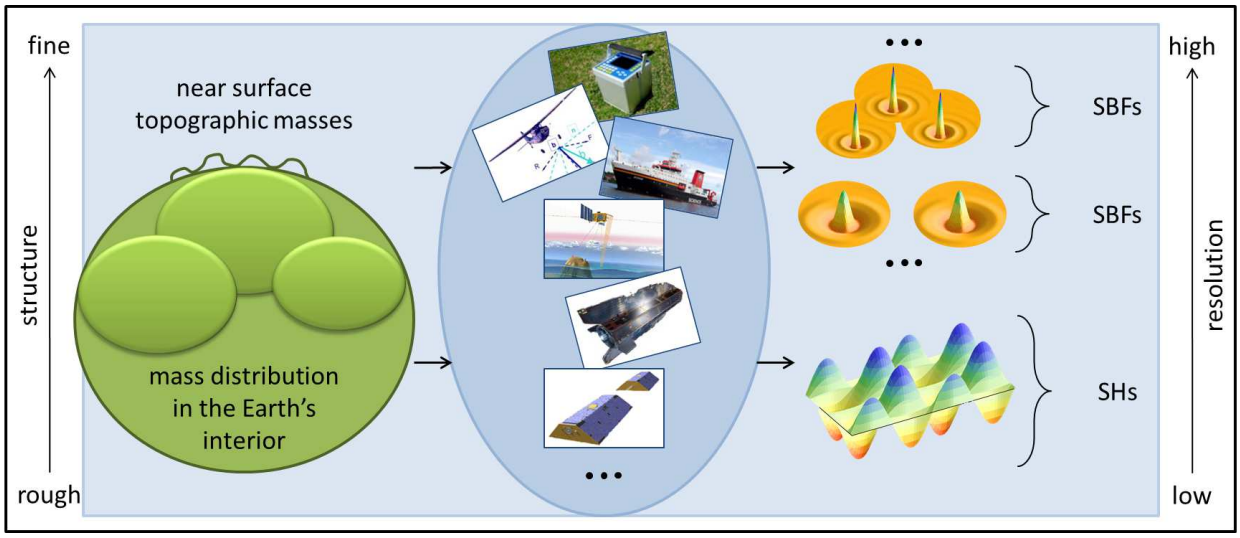

Figure 7.2: Future idea: modeling regional gravitational structure (depending on mass distribution) – from observations (terrestrial, air-/shipborne, altimetry, GOCE, GRACE, ...) – in terms of both SHs and SBFs. The light-blue colored background visualizes the contributing parts which will be included in a future estimation model – in contrast to Fig. 1.1

In analogy to Fig. 1.1 which presents the idea of the regional modeling approach of this thesis, Fig. 7.2 visualizes the idea of a combined estimation model, including both the estimation of high-resolution parts in terms of SBFs, as well as the estimation of low-resolution parts in terms of SHs. A combination strategy of diverse basis functions is, for instance, described by *Fischer* (2011).

As mentioned in the context of Fig. 1.2, SH functions are optimally localizing in the spectral domain, while SBFs are a compromise between spectrally and spatially localizing basis functions; a perfect localization in both domains is not possible. Whereas global gravity field modeling manages the representation of global satellite data very well since many decades, regional modeling by using the content of spatially limited data sets is still a young research field. A large number of trade-offs exist in the regional approaches. Some of them are exemplarily discussed in this work and the methodical settings give a kind of "receipt" for balancing different aspects. As an outcome of the ICCT JSG0.3, the variety of different regional approaches further demonstrates the fact, that there is no "optimal" strategy up to now for regional gravity field modeling.
The primary motivation of this work is to profit from the valuable information of low-, medium- up to high-resolution resolution data sets by using SBFs for regional gravity modeling. The future aim could be to use the strengths of the different basis functions, as well, i. e. not only combining heterogeneous data, but also different basis functions for comprehensively model the Earth's gravity field.

Abbreviations and Nomenclature

Abbreviations

AdV	Arbeitsgemeinschaft der Vermessungsverwaltungen der Länder der Bundesrepublik Deutschland	63
BKG	German Federal Agency for Cartography and Geodesy	46, 63–65
CHAMP	CHAllenging Minisatellite Payload	59, 62
CPU	Central Processing Unit	66
CSR	Center for Space Research	57, 58
DGFI	Deutsches Geodätisches ForschungsInstitut	64, 65
DHHN	Deutsches Haupthöhennetz	63
DLR	Deutsches Zentrum für Luft- und Raumfahrt	56
DNSC	Danish National Space Center	65
DOT	Dynamic Ocean Topography	48, 61
DTM2006.0	Digital Topographic Model 2006.0	125
EGM2008	Earth Gravitational Model 2008	12, 62, 125
EGM96	Earth Gravitational Model 1996	61
EIGEN	European Improved Gravity field of the Earth by New techniques	59
ESA	European Space Agency	51, 60, 66
ETRS89	European Terrestrial Reference System 1989	63
GCG2011	German Combined QuasiGeoid 2011	63–65
GFZ	GeoForschungsZentrum	57–59, 61
GG	Gravity Gradient	39, 50, 51, 54, 132
GMM	Gauß-Markov Model	11, 102, 103
GNSS	Global Navigation Satellite System	37, 40, 46, 47, 51, 63
GOCE	Gravity field and steady-state Ocean Circulation Explorer	12, 22, 43, 44, 51, 53, 54, 56, 66, 174, 175
GOCO	Gravity Observation COmbination	12
GPS	Global Positioning System	51, 61
GRACE	Gravity Recovery And Climate Experiment	12, 35, 44, 56, 62
GRF	Gradiometer Reference Frame	51–53, 56, 66, 173, 174
GRS80	Geodetic Reference System 1980	61
IAG	International Association of Geodesy	125
ICCT	Inter-Commission Committee on Theory	125
ICGEM	International Centre for Global Earth Models	24

IUGG	International Union of Geodesy and Geophysics	61
J2000	Julian Date of 2000	18, 173, 174
JPL	Jet Propulsion Laboratory	57, 58
LNCS	Local North-Oriented Coordinate System	21, 22, 51, 52, 56, 173, 174
LOCS	Local Orbital Coordinate System	22, 51–53, 56, 173, 174
LSC	Least Squares Collocation	8, 10, 11, 56, 109
MBW	Measurement BandWidth	54, 56, 118
MRR	Multi-Resolution Representation	9, 10, 12, 13, 59, 73, 75, 81, 86, 87
NASA	National Aeronautics and Space Administration	56
POD	Precise Orbit Determination	51, 57–59
RMS	Root-Mean-Square	47, 105
SBF	Spherical Basis Function	7–13, 15, 24, 25, 32, 33, 69, 70, 72, 75, 76, 86, 179
SGG	Satellite Gravity Gradiometry	50–52, 54, 56
SH	Spherical Harmonic	7, 9–15, 24–27, 29, 30, 32, 33, 36, 40, 51, 61, 69, 70, 72, 75, 76, 179
SLR	Satellite Laser Ranging	51, 54, 60
SSH	Sea Surface Higth	48, 51
SST	Satellite-to-Satellite Tracking	57, 59
UTCSR	University of Texas Center for Space Research	56
VC	Variance Component	106, 107, 111
VCE	Variance Component Estimation	8, 11, 60, 102–104, 106
WGS84	World Geodetic System 1984	61

Nomenclature

B_l	Legendre coefficients	70
E_f	energy of a non-bandlimited signal f	79
E_g	energy of a bandlimited signal g	79

$F_{l,m}$		spherical harmonic coefficients	25, 26, 29, 30, 72
F	kgm/s^2	magnitude of gravitational force $\boldsymbol{F}$	22
GM	m^3/s^2	standard gravitational parameter	23
$G_j(\boldsymbol{x})$		detail signal at $\boldsymbol{x}$, containing information from level j	85, 88, 89
G	m^3/kgs^2	gravitational constant: 6.6742×10^{-11}	22, 23, 27
$H^R_{l,m}$		surface spherical harmonic function	25, 26, 33
$H_{0,\ldots,L}$		space of dimension $(L+1)^2$	76
H_{norm}	m	normal height	41, 64, 65, 67
H_{orth}	m	orthometric height	40, 41, 51
$H_{l,m}$		solid spherical harmonic function	25, 26
J		maximum resolution level of MRR	100
L^{rank}		upper estimate of modeling resolution in terms of SH degree	101
L_{obs}		maximum spectral resolution of observations in terms of SH degree	100
L		maximum spectral (modeling) resolution in terms of SH degree	100
M_0	kg	total mass of the Earth's normal ellipsoid	27
M	kg	total mass of the Earth	27
N'		normal curvature of an ellipsoid	20
N_L	$=(L+1)^2$	dimension of the space $H_{0,\ldots,L}(\Omega^{\text{ext}}_R)$	76
N^{glob}_L		total global number of Reuter grid points	95
N^{max}_L		upper estimate of the global number of Reuter grid points	94
N	m	geoid height, geoid undulation	31, 36–38, 40, 48, 51, 190
O_{GRF}		origin of GRF	52
O_{J2000}		origin of inertial reference system at J2000	18
O_{LNCS}		origin of LNCS	21, 22, 52
O_{LOCS}		origin of LOCS	22, 51
P_l		Legendre polynomial	24, 26, 187
$P_{l,m}$		(associated) Legendre function	24, 26, 187
P		arbitrary point on or above the Earth's surface	18, 19, 26
Q_L	$=(L+1)^2$	total global number of coefficients at max. degree L for a fundamental point system S_Q	75, 76
Q^{glob}_L		total global number of scaling coefficients	94
Q^{reg}_L		regional number of scaling coefficients	97
Q	$\geq (L+1)^2$	total global number of coefficients at max. degree L for an admissible point system S_Q	73, 74
R	m	constant radius	19, 31, 83
S_Q		admissible point system	74, 76
T	m^2/s^2	disturbing potential	29–32, 36, 37, 39, 41, 43, 44
U	m^2/s^2	normal potential	27, 29, 35, 40
V_{back}	m^2/s^2	gravitational potential of a global background model	30
V_{ab}	s^{-2}	gravity gradients	40, 44, 50, 54, 55

V	m^2/s^2	gravitational potential	15, 22, 23, 26, 30, 32, 35, 36, 39, 40, 43
W_0	m^2/s^2	gravity potential of the geoid	15, 23, 35, 36
W	m^2/s^2	gravity potential	15, 21, 29, 35, 38, 39
X^{l+i}		up-/ downward continuation operator	30, 31, 33, 80, 81
X_{GRF}		X-axis of GRF	52
X_{J2000}		X-axis of inertial reference system at J2000	18
X_{LNCS}		X-axis of LNCS	22, 52
X_{LOCS}		X-axis of LOCS	22, 52
Y_{GRF}		Y-axis of GRF	52
Y_{J2000}		Y-axis of inertial reference system at J2000	18
Y_{LNCS}		Y-axis of LNCS	22, 52
Y_{LOCS}		Y-axis of LOCS	22, 52
$Z'(\boldsymbol{x})$		non-bandlimited gravitational signal at $\boldsymbol{x}$	90
$Z(\boldsymbol{x})$		bandlimited gravitational signal at $\boldsymbol{x}$	85
$Z_j(\boldsymbol{x})$		gravitational signal at $\boldsymbol{x}$, containing information up to level j	89
Z_{GRF}		Z-axis of GRF	52
Z_{J2000}		Z-axis of inertial reference system at J2000	18
Z_{LNCS}		Z-axis of LNCS	22, 52
Z_{LOCS}		Z-axis of LOCS	22, 51, 52, 54
Z	m^2/s^2	centrifugal potential	15, 23, 29, 51
ΔV	$\mathrm{m}^2/\mathrm{s}^2$	gravitational potential difference	35, 44, 67
$\Delta \boldsymbol{V}$	$[3 \times 3]$	tensor of gravity gradients	39, 53, 54, 56
$\Delta \boldsymbol{g}$	$[3 \times 1]$	vector of gravity anomaly	37, 38
Δg	$\mathrm{m/s}^2$	gravity anomaly	37, 38, 44, 46, 190
Λ	°, [rad]	astronomical longitude	21, 23, 39
Ω_R^{ext}		exterior and surface of a sphere with radius R	17, 23, 25, 26, 29, 70, 71, 76, 81, 102, 104
Ω_R		sphere with radius R	16, 17, 19, 25, 26, 31, 71, 72, 76, 81–83, 98, 190
$\Phi_{q,j}$	$= \Phi_j(\boldsymbol{x}, \boldsymbol{x}_q)$	spherical scaling function	88
Φ	°, [rad]	astronomical latitude	21, 23, 39
$\Psi_{q,j}$	$= \Psi_j(\boldsymbol{x}, \boldsymbol{x}_q)$	spherical wavelet function	90
Σ		telluroid	36
$\bar{n}$		total number of observations at locations $\boldsymbol{x}^p$	103
$\boldsymbol{\delta}$	$[3 \times 1]$	components of the GOCE satellite linear accelerations	53, 54
β	°, [rad]	ellipsoidal latitude	20, 28, 39
$\boldsymbol{R}_{\mathrm{GRF}}^{\mathrm{LNCS}}$	$[3 \times 3]$	rotation matrix from GRF to LNCS	53, 66
$\boldsymbol{R}_{\mathrm{GRF}}^{\mathrm{LOCS}}$	$[3 \times 3]$	rotation matrix from GRF to LOCS	53, 56
$\boldsymbol{g}$	$[3 \times 1]$	gravity vector	21, 23, 38, 39
$\boldsymbol{n}'$	$[3 \times 1]$	ellipsoidal normal unit vector	20, 37

$\boldsymbol{n}$	$[3 \times 1]$	unit vector along the plumb line	21, 23, 38
$\boldsymbol{r}$	$[3 \times 1]$	unit vector	19, 37
$\boldsymbol{x}$	$[3 \times 1]$	geocentric position vector $[x, y, z]^T$	15, 18, 22
$\delta \boldsymbol{g}$	$[3 \times 1]$	vector of gravity disturbance	37, 38
δg	$\mathrm{m/s^2}$	gravity disturbance	37, 38, 44, 46, 190
$\dot{\omega}_{ab}$	$[3 \times 3]$	components of the GOCE satellite angular accelerations	53, 54
η^J	°, [rad]	margin width w.r.t. maximum resolution level J	97
η	°, [rad]	deflection of the vertical in east-west direction	38, 39, 44
$\mathcal{Y}[\,\tilde{V}_{\text{back}}\,]$		functional of $\tilde{V}_{\text{back}}$	102
$\mathcal{Y}[\,\tilde{V}\,]$		functional of $\tilde{V}$	16, 30–39, 43, 67, 81, 102, 104, 110, 113, 119, 126
γ_L		control parameter of the Reuter grid	94
$\gamma_{h'}$	m/s^2	normal gravity at height h' above an ellipsoid	28
γ	m/s^2	normal gravity	28, 34, 38
λ_L	m	wavelength at degree L	82
λ	°, [rad]	spherical, ellipsoidal longitude	19, 20, 22, 27, 32, 39
∇^2		Laplace operator	23, 29
$\partial/\partial r$		normal derivative operator	30, 31
ω_{ab}	$[3 \times 3]$	components of the GOCE satellite angular rates	53, 54
ω	rad/s	angular velocity of the Earth: $7\,292\,115 \times 10^{-11}$	27, 47
$\partial\Omega_C$		computation area	96
$\partial\Omega_I$		modeling area, area of investigation	96
$\partial\Omega_O$		observation area	96
$\phi_{l,j}$		Legendre coefficients of scaling functions	89
$\psi_{l,j}$		Legendre coefficients of wavelet functions	89
ψ	°, [rad]	spherical distance angle	19, 24, 190
ρ_L	m	spatial resolution at degree L	82, 83
$\rho_{\max,j}$	m	max. spatial resolution of level j	83
ρ	$\mathrm{kg/m^3}$	density	23
σ^2_{om}		variance of the omission error	79
$\sigma^2_l(g)$		degree variances	79
$\tilde{V}$	m^2/s^2	differential gravitational potential	30–33, 36, 40, 43, 80, 81, 179
$\tilde{b}(\boldsymbol{x}, \boldsymbol{x}_q)$	$= \tilde{b}_q$	adapted SBF	81
φ	°, [rad]	spherical latitude	19, 39
ϑ	°, [rad]	spherical co-latitude: $\vartheta = 90° - \varphi$	19, 22, 32, 39
$\widehat{\boldsymbol{d}}$	$[1 \times Q_L]$	vector of estimated scaling coefficients	104, 105
ξ	°, [rad]	deflection of the vertical in north-south direction	38, 39, 44
ζ	m	quasigeoid height, quasigeoid undulation	36, 37, 41
a	m	major semi-axis of an ellipsoid	19, 27
$b'(\boldsymbol{x}, \boldsymbol{x}_q)$	$= b'_q$	non-bandlimiting SBF	70
$b(\boldsymbol{x}, \boldsymbol{x}_q)$	$= b_q$	bandlimiting SBF	70, 73, 88
b	m	minor semi-axis of an ellipsoid	19
$d\omega_R$		surface element on a sphere with radius R	16, 19, 25, 190

d_q		scaling coefficients of SBFs	76, 103
ds	m	element of distance, element of arc	18, 19
f'		flattening of an ellipsoid	19, 27
f		harmonic function	23, 25, 26, 70
$g_l(r)$		gravity anomaly operator	30, 31, 33, 40, 80
g	Gal	gravity	21, 23, 38, 40, 41, 44
h'	m	height above an ellipsoid	20, 28, 34, 37, 40
h	m	height above a sphere	19, 51
i'	°	inclination angle of a satellite's orbit	22, 51, 56
j'		minimum resolution level of MRR	85
j		resolution level	83
$k'(\boldsymbol{x}, \boldsymbol{x}_q)$	$= k'_q$	non-bandlimiting Abel-Poisson kernel	71
k_L^{glob}		global rank deficiency	95
k_L^{reg}		estimate of the regional rank deficiency	97
l_j		maximum spectral degree of level j	101
$l_{\min}$		minimum spectral resolution in terms of SH degree	99
l		degree	25, 31
m		order	24, 25, 27
n'		direction of the ellipsoidal normal	36–41
n		direction of the plumb line	38, 41
o		base	83
r	m	radial distance	19, 22, 25, 30–32, 39, 51
t		argument of Legendre function/polynomial	24, 187
x	m	Cartesian x-coordinate	18
y	m	Cartesian y-coordinate	18
z	m	Cartesian z-coordinate	18

List of Figures

List of Tables

Bibliography

Arbeitsgemeinschaft der Vermessungsverwaltungen der Länder der Bundesrepublik Deutschland (AdV), Richtlinie für den einheitlichen integrierten geodätischen Raumbezug des amtlichen Vermessungswesens in der Bundesrepublik Deutschland, 25/04/2014, http://www.adv-online.de/.

Arabelos D.N., Tscherning C.C. (2010), A comparison of recent Earth gravitational models with emphasis on their contribution in refining the gravity and geoid at continental or regional scale, *Journal of Geodesy*, *84*, 643-660, DOI 10.1007/s00190-010-0397-z.

Balmino G., Barlier F., Bernard A., Bouzad C., Rivière G., Runavot J. (1985), GRADIO: Project Proposal for Satellite Gradiometry, *NASA Technical Memorandum*, NASA TM-76796, National Aeronautics and Space Administration, Washington DC 20546, USA. Translation of "GRADIO: Gradiométrie par satellite – Proposition de projet (1981)", *Centre National d'Etudes Spatiales, Report*, *244 PRT/AMP/AP*, 1-51, Centre Spatiale de Toulouse, France.

Bentel K., Schmidt M., Gerlach C. (2013a), Different radial basis functions and their applicability for regional gravity field representation on the sphere, *International Journal of Geomathematics*, Springer-Verlag Heidelberg Berlin, DOI 10.1007/s13137-012-0046-1.

Bentel K., Schmidt M., Rolstad Denby C. (2013b), Artifacts in regional gravity representations with spherical radial basis functions, *Journal of Geodetic Science*, *3(3)*, 173-187, DOI 10.2478/jogs-2013-0029.

Bentel K. (2013), Regional Gravity Modeling in Spherical Radial Basis Functions – On the Role of the Basis Function and the Combination of Different Observation Types, *PhD thesis*, *2013:58*, Department of Mathematical Sciences and Technology, Norwegian University of Life Sciences, As, Norway, ISSN 1503-1667, ISBN 978-82-575-1158-6173-187.

Bettadpur S. (2012), UTCSR level-2 processing standards document (for level-2 product release 0005), *GRACE document*, 327-742, ftp://podaac.jpl.nasa.gov/allData/grace/docs/.

Beutler G., Jäggi A., Mervart L., Meyer U. (2010), The celestial mechanics approach: theoretical foundations, *J. Geodesy*, *84*, 605-624, DOI 10.1007/s00190-010-0401-7.

Bundesamt für Kartographie und Geodäsie, Quasigeoid der Bundesrepublik Deutschland GCG 2011, Referat GI5 - Dienstleistungszentrum, Leipzig, Germany, 28/12/2011, http://www.geodatenzentrum.de.

Bloßfeld M. (2015), The key role of Satellite Laser Ranging towards the integrated estimation of geometry, rotation and gravitational field of the Earth, *PhD thesis*, Technical University of Munich, Reihe C der Deutschen Geodätischen Kommission, ISBN 978-3-7696-5157-7.

Bloßfeld M., Müller H., Gerstl M., Stefka V., Bouman J., Göttl F., Horwath M. (2015), Second-degree Stokes coefficients from multi-satellite SLR, *Journal of Geodesy*, *89(9)*, 857-871, DOI 10.1007/s00190-015-0819-z.

Brockmann J.M., Zehentner N., Höck E., Pail R., Loth I., Mayer-Gürr T., Schuh W.D. (2014), EGM TIM RL05: An Independent Geoid with Centimeter Accuracy Purely Based on the GOCE Mission, *Geophysical Research Letters*, *41(22)*, 8089-8099, DOI 10.1002/2014GL061904.

Bruinsma S., Lemoine J.M., Biancale R., Vales N. (2010), CNES/GRGS 10-day gravity field models (release 2) and their evaluation, *Adv. Space Res.*, *45(4)*, 587–601, DOI 10.1016/j.asr.2009.10.012.

Bosch W., Savcenko R., Dettmering D., Schwatke C. (2013), A two-decade time series of eddy-resolving dynamic ocean topography (iDOT), *Ouwehand L. (Ed.) Proceedings of "20 Years of Progress in Radar Altimetry"*, ESA/ESTEC, Sept. 2012, Venice, Italy, *ESA SP-710* (CD-ROM), ISBN 978-92-9221-274-2.

Bosch W., Dettmering D., Schwatke C. (2014), Multi-mission cross-calibration of satellite altimeters: constructing a long-term data record for global and regional sea level change studies. *Remote Sensing*, *6(3)*, 2255-2281, DOI 10.3390/rs6032255.

Boucher C., Altamimi Z. (1992), Terrestrial Reference System and its first realizations, *Astronomisch-Geodätische Arbeiten*, *52*, 205-213, Bayerische Kommission für die internationale Erdmessung.

Bouman J., Rispens S., Gruber T., Koop R., Schrama E., Visser P., Tscherning CC., Veicherts M. (2009), Preprocessing of gravity gradients at the GOCE high-level processing facility, *Journal of Geodesy*, *83(7)*, 659-678, DOI 10.1007/s00190-008-0279-9.

Bouman J., Fuchs M. (2012), GOCE gravity gradients versus global gravity field models, *Geophysical Journal International*, *189*, 846-850, DOI 10.1111/j.1365-246X.2012.05428.x.

Bouman J., Ebbing J., Meekes S., Fattah R.A., Fuchs M., Gradmann S., Haagmans R., Lieb V., Schmidt M., Dettmering D., Bosch W. (2013), GOCE gravity gradient data for lithospheric modeling, *International Journal of Applied Earth Observation and Geoinformation*, *35(A)*, 16-30, Elsevier, DOI 10.1016/j.jag.2013.11.001.

Bouman J., Ebbing J., Abdul Fattah R., Meekes S., Fuchs M., Lieb V., Bosch W., Schmidt M. (2014), Data Set User Manual, *GOCE+ GeoExplore ESA-Project document*, *1.1*, MA-GOCE+-DNT-06.

Bouman J., Ebbing J., Fuchs M., Sebera J., Lieb V., Szwillus W., Haagmans R., Novak P. (2016), Satellite gravity gradient grids for geophysics, *Scientific Reports*, *6(21050)*, DOI 10.1038/srep21050.

Bowring B.R. (1985), The Accuracy of Geodetic Latitude and Height Equations, *Survey Review*, *28(218)*, 202-206, DOI 10.1179/003962685791474982.

Buße K. (2015) Verwendung von Schiffsgravimetermessungen für die verbesserte regionale Schwerefeldmodellierung, *Master thesis*, Deutsches Geodätisches Forschungsinstitut der Technischen Universität München (DGFI-TUM), https://mediatum.ub.tum.de.

Cesare, S. (2002), Performance requirements and budgets for the gradiometric mission. *Technical Note*, *4*, GOC-TN-AI-0027, Alenia Spazio, Turin, Italy.

Chao B.F., O'Connor W.P., Chang A.T.C., Hall D.K., Foster J.L. (1987), Snow load effects on the Earth's rotation and gravitational field, 1979 – 1985, *Journal of geophysical Research*, *92(B9)*, 9415– 9422, DOI 10.1029/JB092iB09p09415.

Chen Y.Q., Schaffrin B., Shum C.K. (2008), Continental water storage changes from GRACE Line-of-sight range acceleration measurements, *VI Hotine-Marussi Symposium on Theoretical and Computational Geodesy*, *132*, 62-66, International Association of Geodesy Symposia, DOI 10.1007978-

3-540-74584-6.

Cui J. and Freeden W. (1997), Equidistribution on the sphere, *SIAM J. Sci. Comput.*, *18(2)*, 595-609, Society for Industrial and Applied Mathematics, DOI 10.1137/S1064827595281344.

Dahle C., Flechtner F., Gruber C., König D., König R., Michalak G., Neumayer K.H. (2012), GFZ GRACE level-2 processing standards document for level-2 product release 0005, *Scientific Technical Report*, *12/02*, Data, Revised Edition, January 2013, Potsdam, DOI 10.2312/GFZ.b103-1202-25.

Dahle C., Gruber C., Fagiolini E., Flechtner F. (2015), Gravity Field Mapping from GRACE: Different Approaches – Same Results?, *IAG Symposia*, Springer, DOI 10.1007/1345_2015_8.

Deutsches Geodätisches Forschungsinstitut der Technischen Universität München, Annual Report 2014, München, Germany, `https://mediatum.ub.tum.de/`.

Dietrich R. (2003), Mathematische Geodäsie, Referenzsysteme, Gravimetrie/Schweremessung, *Script zur Vorlesung*, Technische Universität Dresden, Institut für Planetare Geodäsie, Theoretische und Physikalische Geodäsie.

Ditmar P., van Eck van der Sluijs A.A. (2004). A technique for Earth's gravity field modeling on the basis of satellite accelerations, *J. Geod.*, *78*, 12–33, DOI 10.1007/s00190-003-0362-1.

Driscoll J.R., Healy D.M. (1994), Computing Fourier Transforms and Convolutions on the 2-Sphere, *Advances in Applied Mathematics*, *15(2)*, 202–250, DOI 10.1006/aama.1994.1008.

Ebbing J., Bouman J., Fuchs M., Lieb V., Haagmans R., Meekes J.A.C., Fattah R.A. (2013), Advancements in satellite gravity gradient data for crustal studies, *The Leading Edge*, *32(8)*, 900-906, Society of Exploration Geophysicists, DOI 10.1190/tle32080900.1.

Eicker A. (2008), Gravity Field Refinement by Radial Basis Functions from In-situ Satellite Data, *PhD thesis*, Schriftenreihe des Instituts für Geodäsie und Geoinformation, Hohe Landwirtschaftliche Fakultät, Rheinische Friedrich-Wilhelms-Universität Bonn, Heft 10, Germany.

Eicker A., Schall J., Kusche J. (2013), Regional gravity modelling from spaceborne data: case studies with GOCE, *Geophys J Int*, *196(3)*, DOI 10.1093/gji/ggt485.

Fecher T., Pail R., Gruber T., Holmes S. (2015), Validation of South American Terrestrial Gravity Anomalies by GOCE, European Geosciences Union General Assembly 2015, 12 – 17 April 2015, Vienna, Austria.

Fischer D. (2011), Sparse Regularization of a Joint Inversion of Gravitational Data and Normal Mode Anomalies, *PhD thesis*, Department Mathematik der Naturwissenschaftlich-Technischen Fakultät der Universität Siegen, Germany.

Flechtner F., Dahle C., Neumayer K.H., König R., Förste C. (2010), The Release 04 CHAMP and GRACE EIGEN Gravity Field Models, *Advanced Technologies in Earth Sciences*, System Earth via Geodetic-Geophysical Space Techniques, 41-58, DOI 10.1007/978-3-642-10228-8_4.

Förste C., Schmidt R., Stubenvoll R., Flechtner F., Meyer U., König R., Neumayer H., Biancale R., Lemoine J.M., Bruinsma S., Loyer S., Barthelmes F., Esselborn S. (2012), The GeoForschungsZentrum Potsdam / Groupe de Recherche de G´eod´esie Spatiale satellite-only and combined gravity field models: EIGEN-GL04S1 and EIGEN-GL04C, *Journal of Geodesy*, *82(6)*, 331-346, DOI 10.1007/s00190âĂŘ007âĂŘ0183âĂŘ8.

Förste C., Bruinsma S., Marty J-C., Flechtner F., Abrikosov O., Dahle C., Lemoine J.M., Neumayer H., Biancale R., Barthelmes F., König R. (2014), EIGEN-6C3stat - the newest High Resolution Global Combined Gravity Field Model based on the 4th Release of the GOCE Direct Approach, Potsdam/Toulouse, September 2013.

Förste C., Bruinsma S., Rudenko S., Abrikosov O., Lemoine J.M., Marty J-C., Neumayer H., Biancale R. (2015), EIGEN-6S4 – A time-variable satellite-only gravity field model to d/o 300 based on LAGEOS, GRACE and GOCE data from the collaboration of GFZ Potsdam and GRGS Toulouse, European Geosciences Union General Assembly 2015, 12 – 17 April 2015, Vienna, Austria.

Forsberg R., Olesen A.V. (2010), Airborne gravity field determination, *Sciences of geodesy - I*, Springer, Berlin, 83-104, DOI 10.1007/978-3-642-11741-1_3.

Forsberg R., Olesen A.V., Nielsen E., Einarsson I. (2015), Airborne Gravimetry for Geoid and GOCE, *International Association of Geodesy Symposia*, 1-12, Springer Berlin Heidelberg, DOI 10.1007/1345_2015_47.

Forward R.L. (1974), Review of artificial satellite gravity gradiometer techniques for geodesy, *Proceedings of the International Symposium, Athens, Greece, May 14-21, 1973*, *A75-27082 11-43*, 157-192, The Use of Artificial Satellites for Geodesy and Geodynamics, National Technical University of Athens.

Freeden W., Gervens T., Schreiner M. (1998), Constructive Approximation on the Sphere (With Applications to Geomathematics), *Oxford Science Publications*, Clarendon Press, ISSN 0198536828, ISBN 978-0-19-853682-6.

Freeden W. (1999), Multiscale Modelling of Spaceborne Geodata, *Teubner Stuttgart*, Leipzig, Germany, ISBN 3-519-02600-7.

Freeden W., Michel V. (2001), Basic aspects of geopotential field approximation from satellite-to-satellite tracking data, *Mathematical Methods in the Applied Sciences*, *24(11)*, 827-846, DOI 10.1002/mma.244.

Freeden W., Michel V. (2004), Multiscale potential theory (with applications to Geoscience), *Birkhäuser Verlag*, Boston, ISBN-13 978-1-4612-7395-0, DOI 10.1007/978-1-4612-2048-0.

Friis-Christensen E., Lühr H., Knudsen D., Haagmans R. (2008) Swarm – an earth observation mission investigating geospace *Adv. Space Res.*, *41(1)*, 210-216, DOI 10.1016/j.asr.2006.10.008.

Fuchs M., Bouman J. (2011), Rotation of GOCE gravity gradients to local frames, *Geophys. J. Int.*, *187(2)*, 743-753, DOI 10.1111/j.1365-246X.2011.05162.x.

Gerlach, C. (2003) Zur Höhensystemumstellung und Geoidberechnung in Bayern, *PhD thesis*, DGK Reihe C, *571*, Verlag der Bayerischen Akademie der Wissenschaften, ISBN (Print) 3-7696-5010-7, ISSN 0065-5325.

Gerlach C., Sneeuw N., Visser P., Švehla D. (2003), CHAMP Gravity Field Recovery with the Energy Balance Approach: First Results, *First CHAMP Mission Results for Gravity, Magnetic and Atmospheric Studies I*, 134-139, Springer Berlin Heidelberg, DOI 10.1007/978-3-540-38366-6_20.

Gruber T., Rummel R., Abrikosov O., van Hees R. (2014), GOCE Level 2 Product Data Handbook, *5.0*, GOCE High Level Processing Facility, European GOCE Gravity Consortium EGG-C, GO-MA-HPF-GS-0110.

Haagmans R., Prijatna K., Omang O.D. (2002), An alternative concept for validation of GOCE gradiometry results based on regional gravity, *Proceedings of 3rd Meeting of International Gravity and Geoid Commission*, Thessaloniki, Greece.

Han S.-C., Shum C.K., Jekeli C. (2006), Precise estimation of in situ geopotential differences from GRACE low-low satellite-to-satellite tracking and accelerometer data, *J. geophys. Res.*, *111*, B04411, DOI 10.1029/2005JB003719.

Haberkorn C., Fuchs M., Lieb V., Bouman J., Schmidt M. (2014), Verwendung von GOCE in RegGrav, RegGrav II, AP3.4 N.2, *RegGRAV II, 2. Meilenstein*, 22/09/2014, WRLageZ Uedem.

Heinhold J., Riedmüller B. (1971), Lineare Algebra und Analytische Geometrie, Teil 1 *Carl Hanser Verlag München*, ISBN 3-446-11523-4.

Hobson E.W. (1965), The Theory of Spherical and Ellipsoidal Harmonics, *Chelsea Publ. Comp.*, New York.

Hofmann-Wellenhof B., Moritz H. (2005), Physical Geodesy, *Springer Wien New York*, ISBN-10 3-211-23584-1, ISBN-13 978-3-211-23584-3.

Holschneider M. (1996), Wavelet analysis on the sphere, *Journal of Mathematical Physics*, *37(8)*, 4156-4165, DOI 10.1016/S0031-9201(02)00210-8.

Holschneider M., Chambodut A., Mandea M. (2003), From global to regional analysis of the magnetic field on the sphere using wavelet frames, *Physics of the Earth and Planetary Interiors*, *135*, 107-124, DOI 10.1016/S0031-9201(02)00210-8.

Jäggi A., Dahle C., Arnold D., Bock H., Meyer U., Beutler G., van den IJssel J. (2016), Swarm kinematic orbits and gravity fields from 18 months of GPS data, *Advances in Space Research*, *57(1)*, 218-233, ISSN 0273-1177, DOI 10.1016/j.asr.2015.10.035.

Jekeli, C. (1996), Spherical harmonic analysis, aliasing, and filtering, *Journal of Geodesy*, *70(214)*, DOI 10.1007/BF00873702.

Jekeli C. (1999). The determination of gravitational potential differences from satellite-to-satellite tracking, *Celestial Mech. Dyn. Astron.*, *75*, 85-100, DOI 10.1023/A:1008313405488.

Jekeli C. (2012), Omission Error, Data Requirements, and the Fractal Dimension of the Geoid, VII Hotine-Marussi Symposium on Mathematical Geodesy, Rome, Italy, IAG Symposia *137*, 181-187, DOI 10.1007/978-3-642-22078-4_27.

Keller W. (2003), Geodetic Pseudodifferential Operators and the Meissl Scheme, *Geodesy-The Challenge of the 3rd Millennium*, 207-211, *Springer Berlin Heidelberg*, DOI 10.1007/978-3-662-05296-9_20.

Kern M. (2003), An Analysis of the Combination and Downward Continuation of Satellite, Airborne and Terrestrial Data, *PhD thesis*, UCGE Reports *20172*, Department of Geomatics Engineering, University of Calgary, Canada.

Klees R., Haagmans R. (2000), Wavelets in the Geosciences, *Lecture Notes in Earth Sciences*, *90*, Springer Heidelberg, Berlin, ISBN 978-3-540-66951-7.

Klees R., Tenzer R., Prutkin I., Wittwer T. (2008), A data-driven approach to local gravity field modelling using spherical radial basis functions, *Journal of Geodesy*, *82(8)*, 457-471, DOI 10.1007/s00190-007-0196-3.

Klosko, S. (1998), SLR Contributions to Determining the Gravitational Field and its Variations, *Proc. of 11th International Workshop on Laser Ranging*, 28-39, Deggendorf, Germany, September 20-26.

Koch K.-R. (1977), Least squares adjustment and collocation, *Bulletin géodésique*, *51(2)*, 127-135, DOI 10.1007/BF02522282.

Koch K.-R. (1999), Parameter Estimation and Hypothesis Testing in Linear Models, Second Edition, Springer-Verlag Berlin Heidelberg, Germany, ISBN 3-540-65257-4.

Koch K.-R., Kusche J. (2002), Regularization of geopotential determination from satellite data by variance components, *Journal of Geodesy*, *76*, 259-268, DOI 10.1007/s00190-002-0245-x.

Koop R. (1993), Global Gravity Field Modelling Using Satellite Gravity Gradiometry, *Netherlands Geodetic Commission*, Publications on Geodesy, *38*, Delft, The Netherlands.

Krarup T. (1969), A contribution to the mathematical foundation of physical geodesy, *Mathematical Foundation of Geodesy*, 29-90, Geodaetisk Institut, Meddelelse *44*, Kobenhavn, Denmark.

Krarup T. (1970), The method of least squares collocation, *Studia Geophysica et Geodaetica*, *14(2)*, 107-109, DOI 10.1007/BF02585604.

Kurtenbach E., Mayer-Güerr T., Eicker A. (2009), Deriving daily snapshots of the Earth's gravity field from GRACE L1B data using Kalman filtering *Geophysical Research Letters*, *36*, L17102, DOI 10.1029/2009GL039564.

Lanczos C. (1997), Linear Differential Operators, *Dover Books on Mathematics*, Dover Publications, Inc., Mineola, New York, ISBN 0-486-68035-5.

Lemoine F.G., Kenyon S.C., Factor J.K. Trimmer, R.G., Pavlis N.K., Chinn D.S., Cox C M., Klosko S.M., Luthcke S.B., Torrence M.H., Wang Y.M., Williamson R.G., Pavlis E.C., Rapp R.H., Olson T.R. (1998), The Development of the Joint NASA GSFC and NIMA Geopotential Model EGM96, NASA Goddard Space Flight Center, Greenbelt, Maryland, 20771 USA, NASA/TP-1998-206861.

Lemoine F.G., Smith D.E., Kunz L. , Smith R., Pavlis E.C., Pavlis N.K., Klosko S.M., Chinn D.S., Torrence M.H., Williamson R.G., Cox C.M., Rachlin K.E., Wang Y.M., Kenyon S.C., Salman R., Trimmer R., Rapp R.H., Nerem R.S. (1997), The Development of the NASA GSFC and NIMA Joint Geopotential Model, *Gravity, Geoid and Marine Geodesy*, *117*, 461-469, International Association of Geodesy Symposia.

Lieb V., Bouman J., Dettmering D., Fuchs M., Schmidt M. (2015), Combination of GOCE Gravity Gradients in Regional Gravity Field Modelling Using Radial Basis Functions, *IAG Symposia*, Proceedings of the VIII Hotine-Marussi Symposium, Springer *142*, 1-8, DOI 10.1007/1345_2015_71.

Lieb V., Buße K., Schmidt M., Dettmering D., Bouman J. (2014), Closed-loop tests of a regional gravity field modelling approach using radial basis functions, poster presentation at EGU General Assembly 2014, April 28 – May 2, Vienna, Austria.

Lieb V., Schmidt M., Dettmering D., Börger K. (2016), Combination of various observation techniques for regional modeling of the gravity field, *Journal of Geophysical Research*, *121(5)*, 3825-3845, DOI 10.1002/2015JB012586.

Liu X., Ditmar P., Siemes C., Slobbe D.C., Revtova E., Klees R., Riva R., Zhao Q. (2010), DEOS Mass Transport model (DMT-1) based on GRACE satellite data: methodology and validation, *Geophys J Int*, *181*, 769-788, DOI 10.1111/j.1365-246X.2010.04533.x.

Luthcke S.B., Rowlands D.D., Lemoine F.G., Klosko S.M., Chinn D., McCarthy J.J. (2006), Monthly spherical harmonic gravity field solutions determined from GRACE inter-satellite range-rate data alone, *Geophys. Res. Lett.*, *33*, L02402, DOI 10.1029/2005GL024846.

Mayer-Gürr T. (2006), Gravitationsfeldbestimmung aus der Analyse kurzer Bahnbögen am Beispiel der Satellitenmissionen CHAMP und GRACE, *PhD thesis*, *D 98*, Universität Bonn, `http://hss.ulb.uni-bonn.de/diss_online`.

Mayer-Gürr T., Eicker A., Ilk K.H. (2007), ITG-Grace02s: a GRACE gravity field derived from range measurements of short arcs, *Gravity Field of the Earth*, Proceedings of the 1st International Symposium of the International Gravity Field Service (IGFS), Special Issue 18, 193-198, Gen. Command of Mapp., Ankara, Turkey.

Mayer-Gürr T., Eicker A., Kurtenbach E., Ilk K.H. (2010), ITG-GRACE: Global Static and Temporal Gravity Field Models from GRACE Data, *System Earth via Geodetic-Geophysical*

Space Techniques, 159-168, Springer, Berlin, DOI 10.1007/978-3-642-10228-8_13.

Mayer-Gürr T., Rieser D., Höck E., Brockmann J..M., Schuh W.-D., Krasbutter I., Kusche J., Maier A., Krauss S., Hausleitner W., Baur O., Jäggi A., Meyer U., Prange L., Pail R., Fecher T., Gruber T. (2015), The new combined satellite only model GOCO03s, Symposium on Gravity, Geoid and Height Systems (Poster), Venice, October 9-12 (2012).

Mayer-Gürr T., Zehentner N., Klinger B., Kvas A. (2014), ITSG-Grace2014: a new GRACE gravity field release computed in Graz, GRACE Science Team Meeting (GSTM), Potsdam, 29.09.2014.

Mayer-Gürr T., Pail R., Gruber T., Fecher T., Rexer M., Schuh W.-D., Kusche J., Brockmann J.-M., Rieser D., Zehentner N., Kvas A., Klinger B., Baur O., Höck E., Krauss S., Jäggi A. (2015), The combined satellite gravity field model GOCO05s, Presentation at EGU 2015, Vienna, April 2015.

Meissl P. (1971a), On the linearization of the geodetic boundary value problem, *Report*, *79*, Department of Geodetic Science, Ohio State University, Columbus, AD0728632.

Meissl P. (1971b), A study of covariance functions related to the Earth's disturbing potential, *Report*, *96*, Department of Geodetic Science, Ohio State University, Columbus, AD0728688.

Meyer U., Jäggi A., Beutler G. (2012), Monthly gravity field solutions based on GRACE observations generated with the celestial mechanics approach, *Earth Planet Sci Lett*, *345*, 72-80, DOI 10.1016/j.epsl.2012.06.026.

Michel V. (2013), Lectures on Constructive Approximation – Fourier, Spline, and Wavelet Methods on the Real Line, the Sphere, and the Ball, *Birkhäuser*, Springer Science+Business Media New York, DOI 10.1007/978-0-8176-8403-7.

Morelli C., Gantar C., McConnell R.K., Szabo B., Uotilaet U. (1971), The International Gravity Standardization Net 1971 (I.G.S.N.71), *IUGG IAG Special Publication*, *4*, International Association of Geodesy, Paris (France), SP-4.

Moritz H. (1978), Advanced least-squares methods, *Reports of the Department of Geodetic Science*, *175*, The Ohio State University Research Foundation, Columbus, USA.

Moritz H. (1978), Least squares collocation, *Reviews of Geophysics and Space Physics*, *16(3)*, ISBN 0034-6853/78/038R-030450.

Moritz H. (2000), The Geodesist's Handbook 2000, *Journal of Geodesy*, *74(1)*, Editor O.B. Andersen, Springer, DOI 10.1007/s001900050274.

Naeimi M. (2013), Inversion of satellite gravity data using spherical radial base functions, *PhD thesis*, Fakultät für Bauingenieurwesen und Geodäsie der Gottfried Wilhelm Leibniz Universität Hannover, Germany.

Narcowich F.J., Ward J.D. (1996), Nonstationary wavelets on the m-sphere for scattered data *Applied and Computational Harmonic Analysis*, *3(4)*, 324-336, DOI 10.1006/acha.1996.0025.

Neunhöfer H., Börngen M., Junge A., Schweitzer J. (1997), Zur Geschichte der Geophysik in Deutschland, *Jubiläumsschrift zur 75jährigen Wiederkehr der Gründung der Deutschen Geophysikalischen Gesellschaft*, Deutsche Geophysikalische Gesellschaft, Hamburg.

Pail R., Reguzzoni M., Sansò F., Kühtreiber N. (2009), On the combination of global and local data in collocation theory, *Studia Geophysica et Geodaetica*, *54(2)*, 195-218, DOI 10.1007/s11200-010-0010-1.

Pail R., Goiginger H., Schuh W.-D., Höck E., Brockmann J.M., Fecher T., Gruber T., Mayer-Gürr T., Kusche J., Jäggi A., Rieser D. (2010), Combined satellite gravity field model GOCO01S derived from GOCE and GRACE, *Geophysical Research Letters*, *37*, EID L20314, American Geophysical Union, ISSN 0094-8276, DOI 10.1029/2010GL044906.

Pail R., Bruinsma S., Migliaccio F., Förste C., Goiginger H., Schuh W.-D., Höck E., Reguzzoni M., Brockmann J.M., Abrikosov O., Veicherts M., Fecher T., Mayrhofer R., Krasbutter I., Sansò F., Tscherning C.C. (2011), First GOCE gravity field models derived by three different approaches, *Journal of Geodesy*, *85(11)*, 819-843, Springer, DOI 10.1007/s00190-011-0467-x.

Pail R., Goiginger H., Schuh W.D., Höck E., Brockmann J.M., Fecher T., Mayer-Gürr T., Kusche J., Jäggi A., Rieser D., Gruber T. (2011), Combination of GOCE data with complementary gravity field information (GOCO), Proceedings of 4th International GOCE User Workshop, München, 31.03.2011.

Pail R., Fecher T., Murböck M., Rexer M., Stetter M., Gruber T., Stummer C. (2013) Impact of GOCE Level 1b data reprocessing on GOCE-only and combined gravity field models, *Studia Geophysica et Geodaetica*, Springer, DOI 10.1007/s11200-012-1149-8.

Panet I., Chambodut A., Diament M., Holschneider M., Jamet O. (2006), New insights on intraplate volcanism in French Polynesia from wavelet analysis of GRACE, CHAMP and sea-surface data, *Journal of geophysical Research*, *111*, B09403, DOI 10.1029/2005JB004141.

Pavlis N.K., Factor J.K., Holmes S.A. (2007), Terrain-Related Gravimetric Quantities Computed for the Next EGM, *Gravity Field of the Earth*, *18*, Proceedings of the 1st International Symposium of the International Gravity Field Service (IGFS), Harita Dergisi, General Command of Mapping, Ankara, Turkey.

Pavlis N.K., Holmes S.A., Kenyon S.C., Factor J.K. (2012), The development and evaluation of the Earth Gravitational Model 2008 (EGM2008), *Journal of geophysical Research*, Solid Earth (1978-2012), *117(B4)*, DOI 10.1029/2011JB008916.

Pimenova O. (2013) High resolution gravity field modelling using satellite altimetry data of geodetic mission phases, *Master thesis*, Deutsches Geodätisches Forschungsinstitut der Technischen Universität München (DGFI-TUM), `https://mediatum.ub.tum.de`.

Reguzzoni M. and Sansò F. (2012), On the combination of high-resolution and satellite-only global gravity models, *Journal of Geodesy*, *86*, 393-408, DOI 10.1007/s00190-011-0526-3.

Reigber C., Bock R., Förste C., Grunwaldt L., Jakowski N., Lühr H., Schwintzer P., Tilgner C. (1996), CHAMP, *Phase-B Executive Summary*, GFZ STR96/13, GFZ, Potsdam, Germany.

Reigber C., Balmino G., Schwintzer P., Biancale R., Bode A., Lemoine J.-M., König R., Loyer S., Neumayer H., Marty J.-C., Barthelmes F., Perosanz F., Zhu S.Y. (2002), A high-quality global gravity field model from CHAMP GPS tracking data and accelerometry (EIGEN-1S), *Geophysical Research Letters*, *29(14)*, DOI 10.1029/2002GL015064.

Reigber C., Balmino G., Schwintzer P., Biancale R., Bode A., Lemoine J.-M., König R., Loyer S., Neumayer H., Marty J.-C., Barthelmes F., Perosanz F., Zhu S.Y. (2003a), Global Gravity Field Recovery Using Solely GPS Tracking and Accelerometer Data from Champ, *Space Science Reviews*, DOI 10.1023/A:1026217713133.

Reigber C., Schwintzer P., Neumayer H., Barthelmes F., König R., Förste C., Balmino G., Biancale R., Lemoine J.-M., Loyer S., Bruinsma S., Perosanz F., Fayard T. (2003b), The CHAMP-only Earth Gravity Field Model EIGEN-2, *Advances in Space Research*, *31(8)*, 1883-1888, DOI 10.1016/S0273-1177(03)00162-5.

Reigber C., Schmidt R., Flechtner F., König R., Meyer U., Neumayer K.H., Schwintzer P., Zhu S.Y. (2005), An earth

gravity field model complete to degree and order 150 from GRACE: EIGEN-GRACE02S, *J Geodyn*, *39*, 1-10, DOI 10.1016/j.jog.2004.07.001.

Reuter R. (1982), Über Integralformeln der Einheitssphäre und harmonische Splinefunktionen, *PhD thesis*, *33*, Veröffentlichungen des geodätischen Intituts, RWTH Aachen.

Rowlands D.D., Luthcke S.B., Klosko S.M., Lemoine F.G.R., Chinn D.S., McCarthy J.J., Cox C.M., Anderson O.B. (2005), Resolving mass flux at high spatial and temporal resolution using GRACE intersatellite measurements, *Geophysical Research Letters*, *32*, L04310, DOI 10.1029/2004GL021908.

Rummel R. (1986), Satellite Gradiometry, *Lecture Notes in Earth Sciences*, *7*, 159-169, DOI 10.1111/j.1365-246X.1992.tb00562.x.

Rummel R., van Gelderen M. (1992), Spectral analysis of the full gravity tensor, *Geophys. J. Int.*, *111(1)*, 159-169, DOI 10.1111/j.1365-246X.1992.tb00562.x.

Rummel R., van Gelderen M. (1995), Meissl scheme - spectral characteristics of physical geodesy, *Manuscripta Geodetica*, *20*, 379-385, Springer Verlag.

Rummel R., Balmino G., Johannessen J., Visser P., Woodworth P. (2002), Dedicated gravity field missions – principles and aims, *Journal of Geodynamics*, *33(1-2)*, 3-20, DOI 10.1016/S0264-3707(01)00050-3.

Rummel R. (2007), Erdmessung – Teil III: Physikalische Geodäsie, Institut für Astronomische und Physikalische Geodäsie, Technische Universität München, Oktober 2007, `http://tau.fesg.tu-muenchen.de/~iapg/web/lehre/skripten/skripten.php`.

Rummel, R., Yi W., Stummer C. (2001) GOCE gravitational gradiometry, *Journal of Geodesy*, *85(11)*, 777-790, Springer, DOI 10.1007/s00190-011-0500-0.

Sánchez L. (2014), Ein einheitliches vertikales Referenzsystem für Südamerika im Rahmen eines globalen Höhensystems, *PhD thesis*, *748*, Verlag der Bayerischen Akademie der Wissenschaften in Kommission beim Verlag C. H. Beck, München 2015, ISBN 978-3-7696-5160-7.

F. Sansò F., Barzaghi R., Carrion D. (2012), The Geoid Today: Still a Problem of Theory and Practice, VII Hotine-Marussi Symposium on Mathematical Geodesy, Rome, Italy, IAG Symposia *137*, 173-180, DOI 10.1007/978-3-642-22078-4_26.

Schmidt M. (2001), Grundprinzipien der Wavelet-Analyse und Anwendungen in der Geodäsie. Habilitationsschrift, Technische Universität München, Germany, Shaker Verlag, Aachen, Geodäsie *9*, ISBN 3-8265-8872-X.

Schmidt M., Fabert O., Shum C.K. (2005a), Towards the estimation of a multi-resolution representation of the gravity field based on spherical wavelets. *A Window on the Future of Geodesy*, IAG Symposia *128*, 362-367, Springer, DOI 10.1007/3-540-27432-4_62.

Schmidt M., Fabert O., Shum C.K. (2005b), On the estimation of a multi-resolution representation of the gravity field based on spherical harmonics and wavelets, *Journal of Geodynamics*, *39(5)*, 512-526, DOI 10.1016/j.jog.2005.04.007.

Schmidt M., Han S.C., Kusche J., Sánchez L., Shum C.K. (2006), Regional high-resolution spatiotemporal gravity modeling from GRACE data using spherical wavelets, *Geophysical Research Letters*, *33*, L08403, DOI 10.1029/2005GL025509.

Schmidt M., Fengler M., Mayer-Gürr T., Eicker A., Kusche J., Sánchez L., Han S.C. (2007), Regional gravity modeling in terms of spherical base functions, *Journal of Geodesy*, *81(1)*, 17-38, Springer Verlag, DOI 10.1007/s00190-006-0101-5.

Schmidt M., Fabert O. (2008), Ellipsoidal Wavelet Representation of the Gravity Field, *Geodetic Science and Surveying*, *487*, The Ohio State University, Columbus.

Schmidt M., Gerlach C., Bentel K., Dai C., Dettmering D., Eicker A., Herceg M., Kusche J., Lieb V., Schall J., Shang K., Shum C.K., Tscherning C.C. (2014), Results from IAG's Joint Study Group JSG0.3 on the Comparison of Current Methodologies in Regional Gravity Field Modeling, poster presentation at EGU General Assembly 2014, April 28 – May 2, Vienna, Austria.

Schmidt M., Göttl F., Heinkelmann R. (2015), Towards the Combination of Data Sets from Various Observation Techniques, *IAG symposia*, *140*, 35-43, Proceedings of the 2011 IAG International Workshop on the Quality of Geodetic Observation and Monitoring Systems (QuGOMS'11), Munich, Germany, April 13-15, Springer, DOI 10.1007/978-3-319-10828-5_6.

Schreiner M. (1996), A Pyramid Scheme for Spherical Wavelets, *AGTM-Report*, *170*, Universität Kaiserslautern, DOI 41A58.42C15.44A35.65D15.

Shang K., Guo J., Shum C.K., Dai C., Luo J. (2015), GRACE time-variable gravity field recovery using an improved energy balance approach, *Geophys. J. Int.*, *203*, 1773-1786, DOI 10.1093/gji/ggv392.

Shako R., Förste C., Abrikosov O., Bruinsma S., Marty J.-C., Lemoine J.-M., Flechtner F., Neumayer H., Dahle C. (2014), EIGEN-6C: a high-resolution global gravity combination model including GOCE data. *Springer*, Berlin, 155-161, DOI 10.1007/978-3-642-32135-1_20.

Sigl R. (1973), Einfuührung in die Potentialtheorie, *Sammlung Wichmann*, Neue Folge *4*, Karlsruhe, Germany, ISBN 3879070318 9783879070312.

Simons F.J. (2009), Slepian Functions and Their Use in Signal Estimation and Spectral Analysis, *Handbook of Geomathematics*, *arXiv:0909.5368v1*, Springer Verlag, DOI 10.1007/978-3-642-01546-5_30.

Slepian D., Pollak H.O. (1961), Prolate spheroidal wave functions, Fourier analysis and uncertainty - I, *Bell System Technical Journal*, *40(1)*, pp. 43-63, DOI 10.1002/j.1538-7305.1961.tb03976.x.

Stummer, C., Siemes C., Pail R., Frommknecht B., Floberghagen R. (2012), Upgrade of the GOCE Level 1b gradiometer processor, *Advances in Space Research*, *49(4)*, 739-752, Elsevier, DOI 10.1016/j.asr.2011.11.027.

Swenson S., Wahr J. (2006), Post-processing removal of correlated errors in GRACE data, *Geophys. Res. Lett.*, *33*, L08402, DOI 10.1029/2005GL025285.

Tapley B.D., Bettadpur S., Watkins M., Reigber C. (2004), The gravity recovery and climate experiment: mission overview and early results, *Geophys Research Letters*, *31:L09607*, DOI 10.1029/2004GL019920.

Torge W., Falk R., Franke A., Reinhart E., Richter B., Sommer M., Wilmes H. (1999), Das Deutsche Schweregrundnetz 1994 (DSGN94) - Band I, *Deutsche Geodätische Kommission*, Reihe B 309, München, ISBN 3 7696 8589 X.

Torge W. (2003), Geodäsie, *Walter de Gruyter GmbH & Co. KG*, Berlin, Germany, ISBN 3-11-017545-2.

Tscherning C.C., Rapp R.H. (1974), Closed covariance expressions for gravity anomalies, geoid undulations, and deflections of the vertical implied by anomaly degree varaince models. *Reports of the Departement of Geodetic Science*, Report No. 208, Ohio State University, Columbus, USA.

Tscherning C.C., Arabelos D.N. (2011), Gravity anomaly and gradient recovery from GOCE gradient data using LSC and comparisons with known ground data. *Proceedings of the 4th International GOCE user workshop*, ESA SP-696, March 31 - April 1, Munich, Germany.

Tscherning C.C. (2015), Least Squares Collocation, *Encyclopedia of Geodesy*, Springer International Publishing Switzer-

land, DOI 10.1007/978-3-319-02370-0_51-1.

Vermeer M. (2016), Physical Geodesy, *Maa-6.3271*, Department of the Built Environment, Aalto University, Finland, 01/03/2016, `http://users.aalto.fi/~mvermeer/`.

Watkins M., Yuan D.N. (2012), JPL level-2 processing standards document for level-2 product release 05, *GRACE document*, 327-744, ftp://podaac.jpl.nasa.gov/allData/grace/docs/.

Weber D. (1994), Das neue gesamtdeutsche Haupthöhennetz DHHN 92, *Allgemeine Vermessungs-Nachrichten: AVN*, *101(5)*, 179-193, Zeitschrift für alle Bereiche der Geodäsie und Geoinformation, Berlin Wichmann, VDE Verlag, ISSN 0002-5968.

Wittwer T. (2009), Regional gravity field modeling with radial basis functions, *PhD thesis*, Nederlandse Commissie voor Geodesie, Netherlands Geodetic Commission, Publications on Geodesy 72, Netherlands, ISBN 978-90-6132-315-0.

Zeidler E., Hackbusch W., Schwarz R., (2003), Teubner-Taschenbuch der Mathematik, *Teubner*, Wiesbaden, Germany, published by Zeidler E., adapted from Bronstein I.N. and Semendjajew K.A., ISBN 3-519-20012-0.

Appendices

A Supplementary theory

Relation of SBFs and SHs

Derivatives of Legendre functions and polynomials

The first and second order derivatives of the **Legendre functions** $P_{l,m}(t)$, as well as of the Legendre polynomials $P_l(t)$ are derived w. r. t. $t = \cos\psi$, and $t = \cos\vartheta$ respectively. For $P_{l,m}(\cos\vartheta)$ it yields

$$\frac{\partial P_{l,m}(\cos\vartheta)}{\partial\vartheta} = -P_{l,m+1}(\cos\vartheta) + m\cot\vartheta P_{l,m}(\cos\vartheta) \tag{A.1}$$

$$\frac{\partial^2 P_{l,m}(\cos\vartheta)}{\partial\vartheta^2} = -\cot\vartheta\frac{\partial P_{l,m}(\cos\vartheta)}{\partial\vartheta} - \left(l(l+1) - \frac{m^2}{\sin^2\vartheta}\right) P_{l,m}(\cos\vartheta) \tag{A.2}$$

e. g. after *Rummel* (2007); *Hobson* (1965). The first and second order derivatives of the **Legendre polynomials** $P_l(\cos\psi)$ w. r. t. the spherical coordinates λ, ϑ read

$$\begin{aligned}
\frac{\partial P_l(\cos\psi)}{\partial\lambda} &= \frac{\partial P_l(\cos\psi)}{\partial\cos\psi}\cdot\frac{\partial\cos\psi}{\partial\lambda} \\
\frac{\partial P_l(\cos\psi)}{\partial\vartheta} &= \frac{\partial P_l(\cos\psi)}{\partial\psi}\cdot\frac{\partial\cos\psi}{\partial\vartheta} \\
\frac{\partial^2 P_l(\cos\psi)}{\partial\lambda^2} &= \frac{\partial^2 P_l(\cos\psi)}{\partial\cos\psi^2}\cdot\frac{\partial\cos\psi}{\partial\lambda}\cdot\frac{\partial\cos\psi}{\partial\lambda} + \frac{\partial P_l(\cos\psi)}{\partial\cos\psi}\cdot\frac{\partial^2\cos\psi}{\partial\lambda^2} \\
\frac{\partial^2 P_l(\cos\psi)}{\partial\vartheta^2} &= \frac{\partial^2 P_l(\cos\psi)}{\partial\cos\psi^2}\cdot\frac{\partial\cos\psi}{\partial\vartheta}\cdot\frac{\partial\cos\psi}{\partial\vartheta} + \frac{\partial P_l(\cos\psi)}{\partial\cos\psi}\cdot\frac{\partial^2\cos\psi}{\partial\vartheta^2} \\
\frac{\partial^2 P_l(\cos\psi)}{\partial\lambda\partial\vartheta} &= \frac{\partial^2 P_l(\cos\psi)}{\partial\cos\psi^2}\cdot\frac{\partial\cos\psi}{\partial\vartheta}\cdot\frac{\partial\cos\psi}{\partial\lambda} + \frac{\partial P_l(\cos\psi)}{\partial\cos\psi}\cdot\frac{\partial^2\cos\psi}{\partial\lambda\partial\vartheta}\,.
\end{aligned} \tag{A.3}$$

Hereby, the first and second order derivatives w. r. t. the argument $t = \cos\psi$ yield

$$\frac{\partial P_l(\cos\psi)}{\partial\cos\psi} = \frac{l}{\cos^2\psi - 1}(\cos\psi P_l(\cos\psi) - P_{l-1}(\cos\psi)) \tag{A.4}$$

$$\frac{\partial^2 P_l(\cos\psi)}{\partial\cos\psi^2} = \frac{l(l+1)}{\cos^2\psi - 1}P_l(\cos\psi) - \frac{2\cos\psi}{\cos^2\psi - 1}\frac{\partial P_l(\cos\psi)}{\partial\cos\psi} \tag{A.5}$$

Eq. (A.4) is adapted from *Rummel* (2007) and results from the recursion formula (e. g. *Freeden et al.*, 1998, p. 42); Eq. (A.5) is derived from a differential equation, according to *Hofmann-Wellenhof and Moritz* (2005, p. 14). They have to be inserted in Eqs. (A.3), together the following derivatives of the spherical distance angle ψ w. r. t. λ, ϑ:

$$\begin{aligned}
\frac{\partial\cos\psi}{\partial\lambda} &= -\sin\vartheta\sin\vartheta_q\sin(\lambda - \lambda_q) \\
\frac{\partial\cos\psi}{\partial\vartheta} &= -\sin\vartheta\cos\vartheta_q + \cos\vartheta\sin\vartheta_q\cos(\lambda - \lambda_q) \\
\frac{\partial^2\cos\psi}{\partial\lambda^2} &= -\sin\vartheta\sin\vartheta_q\cos(\lambda - \lambda_q) \\
\frac{\partial^2\cos\psi}{\partial\vartheta^2} &= -\cos\vartheta\cos\vartheta_q - \sin\vartheta\sin\vartheta_q\cos(\lambda - \lambda_q)
\end{aligned} \tag{A.6}$$

$$\frac{\partial^2 \cos\psi}{\partial\lambda\partial\vartheta} = -\cos\vartheta \sin\vartheta_q \sin(\lambda - \lambda_q) \; .$$

Deriving SHs and SBFs from Legendre polynomials

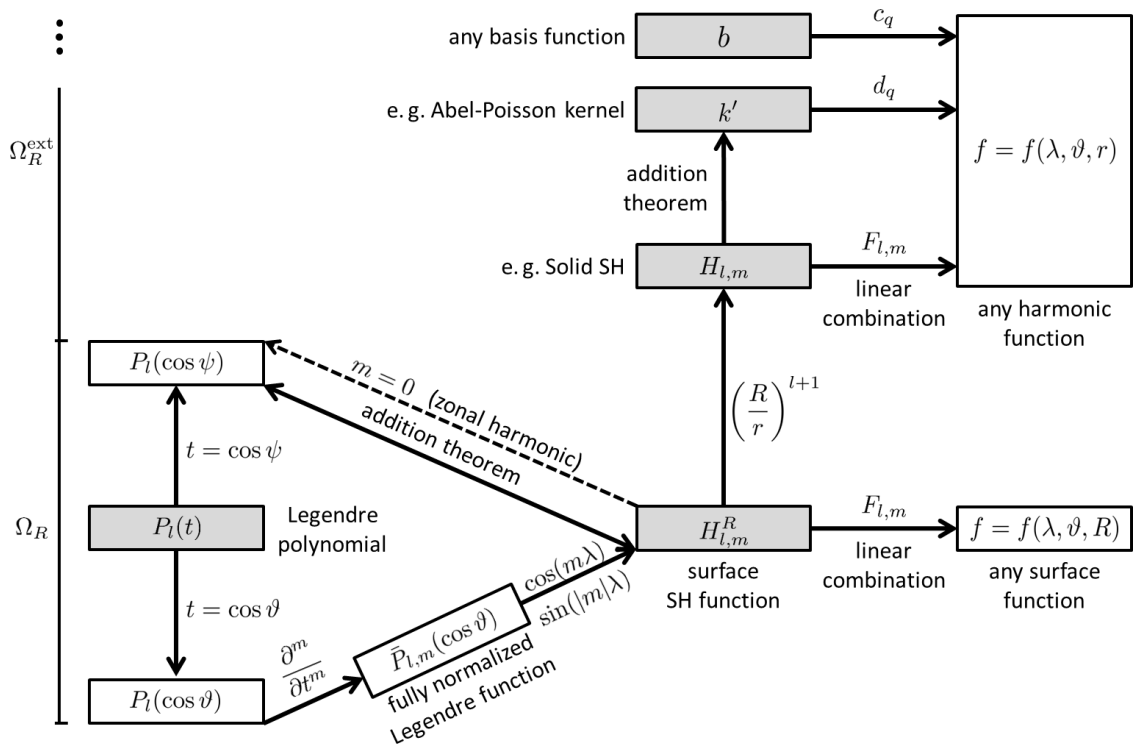

Figure A.1: Relation between Legendre polynomials, functions, and basis functions, extension of Fig. 2.5.

Omission error in terms of SHs

1. Parseval's identity holds for a continuous signal f on the sphere Ω_R, modeled in terms of surface SHs $H_{l,m}^R$. Physically interpreted, the energy of a the signal f is equivalent both in spectral and in spatial domain.
2. The inner product (light green) is equivalently described by the fully normalized Stokes coefficients $F_{l,m}$, i. e. the Fourier transformation of $H_{l,m}^R$, according to Eq. (2.39). In the artificial scenario of completely modeling the continuous signal f up to degree $l \to \infty$, an infinite number of SH coefficients would be required.
3. Modeling the bandlimited signal g by a finite series expansion, i. e. a finite number of Stokes coefficients $G_{l,m}$ (orange), is achieved by convolution, i. e. multiplying the Fourier transformations $F_{l,m}$ with bandlimiting coefficients B_l according to Eq.(4.8) in the spectral domain. The L^2 norm of the truncated series expansion g (purple), cf. Eq. (4.12), delivers the degree variances σ_l^2 of the modeled coefficients $F_{l,m}$, respectively signal g, i. e. $\sigma_l^2(g) = \sum_{m=0}^{l} |F_{l,m}|^2$, providing the errors for different orders m within a degree l (*Jekeli*, 2012).

Mathematical relations between physical and geometrical quantities of the gravity field

Geoid height

The geoid height N following Stokes theory is the geometrical distance between a certain point P_0 of the geoid (potential W_0) and a point Q_0 of the reference ellipsoid with $U = U_0 = W_0$ (*Hofmann-Wellenhof and Moritz*,

Table A.1: Energy (spectral power) of a bandlimited signal g and omission error.

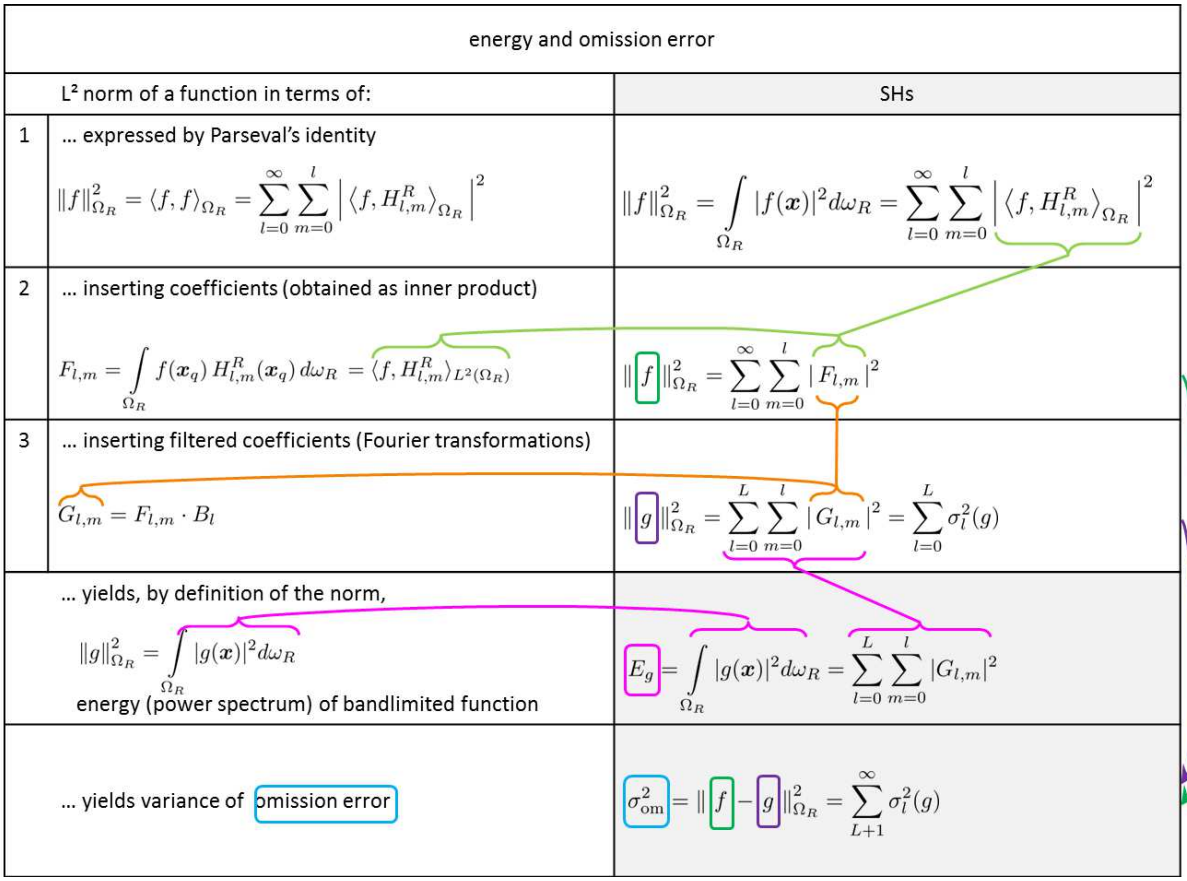

2005, p. 91). The normal potential $U = U(P_0)$ at the geoid point is obtained from

$$U(P_0) = U(Q_0) + \left(\frac{\partial U}{\partial n'}\right)_{Q_0} N$$
$$U(P_0) = U(Q_0) - \gamma(Q_0)\, N \tag{A.7}$$

(*Hofmann-Wellenhof and Moritz*, 2005, p. 93). Further, inserting $U(P_0)$ in Eq. (2.52) at point P_0, i. e.

$$W(P_0) = U(P_0) + T(P_0)$$
$$W(P_0) = U(Q_0) - \gamma(Q_0)\, N + T(P_0)\,, \tag{A.8}$$

it yields with $W(P_0) = U(Q_0)$:

$$T(P_0) = \gamma(Q_0)\, N$$
$$N = \frac{T(P_0)}{\gamma(Q_0)}\,. \tag{A.9}$$

Quasigeoid height

Following Molodensky, the quasigeoid height ζ is defined analogously to N with

$$U(P) = U(Q) + \left(\frac{\partial U}{\partial n'}\right)_{Q} \zeta$$
$$U(P) = U(Q) - \gamma_Q(Q)\, \zeta$$
$$W(P) = U(P) + T(P)$$
$$W(P) = U(Q) - \gamma_Q(Q)\, \zeta + T(P)$$

$$
\begin{aligned}
T(P) &= \gamma_Q(Q)\,\zeta \\
\zeta &= \frac{T(P)}{\gamma_Q(Q)}\,.
\end{aligned}
\tag{A.10}
$$

Stokes formula

The computation of geoid undulations N from gravity anomalies Δg, using Eq. (2.68) reverse, leads to the famous Stokes formula, (e. g. *Hofmann-Wellenhof and Moritz*, 2005, p. 104). On a sphere Ω_R with radius R and surface element $d\omega_R$ defined in Eq. (2.10), it yields

$$
N = \frac{R}{4\pi\gamma_0} \int_{\Omega_R} \Delta g \mathcal{S}(\psi)\, d\omega_R\,. \tag{A.11}
$$

$\mathcal{S}(\psi)$ is the so-called Stokes function or Stokes operator, depending on the spherical distance angle ψ, cf. Eq. (2.11). The key aspect is, that it connects the Earth's geometry with its gravity by relating the metrical quantity N to the physical quantity Δg.

Fundamental equation of physical geodesy

Gravity disturbance δg according to Eq. (2.64) relates the gravity field with potential W to a normal gravity field with potential U. Hereby, the gravity vector $\boldsymbol{g}$ = gradW denotes the change of the total gravity potential W according to Eq. (2.27), while the normal gravity vector $\boldsymbol{\gamma}$ = gradU denotes the change of the normal potential U. Neglecting the small difference between the directions of n and n', and counting h' along the same direction as introduced in Eq. (2.59), it yields for a Point P_0 at the geoid

$$
\begin{aligned}
\delta g &= g(P_0) - \gamma(P_0) \\
&= -\left(-\frac{\partial W}{\partial n} + \frac{\partial U}{\partial n'}\right) \\
&= -\frac{\partial T}{\partial n} \\
&= -\frac{\partial T}{\partial h'}\,.
\end{aligned}
\tag{A.12}
$$

The normal gravity $\gamma(P_0)$ in Point P_0 (with height $h' = N$) is computed from $\gamma_0(Q_0)$, i. e. upward continued from a point Q_0 at the ellipsoid, by applying the Taylor series of Eq. (2.50):

$$
\gamma(P_0) = \gamma_{Q_0}(Q_0) + \frac{\partial \gamma}{\partial h'} N\,. \tag{A.13}
$$

For the gravity anomaly Δg according to Eq. (2.67) it therefore yields

$$
\begin{aligned}
\delta g &= -\frac{\partial T}{\partial h'} \\
&= g(P_0) - \gamma_{Q_0}(Q_0) - \frac{\partial \gamma}{\partial h'} N \\
&= \Delta g - \frac{\partial \gamma}{\partial h'} N \\
\Delta g &= -\frac{\partial T}{\partial h'} + \frac{\partial \gamma}{\partial h'} N\,.
\end{aligned}
\tag{A.14}
$$

And with Bruns formula according to Eq. (2.62) the connection of both functionals Δg,δg results in the **fundamental equation of physical geodesy**

$$
\frac{\partial T}{\partial h'} - \frac{1}{\gamma}\frac{\partial \gamma}{\partial h'} T + \Delta g = 0 \tag{A.15}
$$

(e. g. *Hofmann-Wellenhof and Moritz*, 2005, p. 95).

B Supplementary numerical studies

Regularization

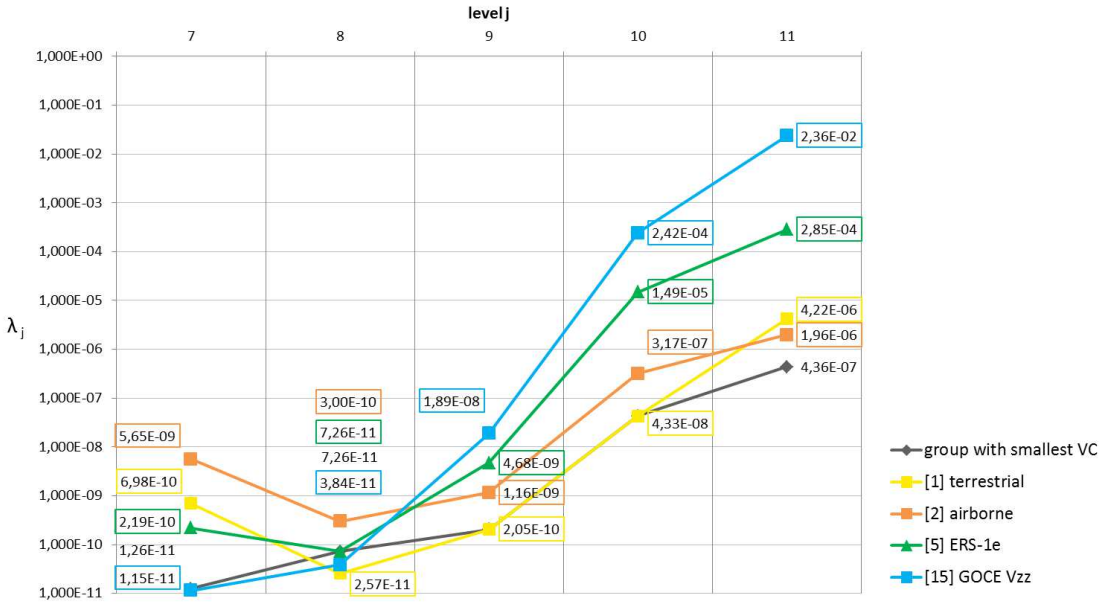

Figure B.1: Study case (g2): Regularization parameter w.r.t. different observation groups.

Fig. B.1 shows the regularization parameter $\lambda_j = \sigma_k^2/\sigma_d^2$ exemplarily w.r.t. the observation groups k = [1], [3], [5], [15] from Tab. 6.19 for different resolution levels j. The ratio of the estimated VC σ_k^2 of the observation group k and the estimated VC σ_d^2 of the prior information describes the contribution of each group to the modeling result relatively to the other groups for each level j. Since the VCs are estimated depending on the accuracy, spectral and spatial resolution of the observations, cf. Sec. 5.2.2, the curves from Fig. B.1 indicate the relative spectral sensitivity of the data sets. The GOCE V_{zz} gradient (blue curve) requires, for instance, with augmenting resolution level more regularization than the other groups. This is reasonable, as GOCE delivers in the MBW, i. e. in the medium frequency domain, most valuable information. For comparison, the black curve from Fig. 6.24 w.r.t. the smallest VC is plotted as well. It indicates the need of regularization at each level independent from the observation type. A more detailed analysis of Fig. B.1 would go beyond the scope of this thesis.

Reducing correlations

In order to reduce correlations between the resolution levels, some investigations are summarized in terms of estimated VCs in Tab. B.1, and corresponding estimated scaling coefficients in Fig. B.2, by strictly using each observation group just once for the levels $j = 8, \ldots, 11$. The estimation model at level $j = 8$ is set up using the [10 – 15] GOCE groups, $j = 9$ using [5 – 9] altimetry groups, $j = 10$ using [2 – 4] air-/shipborne groups, and $J = 11$ using [1] terrestrial data. In Tab. B.1, step (2), they are highlighted in the referring colors. Strong regularization is needed at each level.
The estimated scaling coefficients and their standard deviations are plotted in the left and middle rows of Fig. B.2 for the different levels. The standard deviations show clearly the borderline between the observed and unobserved areas. In the latter, they enormously increase. In the right column the erroneous scaling coefficients are eliminated: (1) the standard deviation s_d of the coefficient must be smaller than or equal to the mean standard deviation $\bar{s}_{d_j}$ of all estimated coefficients of level j; (2) the absolute value $|d_q|$ of the estimated coefficient must be smaller than or equal to (three times) $\bar{s}_{d_j}$, cf. criteria on the right in Fig. B.2.
Replacing the removed coefficients by zero-values and computing the detail signals according to Eq.(5.35)

yields at levels $j = 9, 10, 11$ solutions which are predominated by extremely erroneous effects due to the missing spectral information in wide parts of the study area.

Table B.1: Study case (g2): VCE at different levels; reduced correlations between observation groups.

observation group [k]		j = 8 (L_8 = 280)		j = 9 (L_9 = 550)		j = 10 (L_{10} = 1100)		J = 11 (L_{11} = 2190)	
		step (1)	step (2)	step (1)	step (2)	step (1)	step (2)	step (1)	step (2)
[1]	terrestrial BKG	10^{-9}		10^{-11}		10^{-13}		10^{-14}	10^{-15}
[2]	airborne North Sea	10^{-9}		10^{-10}		10^{-12}	10^{-12}	10^{-13}	
[3]	airborne Baltic Sea	10^{-8}		10^{-10}		10^{-12}	10^{-12}	10^{-14}	
[4]	shipborne BKG	10^{-8}		10^{-9}		10^{-11}	10^{-12}	10^{-13}	
[5]	ERS-1e	10^{-9}		10^{-10}	10^{-10}	10^{-10}		10^{-11}	
[6]	ERS-1f	10^{-9}		10^{-10}	10^{-10}	10^{-10}		10^{-11}	
[7]	Cryosat RADS	10^{-9}		10^{-10}	10^{-10}	10^{-10}		10^{-11}	
[8]	Envisat EM	10^{-9}		10^{-10}	10^{-10}	10^{-11}		10^{-11}	
[9]	Jason-1 GM	10^{-9}		10^{-10}	10^{-10}	10^{-11}		10^{-12}	
[10]	GOCE V_{xx}	10^{-9}	10^{-9}	10^{-9}		10^{-9}		10^{-9}	
[11]	GOCE V_{xy}	10^{-5}	10^{-5}	10^{-5}		10^{-4}		10^{-4}	
[12]	GOCE V_{xz}	10^{-8}	10^{-8}	10^{-8}		10^{-8}		10^{-8}	
[13]	GOCE V_{yy}	10^{-9}	10^{-9}	10^{-9}		10^{-9}		10^{-9}	
[14]	GOCE V_{yz}	10^{-5}	10^{-5}	10^{-5}		10^{-5}		10^{-5}	
[15]	GOCE V_{zz}	10^{-9}	10^{-9}	10^{-9}		10^{-9}		10^{-9}	
	prior information GOCO05s d/o 127	10^{+2}	10^{-6}	10^{-1}	10^{-5}	10^{-5}	10^{-8}	10^{-7}	10^{-10}

Table B.2: MRR study case (g): Coefficients.

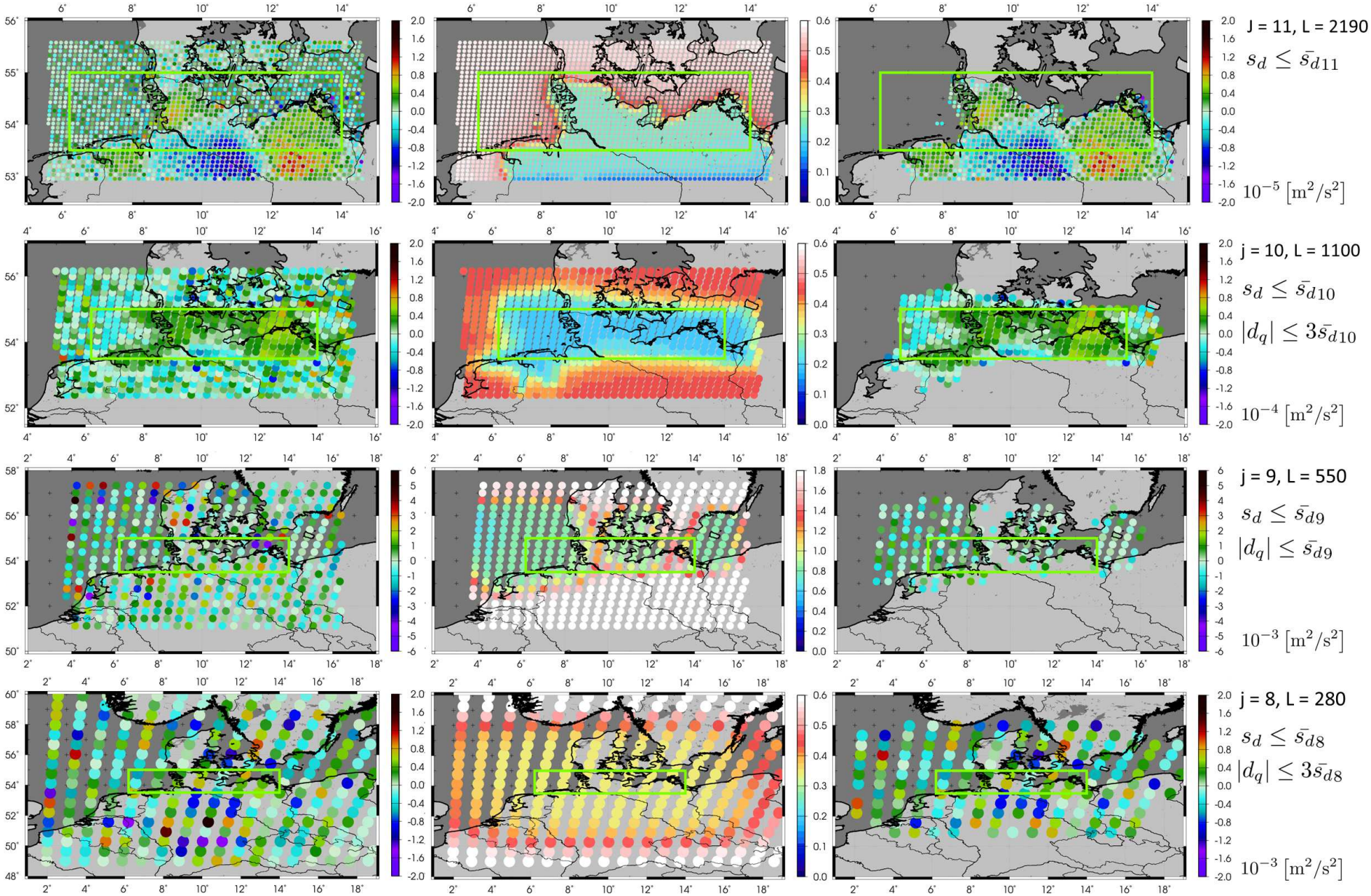

Zusammenhänge zu erforschen, eigene Ideen zu entwickeln, etwas Neues auszuprobieren, ... und am Ende daraus eine Dissertation zu bauen. – Bei all diesen kleinen und großen Herausforderungen unterstützten mich vor allem meine Betreuer: Vielen Dank, Michael Schmidt, für Dein sagenhaftes Engagement, Dein Vertrauen und all die hilfreichen Diskussionen auf dem "Stühlchen ohne Lehne". Vielen Dank, Roland Pail, für Deine einzigartige Betreuung, die so wertvollen und fundierten Gespräche und Deine stets offene Tür. Thank you, Frederik Simons, for the unique chance visiting you and your research group at Princeton University, for the intense discussions and for sharing your great experience. Herzlichen Dank auch an Euch, Johannes Bouman, Wolfgang Bosch und Laura Sánchez, dass ich Euch stets um Euren Rat fragen konnte. Vielen Dank, Denise Dettmering und Klaus Börger, für die hilfreichen Dialoge; Danke an Roger Haagmans für die ideenreichen Denkanstöße; Danke an Euch, Katrin und Majid, für den tollen Austausch quer über die ganze Welt, und Danke, Kirsten und Sabine, für Euer Mitwirken. Liebe Eltern, vor allem möchte ich Euch Danke sagen für Eure unbeschreibliche Rückenstärkung, Euer Dasein, und Eure so selbstlose Herzlichkeit und Liebe.